THÈSE

En vue de l'obtention du

DOCTORAT DE L'UNIVERSITÉ DE TOULOUSE

Délivré par : *l'Université Toulouse 3 Paul Sabatier (UT3 Paul Sabatier)*
Cotutelle internationale *Université Libanaise*

Présentée et soutenue le *12/11/2021* par :
Farah BAZZI

Restauration d'Images en IRM Anatomique pour l'Étude Préclinique des Marqueurs du Vieillissement Cérébral

JURY

CHRISTINE FERNANDEZ	Professeure d'Université	Rapporteure
JEAN-LOUIS DILLENSEGER	Maître de Conférences	Rapporteur
CAROLE LARTIZIEN	Directrice de Recherche	Examinatrice
NICOLAS PASSAT	Professeur d'Université	Examinateur
ADRIAN BASARAB	Maître de Conférences	Directeur de Thèse
HASSAN AMOUD	Professeur d'Université	Directeur de Thèse
MURIEL MESCAM	Maîtresse de Conférences	Co-Directrice de Thèse
AHMAD DIAB	Associate Professor	Co-Directeur de Thèse
DENIS KOUAMÉ	Professeure d'Université	Invité
OMAR FALOU	Associate Professor	Invité

École doctorale et spécialité :
    MITT : Image, Information, Hypermédia
Unité de Recherche :
    Institut de Recherche en Informatique de Toulouse (UMR 5505)
Directeur(s) de Thèse :
    Adrian Basarab et *Hassan Amoud*
Rapporteurs :
    Christine Maloigne-Fernandez et *Jean-Louis Dillenseger*

THESE de doctorat en Cotutelle

Pour obtenir le grade de Docteur délivré par

L'Université Libanaise

L'Ecole Doctorale des Sciences et Technologie

Spécialité : Physique Biomédicale

Présentée et soutenue publiquement par

BAZZI Farah

12/11/2021

Restauration d'Images en IRM Anatomique pour l'Étude Préclinique des Marqueurs du Vieillissement Cérébral

Directeur de thèse **: AMOUD Hassan**

Co-encadrement de la thèse **: BASARAB Adrian**

Membre du Jury

Mme Christine Fernandez, Professeure d'Université, Université de Poitiers   Rapporteure

M. Jean-louis Dillenseger, Maître de Conférences, Université de Rennes1   Rapporteur

Mme Carole Lartizien, Directrice de Recherche, Université de Lyon   Examinatrice

M. Nicolas Passat, Professeur d'Université, Université de Reims   Examinateur

M. Hassan Amoud, Professeur d'Université, Université Libanaise   Directeur de Thèse

M. Adrian Basarab, Maître de Conférences, Université Paul Sabatier   Directeur de Thèse

M. Ahmad Diab, Associte Professor, Université Libanaise   Co-directeur de Thèse

Mme Muriel Mescam, Maîtresse de Conférences, Université Paul Sabatier   Co-directrice de Thèse

M. Omar Falou, Associte Professor, Université Libanaise   Invité

M. Denis Kouamé, Professeur d'Université, Université Paul Sabatier   Invité

Acknowledgements

I own the sincerest gratitude and appreciation to my PhD supervisors, Dr. Adrian Basarab, Prof. Hassan Amoud, Dr. Muriel Mescam, and Dr. Ahmad Diab, whose expertise and consistent guidance and support were invaluable during this research. I would like also to thank Prof. Denis Kouamé and Dr. Omar Falou for co-supervising this thesis with their insightful feedback which pushed me to sharpen my thinking and brought my work to a higher level. I am grateful for all of them as they continuously provided encouragement and were always willing and enthusiastic to assist in any way they could throughout the research project. It is true that without the help you gave me in developing my research methodology and the emotional support you provided, I wouldn't have made it. I'm proud of, and grateful for, my time working with you!

I would like also to thank the members of my PhD committee, Professors Christine Fernandez, Jean-louis Dillenseger, Carole Lartizien, and Nicolas Passat, for being an integral part of me being able to make it to the end of my PhD journey. Your suggestions brought in threads of thought that made my research so much richer, and my dissertation something I can be proud of having written. Thank you for your feedback and comments that refined my defense.

I thank all the former and present members of the IRIT lab especially my colleagues with whom I shared this journey and who showed a great support during the tough days. I would like also to thank my second family in the CerCo lab. I would like to acknowledge Caroline Fonta, Florence Rémy-El Boustani, and Nathalie Vayssiere with whom I had the pleasure to share memorable moments and

Résumé

Les maladies neurovasculaires et neurodégénératives liées à l'âge sont en forte augmentation. Alors que ces changements pathologiques montrent des effets sur le cerveau avant l'apparition de symptômes cliniques, une meilleure compréhension du processus de vieillissement normal du cerveau aidera à distinguer l'impact des pathologies connues sur la structure régionale du cerveau. En outre, la connaissance des schémas de rétrécissement du cerveau dans le vieillissement normal pourrait conduire à une meilleure compréhension de ses causes et peut-être à des interventions réduisant la perte de fonctions cérébrales associée à l'atrophie cérébrale. Par conséquent, ce projet de thèse vise à détecter les biomarqueurs du vieillissement normal et pathologique du cerveau dans un modèle de primate non humain, le singe marmouset (Callithrix Jacchus), qui possède des caractéristiques anatomiques plus proches de celles des humains que de celles des rongeurs. Cependant, les changements structurels (par exemple, de volumes, d'épaisseur corticale) qui peuvent se produire au cours de leur vie adulte peuvent être minimes à l'échelle de l'observation. Dans ce contexte, il est essentiel de disposer de techniques d'observation offrant un contraste et une résolution spatiale suffisamment élevés et permettant des évaluations détaillées des changements morphométriques du cerveau associés au vieillissement. Cependant, l'imagerie de petits cerveaux dans une plateforme IRM 3T dédiée à l'homme est une tâche difficile car la résolution spatiale et le contraste obtenus sont insuffisants par rapport à la taille des structures anatomiques observées et à l'échelle des modifications attendues.

Cette thèse vise à développer des méthodes de restauration d'image pour les images IRM précliniques qui amélioreront la robustesse des algorithmes de segmentation. L'amélioration de la résolution

spatiale des images à un rapport signal/bruit constant limitera les effets de volume partiel dans les voxels situés à la frontière entre deux structures et permettra une meilleure segmentation tout en augmentant la reproductibilité des résultats. Cette étape d'imagerie computationnelle est cruciale pour une analyse morphométrique longitudinale fiable basée sur les voxels et l'identification de marqueurs anatomiques du vieillissement cérébral en suivant les changements de volume dans la matière grise, la matière blanche et le liquide cérébral.

Abstract

Age-related neurovascular and neurodegenerative diseases are increasing significantly. While such pathological changes show effects on the brain before clinical symptoms appear, a better understanding of the normal aging brain process will help distinguish known pathologies' impact on regional brain structure. Furthermore, knowledge of the patterns of brain shrinkage in normal aging could lead to a better understanding of its causes and perhaps to interventions reducing the loss of brain functions. Therefore, this thesis project aims to detect normal and pathological brain aging biomarkers in a non-human primate model, the marmoset monkey *(Callithrix Jacchus)* which possesses anatomical characteristics more similar to humans than rodents. However, structural changes (e.g., volumes, cortical thickness) that may occur during their adult life may be minimal with respect to the scale of observation. In this context, it is essential to have observation techniques that offer sufficiently high contrast and spatial resolution and allow detailed assessments of the morphometric brain changes associated with aging. However, imaging small brains in a 3T MRI platform dedicated to humans is a challenging task because the spatial resolution and the contrast obtained are insufficient compared to the size of the anatomical structures observed and the scale of the xpected changes with age.

This thesis aims to develop image restoration methods for preclinical MR images that will improve the robustness of the segmentation algorithms. Improving the resolution of the images at a constant signal-to-noise ratio will limit the effects of partial volume in voxels located at the border between two structures and allow a better segmentation while increasing the results' reproducibility. This computational imaging step is crucial for a reliable longitudinal voxel-based morphometric analysis

and for the identification of anatomical markers of brain aging by following the volume changes in gray matter, white matter and cerebrospinal fluid.

Acronyms

ADMM   Alternating Direction Method of Multipliers

ANN   Artificial Neural Networks

AWGN   Additive White Gaussian Noise

BCCB   Block Circulant matrix of Circulant Blocks

CNN   Convolution Neural Network

CNR   Contrast-to-Noise Ratio

CSF   Cerebrospinal Fluid

CT   Computed Tomography

DFT   Discrete Fourier Transform

DICE   Dice Similarity Coefficient

EM   Expectation-maximization

FID   Free Induction Decay

fMRI   Functional Magnetic Resonance Imaging

FT   Fourier Transform

FSR   Fast Super Resolution

GGD   Generalized Gaussian Distribution

HR   High Resolution

GM   Gray Matter

IDFT	Inverese Discrete Fourier Transform
IFT	Inverse Fourier Transform
ISNR	Improvement in Signal-to-Noise Ratio
i.i.d	independent and identically distributed
LR	Low Resolution
MI	Mutual Information
MMSE	Minimum Mean Square Error
MR	Magnetic Resonance
MRI	Magnetic Resonance Imaging
NHP	Non-human Primates
NLM	Non-local Means Filter
NMI	Normalized Mutual Information
MSE	Mean Square Error
NRMSE	Normalized Root Mean Square Error
PET	Positron Emission Tomography
PSF	Point Spread Function
PSNR	Peak Signal-to-Noise Ratio
RF	radio-frequency
RMSE	Root Mean Square Error
SNR	Signal-to-Noise Ratio
SPECT	Single-Photon Emission Computed Tomography
SR	Super Resolution
SSIM	Structural Similarity Index Measure
STD	Standard Deviation

TF   Tensor Factorization

TRF   Tissue Reflectivity Function

TV   Total Variation

US   Ultrasound

VBM   Voxel-Based Morphometry

WM   White Matter

Contents

List of publications

International Journal papers

1. F. Bazzi, M. Mescam, A. Diab, O. Falou, H. Amoud, A. Basarab, and D. Kouamé, **Marmoset Brain Segmentation from Deconvolved Magnetic Resonance Images and Estimated Label Maps**, *Magnetic Resonance in Medicine*, 2021.

Conference papers

1. F. Bazzi, J. Rodriguez-Callejas, C. Fonta, M. Mescam, A. Diab, O. Falou, H. Amoud, A. Basarab, and D. Kouamé,**Brain Segmentation from Super-Resolved Magnetic Resonance Images**, *2019 Fifth International Conference on Advances in Biomedical Engineering (ICABME). IEEE*, p. 1-4, Oct. 2019.

2. F. Bazzi, M. Mescam, A. Basarab, and D. Kouamé, **On Single-Image Super-Resolution in 3D Brain Magnetic Resonance Imaging.**, *41st Annual International Conference of the IEEE Engineering in Medicine and Biology Society (EMBC). IEEE*, p. 2840-2843, July 2019.

Submitted conference paper

1. F. Bazzi, M. Mescam, A. Diab, O. Falou, H. Amoud, A. Basarab, and D. Kouamé, **Synthesis of 7T MRI from 3T Brain MRI of Marmosets Using Deep Learning**, *International Conference on Digital Health Technologies (ICDHT 2021).*

CHAPTER 1

Introduction

Contents

Healthy aging is defined as a process that involves functional and cognitive decline and decreased long-term memory without diseases. However, the high risk of neurodegenerative diseases to accompany normal aging process requires a better understanding and quantification of biomarkers of cerebral aging. This helps to distinguish age-related diseases from normal aging and facilitate their treatment. The advances in neuroimaging allowed the study of the macro-structural changes occurring in the brain throughout the life span. In particular, the development of magnetic resonance scanners increased its value as a primary tool for the study of age-related changes in the brain. Due to ethical and practical limitations, researchers investigated animal models possessing homologous brain changes to humans. In this chapter, we will introduce the concept of cerebral aging. Then, we

will provide a general overview of the basics of magnetic resonance imaging and voxel based morphometry analysis that will be further used to detect statistically significant changes in the aging brain. Since this research work is a preclinical study, we will highlight the idea of using animal models for brain age research. Finally, we will present the motivations of the research work and the context of the manuscript.

1.1 Cerebral aging

Globally, life expectancy has been increasing dramatically in the last two centuries due to the increase in the individual's life quality and the advancing technologies. Therefore, researchers are focusing on not only increasing the life span but also on establishing healthy aging that guarantees an improved life quality free of age-related diseases. However, elderly people experience more difficulties in performing daily tasks and eventually lose their autonomy, independence and functional capacity [1, 2]. Since functional capacity is linked with brain structure, a detailed knowledge of healthy brain development is crucial for better understanding of changes that occur as one ages (Figure 1.1).
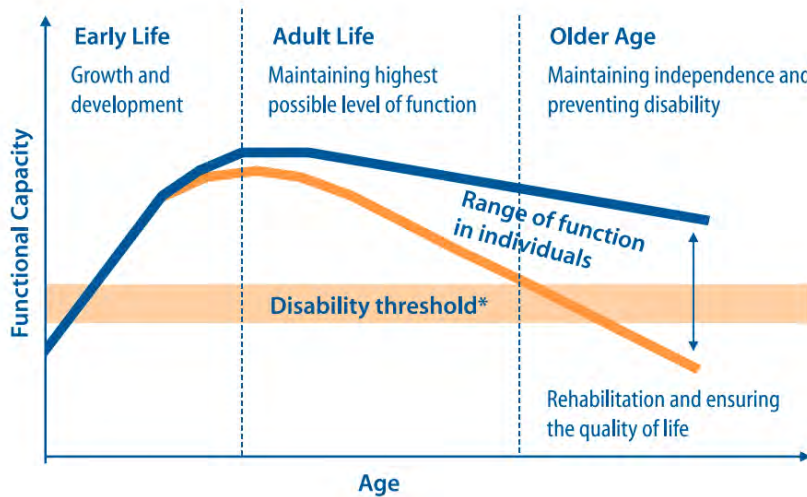
Figure 1.1: Functional capacity with respect to life time course. Figure is collected from [2].

While the brain develops in a complex series of dynamic and adaptive processes, an understanding of the aging process is the first step towards following and treating a broad spectrum of brain

disorders linked to aging, such as learning disability, Parkinson's, and Alzheimer's diseases [3]. These neurodegenerative diseases induce alterations in the brain that can be observed before the clinical symptoms of the disease appear (Figure 1.2). Thus, a better definition of the normal aging biomarkers and age-related patterns of change helps to intervene early to slow the effects of the brain shrinkage on the population. It also leads to a better identification and distinguishing of the neurodegenerative diseases and their effects on the brain [4]. Detecting structural brain changes will thus allow to relate them with functional, cognitive, and behavioral changes and understand the pathways and mechanisms associated with aging, which will help in increasing life span and, more importantly, health span.
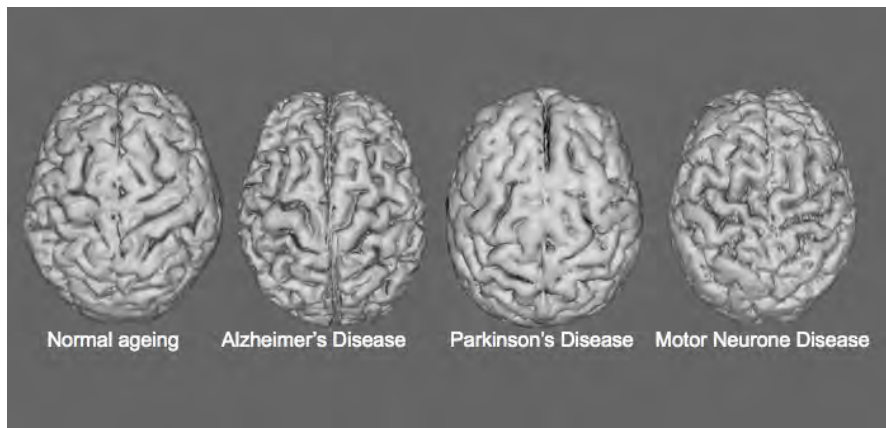
Figure 1.2: Effects of aging and neurodegenerative diseases on the brain. Figure is collected from www.ndcn.ox.ac.uk/research/neurodegeneration-imaging.

Cerebral aging, as defined in [5], is a complex and heterogeneous process that is associated with a high degree of inter-individual variability due to neuronal and synaptic alterations inducing functional and network disruptions and particularly affecting brain regions such as the hippocampus and prefrontal areas. Such age-related brain changes differ in their location, severity, and extent and are associated with loss in sensation, cognition, memory, and motor control. Based on *post mortem* and *in vivo* studies, researchers believe that the brain changes with age, and more specifically shrinks, with the intersubject variability and the extent of these changes still being elusive [6]. Thus, the brain undergoes several structural changes that reflect the normal aging process and

are therefore not necessarily pathologic. Assessment of these changes becomes necessary and can be investigated by the quantitative study of cerebral tissue volumes. Postmortem studies of cultivated brain slices from healthy human brains have shown a great potential in detecting brain tissues that had undergone pathological changes with age [7, 8]. However, postmortem analyses present some methodological constraints that may affect the study's results, such as the small sample size, the interval between death and fixation, the timing of measurement, inclusion or exclusion of the brain stem and meninges, and the ratio of the brain weight to body weight [6]. With the development of advanced and powerful neuroimaging tools, traditional postmortem analysis has been replaced by non-invasive in-vivo technologies. This allows to overcome the mentioned limitations and to study a larger sample of brains at all ages.

Various imaging techniques have proven to be effective in the neuroimaging field. The development of X rays, Computed Tomography (CT), Positron Emission Tomography (PET) and Single Photon Emission Computed Tomography (SPECT) have shown some progress, but their dependence on ionizing radiations presents some limitations for the repeated study of healthy subjects. Magnetic Resonance Imaging (MRI), Functional MRI (fMRI), Magnetic Resonance Spectroscopy (MRS) and Magnetoencephalography (MEG) are better suited for the structural and functional study of the brain with the possibility of having repeated measures since they do not involve ionizing radiations or radioactive isotopes and thus do not present any biological hazard [9]. An effective evidence of age-related changes in the brain has been well characterized using structural and functional MRI. In particular, structural MRI enables the detection of anatomical alterations and brain structure differences contributing to the cognitive and functional symptoms of normal aging [5, 10].

Quantitative cerebral tissue volumes are important for the assessment of age-related changes in the brain. A vast number of cross-sectional and longitudinal studies has been dedicated for the study of whole and regional brain changes associated with normal brain aging. The tissue-based analysis of the brain's main compartments i.e., gray matter (GM), white matter (WM), and cerebrospinal fluid (CSF), demonstrates evidence of brain changes with age [11]. Volumetric GM analysis can reveal cortical and subcortical atrophy patterns and brain networks exhibiting GM loss. Unlike the extensive researches conducted for GM changes with age, the analysis of aging effects on the WM

region remained sparse due to its complexity [12]. However, postmortem and in-vivo MRI studies on age-related changes present conflicting results in the extent, location and severity of these changes mainly due to the difference in the studied population and the study design [8, 13]. Factors such as sexual dimorphism and brain asymmetries may also affect the results of the aging study. Therefore, it becomes essential to have a powerful examination tool and an accurate segmentation technique for the correct monitoring of structural changes in the brain tissue volumes.

1.2 Animal models in aging research

As researchers' interest in understanding the normal aging processes and their effects on the human brain increases, this task remains challenging. The long life span of the human being and the ethical, practical, environmental, and social limitations accompanying the investigation of the human brain renders using humans for experiments and research impractical. A possible alternative for the human aging study is thus to investigate animal species that exhibit similar aging processes to be used as models for therapeutic treatments [14].

1.2.1 Animal models

Researchers are elaborating their work on which animal models to use for study of aging of the human brain. There are several aspects to consider before conducting aging research on animals, including the animal's genetic basis, the physiological pathways regulating the rate of aging, and identifying factors that influence the life span.

Organisms The first primitive organisms that have been used in aging studies are yeast, roundworms, and fruit flies. Although these organisms are not considered animals, they possess genetic and cellular characteristics that aided the aging research. For instance, such models have been helpful to conclude the effect of restriction of caloric intake in increasing the life span of animal species and detecting the genes that may delay the aging process [14, 15].

Rodents   Preclinical research has then turned its interest towards the investigation of mammals that are closer to human beings. Rodents, such as mice and rats, have been the main subjects of interest for scientists in human aging researches. Advantages of using rodents in aging studies include the deep knowledge about their biology, the convenience of use, the capacity to regulate their environmental factors, the ability to manipulate their genes and their short life span that makes them easier to study than the long-lived animals. Results showing that dietary and genetic changes in mice can slow aging have favored the importance of this model for human aging. However, several concerns are raised concerning rodents as an aging model, of which the significant difference in the biological aging between rodents and humans, the fact that they don't develop several important age-related diseases naturally, and that rodents may be distantly related to humans [14–18].

Non-human primates (NHP)   Since the complexity of the human physiology can not be replicated using simple organisms or rodent models, the interest in NHP as models of human brain aging began to grow. NHP are the most logical and appreciated models for the aging study. Preclinical NHP models offer a link between research and clinical applications as they offer findings that are highly translatable to human health issues. The advantages of using NHP as animal models include their long-average life span, the human resemblance in naturally occurring age-associated diseases, and the trade-off between limitations of using rodents or humans in the aging study. Several species have been investigated as a possible model for human brain aging, including the common marmoset, the squirrel monkey, the macaque, the vervet monkey, the baboon and the chimpanzee. Other alternative vertebrate aging models have been also reported in the literature, such as fish, dogs, cats, and birds [14, 19].

Old world monkeys, Rhesus Macaques (*Macaca Mulatta*), exhibit an aging process similar to a human with an aging rate three times faster, as they age at 20 years and show signs of physical decline. Macaques have been the prime focus of aging research as they are well adapted to laboratory research and show genetic, endocrinological, physiological, neuroanatomical, and cognitive similarities to humans. Despite the encouraging traits rendering macaques an important NHP model of aging, several drawbacks limit their use, including their heavyweight and strength, the need for sophisticated

equipment to navigate their daily life, the potential of aggressive behavior, their ability to carry and transmit pathogens, and the expensive cost for the aging study [16]. Apes have also provided interesting findings in the field of aging research. Chimpanzees show more than 98% similarity with humans at the DNA level, which made them the most common used apes in the biomedical research. Reduction in gray and white matter volumes with age have been one of the most relatable results to the aging process in the human brain. However, the use of Chimpanzees was further limited due to ethical principles stated by the National Institute of Health (NIH) [16]. Among the new world monkeys, the common marmoset (*Callithrix jacchus*) is being investigated as a promising model for the aging research. To summarize, Table 1.1 presents the main characteristics of the NHP, and Table 1.2 summarizes the advantages and limitations of using different NHP in the aging study.

Table 1.1: Characteristics of NHP used in aging research. This table has been collected from [16]

Model	Average adult weight (kg)	Average life span (years)	Maximim life span (years)
Grey mouse lemur	0.06 - 0.12	8 - 10	18
Common marmoset	0.35 - 0.40	7 - 8	21
Squirrel monkey	0.60 - 1.30	20	30
Macaques	5 - 10	26	40
Vervet monkey	3 - 7	20	31
Baboon	12 - 25	30	38
Chimpanzee	40 - 65	30	65

Table 1.2: Advantages and limitations of commonly used NHP in aging research. This table was collected from [16].

Species	Scientific name	Classification	Advantages	Limitations
Grey mouse lemur	*Microcebus murinus*	Prosimian	Small body size	Small body sizeavailability,
			short life span	nocturnal, solitary,
			interesting model for thermoregulation research	phylogenetic distance from humans,
				lack of commercially available resources
Common marmoset	*Callithrix jacchus*	New World monkey	Small body size	Small body size
			reasonably short life span	aging process needs further discription
			short generation time	lack of husbandry procedures
			social structure	lack of commercially available resources
			fecundity	
Squirrel monkey	*Saimiri spp.*	New World monkey	Small body size	Long life span for body size
			somewhat realistic aging course	lack of commercially available resources
Macaques	*Macaca spp.*	Old World monkey	Well characterized	Long life span
			closely related to humans	limited availability of aged animals
			large body size	zoonotic concerns
			realistic aging course	
Vervet monkey	*Chlorocebus pygerythrus*	Old World monkey	Closely related to humans	Long life span
			large body size	limited availability of aged animals
			realistic aging course	
Baboon	*Papio hamadryas*	Old World monkey	Closely related to humans	Long life span
			large body size	limited availability of aged animals
			realistic aging course	housing requirements
Chimpanzee	*Pan troglodytes*	Great ape	Closest human relative	Long life span
			realistic aging course	housing requirements
			large body size	imposed limitations on research
				ethical considerations

1.2.2 The Common marmoset

In the study of aging and age-related diseases, researchers aim to establish shorter studies on small-bodied short-lived NHP. A small new world primate, the common marmoset (*Callithrix jacchus*), has been recognized as an effective model for neuroscience, infectious disease, behavioral research, obesity, and reproductive biology. As an NHP model, the common marmoset offers many advantages that render it a popular and effective aging model. With early maturation, short life span, and rapid life history, the use of marmosets allowed researchers to perform a longitudinal aging assessment at shorter scales from young adulthood to old age. Their human-like cooperative breeding structure and their small sizes make them easier to handle and maintain since they need smaller space compared to macaques. However, some difficulties accompany the research work conducted on marmosets. The primary cause of marmoset death has been reported to be bacterial infection, with a linear death rate across middle age not observable in humans or other NHP species. In addition, aging in marmosets may be associated with an increased risk of cardiovascular and renal diseases. Therefore, studying the marmoset population and increasing their survival rate require maintaining the animals in barrier conditions to decrease their exposure to infectious agents and pathogens [3, 19].
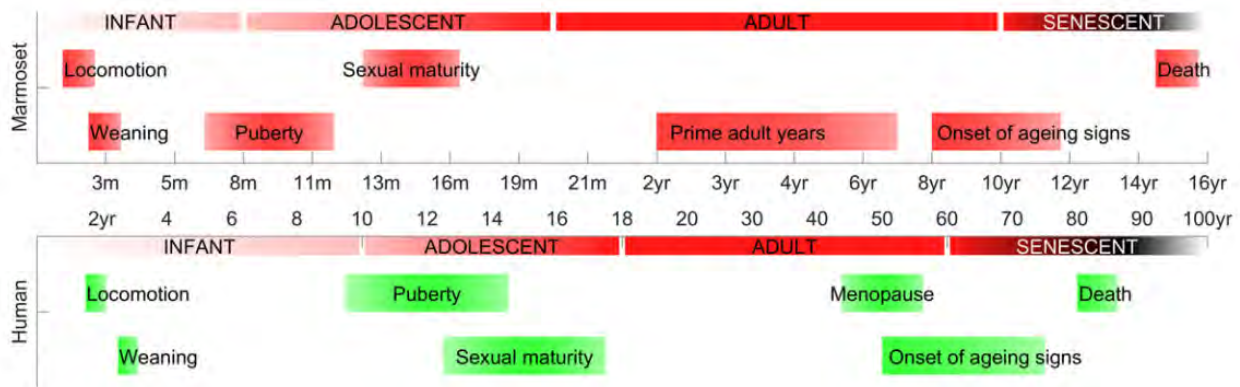
Figure 1.3: Comparison of developmental epochs between marmosets and humans during their life spans. Figure is collected from [20].

The marmoset brain is an isometrically scaled version of the human brain in terms of weight and number of neurons. With a weight of 8*g*, its brain is 11 times smaller than that of macaques (90*g*)

and 190 times smaller than that of humans 1500g (Figure 1.4) [21]. Since its discovery, the marmoset brain model has been used to reflect neurodegenerative diseases of the human brain. The interest in marmoset brain studies increased mainly due to the features analogous to the human brain, especially in regions such as the temporal lobe, the sensory cortices, and the prefrontal cortex. Not only does the marmoset share similar age-related diseases and conditions as humans, but researchers have also found evidence of neurogenesis that occurs before old age. Since marmosets are capable of learning and performing simple cognitive tasks, they are well adapted for the study of disease progression [22, 23]. Thus, the marmoset model has been thoroughly evaluated as a model for Parkinson's, Alzheimer's, Huntington's diseases, and multiple sclerosis [3, 19, 21].
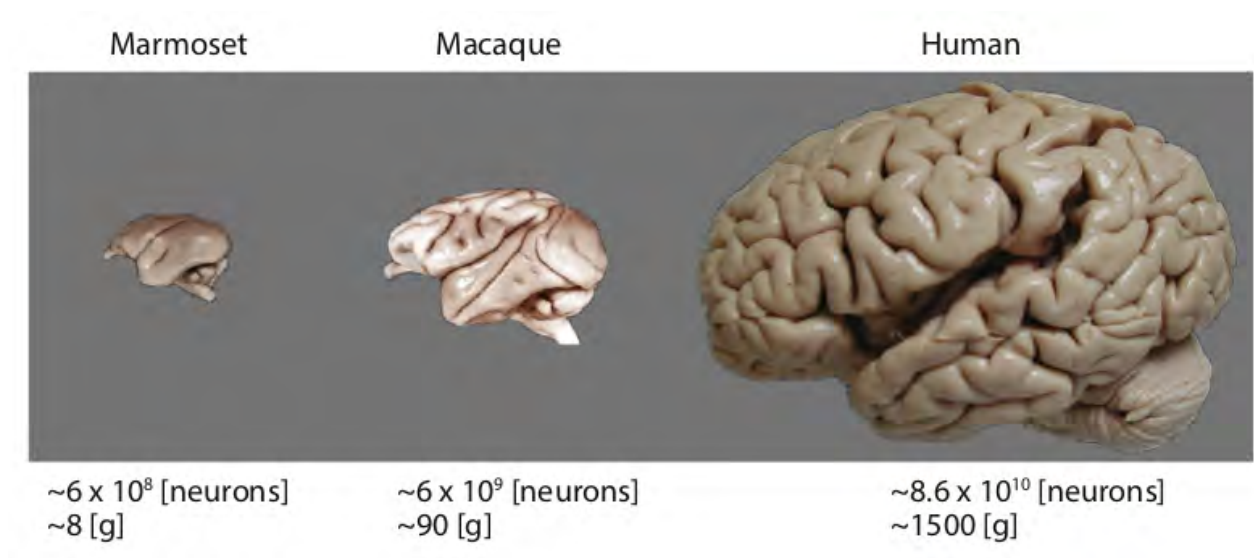
Figure 1.4: Marmoset brain compared to macaques and humans brains in terms of size and number of neurons. This figure is collected from [21] and originally adapted from [24].

The lissencephalic (smooth) cortex of the marmoset brain offers advantages for developing techniques to explore neural processes and their underlying natural behaviors since all cortical substrates are on the surface directly under the skull. However, invasive procedures may cause damage to the brain due to electrode placement and injections. The use of non-invasive imaging techniques, such as MRI, provides an alternative for translational insights in neuroscience and opens the path to answer

many open questions in research.

1.3 Magnetic Resonance Imaging

Clinical neuroimaging has been one of the most useful tool in the diagnosis and detection of pathologies associated to neurodegenerative diseases. In the context of detection of age-related changes in the brain, it is important to have observation techniques allowing sufficiently high contrast and spatial resolution. MRI provides high soft tissue contrast and presents the best imaging modality for measuring volumes of brain regions and its constituents [25].

1.3.1 Basics of MRI

MRI is a non-invasive technique widely used for imaging of humans and animals (Figure 1.5). The Nuclear MR phenomenon was first described and measured by Isidor Rabi in 1938 [26] and then expanded by Felix Bloch and Edward Mills Purcell in 1946 [27, 28]. A fundamental property is that nuclei with odd atomic weights and/or odd atomic numbers, such as 1H, 13C, and 23Na, possess an angular momentum which is often called spin which creates a magnetic field around it called the magnetic moment. In the presence of an external magnetic field B_0, the hydrogen nuclear spins are aligned in two energy states: parallel and anti-parallel. The angular frequency ω_0 of the nuclear precession is proportional to the external magnetic field according to Larmor equation: $\omega_0 = \gamma B_0$, where γ is the gyromagnetic ratio. The spin population difference between the two states generates an observable macroscopic magnetization vector $\overrightarrow{M}$ that points along the positive direction of the external magnetic field.

As a radio frequency (RF) field B_1 with frequency ω_0 is applied, the spins are excited and the magnetization vector $\overrightarrow{M}$, initially in the z-plane, is tilted towards the xy-plane. As a result, magnetization transverse component $\overrightarrow{M}_{xy}$ increases. Meanwhile, its longitudinal component $\overrightarrow{M}_z$ decreases and may totally disappear. A pulse which rotates the magnetization vector by a certain flip angle α is often referred to as an α-pulse (Figure 1.6). After RF excitation, the magnetization returns to its original state: this phenomenon is called relaxation. We can distinguish two types
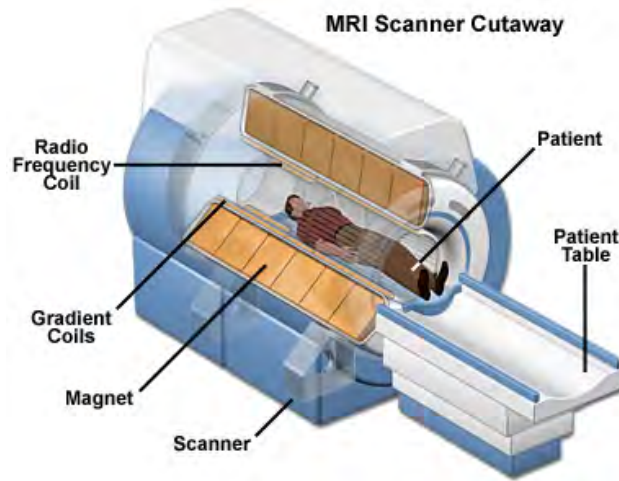
Figure 1.5:   MRI machine setup for image acquisition showing its different components. Figure is collected from www.orthopaedicdoctor.com.sg/magnetic-resonance-imaging/.

of relaxations: the spin-lattice relaxation, characterized by relaxation time T_1 and describing the recovery of the longitudinal magnetization caused by energy exchange between the protons and the surrounding environment (Figure 1.7a), and the spin-spin relaxation, characterized by relaxation time T_2 describing the loss of transversal magnetization (Figure 1.7b). Since the decrease in transversal magnetization is caused by the exchange of energy with the environment and energy changes between spins, T_2 is smaller than T_1 [29]. At the end of the RF pulse, a free induction decay (FID) signal is produced, this is the MR signal. While the MR signal is supposed to decay with a time constant T_2, the process happens more quickly with a shorter effective time constant T_2^*. For instance, a spin echo sequence gets back the lost signal using a 180-degree pulse applied at time τ after a 90-degree RF pulse, and a spin echo is generated after an echo time $T_E = 2\tau$. However, this is a basic sequence in MRI. In practice, marmoset MR images are acquired using the gradient echo sequence (Figure 1.8). A negative gradient pulse applied directly after the RF pulse dephases the spin frequencies. When the polarity of the gradient is reversed, the precessing spins will be in phase again. Therefore, the gradient echo is the measured echo during the rephasing of the FID. The echo time for a gradient echo has to fit into the T_2^* time. This is why the gradient-echo technique is faster than the spin-echo technique [30].
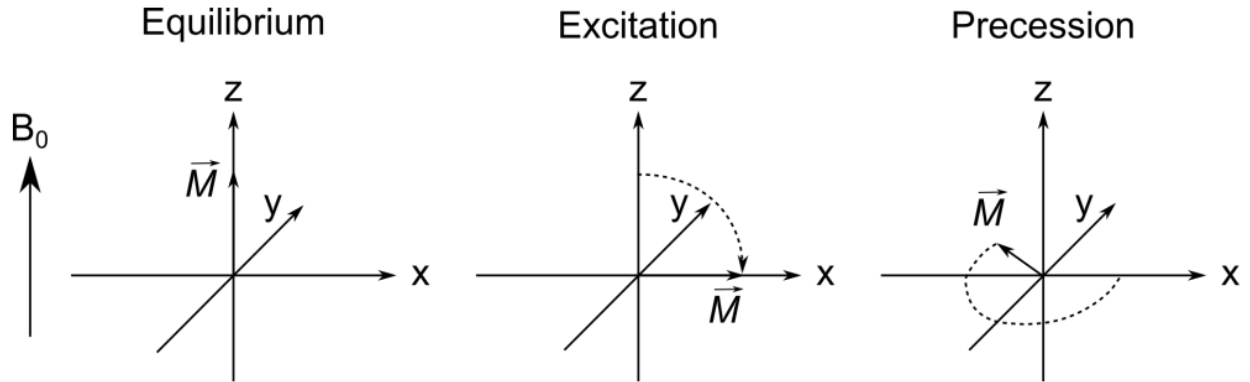
Figure 1.6: In equilibrium, the magnetic moments align themselves along the static magnetic field B_0. After excitation with the RF pulse, the spins are tilted into the xy-plane and precess with the Larmor frequency ω_0. Figure is collected from [29].

(a) Recovery of longitudinal magnetization

(b) Decay of transverse magnetization
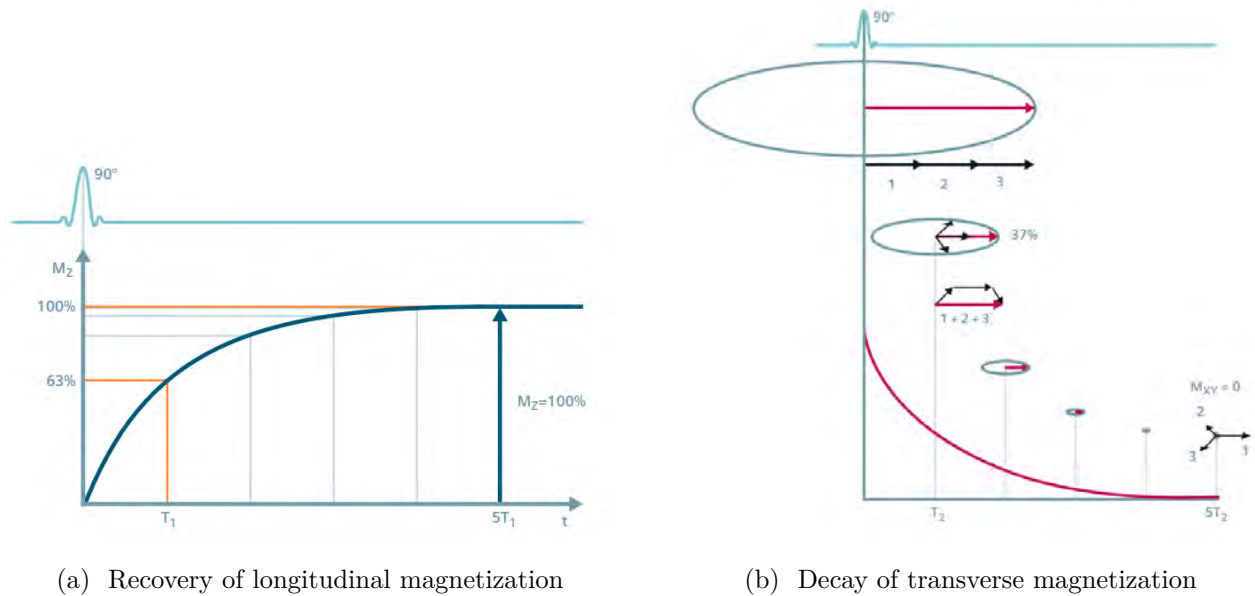
Figure 1.7: Recovery of longitudinal magnetization (a) and decay of the transverse magnetization (b) are exponential processes characterized by the time constants T_1 and T_2 for exponential growth and decay respectively. After the RF-pulse, spins that were phase coherent producing a signal in the receiver coil start to get out of phase again. Figures were collected from [30].
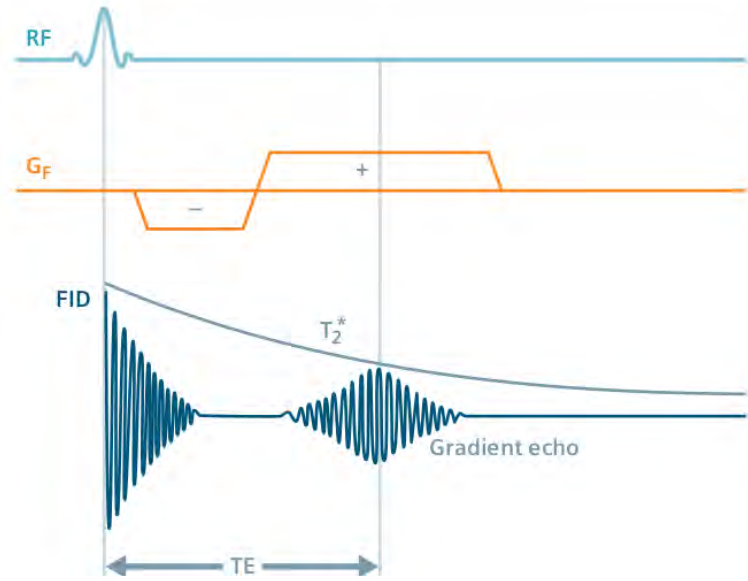
Figure 1.8: Illustration of a Gradient echo sequence achieved using a gradient pulse. Figure is collected from [30].

There are different types of gradient-echo sequences applied in clinical practice. The advantage of a gradient-echo sequence is the possibility to decrease repetition time T_R by using a reduced flip angle α of less than 90 degrees. In this case, only part of the magnetization $\overrightarrow{M}$ is converted into a transverse magnetization $\overrightarrow{M}_{xy}$. On the other hand, the longitudinal magnetization is not zero after such an α-pulse, but continues to have a reduced magnitude $\overrightarrow{M}_z$ [30].

1.3.2 Image formation

The detected MR signal is proportional to the density of all excited proton spins within the reception range of the RF coil. To form the MR image, spatial encoding is introduced by the use of additional gradient coils along with main magnetic field B_0 in x, y and z directions as introduced by Lauterbur in 1973 [31]. By switching them separately or together, a spatial dependent magnetic field can be created (Figure 1.9).

The final image is not directly formed from the signal produced. The use of these additional gradients and a suitable signal processing method produces raw data from which the final image is

(a) Slice selection

(b) Oblique slice selection
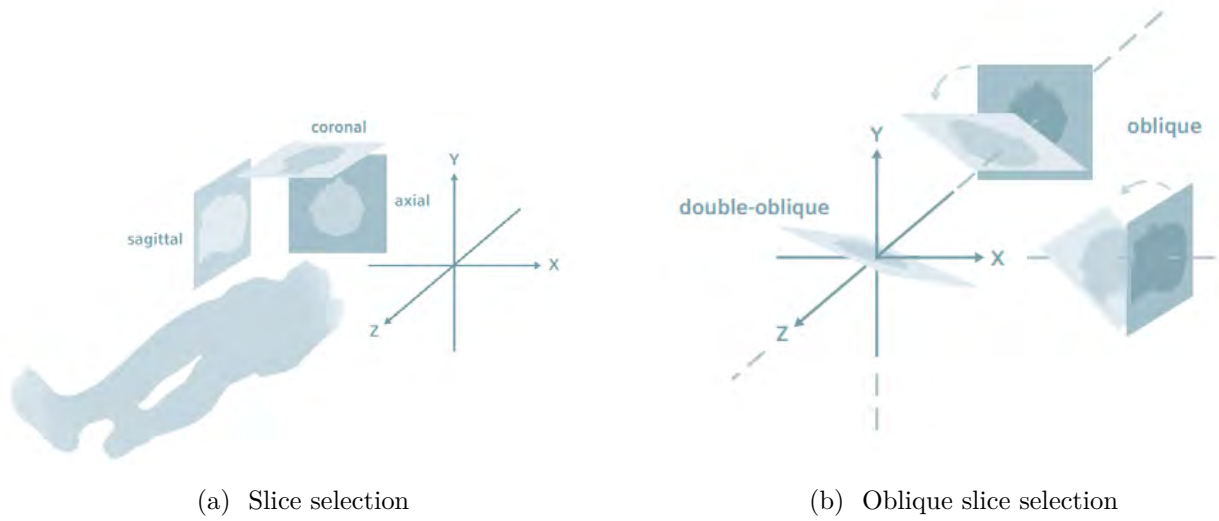
Figure 1.9: For sagittal, coronal or axial slice selection (a), a gradient along x, y or z is switched on. We can then obtain an oblique slice (b) by switching two or three gradients simultaneously. Figure is collected from [30].

computed. Since the MR signal is made up of a mixture of signals resulting from all excited spins, gradients help distinguish these spins from each other and allow the formation of the raw data [30].

Slice selection In order to select a slice of the scanned object, a gradient, called the slice selection gradient G_S, is switched along the z-direction. A RF-pulse of a bandwidth $\Delta\omega_0$ can excite a slice thickness Δz_0. While maintaining $\Delta\omega_0$ constant, the thickness of the slice can be varied according to the ramp slope of the applied gradient (Figure 1.10a). Only within the selected slice a transverse magnetization is created [30].

Frequency encoding During the measurement of the spin echo, a gradient is switched along the x-direction allowing the spins to process along the x-axis with increasing frequencies. This process is called frequency encoding (Figure 1.10b). Application of Fourier transform (FT) allows then to determine the signal's contribution and the exact localization of the frequency component along the x-axis. The strength of the signal detected defines the gray intensity level in the final image. During the formation of the image matrix, the line voxels are defined by switching this frequency gradient

(G_F) [30].

Phase encoding   In fact, two different voxels may have the same frequency and thus could not be distinguished from each others. To further form the whole matrix, a brief gradient along the y-axis is introduced and the spins precess now at different speeds (Figure 1.10b). After the gradient is switched off, these spins show different phase shifts. FT is also used to separate these phase shifts as well. The associated gradient with the formation of multiple lines of voxels is then called the phase gradient (G_P) [30].

(a) Slice selection gradient   (b) Frequency and phase encoding
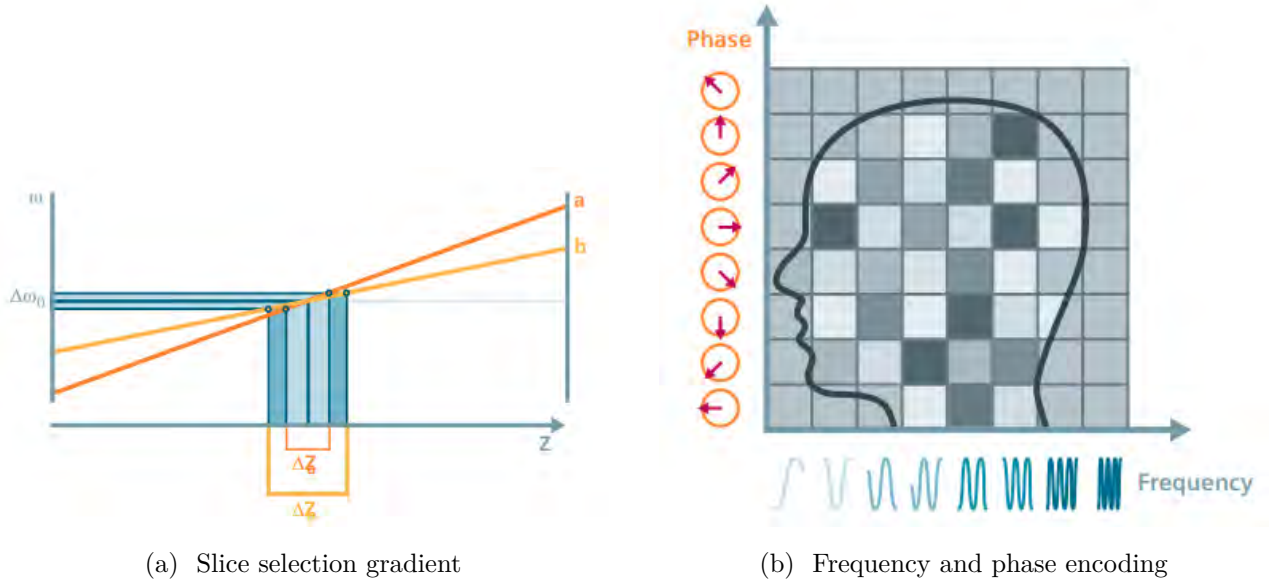
Figure 1.10:   For slice selection, frequency encoding, and phase encoding, magnetic field gradients are applied along z, x, and y axes respectively. The raw data is then collected from the signals detected. Figure is collected from [30].

The pulse sequence has to be repeated until all phase-encoding steps of the scan matrix have been acquired. The time interval between the repetitions is called repetition time T_R. T_E and T_R are important parameters for controlling the contrast of MRI images.

MR image   The signal matrix, filled line by line from echoes, is preprocessed to form the raw data matrix, i.e. the k-space. The application of the FT enables to transform the raw data of the k-space into gray value distributions in the image. Low spatial frequencies at the center of the k-space define the structure and contrast of the formed image whereas high spatial frequency components far from the center define its resolution (Figure 1.11) [30].
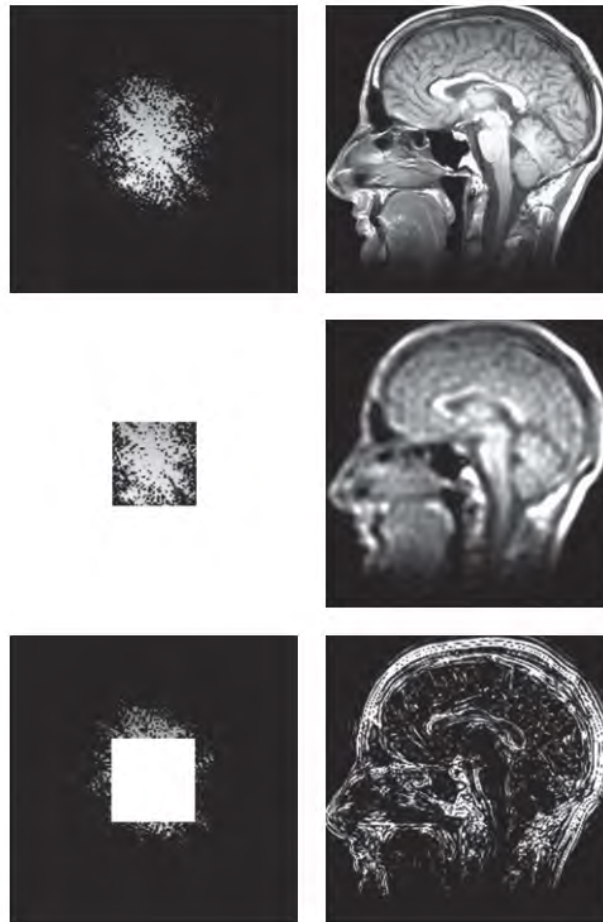
Figure 1.11: Raw data versus image data. Note that a point data in the k-space does not correspond to a pixel in the image. Rather, each part of the k-space contains information of the whole image. Figure is extracted from [30].

1.3.3   MR image contrast

Because of their dependence on the individual sample material, T_1 and T_2 offer a powerful tool to distinguish human tissues in clinical MRI. Different tissue types show different relaxation times and this is the key of sharp image contrast obtained with MR (Figure 1.12).

(a) T_1 relaxation   (b) T_2 relaxation
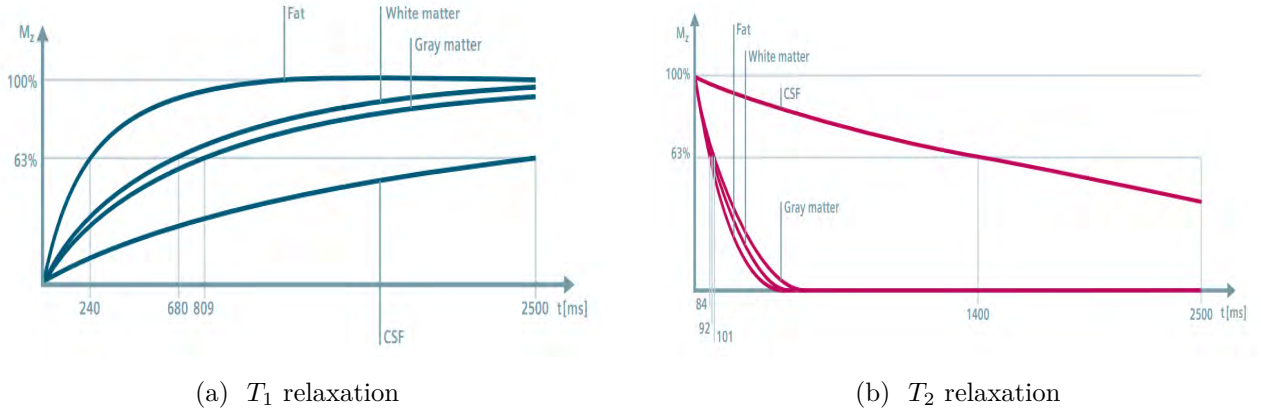
Figure 1.12: Different tissues have different T_1 and T_2 relaxation times offering high contrast images. Figure is collected from [30].

MRI contrast can be determined based on the difference in the number of protons per voxel, the speed of transverse relaxation or the speed of longitudinal relaxation according to the selected parameters (T_E and T_R) during the MRI acquisition. Therefore, signals with different contrast can be generated. We can distinguish three important combinations of T_E and T_R resulting in different contrasts (Figure 1.13):

- T_R short, T_E short $\longrightarrow T_1$ contrast (T_1-weighted)

- T_R long, T_E long $\longrightarrow T_2$ contrast (T_2-weighted)

- T_R long, T_E short $\longrightarrow$ Proton Density (PD) contrast

The MR tissue contrast visualized in the final image depends on the sequence chosen. For example, a tissue with long T_1 and T_2 is dark in the T_1-weighted images while bright in T_2-weighted images. Whereas, a tissue with a short T_1 and a long T_2 is bright in the T_1-weighted image while gray in the

T_2-weighted image. Figure 1.14 shows a comparison of the effect of different sequences and contrasts on the structures' appearance in the final image formed.

<div align="center">(a) T_1 contrast   (b) T_2 contrast   (c)   PD contrast</div>
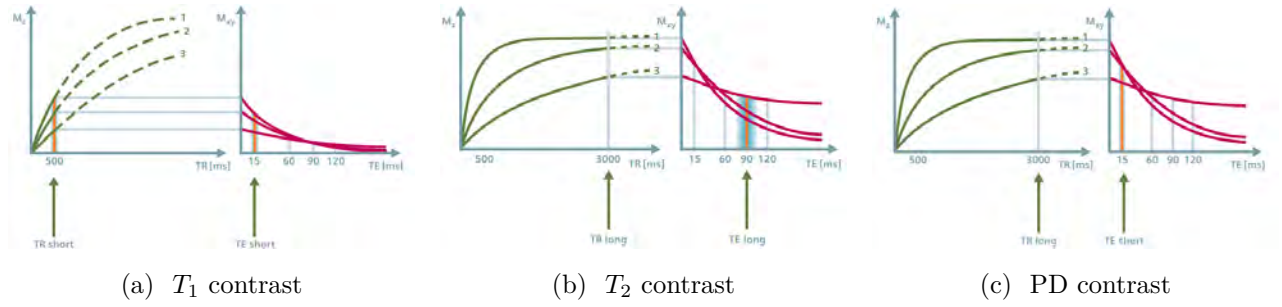
Figure 1.13: Three types of contrast distinguished: T_1 contrast (a), T_2 contrast (b) and PD contrast (c). Figure is collected from [30].
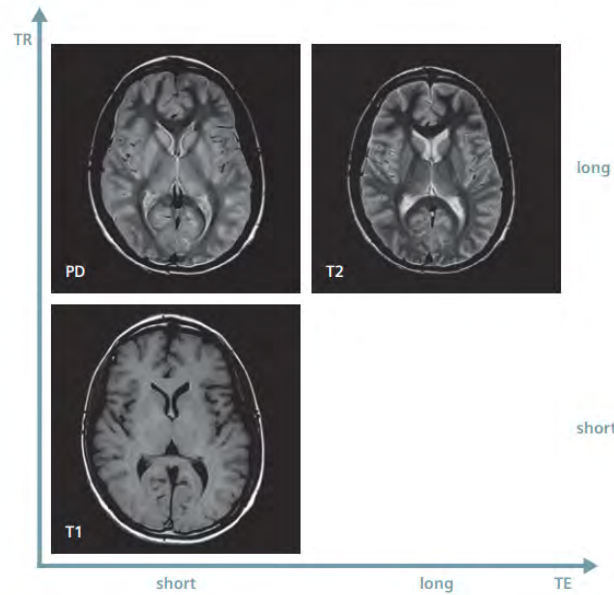
Figure 1.14: Effect of different contrasts on tissue appearance on an axial slice of the human brain. Figure is extracted from [30].

1.3.4 Structural brain MRI

Structural MRI provides static anatomical information used in research and clinical practice. It reveals signals of pathological processes and morphological characteristics by providing information to qualitatively and quantitatively describe the shape, size, and integrity of gray and white matter structures in the brain. Morphometric techniques measure the volume or shape of brain structures such as GM, WM, CSF, as well as the cortical thickness. Since brain function depends on the integrity of brain structures, measures that characterize the underlying tissue integrity also allow one to examine the impact of tissue loss or damage on functional signals. For example, morphological modifications due to aging can generally be assessed with structural MRI. Furthermore, structural MRI provides an anatomical reference for visualization of activation patterns and regions of interest to extract functional signal information.

Many techniques are used in structural MRI including high resolution T_1, T_2, and T_2^* weighted imaging, magnetization transfer imaging, and diffusion imaging [32]. Because they provide excellent anatomical details, T_1-weighted volume scans have become a central component of scanning protocols for structural imaging as they are the most useful and informative structural MRI method. Applications of T_1–weighted imaging include the quantification of signal changes in lesions (based on serial scanning and high-precision image registration), the analysis of cortical morphology, the quantitative analysis of surgical resections and correction of the partial volume effect in magnetic resonance spectroscopy [33]. Given that T_1-weighted sequences generate images that typically maximize the contrast difference between different brain tissues (Figure 1.15), they have been well suited for the detection of the subtle volumetric brain changes by the segmentation and quantification of the shape and volume of these tissues. T_1-weighted images provide a good contrast between GM appearing in gray, WM appearing in white, and CSF being black. However, bone region (skull) can not be distinguished from the CSF on T1-weighted images and requires additional head CT scans to be performed in order to separate these regions.
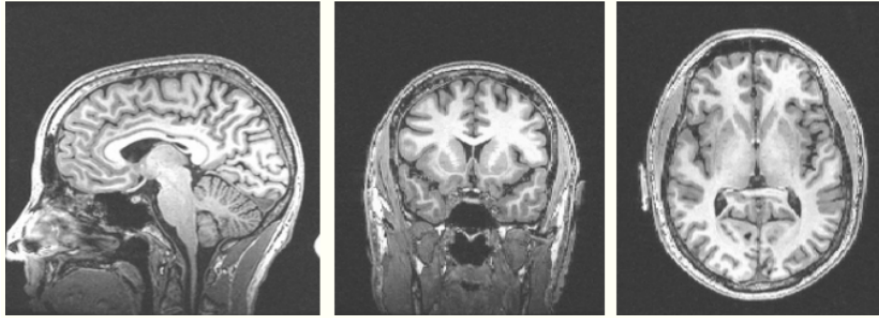
Figure 1.15:   Example of a structural T1-weighted slices of the human brain. It shows the good contrast provided between the GM and WM tissues.   Figure is collected from cfmri-web.ucsd.edu/Howto/3T/structure.html.

1.3.5   MRI of the marmoset brain

In general, the marmoset brain can be imaged with specialized MRI scanners dedicated to rodents. These scanners are characterized by high field strength $(4.7 - 11.7$ T$)$ and customized RF coils that produce high resolution MR images with high signal to noise (SNR) ratios outperforming human brain scanners. While commercially available coils and the adapted sequences for rodents may not be practical for large-headed marmosets, it is possible to acquire these images using clinical MRI scanners dedicated to humans. Utilizing small receiver coils, such as those dedicated for the wrist or knees, and adapted MRI sequences from the human brain can help maintain good signal quality and resolution of structural marmoset brain images. Therefore, the acquisition of structural brain images of the marmosets is feasible with standard MRI scanners without the need for commercial platforms dedicated for animals. However, the major challenge remains in reducing the head motion of the marmoset during the whole procedure to acquire high quality images. Thus, it is necessary to resort to anesthetic regimes and adapt the acquisition sequences according to the anesthetic duration. In general, isotropic structural T1-weighted images of $0.4mm$ resolution best compromises between SNR and anatomical details with a fast sequence for the anesthetized animal. MRI provides similar structural data across all species and it remains necessary to establish a data analysis procedure adapted to the marmoset brain taking into consideration possible artifacts from the sequence used

and the animal examined, as well as the brain extraction parameters [34, 35].

1.3.6   MRI artifacts

During image acquisition, some structures appear in the image that do not really correspond to any spatial distribution in the image plane and may be confused with a pathology; these are the artifacts. Artifacts may result either from the hardware or from the interaction of the subject with the hardware resulting in image quality reduction. MR images are prone to different kinds of artifacts that can belong to one of these groups [36, 37]:

1. Subject- and tissue-related artifacts

   - Ghosting and smearing artifacts due to motion during acquisition (respiration, heart rate, blood flow, eye movement, sudden subject movement, etc..)

   - Contour artifacts (black boundary) caused by chemical shifts at the lipid - water interface

   - Relief artifacts caused by chemical shifts of voxels with direct transition between tissues

   - Distortion artifacts caused by altered or shifted signal intensities due to local field inhomogenity especially in susceptible areas of transition between tissues and bones

2. System-related artifacts

   - Image Distortion artifacts due to the magnetic field inhomogenity, gradient non-linearity or presence of ferromagnetic materials near the acquisition field

   - RF image interference due to the presence of RF pulses from external sources

3. Use- and application-related artifacts

   - Truncation artifacts and data sampling due to abrupt signal transition in tissues that appear in high contrast tissue interfaces

   - Aliasing (wrap around) artifacts that occur when the tissue is outside the field of view but within the sensitive volume of the coil

Several proposals have been made to reduce the effects of these artifacts on the resulting image of which we mention:

- reduce patient movement or perform fast acquisitions

- adjust acquisition parameters during the examination

- perform in-phase and opposed-phase MR to reduce contour artifacts

- use different acquisition sequences to suppress the effect of distortion

- correct images during reconstruction for magnetic field inhomogenity

- apply filtering or increase the size of the measurement matrix to reduce truncation effects

- double the sampling points or increase the field of view to reduce aliasing

It remains crucial to understand the type and the source of artifacts during image acquisition to be able to reduce their effects on the image. Moreover, it is important to take them into consideration during the interpretation of the images to avoid mixing them up with normal or pathological changes. However, if these artifacts were inevitable during the acquisition phase, post processing of the images remain the final solution for image enhancement and better quantification of the results.

1.4 Voxel-Based Morphometry

Advancing age is associated with structural changes and brain shrinkage that can be different across different regions in extent and severity. Identification of these changes is an important step to recognize the underlying pathological changes and neurodegenerative diseases. Each of these diseases exhibits loss of tissue brain and abnormal changes that are well detectable using MRI. Old methods, including delineation of region of interest, manual measurement of atrophy, or visual inspection by radiologists, are time-consuming and prone to errors. Voxel based morphometry (VBM) [38] is an automatic technique well suited for the statistical estimation of tissue brain atrophies for large groups of subjects. Accordingly, VBM techniques have facilitated the detection of brain alterations occurring

through life time by defining regional pattern changes of GM and WM. Such studies can be conducted in a cross-sectional (for a group of subjects) and longitudinal (within the same subject) manners [39].

VBM is the voxel-wise study of the local volume and concentration of gray matter between different scans. It works on structural T1-weighted images that are further segmented into GM, WM and CSF and requires a statistical analysis usually based on a general linear model. Prior to any analysis, raw MR images should follow a common general process of four steps [38, 40]:

1. segmentation of the brain volume into its main compartments; GM, WM and CSF

2. normalization of the individual segmentation into a stereotactic space to correct for differences in brain shape and dimension allowing the direct comparison between brains

3. modulation of the normalized segments to a common template to compensate for volume changes during normalization

4. smoothing the segmented volumes to reduce inter-individual variability and to make sure the residuals follows a normal distribution (which is the basic assumption of VBM work)

While applying a VBM protocol requires to follow standard steps in order to achieve the final statistical results, choosing the appropriate tools for performing the above tasks remains necessary. The choice depends on the quality of MR images acquired and the studied group of subjects. For instance, longitudinal studies require specific additional steps that take into account intra-individual variability. Moreover, the process should consider the studied species, whether human or animal models, upon choosing the appropriate tools.

1.5   Motivations and context

1.5.1   Motivations

The marmoset monkey shows advantages compared to other primate models, with a short lifespan, or compared to rodent models, with a higher phylogenic and anatomical proximity with the human. Marmosets are studied longitudinally at CerCo (Centre de recherche Cerveau et Cognition) lab, where

they are trained for behavioral tasks aimed to investigate cognitive deficits [22, 23]. In parallel, they are scanned regularly on a 3T MRI scanner to explore possible anatomical alterations of the brain. However, structural modifications (e.g., volumes, cortical thickness) occurring during adult life can be very small with respect to the observation scale. The limited resolution and contrast of images acquired at 3T on small animals (Figure 1.16) make it hard to extract pertinent information using image processing tools originally dedicated to MR images of the human brain or contrast-enhanced preclinical images. In general, the spatial resolution in MRI mainly depends on the main magnetic field power, but increasing the magnetic field is an issue in practical situations for different reasons, such as the need for a uniform magnetic field pattern during the acquisition time. Moreover, fast sequences performed to compensate for the time during which the animal is anesthetized affects the overall quality of the images.
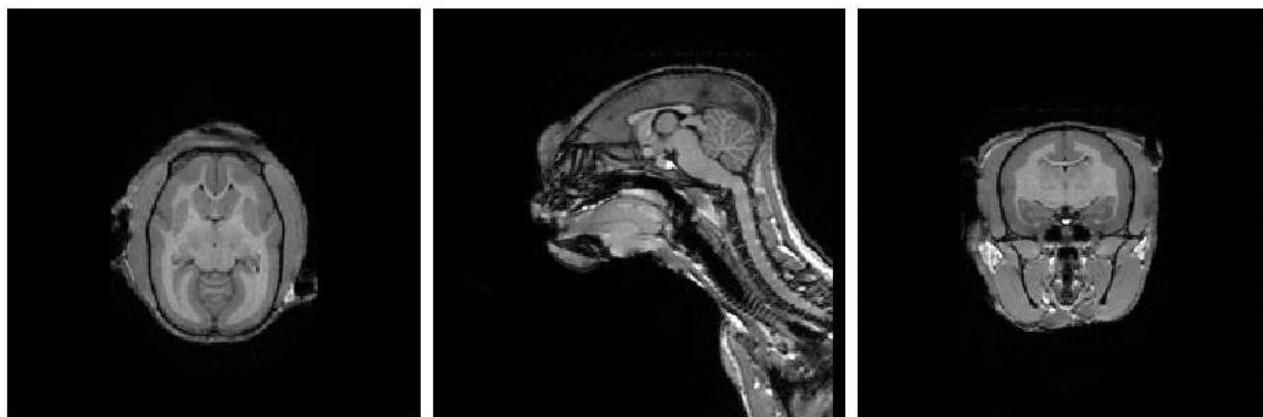
Figure 1.16: Example of axial, coronal and sagittal slices acquired for a marmoset brain on a 3T MRI platform dedicated to human and large animal research.

To overcome the physical limitations of MRI hardware and the practical conditions of the animal scanned, this thesis project aims at developing resolution enhancement methods for preclinical MR images. Such post-processing image restoration methods increase, *a posteriori*, the spatial resolution of biomedical images, in our case of MR images. The success of these techniques relies on the precise mathematical model describing the imaging system, the robustness of prior information on the images to reconstruct, and the numerical optimization algorithms solving the inverse problem of estimating

high resolution images from acquired data. Ultimately, this work will help to improve the robustness and reproducibility of segmentation algorithms, which are crucial steps for a reliable longitudinal morphometric analysis and the correct identification of cerebral aging anatomical markers. The longitudinal assessment of the subtle changes accompanying aging will be performed following a pipeline well-adapted to the available data set of marmoset images. VBM statistical analysis and modeling brain tissue changes will help identify regions that are mainly affected by the normal aging process.

1.5.2   Thesis Context and Outline

The objective of this thesis is to propose approaches to tackle the challenges described in Section 1.5.1. To elaborate, we aim to investigate the effectiveness of several image enhancement methods on the low-resolution (LR) MRI data set of the marmoset brain. Since our final objective is to assess the compartmental changes occurring in the brain during the life span of the marmoset, we wish to explore the effect of super-resolution (SR) on the segmentation of brain tissues, i.e., GM, WM, and CSF. The thesis is structured as follows.

- Chapter 2 will present the theoretical background of image enhancement methods for MR images, methods for brain segmentation. The first part of this chapter will go through existing SR methods that start with LR observations and exploit the high-resolution (HR) images starting from the image formation model in MRI. The second part will then present the literature overview of the basic segmentation tools and techniques for extracting brain tissues and focus on those used for animal images. Finally, We will elaborate on the concepts of cross-sectional and longitudinal segmentation methods used in other studies.

- Chapter 3 introduces a method for marmoset brain segmentation from deconvolved MR image and their associated label maps that does not rely on a brain template or atlas. The proposed method creates label maps based on modeling the image statistics locally using a Generalized Gaussian distribution (GGD) and couples the deconvolved image and its corresponding labels map using the GGD-Potts model. The output labels are further considered as prior maps

for the deconvolved and the native images used to obtain the final segmentation of the brain tissues.

- Chapter 4 evaluates several methods for SR of marmoset brain MR images. The first part of this chapter introduces model-based techniques for the SR task. In particular, we assess a 2D fast SR method (FSR) and a 3D tensor-factorization (TF) method for general image reconstruction and compare them to the existing state-of-the-art methods. The second part covers deep learning networks that have been initially published for the SR of human brain MR images and trained using a marmoset data set. The results of these methods are evaluated from a brain segmentation perspective, using a state-of-the-art brain segmentation method applied to native, LR, and estimated HR volumes.

- Chapter 5 presents a longitudinal segmentation pipeline for the marmoset population and a structural analysis, including VBM and modelling, of the changes occurring in GM and WM with age. We will go through the critical findings in the context of changes reported in different brain regions with aging in the human brain, and compare them to our findings in the marmoset brain. In order to demonstrate the efficiency of super resolution in improving the study of morphological brain changes, we will compare the developmental analysis of the native data set with that of super-resolved volumes using the 2D FSR method and a 3D deep learning method.

- Chapter 6 details the final conclusions of this thesis, presents the limitations of the study conducted, and states possible future work directions.

State-of-the-art

Contents

This chapter focuses on describing the background of SR and longitudinal segmentation of MR images, two frameworks that represent the main objective of this thesis. We will first introduce the image formation model and the basic theory of model-based image reconstruction for MRI which represents the basis of the enhancement techniques. Then, we will present the fundamental background of post-processing techniques reported in the literature for MR image enhancement, starting with basic deblurring methods and expanding to model-based and deep learning SR techniques. Following our main objective of improving the brain segmentation for a more accurate longitudinal analysis of morphological changes with aging, we will further report existing methods for MR longitudinal segmentation, taking into account the intra-individual variability. Based on the advantages and limitations of these algorithms, we will finally conclude by highlighting the proposed and adapted frameworks in this thesis.

2.1   General acquisition model

2.1.1   Image resolution

The spatial resolution of an imaging system is defined as its ability to separate two close source points [41]. In other words, it is the ability of the system to separate two close targets. In most imaging applications, an HR image is always desired since it offers more accurate details that facilitate the medical condition diagnosis. For instance, the spatial resolution of an MRI scanner is determined by the gradients' intensities, the digital imaging filter bandwidth, the number of readout points, and the phase encoding steps. Therefore, a sufficiently HR image can be obtained by decreasing the field of view (FOV), increasing the number of readout points, increasing the number of phase encoding steps, increasing the number of coil receiver channels, or increasing the main magnetic field of the MRI core [42]. In practice, MRI scanners used in medical applications are of strength of 1.5T or 3T with a typical spatial resolution of $1.5 \times 1.5 \times 4 \ mm^3$. As higher resolutions are achieved with increasing the field strength, an isotropic resolution of 250 μm for whole brain T1-weighted images has been reported using a 7T MRI scanner in [43], and an $80 \times 80 \times 200 \ \mu m^3$ resolution have been attained using an 11.7T MRI scanner dedicated to research in [44]. However, hardware improvements and scanners with higher magnetic fields are not always feasible, and the acquisition parameters limit the resolution of the images [41, 45].

2.1.2   Image formation model

As mentioned before, the observed images are usually low in resolution limited by the available hardware and methods of acquisition. Therefore, the first step of understanding the concept of image enhancement is to model the image formation process that relates the LR observations to the unobserved HR images. The process includes identifying different operations applied on the original HR image during its construction phase [45]. The most common model for static images assumes that the HR image is subject to warping, blurring, and sub-sampling which finally results into the observed LR image. Figure 2.1 represents an overview of the observation model relating LR to HR images. Therefore, the k-th LR observation y_k can be expressed as a function of the HR image x,
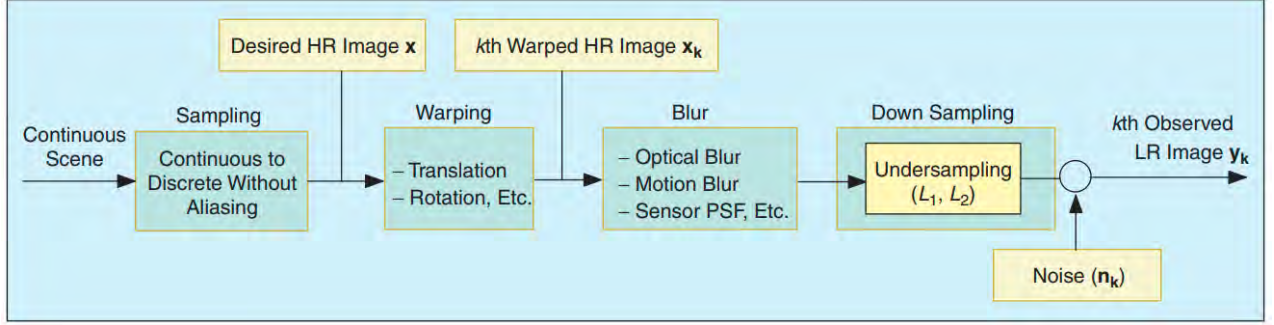
Figure 2.1: Observation model relating LR to HR images. Figure is collected from [45].

that is sampled at or above the Nyquist rate from a band-limited scene, as:

$$y_k = DB_k M_k x + n_k, \quad k = 1, ..., p \tag{2.1}$$

where p is the total number of observed LR images, and for the k-th LR image:

- D is the decimation operator that defines the sampling rates $(L1, L2)$, in horizontal and vertical directions, of the high-resolution scene

- B_k is the blurring operator, sometimes referred to as the point spread function (PSF) of the system

- M_k is the geometric transformation operator that brings all the LR input images to the same base point (reference grid) so that they could be combined

- n_k is the white additive noise which exists due to the nature of the imaging device.

Therefore, reconstructing a HR image from the observed LR ones following the observation model in equation 2.1 requires a proper modelling for these operators depending on the imaging system.

2.2 MRI reconstruction model

Following our desire to investigate the SR problem for the MRI system, the application requires first to model the MR image reconstruction in order to link it to image restoration techniques. The idea

has been addressed significantly in the literature [29, 46, 47], and we thereby summarize the image reconstruction model for an MRI scanner as fully described in [46].

2.2.1   MRI physics

Based on the physical principles of MR image formation, stated in Section 1.3, a static magnetic field B_0 induces a net magnetization vector $\overrightarrow{M}$, at a point $\overrightarrow{r} = (x, y, z)$ in the space body being scanned, that is given by

$$\overrightarrow{M} = M_x \vec{i} + M_y \vec{j} + M_z \vec{k}, \tag{2.2}$$

In practice, a time-varying magnetic field is used $\overrightarrow{B}(r, t)$ inducing time-varying changes in the magnetization:

$$\overrightarrow{M}(\vec{r}, t) = M_x(\vec{r}, t)\vec{i} + M_y(\vec{r}, t)\vec{j} + M_z(\vec{r}, t)\vec{k}. \tag{2.3}$$

Two main phases are distinguished, excitation and readout. During the excitation phase, spins are tilted into the xy-plane and precess with the Larmor frequency ω. The transverse magnetization can be then expressed as a single complex vector:

$$\overrightarrow{M}(\vec{r}, t) = M_x(\vec{r}, t)\vec{i} + iM_y(\vec{r}, t)\vec{j}. \tag{2.4}$$

Let $t = 0$ be the time when the excitation pulse is completed, with $\overrightarrow{M}(\vec{r}, 0)$ being the object's transverse magnetization directly after excitation, and $t > 0$ be the readout time. The evolution of the transverse magnetization can be written as:

$$\overrightarrow{M}(\vec{r}, t) = \overrightarrow{M}(\vec{r}, 0) \exp\left(-i \int_0^t \omega(\vec{r}, t)\, dt'\right), \tag{2.5}$$

where $\omega(\vec{r}, t)$ represents the instantaneous frequency at a given spatial location and is expressed by the Larmor relationship as a function of the longitudinal field strength $B_z(\vec{r}, t)$ and the gyromagnetic ratio γ:

$$\omega(\vec{r}, t) = \gamma B_z(\vec{r}, t). \tag{2.6}$$

An accurate model of this evolution takes into consideration the shorter effective time constant T_2^* and can be re-written as:

$$\overrightarrow{M}(\vec{r}, t) = \overrightarrow{M}(\vec{r}, 0) e^{\frac{-t}{T_2^*}(\vec{r})} \exp\left(-i\gamma \int_0^t B_z(\vec{r}, t)\, dt'\right). \tag{2.7}$$

2.2.2 MRI signal

According to Faraday's law, the time-varying magnetization $\vec{M}(\vec{r}, t)$ induces an electromotive force in the receiver coil resulting in an electrical potential $v(t)$ defined as:

$$v(t) = real\left(\int c(\vec{r})\frac{d}{dt}M(\vec{r}, t)\, d\vec{r}\right),\tag{2.8}$$

where $real(.)$ is the real part of a complex number and $c(\vec{r})$ represents the coil response pattern. The signal in the receiver coil is then amplified and demodulated using quadrature modulation resulting in an in-phase signal $I(t)$ and a base-band signal $Q(t)$. These signals are further digitized and stored as complex values. The demodulated MRI signal, $s(t)$, is expressed as:

$$s(t) \triangleq I(t) + iQ(t) = e^{i\omega_0 t}\int c(\vec{r})M(\vec{r}, t)\, d\vec{r}.\tag{2.9}$$

In order to increase the SNR and decrease the acquisition time, several receiver coils are usually used. By combining (2.7) and (2.9), the MRI signal associated to the l_{th} coil is given as:

$$s_l(t) = \int c_l(\vec{r})y(\vec{r})e^{\frac{-t}{T_2^*}(\vec{r})}e^{-i\phi(\vec{r},t)}\, d\vec{r},\tag{2.10}$$

where $s_l(t)$ is the signal received by the l_{th} coil , $c_l(\vec{r})$ is the sensitivity (response pattern) of the l_{th} coil, $y(\vec{r}) = \vec{M}(\vec{r}, 0)$ is the unknown function representing the proton spin density , and $\phi(\vec{r}, t)$ is space- and time-varying phase defined as:

$$\phi(\vec{r}, t) \triangleq \int_0^t \left(\gamma B_z(\vec{r}, t')\, dt'\right).\tag{2.11}$$

To summarize, the longitudinal component of the magnetic field applied consists of three components: the constant field strength B_0, the spatial deviation of the field strength $\Delta B_0(\vec{r})$, and the field gradient $\vec{G}$ applied during image acquisition. Thus, we re-write $B_z(\vec{r}, t)$ as:

$$B_z(\vec{r}, t) = B_0 + \Delta B_0(\vec{r}, t) + \vec{G}(t).\vec{r}.\tag{2.12}$$

Substituting (2.12) in (2.11), and defining the k-space trajectory during frequency encoding as

$$\vec{k}(t) \triangleq \frac{1}{2\pi}\int_0^t \gamma\vec{G}(t)\, dt\tag{2.13}$$

yield, finally, to the general form of the MRI signal in the l_{th} receiver coil:

$$s_l(t) = \int c_l(\vec{r})y(\vec{r})e^{\frac{-t}{T_2^*}(\vec{r})}e^{-i\Delta\omega_0(\vec{r})t}e^{-i2\pi\vec{k}(t).\vec{r}}\, d\vec{r}.\tag{2.14}$$

2.2.3 Linear image reconstruction

In the discrete form, $y(\vec{r})$ can be approximated by finite series expansion as:

$$y(\vec{r}) = \sum_{j=1}^{N} y_j b(\vec{r} - \vec{r}_j), \tag{2.15}$$

where $b(.)$ is object – basis function, $\vec{r}_j$ is center of the j_{th} translated function and N is the number of parameters. Therefore, using (2.15), the discrete forward model of the MRI signal can be simplified to:

$$s_l(t) = \sum_{i=1}^{N} a_{lij} y_j, \tag{2.16}$$

where a_{lij} are the elements of the system matrix A_l associated to the l_{th} coil and combining the scanning parameters. Since the basis function is highly localized, center of voxel approximation is usually used. Let $z(\vec{r}) = \dfrac{1}{T_2^*}(\vec{r}) + i\Delta\omega_0(\vec{r})$ be the rate map, then a_{lij} is simplified to:

$$a_{lij} \approx c_l(\vec{r}_j) e^{-z(\vec{r}_j)t_i} e^{-i2\pi\vec{k}(t_i).\vec{r}_j} \tag{2.17}$$

The recorded MR measurements are noisy samples of the induced MR signals given by:

$$g_{li} = s_l(t_i) + \epsilon_{li}, \tag{2.18}$$

where $l = 1, ..., L$ is the number of receiver coils, $t_{i=1,...,n_d}$ is the number of time samples, g_{li} is the ith sample of the lth coil's signal at time t_i, and ϵ_{li} is the additive, complex, zero mean, and white Gaussian noise. Combining (2.18) with the discrete forward model in (2.16) yields to:

$$g_l = A_l y + \epsilon_l, \tag{2.19}$$

where $y = (y_1, ..., y_N)$ is the vector of parameters (pixel values) that we wish to estimate from the collected data g. By stacking up all L measurement vectors as $g = (g_1, ..., g_L)$ and defining the $(n_d L) \times N$ system matrix $A = (A_1, ..., A_L)$, the linear model of model-based image reconstruction is expressed as:

$$g = Ay + \epsilon. \tag{2.20}$$

During image reconstruction of MRI data y, a significant challenge is that the elements of A can be quite complicated. Because the noise in MRI measurements is assumed Gaussian and the inverse problem is ill-posed, a natural approach is to estimate y by minimizing a regularized cost function:

$$\widehat{y} = \arg\min_y \|g - Ay\|^2 + \beta R(y), \tag{2.21}$$

where $R(.)$ is the regularization function chosen during the reconstruction process. Popular regularization methods for MRI data are Tikhonov and Total Variation regularization. Conventionally, reconstructed MR images with FFTs from complex-valued raw data in the frequency domain (k-space) result in complex-valued image data that represents the phase and magnitude images [48, 49]. While certain MRI applications require phase images (such as flow measurements with velocity encoding, quantitative susceptibility mapping (QSM), susceptibility-weighted imaging (SWI), etc.), diagnostic and post-processing applications require only the magnitude images. In the rest of the work, the reconstructed image $\widehat{y}$ will represent the magnitude MR image.

Beyond the acquisition stage, the reconstructed volume $\widehat{y}$ can be corrupted with noise, blur, and artifacts due to post-acquisition processing. The distortions in the acquisition and reconstruction phases thus limit the possibility of obtaining the desired HR images. However, the loss of spatial resolution in the acquisition process can be expressed through a linear model, similar to the model provided in (2.1), which relates the observation image y to a non-noisy, non-blurry, and HR image x to be estimated. Therefore, the linear observation model for an MR image used for the SR task can be given as:

$$y = Wx + n, \tag{2.22}$$

where W is the global transformation operator that includes geometric transformation, blur and down-sampling from the high resolution to the low-resolution image. The noise n in the reconstructed complex MR data is usually assumed to follow a Gaussian distribution. Since the computation of the magnitude image is non-linear operation, the distribution changes from Gaussian to Rician when considering magnitude images [50]. However, it has been shown that in the case of an SNR larger than $2dB$, the noise distribution affecting the magnitude images can be also assumed Gaussian [51].

2.3   Post-processing techniques in MRI

Several approaches have been proposed in the literature for enhancing the resolution of MR images after their reconstruction. We distinguish two main post-processing techniques: image deblurring and image super-resolution, both based on the linear formation model of the MR image and the assumptions made on the global transformation operator W of equation (2.22).

2.3.1   MR image deblurring

During image acquisition, the partial volume effect in regions where the boundaries are not orthogonal to the image slice and post-acquisition processes, such as denoising filters, result in blurring. In general, blurred images are characterized by weak strength of edges defining details of the image, eroded texture features of smoothly varying regions, loss of edges' sharpness, and reduced contrast between anatomical structure [52]. While blurring consequences on the MR image are inevitable, researchers continue to investigate methods for its assessment as a step for image enhancement approach. Since deblurring is important for the effective analysis and diagnosis of medical images, several methods and theories have been proposed for the automatic estimation of a blur. For example, Noll et al. [53] proposed a method using the raw MR data modulated to several different frequencies and reconstructed to create a series of base images. The degree of blurring was then determined after computing the focusing measure for each point in the base and composite images. Moreover, Osadebey et al. [52] proposed a method to assess blur level in MRI based on convolving the image with two multi-scale difference Gaussian filters, with their parameters tuned according to edge sharpness, which allows extracting contrast and sharpness maps. Finally, blur level is assessed from the difference between the contrast and sharpness quality features in the images at the output of each filter. However, most studies are based on the assumption that the blurring in an MR image may be viewed as the convolution of the image by a blurring kernel (the PSF). This introduces the basis of image deconvolution task, considered as a deblurring method, detailed hereafter.

2.3.1.1 Deconvolution model for MRI

Based on the general linear formation model in (2.1), and as a consequence of the MR image restoration model in (2.22), the MR image can be modelled as the convolution between a blurring kernel, referred to as the PSF of the imaging system, and the unknown HR. The resulting linear model can be re-written as:

$$y(\mathbf{r}) = h(\mathbf{r}) * x(\mathbf{r}) + n(\mathbf{r}), \quad \mathbf{r} \in R. \tag{2.23}$$

where $y(\mathbf{r})$ is the observed imaged pixel at the location $\mathbf{r}$, $x(\mathbf{r})$ is the enhanced image to be estimated, $h(\mathbf{r})$ is the blurring matrix classically constructed from the imaging PSF, $n(\mathbf{r})$ is an additive, zero-mean white Gaussian noise and R is the image domain. This general model can be applied in 1D, 2D or 3D depending on the convolution problem we have. It is also possible to perform the deconvolution of a 3D volume slice by slice, i.e. in 2D. After lexicographical ordering the corresponding images $y(\mathbf{r})$, $x(\mathbf{r})$, $n(\mathbf{r})$ and forming the convolution matrix $\mathbf{H} \in N \times N$ associated with $h(\mathbf{r})$, we obtain the following equivalent model:

$$\mathbf{y} = \mathbf{H}\mathbf{x} + \mathbf{n} \tag{2.24}$$

At this point, the objective is to estimate the unknown, non-blurry image $\mathbf{x}$ from the corrupted observation $\mathbf{y}$. Based on the knowledge of the system PSF, $\mathbf{H}$, we can distinguish two types of deconvolution problems: blind and non-blind. In blind deconvolution, deblurring of an image is achieved with no or very little prior information about the degrading PSF kernel. Whereas, when sufficient information about the PSF is available, the process is referred to non-blind deconvolution. Therefore, the key for the deconvolution problem is a good estimation of the PSF.

In general, the PSF of an imaging system is defined as a function that specifies how points in the image are distorted. It represents the amount of blur added during the overall acquisition process and is often assimilated to the blur introduced by the imaging system. The PSF is difficult to measure precisely in MRI, especially for complex sequences [54]. Phantom-based techniques have been proposed for measuring the PSF by producing an image weighted by the integral of the PSF that can monitor its spatial, temporal, and platform variance [55, 56]. Despite being an effective method for precise PSF calculation, phantoms are not always available in practice, and PSF estimation

becomes necessary. In the context of PSF measurement for an MRI system, Robson et al. [54] proposed a constant time imaging technique that uses additional phase encoding gradients that are constant in length but vary in amplitude before the echo-planar acquisition. An alternative approach to PSF calculation or measurement is its reconstruction along with the image during the acquisition phase. Tan and Zheng [57] formulated a PSF minimization problem during image reconstruction, which optimizes individual weights of the k-space sampling points in order to obtain the minimum side-lobe level for a given main-lobe width of the PSF. When PSF can not be calculated directly during image acquisition, estimating it from the observation images remains important for the deblurring process. In MRI, it is commonly assumed that the PSF induced during acquisition is space invariant. Most studies on PSF estimation for MR images conclude that PSF can be well estimated as a Gaussian function in the three dimensions where its full-width of half maximum (FWHM) equals the slice thickness of the MR volume in the slice-select dimension [42, 58–60]. Moreover, Greenspan et al. [61] compared using a Gaussian-PSF and a rectangular Box-PSF for image enhancement. They have observed that a Gaussian-PSF gives better results than a Box-PSF on phantom and real MRI data.

Once the PSF kernel is well-estimated, the deconvolution task can be referred to as non-blind deconvolution. Several methods for non-blind deconvolution have been addressed in the literature. Ahunbay et al. [62] proposed a method performed during the reconstruction of spiral MR images where the image is convolved by the inverse of the PSF derived from the off-resonance frequencies. Getreuer et al. [63] solved the restoration problem under the assumption that the image is degraded by a Gaussian blur and Rician noise. They solved the variational model of deconvolution using L^2 and Sobolev (H^1) gradient descents and split Bregman methods with Total variation (TV) regularization. Results were validated on MRI phantoms of T1-weighted brain volumes.

However, when no data is available for the shape of the PSF kernel, image deconvolution becomes a blind problem, where the PSF should be recovered along with the non-blurry image. Sainarayanan et al. [64] proposed an iterative blind deblurring method for the enhancement of cardiac MR images. The PSF was first estimated from the degraded image then the restoration was done using the simulated annealing technique. Another blind deconvolution method was evaluated for dynamic

MRI of the lung by Gou et al. [65] using low-rank decomposition and dictionary learning. It is based on approximating the low-rank, sparse, and noise components of the input degraded image, supposing that the data follows Poisson distribution, then estimating the blur kernel using an adaptive dictionary learning, and finally solving the deblurring problem using the Lucy-Richardson algorithm. In the same context, Liyan et al. [66] blindly recovered the degraded images from blur by assuming that the noise contaminating the images follows a Poisson distribution, unlike the studies concluding that the noise in MR images is Gaussian. They then solve the variational model of image formation using two types of priors: patch-based sparse representation prior over a learned dictionary and the pixel-based TV regularization. An example of their results on human brain MR data is illustrated in Figure 2.2. Although some of these methods were not applied to brain images, yet they present important techniques for deblurring MR images that could be further tested on brain images.

Based on the extensive researches in MRI deblurring, we will explore in our work the importance of the deconvolution problem for the restoration of brain MR images of marmosets. In this context, we are interested in the technique proposed by Zhao et al. [67] which performs the restoration using the statistical properties of the image noise. The interest behind this method is that the segmentation task is conducted jointly with the deconvolution one by defining a Potts Markov random field for the hidden image labels and assigning GGD priors to the unknown image to be restored. However, while deblurring methods help remove the blur contaminating MR images due to reconstruction artifacts, it does not improve its spatial resolution. Therefore, another enhancement method, the super-resolution (SR), is introduced.

2.3.2 Image super-resolution

2.3.2.1 Introduction

Acquiring images beyond the system resolution is referred to as super-resolution (SR). Here, SR is a post-acquisition image restoration technique that allows the reconstruction of high-SNR and HR representations of objects that could only be acquired at low resolution, thus overcoming instrumental limitations and physical constraints. SR methods were mainly introduced to increase the spatial resolution by extracting information from a set of LR images that may have been translated, blurred,

(a) Degraded   (b) PIDSplit+ (25.52dB)   (c) PIDAL-FA (26.02dB)   (d) Ours (27.21dB)   (e) Original
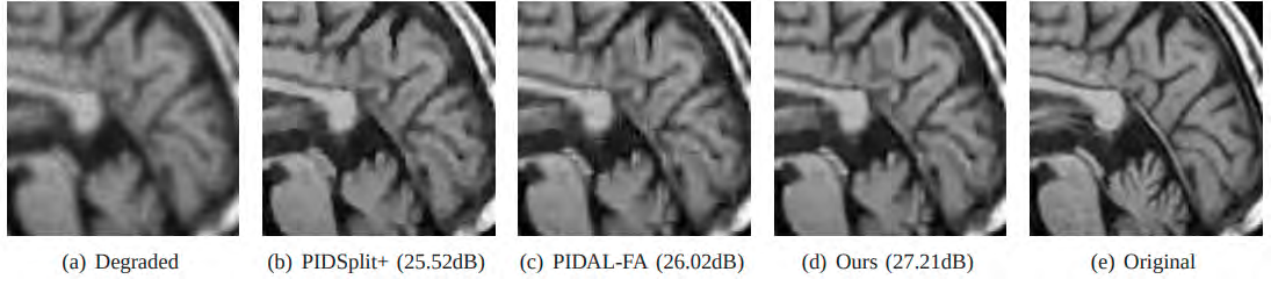
Figure 2.2: Illustration of the deblurring result of the method proposed in [66] on a MR brain image corrupted by a 5×5 uniform blur and Poisson noise with peak intensity 600 compared to a TV-based algorithm (denoted by PIDSplit+) [68] and to a frame-based algorithm (denoted by PIDAL-FA) [69]. This figure was collected from [66].

rotated, or scaled. It has been proved helpful in many applications where multiple frames of the same scene can be obtained, such as in medical imaging (e.g., computed tomography and MRI since the acquisition of multiple images with limited resolution can be achieved), satellite imaging (e.g., remote sensing and LANDSAT: several images of the same area are available) and video applications (conversion from an NTSC video signal to an HDTV signal) [41, 45]. In general, SR restoration techniques fall into one of the three following categories: frequency domain techniques, iterative algorithms, and statistical methods [42].

Frequency domain techniques These techniques are based on the generalized sampling theorem laid by Papoulis [70] and Yen [71]. Tsai, and Huang [72] suggested the first SR algorithm, where they assumed non-blurred and non-noisy images. Their work was followed by Kim et al. [73] who used least-square minimization on noisy and blurred images. Most frequency-domain methods are based on transforming the input images to the frequency domain (using 2D DFT), combining the spectral data, and returning the output image (after applying 2D IDFT). Because the images are reconstructed in the frequency domain, these methods have "recursive" properties, and new samples can be combined into the final reconstructed image as they arrive [42]. Three main principles govern this approach: the shifting property of the Fourier transform, the aliasing relationship between the continuous Fourier transform (CFT) of an original HR image and the discrete Fourier transform

(DFT) of observed LR images, and the assumption that an original HR image is band limited. These make it possible to formulate the equation relating the aliased DFT coefficients of the observed LR images to a sample of the CFT of an unknown image [74]. However, frequency-domain methods have apparent limitations (sensitivity to model errors, difficulty handling complicated motion models), which prevented their development.

Iterative algorithms   These algorithms include Iterative Back Projection, Projection onto Convex Sets (POCS), and Regularized Methods. Irani and Peleg [75, 76] first discussed the main concept of Iterative Back Projection. In this algorithm, the high-resolution output image is built iteratively to best describe the input sample images. In every step, a set of back projected LR images is generated using the current best guess as to the high-resolution scene. The algorithm then refines the best guess such that the back projections better describe the input images. The advantage of IBP is that it is understood intuitively and easily. However, this method has no unique solution due to the ill-posed nature of the inverse problem, and is known for its low rate of convergence and sensitivity to noise. [42, 45]. Other iterative methods were suggested, such as the Projection onto Convex Sets (POCS) algorithm, proposed by Patti et al. [77]. The POCS algorithm resembles IBP and assumes that the solution updates the current best guess iteratively according to known convex constraints (data constraints, amplitude constraints...). The advantage of POCS is that it is simple, and it utilizes the powerful spatial domain observation model. It also allows a convenient inclusion of *a priori* information. However, it presents disadvantages of non-uniqueness of the solution, slow convergence, and a high computational cost [45].

Statistical methods   These methods rely on the image formation model and restore the HR image with the maximum probability of creating the LR observations. Such algorithms were first presented by Cheeseman [78] who used the Bayes' Theorem and Shekarforoush [79] who used Markov Random Field to model and solve the problem. Regularized SR approaches are adopted to stabilize the inversion of the ill-posed problem of the reconstruction. Two techniques are present: stochastic and deterministic. The deterministic regularized SR approach solves the inverse problem equation

by using the prior information about the solution rendering the problem well-posed. Stochastic SR image reconstruction, typically a Bayesian approach, provides a flexible and convenient way to model *a priori* knowledge concerning the solution. Bayesian estimation methods are used when *a posteriori* probability density function (PDF) of the original image can be established. The MAP estimator of the HR image maximizes the PDF with respect to it [45].

D. Fiat first presented the idea of attaining sub-pixel resolution in MRI in [80]. The applications of SR reconstruction from different scenes have consequently started to elaborate. Peled and Yeshurun [81] acquired eight low-resolution images with sub-pixel shifts, and combined them using the IBP [75] model-based algorithm to super resolve spatially shifted, single-shot, diffusion-weighted brain images. Similarly, Greenspan et al. [61] proposed to perform the 3D inter-slice SR reconstruction in the slice-select direction using several 2D LR images also based on the IBP of Irani and Peleg [75]. Carmi et al. [42] introduced a novel method for sub-pixel SR of MRI by introducing a simplified model of the LR images. However, multiple LR frames are not always available for the SR task where only one LR observation can be obtained. Thus, the problem is referred to as single-image SR. We will thereby define the image observation model related to this problem.

2.3.2.2   Image observation model

Having defined the general image formation model in (2.1), one can estimate the unknown HR image using several interrelated LR images and some linear constraints. However, only one LR image is available in our work, referring the problem to as single-image SR. Therefore, we aim to estimate the HR image from one corresponding LR image that is modeled as a noisy version of the blurred and decimated HR image as follows:

$$\mathbf{y} = \mathbf{SHx} + \mathbf{n}, \tag{2.25}$$

where $\mathbf{y} \in \mathbb{R}^{N_l \times 1}$ and $\mathbf{x} \in \mathbb{R}^{N_h \times 1}$ $(N_h = d^2 N_l)$ are the vectorized versions of the LR and HR images. $\mathbf{H} \in \mathbb{R}^{N_h \times N_h}$ represents the 2D convolution of the HR image with the PSF of the imaging system. $\mathbf{S} \in \mathbb{R}^{N_l \times N_h}$ corresponds to the down sampling operator with an integer sampling rate d. $\mathbf{n} \in \mathbb{R}^{N_l \times 1}$ is an independent identically distributed (IID) additive white Gaussian noise (AWGN). Although this model has been addressed in 2D, the application of SR to a 3D volume can be performed slice

by slice. However, we will re-write this convolution problem in 3D whenever necessary in our work.

The reconstruction of the HR image from the LR image is an ill-posed problem, i.e., the solution is not unique for an observed input. In fact, the observation matrix represented by **SH** may be unknown due to the complexity of real imaging systems and requires several assumptions on the shape of the operators [82, 83]. Thus, many solutions have been discussed in the literature to solve the SR problem and which fall into one of two main categories: model-based and learning-based methods. In the next sections, we will introduce some basic techniques proposed in the literature .

2.3.2.3 Model-based SR methods

Model-based methods formulate the image SR as a reconstruction problem, either by incorporating priors in a Bayesian framework or by introducing regularizations into the variational inverse problem. Starting from (2.25), the SR problem can be formulated as the following optimization problem:

$$\min_x \underbrace{\phi(\mathbf{y} \text{ - } \mathbf{SHx})}_{\text{data fidelity}}, \tag{2.26}$$

where $\phi(\mathbf{y} \text{ - } \mathbf{SHx})$ is the data fidelity term, i.e., the likelihood of the observations, related to the noise distribution. This term usually penalizes the difference between the degraded SR image and the observed LR image. Given an additive white Gaussian noise (AWGN), the data fidelity term can be rewritten as:

$$\phi(\mathbf{y} \text{ - } \mathbf{SHx}) = \frac{1}{2}\|\mathbf{y} - \mathbf{SHx}\|_2^2. \tag{2.27}$$

Thus the HR image can be estimated by minimizing a least-square cost function as:

$$\widehat{\mathbf{x}} = \arg\min_x \frac{1}{2}\|\mathbf{y} - \mathbf{SHx}\|_2^2, \tag{2.28}$$

where $\|.\|_2$ stands for the standard l_2-norm.

The IBP method, proposed by Irani and Peleg [84], calculates the residual between a simulated LR image with the LR observation **y** and then sum the reconstruction error back to the estimated HR image $\widehat{\mathbf{x}}$ as

$$\begin{cases} \widehat{\mathbf{x}}^0 = \mathbf{Uy} \\ \widehat{\mathbf{x}}^{t+1} = \widehat{\mathbf{x}}^t + \mathbf{U}(\mathbf{SH}\widehat{\mathbf{x}}^t + \mathbf{y}) \end{cases} \tag{2.29}$$

where t is the current iteration, and $\mathbf{U}$ is an up-scaling operation chosen to be the nearest-neighbor interpolation. However, the IBP technique is highly sensitive to noise and outliers. In this case, the result may contain high frequency artifacts because of ignoring the visual complexity of the ill-posed problem. Thus, these limitations raise the importance of introducing a regularization constraint. Therefore, the optimization problem in (2.28) becomes:

$$\widehat{\mathbf{x}} = \frac{1}{2}\|\mathbf{y} - \mathbf{SHx}\|_2^2 + \underbrace{\tau R(\mathbf{x})}_{\text{regularization}}, \qquad (2.30)$$

where $R(\mathbf{x})$ is the regularization constraint, which usually reflects the prior knowledge about x, and τ is the regularization parameter which weights the importance between the data fidelity term and the regularization term. Various regularizations have been already advocated to regularize the image super-resolution problem, such as, Tikhonov [85], $l1$-norm [86], or total variation (TV) [87]. Different regularizers result in different cost functions, (2.31), (2.33), and (2.39) respectively, under the assumption of AWGN.

- Tiknonov regularization: $R(x) = \|\mathbf{x} - \overline{\mathbf{x}}\|_2^2$

  Where $\overline{\mathbf{x}}$ is a rough estimation of the HR image such as the interpolation of the LR image or a clean image obtained from other sensors. In this case, the optimization problem is given by:

  $$\widehat{\mathbf{x}} = \frac{1}{2}\|\mathbf{y} - \mathbf{SHx}\|_2^2 + \tau\|\mathbf{x} - \overline{\mathbf{x}}\|_2^2. \qquad (2.31)$$

Thus, the solution can be expressed as:

$$\widehat{\mathbf{x}} = (\mathbf{H}^H\mathbf{S}^H\mathbf{SH} + 2\tau\mathbf{I}_{N_h})^{-1}(\mathbf{H}^h\mathbf{S}^H y + 2\tau\overline{\mathbf{x}}). \qquad (2.32)$$

  Where $\mathbf{H}^H$ and $\mathbf{S}^H$ are the conjugate transpose of H and S respectively, and $\mathbf{I}_{N_h}$ is an identity matrix

- $l1$-norm regularization: $R(\mathbf{x}) = \|\mathbf{x}\|_1 = \max_{1 \leq j \leq n} \sum_{i=1}^{m} |x_{ij}|$

  The optimization problem becomes:

  $$\widehat{\mathbf{x}} = \frac{1}{2}\|\mathbf{y} - \mathbf{SHx}\|_2^2 + \tau\|\mathbf{Wx}\|_1. \qquad (2.33)$$

The solution of (2.33) can not be obtained directly since the cost function is not differential. However, variable splitting methods can be used, such as the alternating direction method of multipliers (ADMM) [88], the forward-backward algorithm (FBA) [89], the fast iterative shringkage thresholding algorithm (FISTA) [90].

- Total variation (TV) regularization: The TV norm was introduced by Rudin et al. [91] as an isotropic l_2-based function defined as:

$$TV(x) = \sum_{i,j} \sqrt{|x_{i+1,j} - x_{i,j}|^2 + |x_{i,j+1} - x_{i,j}|^2 + \alpha^2}, \tag{2.34}$$

where α is a small constant added since it is not possible to differentiate TV(x) at zero [92]. However, based on the choices of discretization for the image gradient, then an alternative form of TV exists relying on the l_1-norm given by:

$$TV(x) = \sum_{i,j} \{|x_{i+1,j} - x_{i,j}| + |x_{i,j+1} - x_{i,j}|\}. \tag{2.35}$$

In our work, we will use the original TV norm definition as a regularizer for the inverse problem given as:

$$R(\mathbf{x}) = \|\mathbf{x}\|_{TV} = \sqrt{\|\partial_h \mathbf{x}\|^2 + \|\partial_v \mathbf{x}\|^2}, \tag{2.36}$$

where ∂_h and ∂_v are horizontal and vertical gradient operators that, for an image $x \in \mathbb{R}^{m \times n}$ and under the periodic boundary conditions, are defined as:

$$(\partial_h x)(i,j) = \begin{cases} x(i+1,j) - x(i,j), & \text{if} \quad i < m \\ x(m,j) - x(1,j), & \text{if} \quad i = m \end{cases} \tag{2.37}$$

$$(\partial_v x)(i,j) = \begin{cases} x(i,j+1) - x(i,j), & \text{if} \quad j < n \\ x(i,n) - x(i,1), & \text{if} \quad j = n \end{cases} \tag{2.38}$$

The non-differentiable cost function is then expressed as:

$$\widehat{\mathbf{x}} = \frac{1}{2}\|\mathbf{y} - \mathbf{SHx}\|_2^2 + \tau \|\mathbf{x}\|_{TV} \tag{2.39}$$

Variable splitting methods, such as ADMM and FBA, are employed to tackle the solution of (2.39).

Single image SR in MRI   Super-resolution based on the physical model of acquisition has been addressed significantly for anatomical brain MR images. Single-image SR was performed by Luo et al. [93] based on the intrinsic link in k-space between the modulus LR image and the desired HR image. Reconstruction of the HR image was done by estimating low-frequency k-space data from the LR image then filling the high-frequency data with zeros followed by the IFT operation. On the other hand, Rousseau [94] proposed a new regularization approach for the model-based SR problem using an example-based framework that integrates non-local similarity constraints. Later on, they developed a non-local patch approach to define the regularization term taking into account the complex spatial interactions [95]. Following the work done in [94], Manjón et al. [96] used information from co-planar HR images to super-resolve LR images acquired for the same subject. In another work [97], they proposed a reconstruction method that uses a data-adaptive patch-based regularization in combination with a sub-sampling coherence constraint. This non-local mean up-sampling (NMU) method performs high-quality reconstructed images via the iteration patch-based filtering. Gholipour at al. [60, 98] and Rousseau et al. [99] used the l_2-regularization to solve the minimization optimization problem of image SR given by:

$$\widehat{\mathbf{x}} = \arg\min_x \|\mathbf{y} - \mathbf{W}\mathbf{x}\|^2 + \lambda \|C\mathbf{x}\|_2^2, \tag{2.40}$$

where **H** incorporates motion compensation, degradation effects, and sub-sampling for each slice **Y**, and **C** is a positive definite matrix.

Shi et al. [100] proposed a super–resolution method that integrates both local and global information. This approach is based on the idea of matrix completion i.e. considering the recovery of the HR matrix from a low rank (incomplete) matrix by combining Low Rank and TV regularizations for the effective image SR as:

$$\widehat{\mathbf{x}} = \arg\min_x \|\mathbf{y} - \mathbf{S}\mathbf{H}\mathbf{x}\|^2 + \lambda_{rank} Rank(\mathbf{x}) + \lambda_{TV} TV(\mathbf{x}), \tag{2.41}$$

where λ_{rank} and λ_{TV} are the tuning parameters for the low–rank and TV terms respectively, *Rank* is the weighted sum of trace norms of all slices along each dimension of an image and *TV* denotes the integral of the absolute gradients of data. The regularizer *Rank* takes advantages of the similarity

between the slices in different directions. Figure 2.3 shows an example of the results collected in [100] for the SR of brain MR images using their proposed method compared to nearest-neighbor interpolation (NN), spline interpolation (Spline), IBP based up-sampling [84], NLM based up-sampling [97], and TV based up-sampling [101]. While NN, Spline and IBP methods resulted in blurry images, TV provides a better reconstruction and the proposed LRTV shows better details.
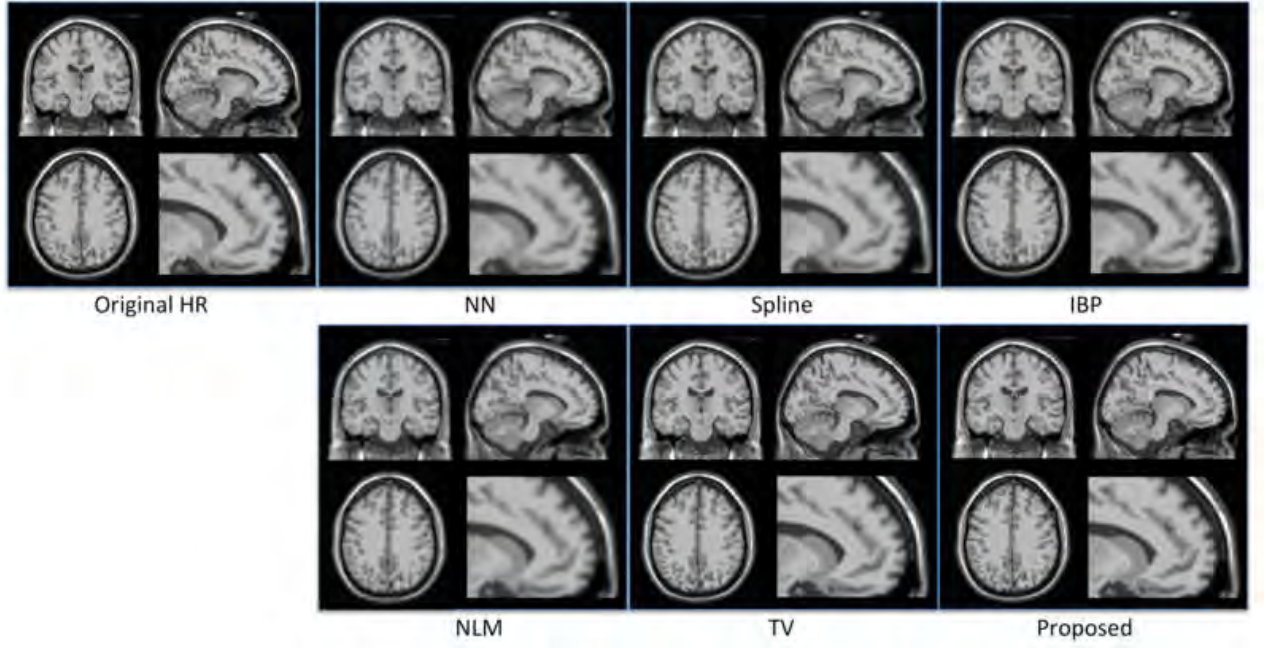
Figure 2.3: Illustration of upsampling results for simulated data on a typical slice for each of coronal, sagittal, and axial views, and a zoom-up of frontal region in the sagittal view. LR data with $2 \times 2 \times 2mm^3$ resolution was upsampled to $1 \times 1 \times 1mm^3$. This figure was collected from [100].

In this PhD thesis, we will evaluate several model-based methods for single image SR that have not been applied in MR images before. Among the existing methods for single image SR, we wish to assess a proposed Fast Single Image Super-resolution method by Zhao et al. [102] which solves the SR problem in an ADMM framework for US imaging by exploring the intrinsic properties of blur and decimation kernels in the frequency domain. The main interest in this approach is in the reduced computational cost compared to other model-based SR methods. While this method defines the

convolution problem in 2D, we will therefore apply it on 3D volumes slice by slice. Moreover, driven by the interest to explore the SR problem in 3D, we will continue to evaluate a tensor-factorization-based approach, originally proposed by Hatvani et al. [103] for dental CT images, which offers a fast solution without the use of known image pairs or strict prior assumptions. We will then compare the results to the technique proposed by Shi et al. [100], where they have presented interesting results for the SR of brain MR images.

2.3.2.4   Deep learning-based SR methods

Learning based approaches establish the relationship of HR images with their corresponding LR images by assuming available external data. Given a set of extracted patch pairs $\{(x_i, y_i)\}_{i=1}^{N}$ these methods consist in learning a direct mapping $\phi(x_i, y_i)$ between the LR patches y_i to the HR patches x_i. This section gives an introduction to deep learning generalities and a review of the application of deep learning methods for the super resolution problem in MRI [82, 104].

Deep learning introduction   Deep learning refers to artificial neural networks (ANN) with complex multilayers. It has been remarkably used in the fields of speech recognition, computer vision, pattern recognition, natural language processing, image identification, object detection, image classification, and face identification [105]. Deep learning approaches learn high-level features from data using multiple layers of neurons having linear transformations and non-linear activation functions. A classical deep learning network is made up of an input layer, an output layer, and intermediate hidden layers. Figure 2.4 shows a classical 5 layers Multi Layer Perception (MLP) neural network [104].

Each node (neuron) of a layer combines input from the data of the previous layer with a set of coefficients, or weights assigning significance to these inputs. Denoting h^l the output of layer l, the output h^{l+1} of layer $l + 1$ can be written as :

$$h^{l+1} = \sigma^l(W^l h^l + b^l), \quad l = 1, 2, ..., L \tag{2.42}$$

where L is the total number of layers, W^l represents the weights assigned for each neuron at layer l, b^l is the bias, and σ^l is the non-linear activation function [106]. Several activation functions have been
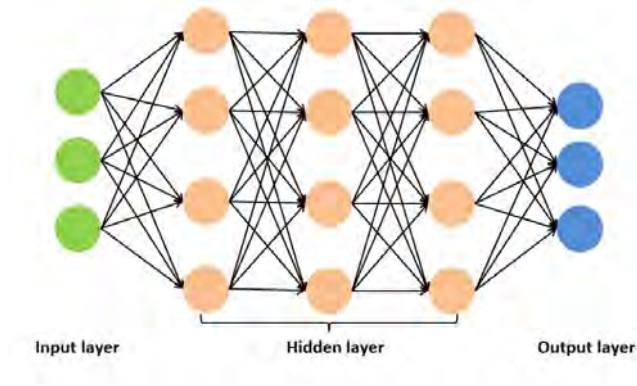
Figure 2.4: MLP neural network showing the input layer, the output layer, and the hidden layers. Figure is extracted from [104].

used for ANN such as the Rectified Linear Unit (ReLU) (Figure 2.5(a)), the Parametric Rectified Linear Unit (PReLU)(Figure 2.5(b)), and the Sigmoid function (Figure 2.5(c)) defined as:

$$ReLU(x) = \begin{cases} x, & \text{if } x \geq 0 \\ 0, & \text{otherwise} \end{cases} \tag{2.43}$$

$$PReLU(x) = \begin{cases} x, & \text{if } x \geq 0 \\ ax, & \text{otherwise} \end{cases} \tag{2.44}$$

$$sigmoid(x) = \frac{1}{1 + \exp(-x)} \tag{2.45}$$

During the training phase, input data are fed into the input layer and the network minimizes a selected loss function with respect to parameters optimized within the network [104]. The loss function measures the performance of the network and is usually a differentiable function. One of the most used loss functions is the Mean Squared Error (MSE) defined as:

$$MSE = \frac{1}{N} \sum_{i=1}^{N} (y_i - h_{i,l})^2 \tag{2.46}$$

MSE is meant to measure how different the target output y is from the predicted output in the output layer h_L in terms of the averaged square of its elements.
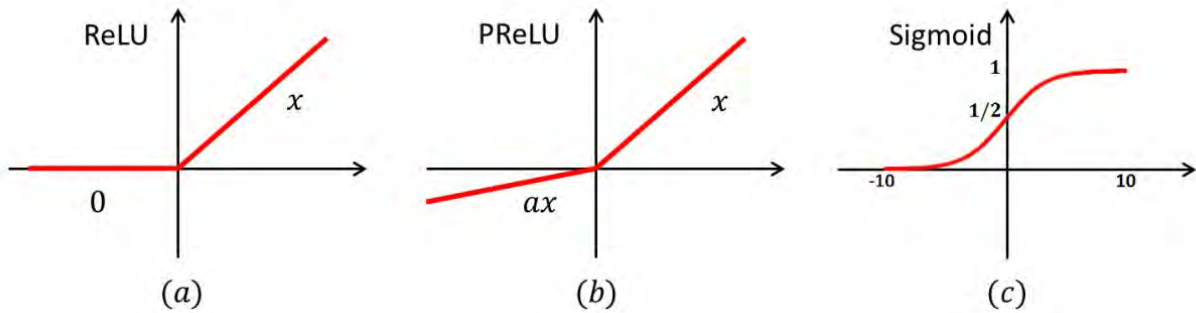
Figure 2.5: Illustration of the ReLU, PReLU, and sigmoid activation functions. The figure was extracted from [104].

With optimization, the objective is to minimize the loss function. The idea is that if the loss is reduced to an acceptable level, the model has indirectly learned the function that maps inputs to outputs. The most commonly used optimizers are Stochastic Gradient Descent (SGD) [107], Adaptive Moments (Adam) [108], and Root Mean Squared Propagation (RMSprop). Each optimizer features tunable parameters like learning rate, momentum, and decay. Adam and RMSprop are variations of SGD with adaptive learning rates [109].

Advanced network architectures have been proposed in the literature and have proven their efficiency in the image processing domain, including Generative Adversarial Networks (GANs), Google's inception network, Ronneberger's U-net, ResNets, Variational Networks, Recurrent Neural Networks (RNNs), and Convolution Neural Networks (CNN) [110]. CNN architectures that emerge from deep learning are computationally very efficient. CNN have multiple layers including fully-connected layers, pooling layers, convolutional, and non-linearity layers. While convolutional layers only face a limited perceptive field and all neurons share the same weight, pooling layers reduce the total input size and their combination in an alternating manner constructs CNNs (see Figure 2.6).
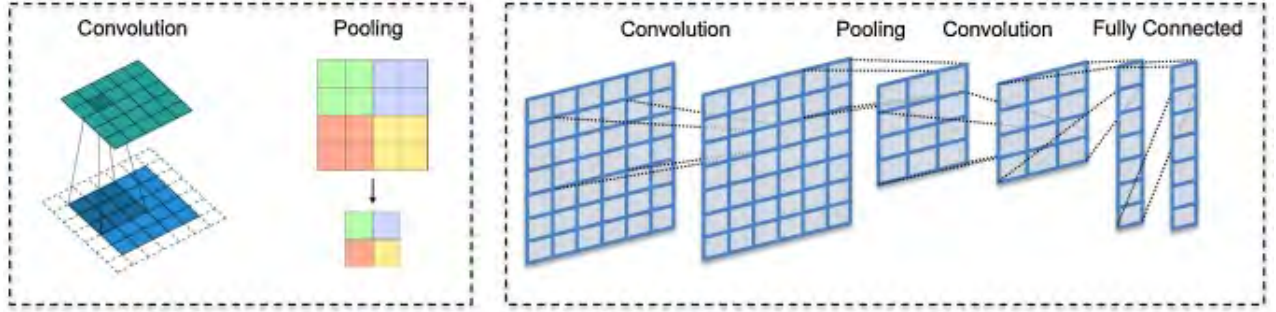
Figure 2.6: CNNs architecture based on convolutional and pooling layers. Figure is collected from [110].

Deep learning for MRI SR   Several deep learning methods have been proposed in the literature for the SR of medical images [111–114]. For conciseness, we focus in this section only on the application of deep learning methods in MRI super resolution problems. Oktay el al. [115] proposed an anatomically constrained convolutional neural network (ACNN) for image segmentation and super-resolution tasks evaluated on multi-modal cardiac MR and Ultrasound (US) data sets. They used auto-encoder (AE) and T-L networks as regularizers to train neural network (NN) models (Figure 2.7). They introduced two losses, the X-Entropy Loss (L_x) for segmentation and the Smooth L_1 loss for super resolution, to integrate shape prior and improve the accuracy of estimation at pixel level. The idea is to non-linearly transform the estimation and the reference into a low dimensional space and to penalize the dissimilarity between them [104].

Chaudhari et al. [116] developed a SR technique using convolutional neural networks to generate thin-slice knee MR images from thicker input slices. Their DeepResolve network learns a residual-based transformations between high-resolution thin-slice images and lower-resolution thick-slice images at the same center locations (see Figure 2.8).
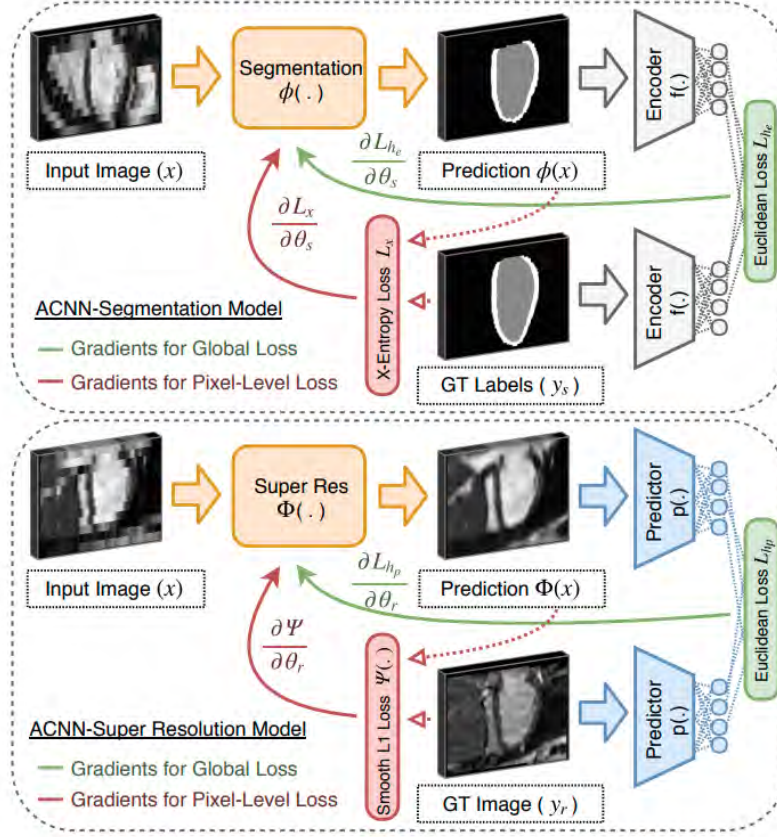
Figure 2.7: ACNN network proposed in [115] and regularized using AE and T-L networks for segmentation and super-resolution tasks. The figure was collected from [115].
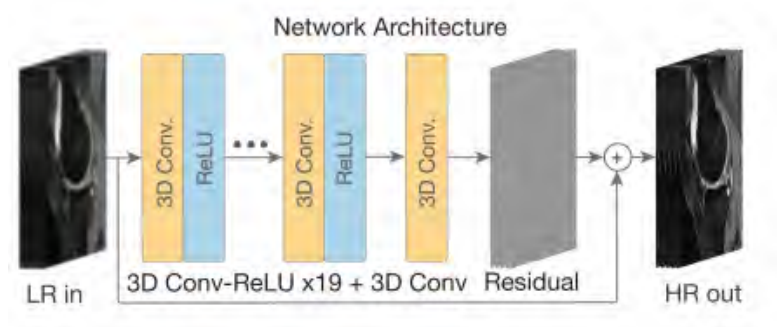
Figure 2.8: The DeepResolve network architecture that computes a residual image from an input LR image in order to generate the corresponding HR image. The figure was collected from [116].

Mansoor at al. [117] investigated the application of SR Generative adversarial network (SRGAN), presented first in [118] for photo realistic images, on volumetric CT and MRI data sets. A generator was trained to estimate HR diagnostic quality images from LR observations. A discriminator then distinguished the real diagnostic quality image from the estimated diagnostic quality image. A perceptual loss function, rather than pixel-based mean-squared error (MSE) loss, was calculated on the feature maps of the network. The network was trained on LR images that were simulated by blurring and down-sampling HR diagnostic quality images. The proposed framework is presented in Figure 2.9.

Zhao et al. [119] presented a self SR algorithm (SSR) for single image SR of brain MRI that was inspired by [120] and extended from the enhanced deep super-resolution network (EDSR) [121]. In their approach, MR images acquired were low in resolution in the coronal and sagittal planes and high in resolution in the axial plane. Consequently, the HR axial slice was degraded to resemble the LR ones, and the EDSR network was then trained with the paired low and high resolution axial slices. The trained network was further used to reconstruct the LR slices in the coronal and sagittal planes. An overview of the proposed work is provided in Figure 2.10.
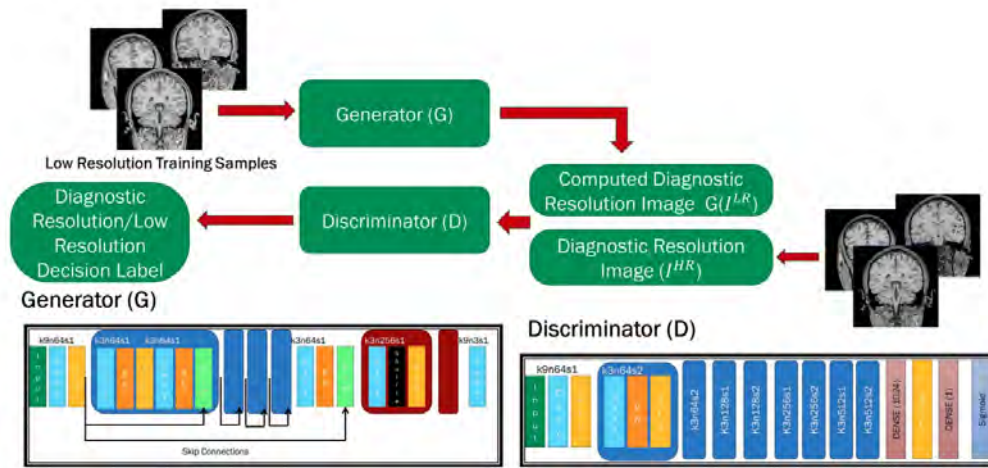
Figure 2.9: SRGAN method proposed for the enhancement of MR and CT scans. The figure was collected from [117].
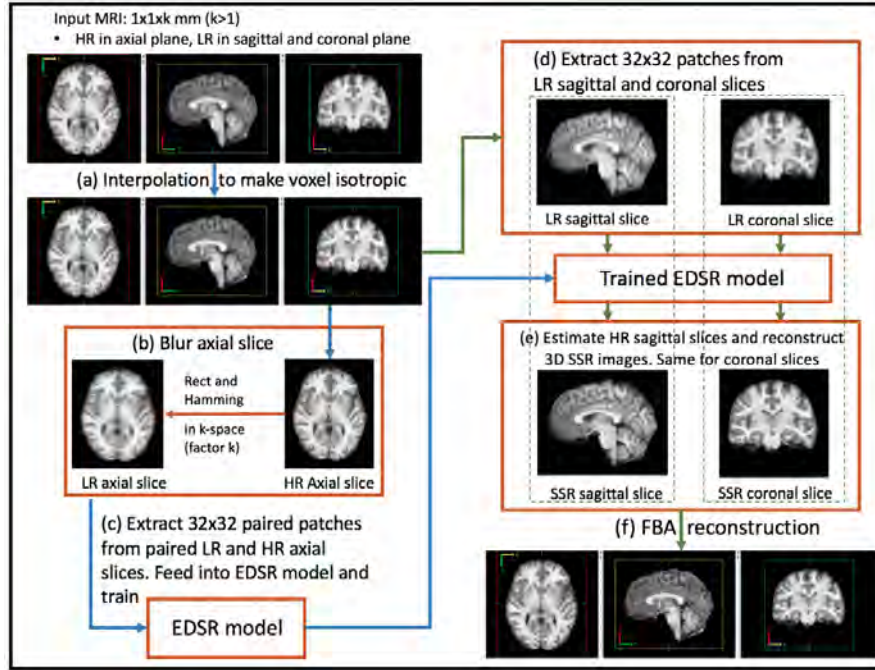
Figure 2.10: The proposed framework for MRI single image SR. The figure was extracted from [119].

Chen et al. [122] proposed a single image densely connected SR network (DCSRN) for brain MRI images where the output of each layer is connected to the following layers. The authors claimed that their proposed method offers three main advantages: faster training due to shorter paths, a light-weight due to weight sharing, and less over-fitting during training since the number of parameters is greatly reduced and features are reused. For the training task, LR images were created in the frequency domain rather than the classical image-domain simulations. The proposed network architecture is presented in Figure 2.11.

Chun et al. [123] developed a framework, based on the concept named cascaded deep learning, that consists of three main components: a CNN-based denoising auto-encoder (DAE) trained using clinical LR noisy MRI scans that have been processed with a non-local means (NLM) filter, a down-sampling network (DSN) trained with a small amount of paired LR/HR data, and a proposed SR generative model (p-SRG) trained with data generated by the DSN that maps from LR inputs to HR outputs. The authors concluded that their robust SR MRI reconstruction method enabled 3D
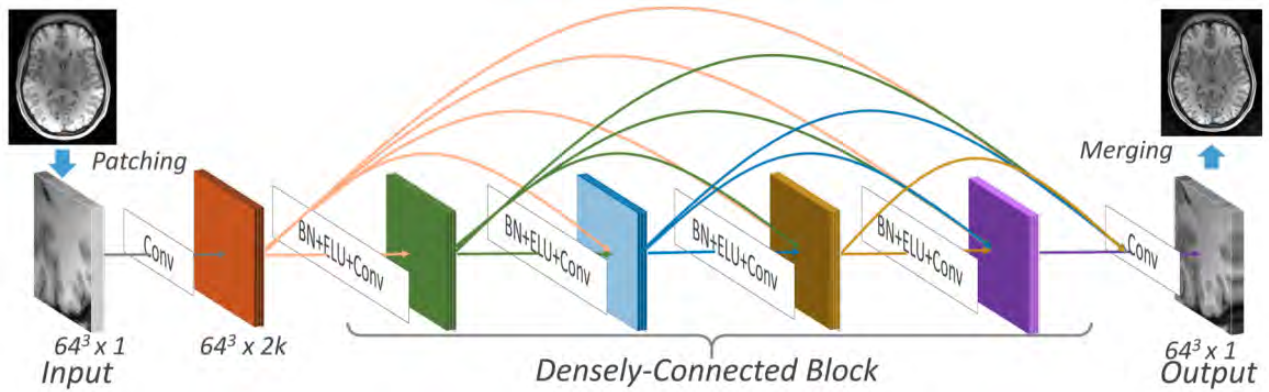
Figure 2.11: DCSRN for single image SR of brain MR images. The figure was collected from [122].

LR breath-hold MRI as well as 4D-MRI within a clinically feasible time frame without sacrificing spatial resolution or image quality. Figure 2.12 shows a summary of the proposed network.

Investigations in single image SR of MRI, applied to brain image enhancement, continued using different deep learning approaches. Zeng et al. [124] proposed a deep convolutional neural network model, which performs single- and multi-contrast super-resolution reconstructions where a HR image from another modality is used as a reference. More recently, Du et al. [125] developed a gradient-guided convolutional neural network for improving the reconstruction accuracy of high-frequency image details from the LR image where a gradient prior is used to supply the information of high-frequency details during the super-resolution process. Finally, Zhao et al. [126] presented a novel channel splitting network (CSN) which divides the hierarchical features into two branches, i.e., a residual branch and a dense branch, with different information transmissions. The residual branch is able to promote feature reuse, while the dense branch is beneficial to the exploration of new features. In this thesis, we will focus on two deep learning networks that have been proposed in the literature: the framework proposed by Pham et al. [82, 127] which performs the restoration of brain MR images using 3D residual-learning convolutional neural networks, and the work developed by Georgescu et al. [128] based on deep convolutional neural networks (CNNs) and an intermediate up-scaling layer. Further details about these methods will be elaborated in Chapter 4.

To sum up, with the development of the application of deep learning in the SR problem, researchers in medical image processing have been influenced by deep learning methods. They now propose new architectures that permit the integration of priors to boost the network's performance and facilitate the follow-up analysis and research. Moreover, increasing image resolution through super-resolution, whether model- or learning-based, is a key to a better understanding of the anatomy [61]. Indeed, the first step is to obtain a better quality of an image that will, then, result in more accurate segmentation and registration. Therefore, based on our desire to enhance marmoset brain MR images for the better detection of biomarkers of cerebral aging, the next section will provide a literature overview of segmentation methods used for brain MR images. In particular, we will highlight the importance of performing longitudinal segmentation, i.e., taking into consideration intra-subject variability in such studies.
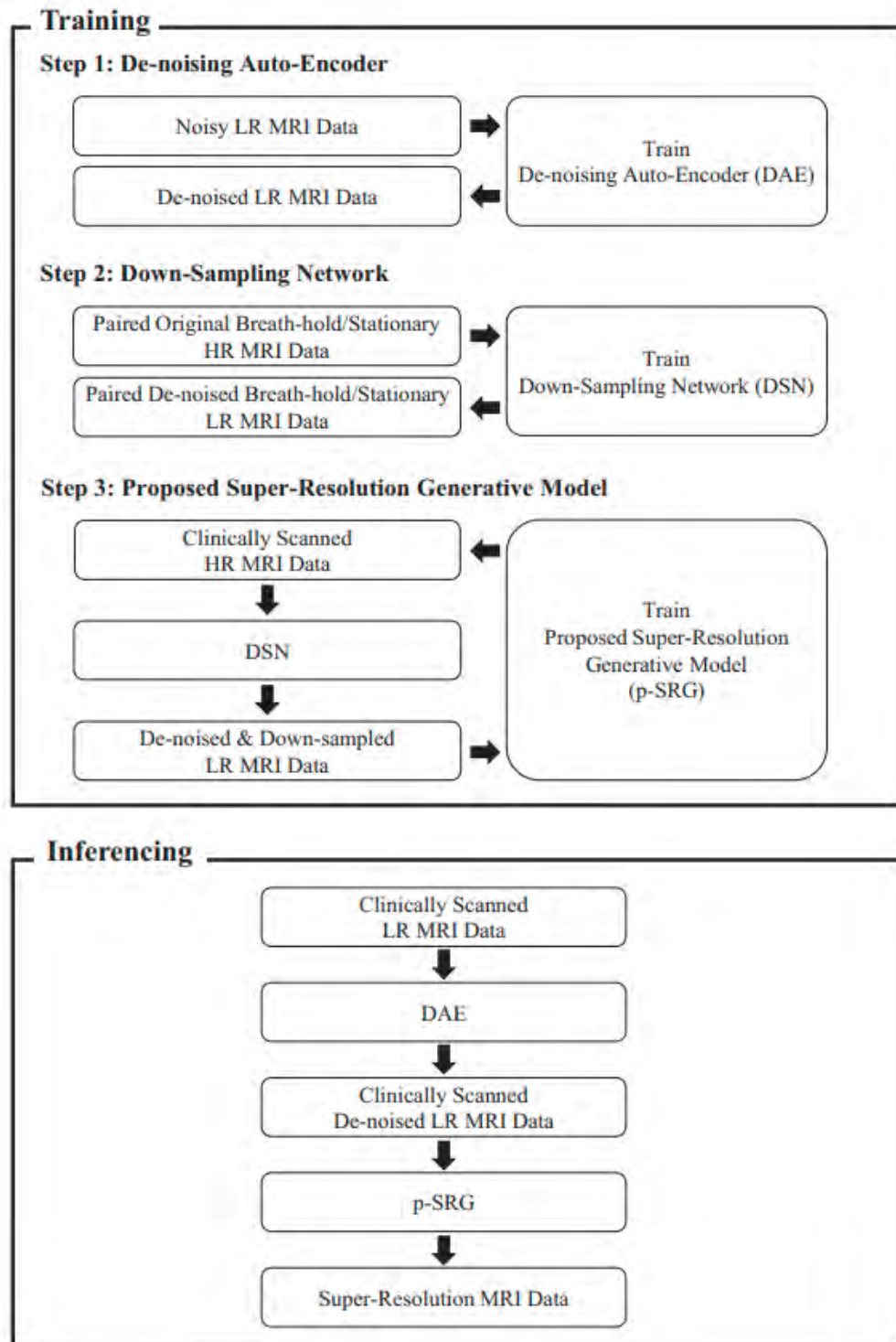
Figure 2.12: Proposed framework for SR MRI reconstruction using cascaded deep learning. The figure was collected from [123].

2.4 MR Image Segmentation

Developing post-processing methods to enhance degraded images reduces the partial volume effect, improves the relative contrast between adjacent tissues, and improves the segmentation accuracy. In this section, we will provide an overview of the segmentation techniques used for brain MR images while highlighting those proposed for animal volumes in particular, and we will introduce the basics of Statistical Parametric Mapping (SPM), the segmentation tool that will be used in our work. Moreover, we will present longitudinal segmentation methods as they appeared in the literature with their advantages over using cross-sectional methods.

2.4.1 Brain Segmentation in MRI

Segmentation of human brain images has been extensively discussed in the literature benefiting from the availability of rich databases and templates of human MRI. Consequently, several methods have been investigated to perform brain segmentation [129, 130]. According to the survey done by Gordillo et al. [131] and the review done by Balfar et al. [132] on segmentation techniques for brain MR images, methods of segmentation fall into one of these categories: threshold-based methods (global thresholding or local thresholding), region-based methods (region growing or watershed), pixel classification methods (Fuzzy C-means, Markov random fields or artificial neural networks [133, 134] and model-based methods (parametric deformable models or geometric deformable models/ level sets). Some segmentation techniques use multi-spectral MR images for the segmentation task. For example, Amato et al. Amato et al. [135] tested three non-parametric and one parametric discriminant analysis methods for the segmentation of a computer-built brain phantom using T1-weighted (T1-w), T2-weighted (T2-w) and proton density (PD) weighted images. Similarly, Anbeek et al. [136] investigated the optimal combination of different MR modalities for the best segmentation results. In their study, a probabilistic segmentation technique based on the supervised K-nearest neighbor (KNN) classification was used to extract information from T1-w, T2-w, PD, inversion recovery (IR) and fluid attenuation inversion recovery (FLAIR) scans. However, other researchers used only single model MR images (mainly T1-w) for the segmentation process. For example, Dong et al. [137]

used a local Gaussian mixture model for brain segmentation and non-local bias regularization for bias correction. [138] proposed an automatic segmentation technique based on a iterative clustering approach followed by denoising and bias field removal and Ballester et al. [139] combined a statistical classification method for indicating partial volume effect voxels and a geometry-driven segmentation to ensure continuous output segmentation.

Due to the complex process of image acquisition, several factors affect the quality of the output image [29], which results in the corruption of the image, a reduction in the contrast and spatial resolution and consequently makes the segmentation procedure a challenging task. This problem accentuates when imaging small sized anatomical structures in animal models. For instance Mclaren et al. [140] compared between the segmentation of the rhesus macaque (*Macaca mulatta*) brain using FAST (FMRIB's Automated Segmentation Tool) from FSL (FMRIB's Software Library), which does not require prior maps but only a template, and SPM, which requires both the priors and the template. They finally recommended to use SPM for segmentation in non-human primates. Moreover, SPM has been systematically used in the literature for the segmentation of marmoset brain. For example, it has been used for the detection of regional volume loss in the marmoset brain in [141]. In [142], Hikishima et al. created priors for the marmoset brain using the FAST algorithm from FSL (depending on the marmoset atlas). These priors were further used in SPM for the final segmentation of the brain into GM, WM and CSF in order to create a marmoset brain template. Although a few attempts of marmoset brain atlases have been proposed in the literature [143–146], the construction of such an atlas is limited by the availability of sufficient data. However, even for the most advanced methods of segmentation using deep learning [147, 148], the presence of huge validation and training data sets along with their manually labeled annotations is essential.

Another axis of image segmentation methods emerges with the development of machine learning and deep learning algorithms, especially with the increase of medical imaging data sets. However, automated image segmentation methods using deep learning techniques require the presence of a huge dataset with ground truth labels for training, validation and evaluation of the proposed networks. Akkus et al. [149] provide a detailed review on deep learning for brain MRI segmentation. To summarize, there exist several convolutional neural network (CNN) architecture styles for the

segmentation task (see Figure 2.13). Patch-wise CNN architecture extracts image patches and train the network using their corresponding labels [150–152]. Semantic-wise CNN architecture includes encoder and decoder parts to extract features and classify pixels of an image [153]. Cascaded CNN architecture, which combines two CNN architectures for the classification task, is extensively used for brain tumor segmentation [154].

Despite the high accuracy of segmentation results using deep learning algorithms [149], the presence of ground truth labels for the training and evaluation sets is necessary. However, in our work, obtaining the ground truth labels of the marmoset brain is time-consuming and requires an expert in the domain. For instance, we were able to obtain the manual segmentation of only three volumes with the help of a marmoset brain specialist. Therefore, with the lack of ground truth labels, segmentation techniques using deep learning were not a choice in this thesis. However, based on the recommendation provided in [140] for the use of SPM for the segmentation of non-human primates' brains, we will thereby perform the marmoset brain segmentation using SPM throughout all our work.

Tissue classification and segmentation using SPM, as proposed by Ashburner and Friston in [155], relies on a generative model based on the mixture of Gaussian model (MOG) that takes into account bias correction and registration with probability maps of the main brain compartments (GM, WM and CSF). It minimizes the following objective function (ϵ):

$$\epsilon = \sum_{n=1}^{N} \log \frac{\rho_i(\beta))}{\sum_{k=1}^{K} \gamma_k b_{ik}(\alpha))} \sum_{k=1}^{K} \gamma_k b_{ik}(\alpha)(2\pi\sigma_k^2)^{1/2} \times \exp\left(-\frac{(\rho_i(\beta)y_i - \mu_k)^{1/2}}{2\sigma_k^2}\right) \tag{2.47}$$

where K is the total number of Gaussians considered in the mixture model, $\rho_i(\beta)$ accounts for smooth intensity variations related to bias correction, b_{ik} is the tissue probability to belong to class k at voxel i, α represents the parameter allowing the registration to a standard space through map deformation, y_i is the ith element of the observed data y, μ_k and σ_k are the mean and standard deviation of the kth Gaussian to which y_i belongs and γ_k is the probability of a voxel to belong to the kth Gaussian. In our work, the number of Gaussians assigned for each region are two for GM, two for WM, two for CSF, and four for everything else. Starting by prior tissue probability maps containing the values b_{ik}, the goal is to optimize the model's parameters to obtain the final segmentation maps using information

from the image pixels. The mixture of parameters $\{\mu, \sigma, \gamma, \alpha, \beta\}$ are optimized using the iterative Expectation-Maximization (EM) algorithm [156]. Furthermore, the estimate of the bias field (β) is updated following the Levenberg–Marquardt (LM) [157] optimization approach. In the proposed objective function, the tissue probability maps are allowed to be deformed according to α that is updated using the same LM strategy. A detailed mathematical explanation of the optimization problem is presented in [38].

Tissue probability maps represent the prior information to which the brain volume will be registered to in order to create the final segmentation. Producing these maps involves warping a given template to match the target brain volume to be segmented. Similar to most existing brain segmentation methods that will be discussed afterwards, SPM requires these information to be contained in a brain template built from an atlas.

Generating tissue probability maps is a relatively easy task when the template is available such as in the case of human brain applications. However, obtaining a template is more challenging for animals, especially when data is readily available, making brain segmentation more difficult in such situations compared to human brain applications. Therefore, it becomes important to develop methods for creating such maps without the need for a template available, which is one of the main objectives of the work proposed in the thesis and that will be addressed in Chapter 3.

Most segmentation algorithms proposed are categorized as cross-sectional techniques since only one measurement per individual is available for the study. Although informative, cross-sectional studies are limited because they cannot provide information about change within individuals since data is analyzed individually. However, when multiple measurements of the same individual are acquired for the segmentation task, the technique is referred to as being longitudinal. Longitudinal segmentation takes into account intra-individual variability, i.e. differences observed within the same subject when assessed at different times.
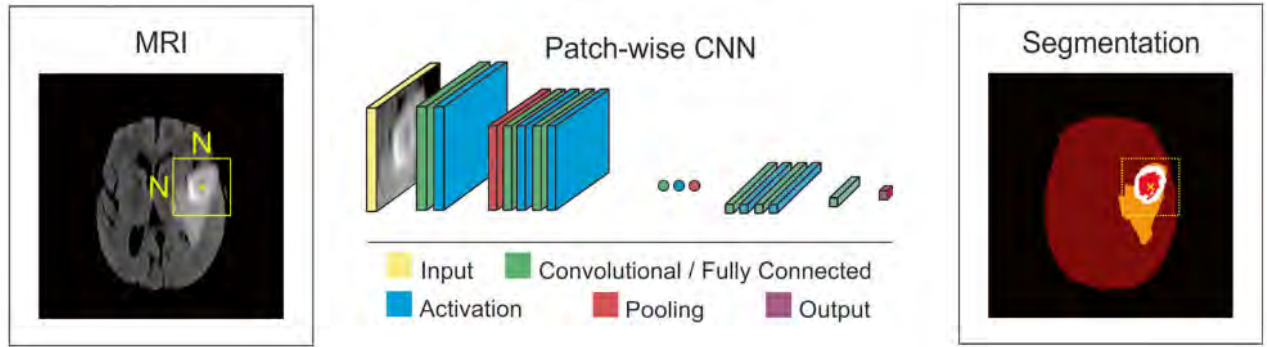
(a) Patch-wise CNN architecture
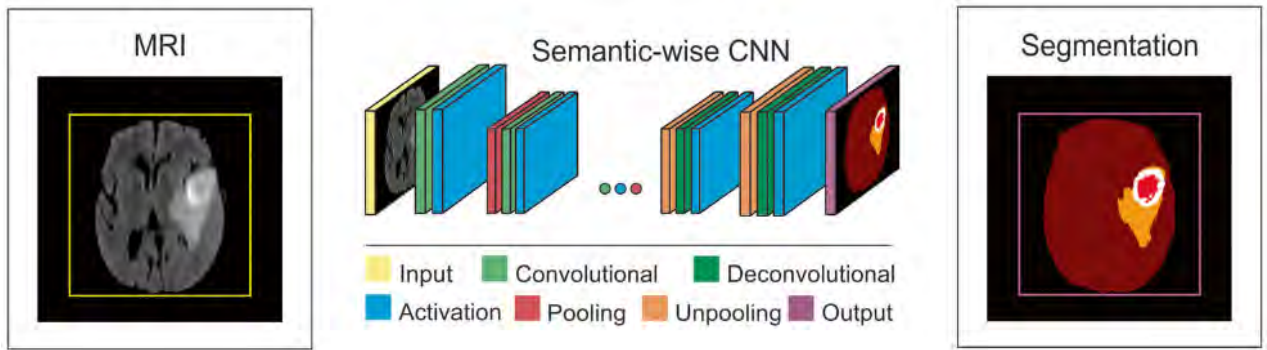
(b) Semantic-wise CNN architecture
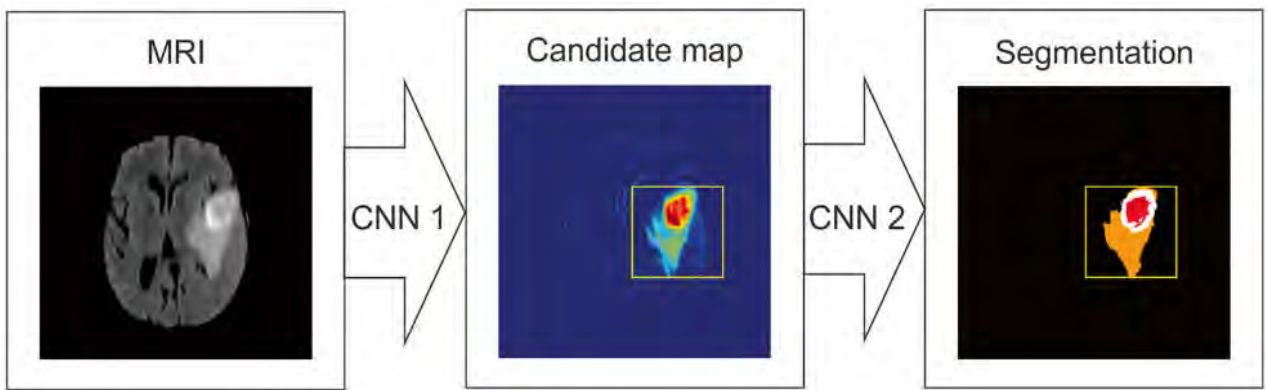
(c) Cascaded CNN architecture

Figure 2.13:   Schematic representation of CCN architecture styles for brain segmentation in MRI. Figures are collected from [149].

2.4.2 Longitudinal Segmentation

Longitudinal studies of aging collect abundant health measures throughout the life span of the same individuals. Data generated from these studies help identify trajectories associated with aging in a given population, leading to a greater understanding of the link between aging and age-associated chronic diseases. Consequently, the treatment of longitudinal data requires adapted processing methods that differ from the cross-sectional ones. In this context, several longitudinal segmentation schemes have been reported in the literature to follow the longitudinal brain changes with aging.

Since information is often transferred across time within each subject, Xue et al. [158] designed an algorithm that optimizes all time points simultaneously by jointly segmenting the 4D volume, within subject, via longitudinal high-order warps to the baseline scan using an elastic warping algorithm. They treated the baseline scan differently from follow-up images by using it as the reference frame for their registration.

Reuter et al. [159] proposed a longitudinal segmentation scheme enabling temporally unbiased evaluation of an arbitrary number of time points by treating all inputs the same. The method was based on generating an unbiased within-subject template. The template was designed by individually segmenting all time points followed by solving an iterative minimization problem that computes a median image of the time points then registers and re-samples each input until convergence. Longitudinal segmentation was then performed based on information from the built template and initialized by the individual cross-sectional segmentation of the time points. The pipeline of the proposed method is presented in Figure 2.14.

Hadj-Hamou et al. [160] presented a deformation-based morphometry framework relying on three main steps: preprocessing of raw data by standard orientation, FOV reduction, and intensity non-uniformity correction, longitudinal position correction by rigidly aligning follow-up images to the base-line image, and normalization of the residual morphological differences using non-linear registration. The resulting intra-subject model in the subject's space is estimated using ordinary least squares regression in the tangent space of Stationary Velocity Fields (SVF). It is equivalent to the assumption that the deformation noises are centered, uncorrelated and have equal variance in the space of SVFs. Then for a given template and subject-to-template deformation, the intra-subject

model can be transported using parallel transport in the template space. This deformation can be decomposed along the template trajectories giving a morphological aging rate, a disease progression rate, and an orthogonal component. The framework is summarized in Figure 2.15.

Figure 2.14: Proposed pipeline for longitudinal segmentation using within-subject template. The figure was collected from [159].

Aubert-Broche et al. [161] proposed a longitudinal registration and classification scheme based on the creation of subject-specific linear and non-linear templates in which participant-specific information is used for both registration and segmentation. The longitudinal scheme is designed to be unbiased with respect to any time point (TP). Instead of initializing it with information from a specific time point, a template volume is created. This template can be seen as an initial guess for the segmentation and surface reconstruction. Each T1-weighted time point is pre-processed individually by performing image denoising using the NLM filter, intensity inhomogeneity correction, and intensity scaling. Images are then subject to a longitudinal registration method, including a rigid registration to the ICBM152 template, linear registration to a linear subject-specific template, and a non-linear registration to a non-linear subject-specific template. These templates are created iteratively from the data studied. Longitudinal classification of regional brain volumes is then achieved by an initial

cross-sectional classification of GM, WM, and CSF, followed by an Expectation Minimization (EM) used to obtain the final classification. Details of the proposed framework are presented in Figure 2.16.
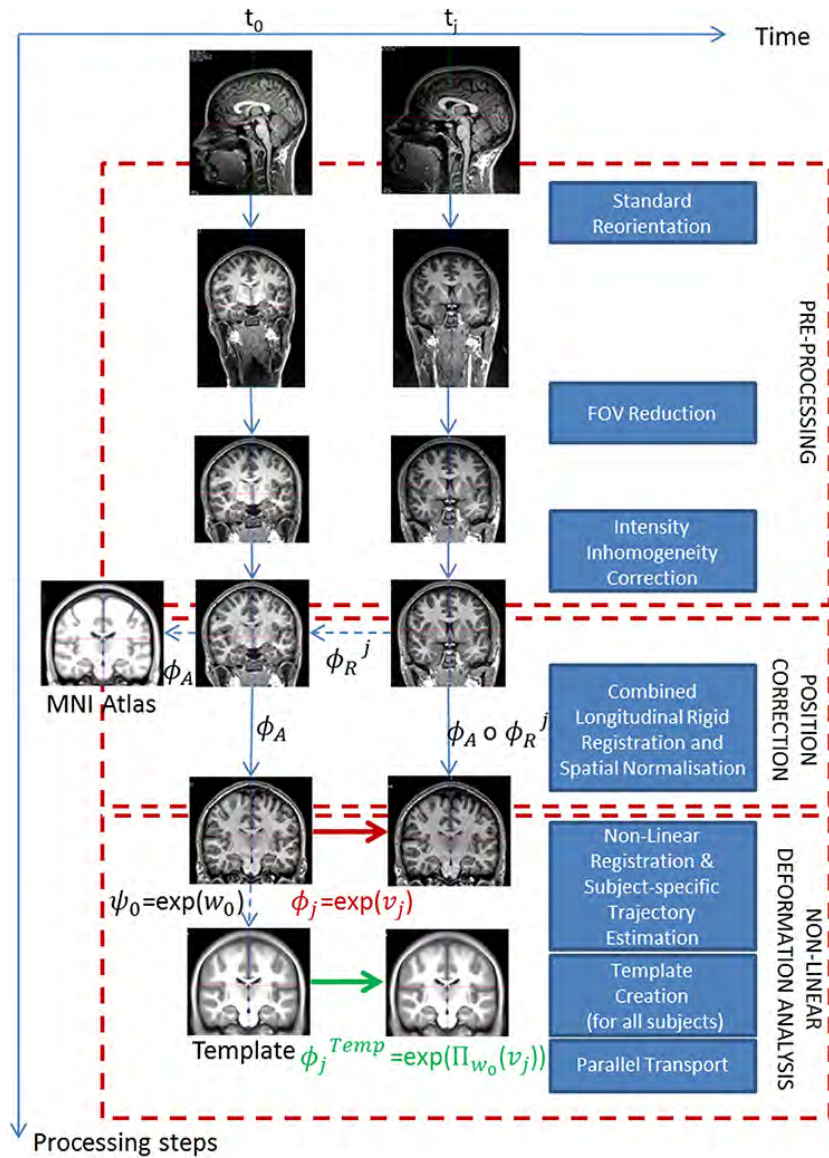
Figure 2.15: Longitudinal log-Demons framework (LLDF) for longitudinal segmentation as proposed by Hadj-Hamou et al [160]. The figure was extracted from [160].
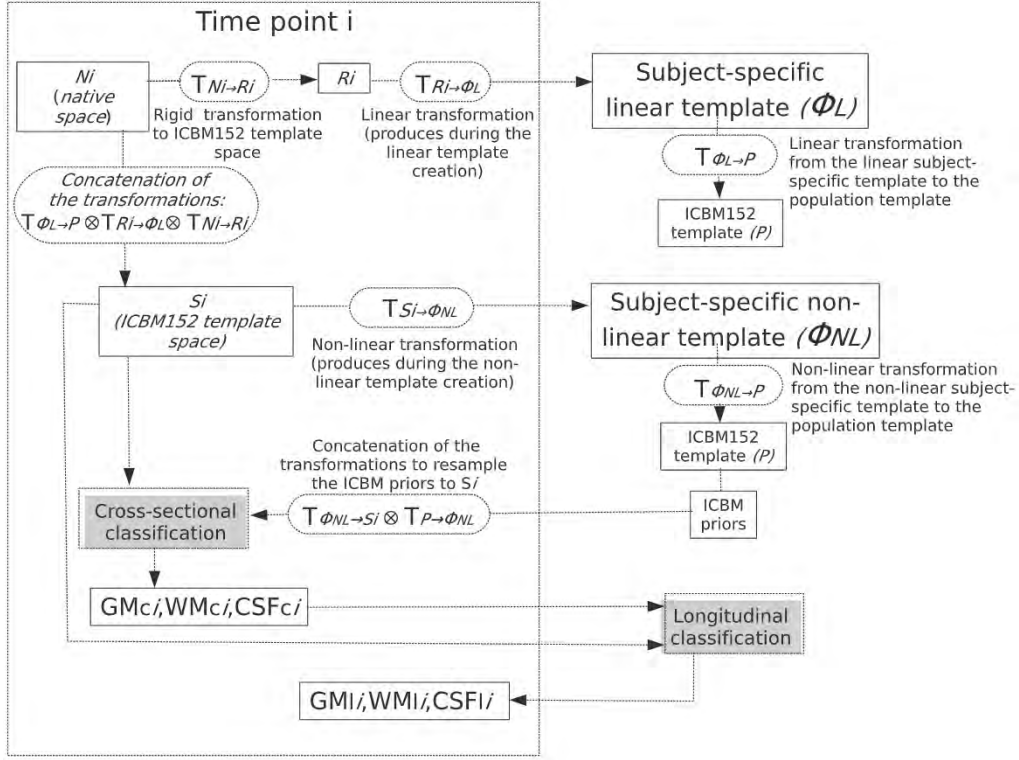
Figure 2.16: Longitudinal registration and longitudinal classification (LL) scheme as proposed by Aubert-Broche et al. The figure was extracted from [161].

Several tools are available online to perform the longitudinal segmentation task of human brain images. For instance, the longitudinal segmentation stream in FreeSurfer, based on the method proposed by Reuter et al. [159], allows for a probabilistic voting scheme of independently processed label maps from all time points, to determine the probability of a specific voxel having a specific label by weighting labels across time according to their intensity similarity. This fused segmentation is then used to initialize the segmentation algorithm for each time point instead of the fixed segmentation of the subject template to allow for larger departures from the subject average. Similarly, the aBeat tool box proposed by Dai et al. [162] integrates a group of image processing tools, including 4D brain extraction, 4D tissue segmentation, and 4D brain labeling to provide robust and accurate analysis of the longitudinal adult brain MR images. The architecture of the aBeat toolbox is provided in Figure 2.17 showing its five main processing modules.
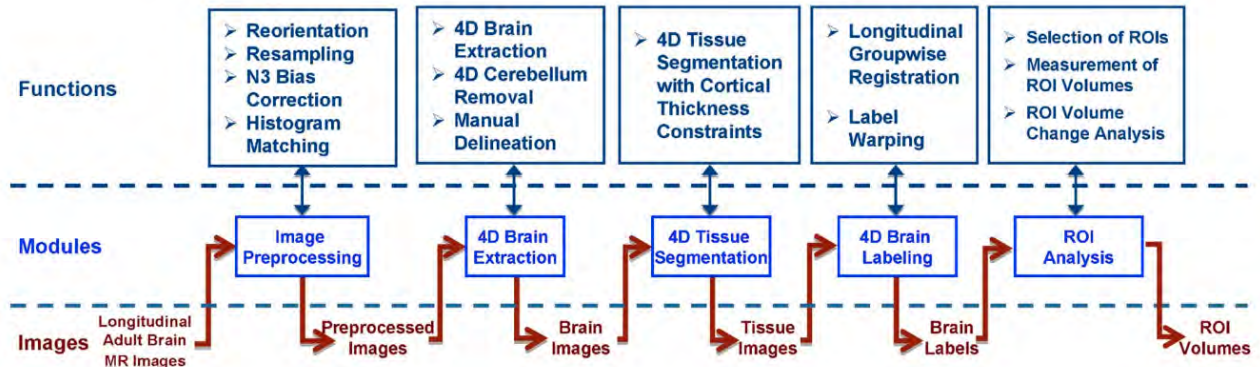
Figure 2.17: aBEAT toolbox architecture. The figure was collected from [162].

The image preprocessing module normalizes the original images and corrects their intensities. The 4D brain extraction module consistently removes non-brain tissues (such as scalp and skull) and keeps brain tissues (including GM, WM, and CSF) from the preprocessed longitudinal images of each subject. The serial brain tissues of each subject are then jointly segmented by the 4D tissue segmentation module. Next, the 4D brain labeling module simultaneously warps an atlas with pre-labeled ROIs onto the longitudinal images for ROI labeling. Finally, longitudinal ROI volumes and the volume changes for all subjects can be automatically measured and displayed using the ROI analysis module [162].

As an extension to the optimized VBM framework in [6], CAT12 toolbox (`www.neuro.uni-jena.de/cat/`), integrated as an SPM module, offers a longitudinal segmentation pipeline of the human brain for detecting small brain changes. Figure 2.18 shows the steps for processing longitudinal data. First, initial inverse-consistent rigid registration, including bias-correction between time points, is performed on images of all time points. These images are then re-aligned and segmented into different tissue types (i.e. gray and white matter and CSF). In the following step, the registration parameters (i.e. deformation fields) are estimated using a non-linear spatial registration (Dartel or Geodesic Shooting) and then averaged. Finally, the resulting mean deformation is applied to the tissue segmentation of all time points and modulated with the Jacobian determinant of the deformation.
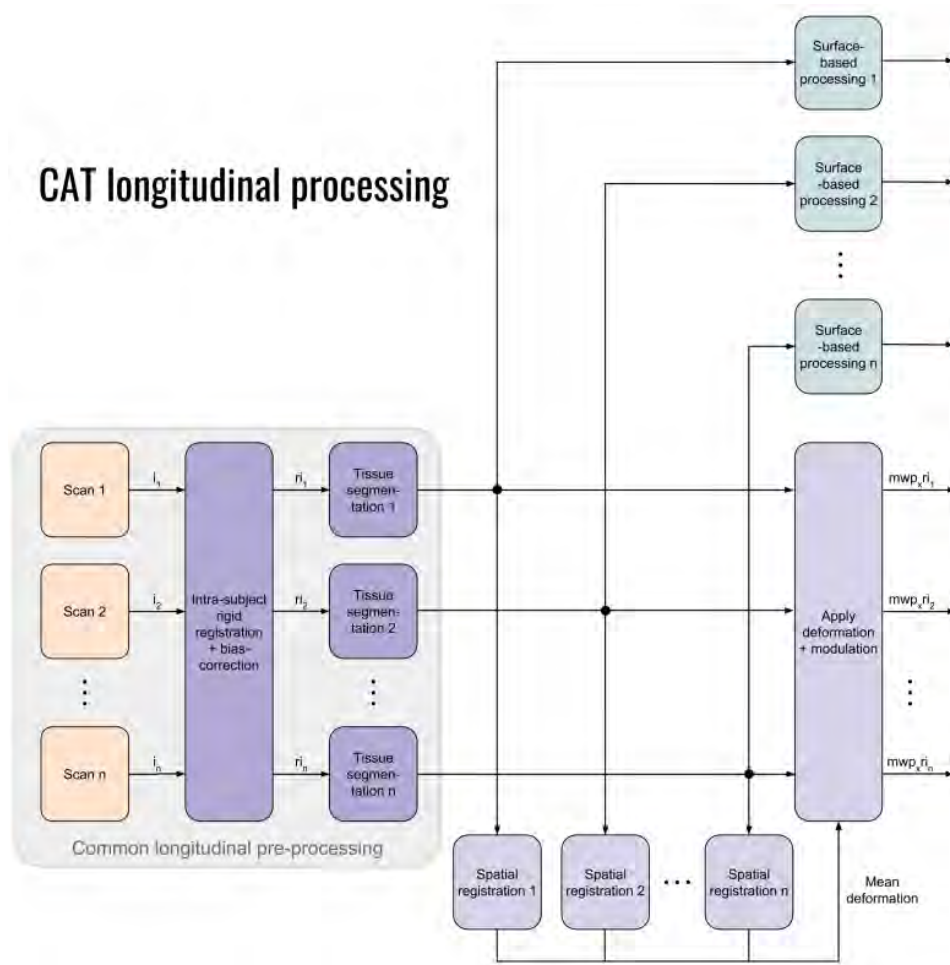
Figure 2.18: CAT12 framework for longitudinal brain segmentation. Figure was collected from the CAT12 manual (www.neuro.uni-jena.de/cat12/CAT12-Manual.pdf).

2.5   Conclusion

Longitudinal image processing aims at reducing within-subject variability by transferring information across time, i.e. informing the processing of later time points with results from earlier scans. While within-subject anatomical changes are usually significantly smaller than inter-individual morphological differences, developing longitudinal schemes to detect these changes becomes inevitable. However, accurate and robust segmentation and analysis of these changes require sufficiently high-resolution MR images that offer high contrast and spatial resolution between adjacent tissues. This chapter covers the existing work related to these two main topics: MRI super resolution and longitudinal image segmentation and analysis.

In our thesis work, we will evaluate the effectiveness of several SR approaches that have been reported in the literature. We will compare the performance of model- and learning-based methods in the enhancement problem. Moreover, starting from the longitudinal segmentation scheme proposed in CAT12, we will present a pipeline developed and adapted for the longitudinal segmentation and analysis of marmoset brain. At the end, we will compare the VBM analysis of the native images to that using super-resolved images to highlight the importance of image quality in the accuracy of the analysis.

In the next chapter, we will present a joint deconvolution and segmentation method for Marmoset brain segmentation based on modeling locally the image statistics using a Generalized Gaussian distribution (GGD) and coupling the deconvolved image and its corresponding labels map using GGD-Potts model.

CHAPTER **3**

Marmoset Brain Segmentation from Deconvolved Magnetic Resonance Images and Estimated Label Maps

This chapter presents material from the journal paper [163].

Contents

    This chapter introduces a joint deconvolution and segmentation method for marmoset brain MR images. The proposed approach aims to create label maps that can be used for the segmentation of animal brain MR images without the need for a brain template. This is achieved by performing a joint deconvolution and segmentation of the brain MR images. It is based on modeling locally the image statistics using a Generalized Gaussian distribution (GGD) and couples the deconvolved image and its corresponding labels map using a GGD-Potts model. Due to the complexity of the resulting Bayesian estimators of the unknown model parameters, Gibbs sampler is used to generate samples

following the desired posterior distribution. The performance of the proposed algorithm is assessed on simulated and real MR images by the segmentation of enhanced marmoset brain images into its main compartments using the corresponding label maps created. The proposed method of using labels as prior information for brain segmentation provides similar or slightly better performance compared to the classical reference method based on a dedicated template.

3.1   Introduction

MRI has been widely used in the past decades for the non-invasive exploration of the structural and functional properties of organs and tissues due to its high contrast and spatial resolution. MRI presents a powerful tool for extracting diagnostic information, measurements and statistics which aid the study of the progression and regression of some diseases [29]. It also allows for the quantitative calculation of volumes and helps in extracting valuable biomarkers characterizing a specific condition [164]. More specifically, T1-weighted anatomical MRI remains the main protocol for the analysis of structural brain changes that occur with age and which plays a significant role in the development of brain related diseases such as epilepsy, Parkinson, Alzheimer, etc. The study of such changes, as well as the differentiation between normal aging and brain pathologies [165], on human brains or on animal brain models, as in the case of the marmosets (*Callithrix jacchus*) considered in this thesis, require the brain's segmentation into its main compartments: gray matter (GM), white matter (WM) and cerebrospinal fluid (CSF). However, imaging small brains in a 3T MRI platform dedicated to humans is a challenging task because the spatial resolution and the contrast obtained are insufficient compared to the size of the anatomical structures observed. Degradation in the quality of images during acquisition and reconstruction results in miss-classification or over segmentation of different regions of interest [166]. In the absence of a higher field MRI scanner for generating high quality images, it becomes crucial to develop appropriate post-processing methods for the enhancement of preclinical images which allows the analysis of morphological changes. The goal of image enhancement is thus to improve the usefulness of an image for a given task [167], in our case image segmentation.

While enhancement and segmentation are usually done separately, several researchers have investigated the joint enhancement and segmentation for different medical imaging modalities. To further combine between both tasks, Zhao et al. [67] proposed a joint segmentation and deconvolution Bayesian method for medical ultrasound (US) images. This method defines a Potts Markov random field for the hidden image labels and assigns GGD priors to the image tissue reflectivity function to investigate the joint segmentation and deconvolution problem. Visual impression and numerical results on simulated and real US data confirmed that a better contrast and more defined boundaries between the different tissues is achieved with their method. Similarly, Ayasso and Djafari [168] proposed a method to simultaneously restore and to segment piecewise homogenous images degraded by a known point spread function (PSF) using a family of non-homogeneous Gauss-Markov fields with Potts region labels model in a Bayesian estimation framework. Toma [169] and Li [104] developed joint super-resolution and segmentation approaches for trabecular bone computed tomography (CT) images. In her work, Toma [169] investigated variational approaches to perform the SR task using TV regularization and the 3D joint SR and segmentation task using a convexification of the regularization functional with additional box constraints. As an extension to her work, Li [104] proposed a semi-coupled dictionary learning approach in which two dictionaries are learned corresponding to the high and low resolution CT images and a deep learning approach inspired by the Fast Super-Resolution Convolutional Neural Networks (FSRCNN) suggested by Dong et al. [170]. Finally, Bahrami et al. [171] proposed a mutual deep-learning based framework, composed of cascaded CNNs, to estimate 7T-like MR images and their corresponding segmentation maps from 3T MR images. Their method presented higher restoration and segmentation accuracy when compared to state of the art methods.

In this context, the aim of this chapter is to propose a joint deconvolution and segmentation method, relying on the method proposed in [67], to create prior maps for marmoset brain MR images. The output label maps, considered as prior maps, are further used in SPM along with the enhanced image for the final segmentation of the brain into GM, WM, and CSF. In this method, we assume that the priors of the image follow a generalized Gaussian distribution (GGD), and we define a Potts Markov random field for the hidden discrete labels representing the segmentation of

the image. The originality of this work is to propose a segmentation method which does not depend on the registration of the brain template to the MR image. Rather, it is based on the statistical properties of the regions and the correlation between the neighboring pixels forming these regions. The computation of the Bayesian estimators corresponding to the posterior distribution is then given by a Markov Chain Monte Carlo (MCMC) method based on a Gibbs sampler, which reduces their computational complexity. The interest of this approach goes beyond the study of marmoset brain MRI since it can be applied to the study of human brain such as in the fetal brain study or of any animal model, especially when specific templates are not available.

3.2   Methods

The aim of this chapter is to introduce a method for brain segmentation without the need for a template with an application to marmoset MR images. More precisely, the probability maps required by SPM segmentation method are replaced by the label maps estimated with the proposed algorithm, referred to as joint MCMC (JMCMC) hereafter. Figure 3.1 summarizes the proposed label-based segmentation methodology (referred to as segLabels) by comparison to the existing template-based segmentation approach (called segTemp). Instead of creating probability maps from the template registration to the MR volume to be segmented, further used by SPM, JMCMC algorithm outputs an enhanced version of the volume along with label maps that partition the images into statistically homogeneous regions. Once these labels are estimated, segLabels can then be applied either to the native MR volume or its enhanced version estimated by the proposed segmentation and deconvolution algorithm. Starting from an MR image observation model, this method based on a Bayesian approach aims at jointly estimating enhanced MR images and label maps corresponding to statistical homogeneous regions.
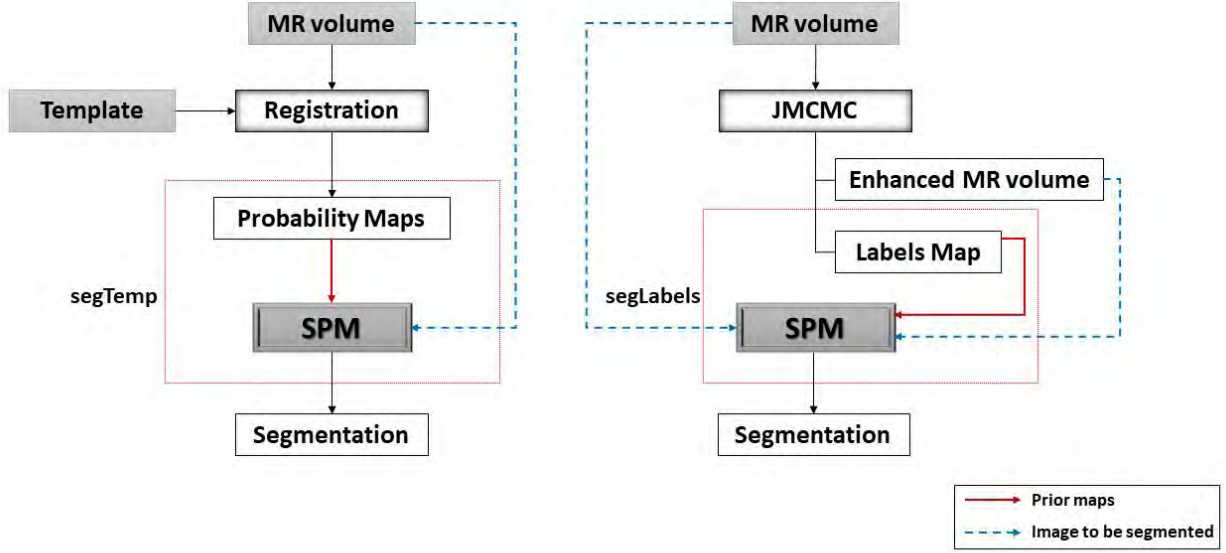
Figure 3.1: Workflows of existing segTemp and proposed segLabels methods. While segTemp requires a template registration procedure to generate probability maps, the JMCMC method produces enhanced MR volumes and estimated label maps that serve as priors for the proposed segLabels segmentation in SPM, thus not requiring neither a brain template nor a registration method. segTemp and segLabels can be further applied to the native MR volume or its enhanced version obtained by deconvolution to get the final segmentation.

3.2.1 Image Formation Model

As stated in Chapter 2, taking as input the reconstructed MR image and considering the convolution (blur) operator as the only degradation in addition to noise, this results into the simplified model as follows:

$$\mathbf{y} = \mathbf{Hx} + \mathbf{n}, \tag{3.1}$$

where $\mathbf{y}$ is the observed image, $\mathbf{x}$ is the image to be estimated, $\mathbf{H}$ is the blurring matrix classically constructed from the imaging system PSF and $\mathbf{n}$ is an additive, zero-mean white Gaussian noise.

At this point, the objective is to estimate $\mathbf{x}$ from $\mathbf{y}$ given a known PSF, $\mathbf{H}$, which is a typical deconvolution problem. However, as previously stated and in order to avoid the use of a registered template within SPM, the proposed method aims at estimating, at the same time, $\mathbf{x}$ and a label map dividing the image into statistically homogeneous regions. To this end, suppose that the clean image $\mathbf{x} = (x_1, \cdots, x_N)^T$ can be divided into K regions $\{\mathcal{R}_1, ..., \mathcal{R}_K\}$ and that a hidden label field $\mathbf{z} = (z_1, \cdots, z_N)^T \in \mathbb{R}^N$ maps the N image pixels into these K regions. Suppose also that pixel intensities are distributed following a generalized Gaussian distribution (GGD). Then, the conditional distribution for a pixel x_i to belong to the region R_k (*i.e.* $z_i = k$) where $i \in \{1, \cdots, N\}$ and $k \in \{1, \cdots, K\}$ is:

$$x_i | z_i = k \sim \mathcal{GGD}(\mu_k, \xi_k, \gamma_k), \tag{3.2}$$

where μ_k, ξ_k and γ_k are respectively the mean, shape and scale parameters of the GGD associated to the region $\mathcal{R}_k$. The probability density function (pdf) of a univariate GGD with a mean μ, shape parameter ξ and scale parameter γ is:

$$p(x) = \frac{1}{2\gamma^{1/\xi}\Gamma(1 + 1/\xi)} \exp\left(-\frac{|x - \mu|^\xi}{\gamma}\right), \quad x \in \mathbb{R}. \tag{3.3}$$

Assuming that pixels from different regions are conditionally independent, the pdf of $\mathbf{x}$ is given by

$$p(x_i) = \sum_{k=1}^{K} w_k \mathcal{GGD}(\mu_k, \xi_k, \gamma_k) \text{ with } w_k = P(z_i = k). \tag{3.4}$$

A Potts model is used in the following for the hidden field $\mathbf{z}$, imposing high probability for neighbouring pixels to have the same label, i.e., to belong to the same region, and thus promoting smooth label maps [168].

3.2.2 Hierarchical Bayesian model

Using the Bayes rule, the joint posterior distribution of the unknown image $\mathbf{x}$ and its corresponding labels $\mathbf{z}$ can be written as:

$$p(\mathbf{x}, \boldsymbol{\theta}, \mathbf{z} | \mathbf{y}) \propto p(\mathbf{y} | \mathbf{x}, \boldsymbol{\theta}) p(\mathbf{x} | \mathbf{z}, \boldsymbol{\theta}) p(\mathbf{z} | \boldsymbol{\theta}), \tag{3.5}$$

where $\boldsymbol{\theta}$ is a parameter vector containing the unknown hyperparameters including the noise variance, and the mean, shape and scale parameters of the GGD characterizing each region. The posterior

distribution requires the knowledge of the likelihood $p(\mathbf{y}|\mathbf{x}, \boldsymbol{\theta})$, which depends on the noise model, and the prior distributions $p(\mathbf{x}|\mathbf{z}, \boldsymbol{\theta})$ and $p(\mathbf{z}|\boldsymbol{\theta})$, which are based on the GGD-Potts model.

3.2.2.1 Likelihood

The likelihood function derived from the linear model, defined in equation (2), depends on the noise $\mathbf{n}$ being an additive white Gaussian noise (AWGN) with a constant variance σ_n^2:

$$p(\mathbf{y}|\mathbf{x}, \sigma_n^2) = \frac{1}{(2\pi\sigma_n^2)^{N/2}} \exp\left(-\frac{1}{2\sigma_n^2}\|\mathbf{y} - \mathbf{H}\mathbf{x}\|_2^2\right), \tag{3.6}$$

where $\|\cdot\|_2$ is the Euclidean ℓ_2-norm.

3.2.2.2 Prior distributions

Deblurred image x Assuming that $\mathbf{x}$ follows a mixture of GGD and that the pixels of different regions are conditionally independent, the prior distribution of $\mathbf{x}$ can be written as:

$$\begin{aligned}
p(\mathbf{x}|\mathbf{z}, \boldsymbol{\mu}, \boldsymbol{\xi}, \boldsymbol{\gamma}) &= \prod_{k=1}^{K} \prod_{i=1}^{N_k} \frac{1}{2\gamma_k^{1/\xi_k}\Gamma(1 + 1/\xi_k)} \exp\left(-\frac{|x_i - \mu_k|^{\xi_k}}{\gamma_k}\right) \\
&= \prod_{k=1}^{K} \frac{1}{\left[2\gamma_k^{1/\xi_k}\Gamma(1 + 1/\xi_k)\right]^{N_k}} \exp\left(-\frac{\sum_{i=1}^{N_k}|x_i - \mu_k|^{\xi_k}}{\gamma_k}\right) \\
&= \prod_{k=1}^{K} \frac{1}{\left[2\gamma_k^{1/\xi_k}\Gamma(1 + 1/\xi_k)\right]^{N_k}} \exp\left(-\frac{\|\mathbf{x}_k - \mu_k\|_{\xi_k}^{\xi_k}}{\gamma_k}\right),
\end{aligned} \tag{3.7}$$

where $\boldsymbol{\mu} = (\mu_1, \cdots, \mu_K)^T$, $\boldsymbol{\xi} = (\xi_1, \cdots, \xi_K)^T$ and $\boldsymbol{\gamma} = (\gamma_1, \cdots, \gamma_K)^T$. μ_k, ξ_k and γ_k are the mean, shape and scale parameters of the kth region $\mathcal{R}_k$ and N_k is the number of pixels in $\mathcal{R}_k$. $\mathbf{x}_k$ contains all the pixels assigned to $\mathcal{R}_k$. $\Gamma(\cdot)$ is the gamma function and $\|\mathbf{x}_k - \mu_k\|_{\xi} = (\sum_{i=1}^{N_k}|x_i - \mu_k|^{\xi})^{1/\xi}$ denotes the ℓ_ξ-norm.

Labels z The Potts Markov Random Field (PMRF) imposing high priority that neighboring pixels belong to the same region [172] is chosen to describe the conditional distribution of z_n given by:

$$p(z_n|\mathbf{z}_{-n}) = p(z_n|\mathbf{z}_{\mathcal{V}(n)}), \tag{3.8}$$

where $\mathbf{z}_{-n} = (z_1, ..., z_{n-1}, z_{n+1}, ..., z_N)^T$ and $\mathcal{V}(n)$ contains the 4-nearest neighbors of label z_n. Using an Ising model [173], the prior distribution of $\mathbf{z}$ can then be written as:

$$p(\mathbf{z}) = \frac{1}{C(\beta)} \exp \left[\sum_{n=1}^{N} \sum_{n' \in \mathcal{V}(n)} \beta \delta(z_n - z_{n'}) \right], \tag{3.9}$$

where β is the granularity coefficient tuned manually, $\delta(\cdot)$ is the Kronecker function and $C(\beta)$ is a normalization constant.

Noise variance (σ_n^2)   The non-informative conjugate inverse gamma $(\mathcal{IG})$ distribution was assigned to noise variance:

$$\begin{aligned} p(\sigma_n^2) &\sim \mathcal{IG}(\alpha, \nu) \\ &= \frac{\nu^\alpha}{\Gamma(\alpha)} (\sigma_n^2)^{-\alpha-1} \exp \left(-\frac{\nu}{\sigma_n^2} \right) \mathcal{I}_{\mathbb{R}+}(\sigma_n^2), \end{aligned} \tag{3.10}$$

where α is the shape parameter and ν is the scale parameter of the inverse gamma distribution, and $\mathcal{I}_A$ is the indicator function on the set A.

GGD parameters   Independent Gaussian prior distribution was used for modeling the mean [174], the uninformative Jeffreys prior for the scale parameter γ_k and uniform distribution in the range $[0,3]$ for the shape parameter ξ_k.

$$p(\boldsymbol{\mu}) = \prod_{k=1}^{K} p(\mu_k) = \prod_{k=1}^{K} \frac{1}{2\pi\sigma_0^2} \exp \left(-\frac{(\mu_k - \mu_0)^2}{2\sigma_0^2} \right) \tag{3.11}$$

$$p(\boldsymbol{\gamma}) = \prod_{k=1}^{K} p(\gamma_k) = \prod_{k=1}^{K} \frac{1}{\gamma_k} \mathcal{I}_{\mathbb{R}+}(\gamma_k) \tag{3.12}$$

$$p(\boldsymbol{\xi}) = \prod_{k=1}^{K} p(\xi_k) = \prod_{k=1}^{K} \frac{1}{3} \mathcal{I}_{[0,3]}(\xi_k) \tag{3.13}$$

3.2.2.3 Joint distributions

The joint posterior distribution of the unknown parameters $\mathbf{x}, \sigma_n^2, \boldsymbol{\mu}, \boldsymbol{\xi}, \boldsymbol{\gamma}, \mathbf{z}$ can be written as:

$$p(\mathbf{x}, \sigma_n^2, \boldsymbol{\mu}, \boldsymbol{\xi}, \boldsymbol{\gamma}, \mathbf{z}|\mathbf{y}) \propto p(\mathbf{y}|\mathbf{x}, \sigma_n^2, \boldsymbol{\mu}, \boldsymbol{\xi}, \boldsymbol{\gamma}, \mathbf{z}) \times p(\mathbf{x}, \sigma_n^2, \boldsymbol{\mu}, \boldsymbol{\xi}, \boldsymbol{\gamma}, \mathbf{z})$$

$$\propto p(\mathbf{y}|\mathbf{x}, \sigma_n^2, \boldsymbol{\mu}, \boldsymbol{\xi}, \boldsymbol{\gamma}, \mathbf{z}) \times p(\mathbf{x}|\boldsymbol{\mu}, \boldsymbol{\xi}, \boldsymbol{\gamma}, \mathbf{z}) \times p(\sigma_n^2) \times p(\boldsymbol{\mu}) \times p(\boldsymbol{\xi}) \times p(\boldsymbol{\gamma}) \times p(\mathbf{z})$$

$$\propto \frac{1}{(2\pi\sigma_n^2)^{N/2}} \exp\left(-\frac{1}{2\sigma_n^2}\|\mathbf{y} - \mathbf{Hx}\|_2^2\right) \times \frac{1}{(\sigma_n^2)^{\alpha+1}} \exp\left(-\nu/\sigma_n^2\right)$$

$$\times \prod_{k=1}^{K} \left\{ a_k^{N_k} \exp\left(-\frac{\|\mathbf{x}_k - \mu_k\|_{\xi_k}^{\xi_k}}{\gamma_k}\right) \times \frac{1}{2\pi\sigma_0^2} \exp\left(-\frac{(\mu_k - \mu_0)^2}{2\sigma_0^2}\right) \right.$$

$$\left. \times \exp\left[\sum_{n=1}^{N} \sum_{n'\in\mathcal{V}(n)} \beta\delta(z_n - z_{n'})\right] \times \frac{1}{3}\mathcal{I}_{[0,3]}(\xi_k)\frac{1}{\gamma_k}\mathcal{I}_{\mathbb{R}+}(\gamma_k) \right\}, \qquad (3.14)$$

where $a_k = \frac{1}{2\gamma_k^{1/\xi_k}\Gamma(1+1/\xi_k)}$ and the hyperparameters are supposed to be *a priori* independent.

Figure 3.2 represents the proposed hierarchical Bayesian model which mainly differs from the model provided by [67] in modeling the mean value of each segmented region which, unlike ultrasound images, was necessary when using MR images. Moreover, the final objective of the authors in [67] was not the quality of the segmentation but rather to propose a method to perform both tasks of deconvolution and segmentation jointly.

3.2.3 Sampling the posterior distribution

Given the complexity of the posterior distribution in (3.14) and the need for estimating both continuous variables such as the deconvolved image and discrete value variables, i.e., the labels, a simulation method is used in this work instead of numerical optimization routines. More precisely, an MCMC method is employed, following the sampling scheme proposed in [67]. Hybrid Gibbs sampler is used to generate a great number of samples distributed according to the joint posterior law (3.14) due to the complexity of computing the estimators of the unknown parameters directly. The generated samples are further used to calculate the marginal MAP estimator of $\mathbf{z}$ and the MMSE estimators for $\mathbf{x}$, σ_n^2, $\boldsymbol{\mu}$, $\boldsymbol{\xi}$ and $\boldsymbol{\gamma}$. In the following subsection, the conditional distribution of each unknown is given, and the way they are sampled following these distributions is described.
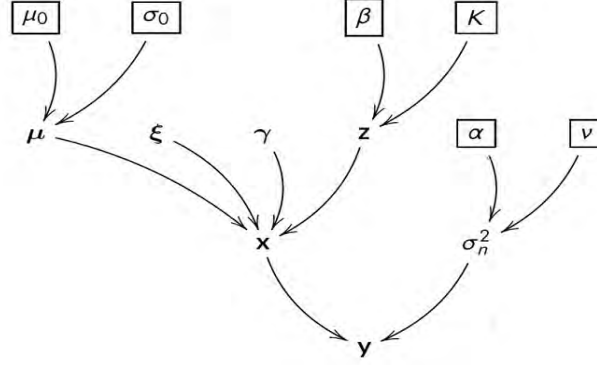
Figure 3.2: Hierarchical Bayesian model for the parameters' and hyperparameters' priors, where the deblurred image $\mathbf{x}$ is modeled by a mixture of GGDs, the hidden label field $\mathbf{z}$ follows a Potts MRF and the mean $\boldsymbol{\mu}$ follows a Gaussian distribution. The parameters appearing in the boxes are fixed in advance.

3.2.3.1 Sampling the noise variance

$$p(\sigma_n^2|\mathbf{y}, \mathbf{x}, \boldsymbol{\mu}, \boldsymbol{\xi}, \boldsymbol{\gamma}, \mathbf{z}) \propto p(\mathbf{y}|\mathbf{x}, \sigma_n^2, \boldsymbol{\mu}, \boldsymbol{\xi}, \boldsymbol{\gamma}, \mathbf{z})p(\sigma_n^2)$$
$$= \mathcal{IG}\left(\alpha + N/2, \nu + \frac{1}{2}\|\mathbf{y} - \mathbf{Hx}\|_2^2\right). \tag{3.15}$$

The samples are generated directly following (3.15). The choice of modelling the noise variance as an inverse gamma distribution has been guided by existing works such as [168] and [175].

3.2.3.2 Sampling the hyperparameters

Mean vector $\boldsymbol{\mu}$ The conditional distribution of the vector $\boldsymbol{\mu}$, containing the mean values $(\mu_1, \cdots, \mu_K)^T$ of regions $\mathcal{R}_k$, is:

$$p(\boldsymbol{\mu}|\mathbf{y}, \mathbf{x}, \sigma_n^2, \boldsymbol{\xi}, \boldsymbol{\gamma}, \mathbf{z}) \propto p(\mathbf{y}|\mathbf{x}, \sigma_n^2, \boldsymbol{\mu}, \boldsymbol{\xi}, \boldsymbol{\gamma}, \mathbf{z})p(\mathbf{x}|\boldsymbol{\mu}, \boldsymbol{\xi}, \boldsymbol{\gamma}, \mathbf{z})p(\boldsymbol{\mu})$$
$$\propto p(\mathbf{x}|\boldsymbol{\mu}, \boldsymbol{\xi}, \boldsymbol{\gamma}, \mathbf{z})p(\boldsymbol{\mu}). \tag{3.16}$$

Assuming that the mean values are *a priori* independent, we have

$$p(\mu_k|\mathbf{x}, \boldsymbol{\xi}, \boldsymbol{\gamma}, \mathbf{z}, \boldsymbol{\mu}_{-k}) \propto p(\mathbf{x}_k|\mu_k, \xi_k, \gamma_k, \mathbf{z}_k)p(\mu_k)$$

$$\propto a_k^{N_k} \exp\left(-\frac{\|\mathbf{x}_k - \mu_k\|_{\xi_k}^{\xi_k}}{\gamma_k} - \frac{(\mu_k - \mu_0)^2}{2\sigma_0^2}\right), \quad (3.17)$$

where $\boldsymbol{\mu}_{-k} = (\mu_1, ..., \mu_{k-1}, \mu_{k+1}, ..., \mu_K)$. $\mathbf{x}_k$ contains the pixels belonging to class k and having a mean $\boldsymbol{\mu}_k$, shape parameter $\boldsymbol{\xi}_k$ and scale parameter $\boldsymbol{\gamma}_k$. The conditional distribution (3.17) is sampled using random walk Metropolis Hastings (RWMH) [176].

Shape parameter vector $\boldsymbol{\xi}$

$$p(\boldsymbol{\xi}|\mathbf{y}, \mathbf{x}, \sigma_n^2, \boldsymbol{\mu}, \boldsymbol{\gamma}, \mathbf{z}) \propto p(\mathbf{y}|\mathbf{x}, \sigma_n^2, \boldsymbol{\mu}, \boldsymbol{\xi}, \boldsymbol{\gamma}, \mathbf{z})p(\mathbf{x}|\boldsymbol{\mu}, \boldsymbol{\xi}, \boldsymbol{\gamma}, \mathbf{z})p(\boldsymbol{\xi})$$

$$\propto p(\mathbf{x}|\boldsymbol{\mu}, \boldsymbol{\xi}, \boldsymbol{\gamma}, \mathbf{z})p(\boldsymbol{\xi}). \quad (3.18)$$

Assuming that the shape parameters are *a priori* independent:

$$p(\xi_k|\mathbf{x}, \boldsymbol{\mu}, \boldsymbol{\gamma}, \mathbf{z}, \boldsymbol{\xi}_{-k}) \propto p(\mathbf{x}_k|\mu_k, \xi_k, \gamma_k, \mathbf{z}_k)p(\xi_k)$$

$$\propto a_k^{N_k} \exp\left(-\frac{\|\mathbf{x}_k - \mu_k\|_{\xi_k}^{\xi_k}}{\gamma_k}\right)\mathcal{I}_{[0,3]}(\xi_k), \quad (3.19)$$

where $\boldsymbol{\xi}_{-k} = (\xi_1, ..., \xi_{k-1}, \xi_{k+1}, ..., \xi_K)$ for $k \in \{1, ..., K\}$. Similar to μ_k, the conditional distribution (3.19) is sampled by RWMH.

Scale parameter vector $\boldsymbol{\gamma}$

$$p(\boldsymbol{\gamma}|\mathbf{y}, \mathbf{x}, \sigma_n^2, \boldsymbol{\mu}, \boldsymbol{\xi}, \mathbf{z}) \propto p(\mathbf{y}|\mathbf{x}, \sigma_n^2, \boldsymbol{\mu}, \boldsymbol{\xi}, \boldsymbol{\gamma}, \mathbf{z})p(\mathbf{x}|\boldsymbol{\mu}, \boldsymbol{\xi}, \boldsymbol{\gamma}, \mathbf{z})p(\boldsymbol{\gamma})$$

$$\propto p(\mathbf{x}|\boldsymbol{\mu}, \boldsymbol{\xi}, \boldsymbol{\gamma}, \mathbf{z})p(\boldsymbol{\gamma}). \quad (3.20)$$

Assuming that the scale parameters are independent:

$$p(\gamma_k|\mathbf{x}, \boldsymbol{\mu}, \boldsymbol{\xi}, \mathbf{z}, \boldsymbol{\gamma}_{-k}) \propto p(\mathbf{x}_k|\mu_k, \xi_k, \gamma_k, \mathbf{z}_k)p(\gamma_k)$$

$$\propto \mathcal{IG}\left(\frac{N_k}{\xi_k}, \|\mathbf{x}_k - \mu_k\|_{\xi_k}^{\xi_k}\right), \quad (3.21)$$

where $\boldsymbol{\gamma}_{-k} = (\gamma_1, ..., \gamma_{k-1}, \gamma_{k+1}, ..., \gamma_K)$ for $k \in \{1, ..., K\}$. Samples are generated directly from (3.21).

3.2.3.3 Sampling the labels

$$p(\mathbf{z}|\mathbf{y}, \mathbf{x}, \sigma_n^2, \boldsymbol{\mu}, \boldsymbol{\xi}, \boldsymbol{\gamma}) \propto p(\mathbf{y}|\mathbf{x}, \sigma_n^2, \boldsymbol{\mu}, \boldsymbol{\xi}, \boldsymbol{\gamma}, \mathbf{z})p(\mathbf{x}|\boldsymbol{\mu}, \boldsymbol{\xi}, \boldsymbol{\gamma}, \mathbf{z})p(\mathbf{z})$$

$$\propto p(\mathbf{x}|\boldsymbol{\mu}, \boldsymbol{\xi}, \boldsymbol{\gamma}, \mathbf{z})p(\mathbf{z}). \tag{3.22}$$

Based on the dependency between neighboring pixels, the conditional distribution of the label z_n is:

$$p(z_n = k|\mathbf{z}_{-n}, \mathbf{x}, \boldsymbol{\mu}, \boldsymbol{\xi}, \boldsymbol{\gamma}) \propto p(x_n|z_n = k, \boldsymbol{\mu}, \boldsymbol{\xi}, \boldsymbol{\gamma})p(z_n = k|\mathbf{z}_{\mathcal{V}(n)}), \tag{3.23}$$

where $\mathbf{z}_{-n}$ is the vector $\mathbf{z}$ whose nth element has been removed and $\mathbf{z}_{\mathcal{V}(n)}$ represents the 4-pixel neighborhood structure of z_n. Denoting the left hand side of 3.23 as $\pi_{n,k}$:

$$\pi_{n,k} \propto a_k \exp\left(-\frac{|x_n - \mu_k|^{\xi_k}}{\gamma_k}\right) \exp\left(\sum_{n' \in \mathcal{V}(n)} \beta\delta(k - z_{n'})\right). \tag{3.24}$$

The normalized conditional probability of the label z_n is defined as

$$\tilde{\pi}_{n,k} = \frac{\pi_{n,k}}{\sum_{k=1}^{K} \pi_{n,k}}. \tag{3.25}$$

The label z_n can be drawn from the set $\{1, ..., K\}$ with the respective probabilities $\{\tilde{\pi}_{n,1}, ..., \tilde{\pi}_{n,K}\}$

3.2.3.4 Sampling the unknown, deblurred image

$$p(\mathbf{x}|\mathbf{y}, \sigma_n^2, \boldsymbol{\mu}, \boldsymbol{\xi}, \boldsymbol{\gamma}, \mathbf{z}) \propto \exp\left(-\frac{\|\mathbf{y} - \mathbf{Hx}\|_2^2}{2\sigma_n^2} - \sum_{k=1}^{K} \frac{\|\mathbf{x}_k - \mu_k\|_{\xi_k}^{\xi_k}}{\gamma_k}\right). \tag{3.26}$$

Given the high dimensionality of $\mathbf{x}$, for computational reasons, a Hamiltonian Monte Carlo (HMC) [177] method was used to sample the conditional distribution of the deblurred image $\mathbf{x}$ [67].

3.3 Results

This section presents the SPM segmentation results of simulated and *in vivo* MR volumes into GM, WM and CSF using both the conventional segTemp method based on template registration, and the proposed segLabels method based on the labels resulting from the joint deblurring and segmentation algorithm.

The proposed method was evaluated using four MR volumes, one simulated (simulation results) and three real (experimental results). The hyperparameters ($\boldsymbol{\mu}$, $\boldsymbol{\xi}$, $\boldsymbol{\gamma}$ and σ_n^2) are estimated automatically by the Bayesian method. Note that although the noise variance can be determined from the background signals of MR images, the computational cost of sampling the noise variance is negligible and these background signals are not always easy to identify. Thus, avoiding to estimate it in preprocessing is an advantage of the proposed algorithm. However, a detailed analysis on the difference between modelling the noise variance during the deconvolution process and pre-estimating it is presented in Section 3.3.4. On the other hand, the set of parameters (μ_0, σ_0, β, α and ν) was fixed by cross-validation to ($mean(y)$, $std(y)$, 0.6, 0, 0), where **y** is the input image, using simulated data with label ground truth available in order to ensure the best performance of the algorithm. Since the simulation data was extracted from real MR images, the same fixed values were successfully used within the experimental study. While the value of the granularity coefficient (β) could be determined by automatic approaches such as the one proposed in [172], this coefficient was tuned herein by cross-validation to ensure estimated label maps as close as possible to the true labels in the simulation study. Additional information on the influence of β is also presented in Section 3.3.4.

The number of classes K should be set by the user according to the number of regions to be segmented in the given volume. 50 chains of 2450 iterations including a given burn-in period of 800 iterations were run for each scenario. The choice of number of iterations was done based on the systematic study on the effect of number of iterations on the output of the JMCMC algorithm (See Section 3.3.4). The labels created by the JMCMC algorithm were smoothed by a Gaussian kernel with a full width at half maximum (FWHM) of 0.8 mm^3 to be further used in segLabels as priors for SPM segmentation. Experiments were conducted using MATLAB R2018a.

3.3.1 Evaluation metrics

Performance assessment of the proposed algorithm in terms of deblurring and the results of segmentation using the output labels were done quantitatively using the improvement in SNR (ISNR), normalized root mean square error (NRMSE) and image structural similarity (SSIM) and respectively

Dice coefficient. These metrics are defined as follows:

$$\text{ISNR} = 10 \log_{10} \frac{\|\mathbf{x} - \mathbf{y}\|^2}{\|\mathbf{x} - \hat{\mathbf{x}}\|^2}, \tag{3.27}$$

$$\text{NRMSE} = \sqrt{\frac{\|\mathbf{x} - \hat{\mathbf{x}}\|^2}{\|\mathbf{x}\|^2}}, \tag{3.28}$$

$$\text{SSIM} = \frac{(2\mu_A \mu_B + C_1)(2\sigma_{AB} + C_2)}{(\mu_A^2 + \mu_B^2 + C_1)(\sigma_A^2 + \sigma_B^2 + C_2)}, \tag{3.29}$$

$$\text{Dice} = 2 \frac{A \cap B}{A + B}, \tag{3.30}$$

where $\mathbf{x}, \mathbf{y}$, and $\hat{\mathbf{x}}$ are the ground truth, the corrupted image and the restored image respectively. μ_A and μ_B are the local means, σ_A and σ_B are the local standard deviations, and σ_{AB} is the cross–covariance of the two images A and B to be compared. The Dice coefficient is given as twice the number of elements common in A and B ($A \cap B$) divided by the sum of the number of elements in each (A+B).

3.3.2 Simulation results

A simulated MRI brain volume of size $78 \times 108 \times 52$ was created such that each region follows a GGD with known parameters ($\boldsymbol{\mu}$, $\boldsymbol{\xi}$ and $\boldsymbol{\gamma}$). The simulation scenario is summarized in Figure 3.3. A map of labels is created out of the registration of a selected MRI volume which was further used to create an MRI volume with simulated GGDs having parameters estimated from the initial volume. This simulated volume, considered as the ground truth (**gtVol**), was convolved by a Gaussian blurring kernel, of size 3×3 and standard deviation 0.6, and contaminated by an AWGN noise to mimic the degradation induced by the MRI scanner. The choice of this blurring PSF was based on the conclusions drawn by [42] and [81] stating that the PSF in MRI can be approximated by a Gaussian function with its FWHM being the selected slice width. The additive noise is characterized by its blurred signal to noise ratio (BSNR) defined as:

$$\text{BSNR} = 10 \log_{10} \left(\frac{\|\mathbf{Hx} - E(\mathbf{Hx})\|_2^2}{N\sigma_n^2} \right), \tag{3.31}$$

where $E(\cdot)$ is the empirical average and N is the total number of image pixels. The BSNR was set to 30 dB.
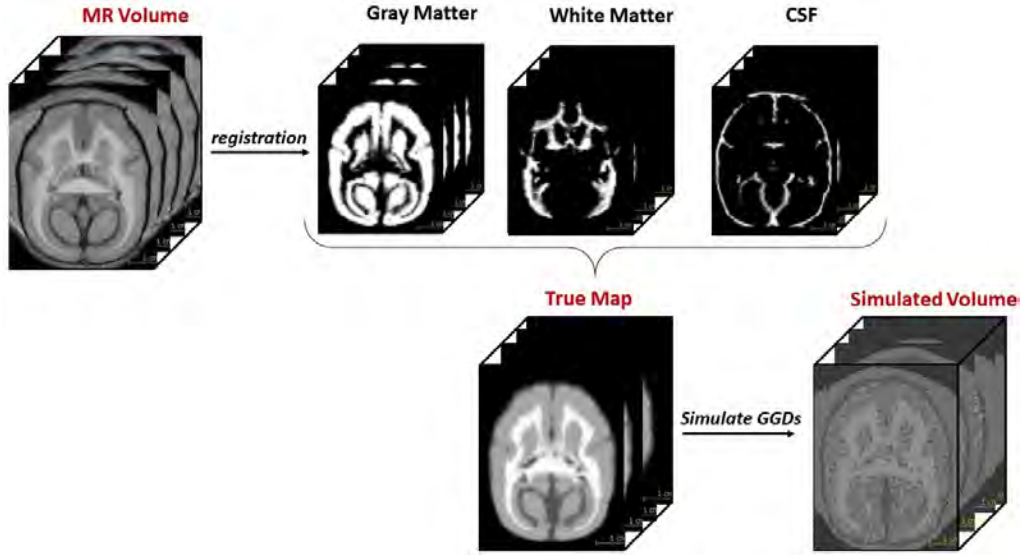
Figure 3.3: Simulation scenario of an MRI volume with voxel intensities following GGDs with known parameters.

The quality of the deblurring by deconvolution using JMCMC was quantitatively assessed by comparing the recovered volume to the ground truth in terms of ISNR, NRMSE and SSIM. The average of these metrics ($\pm$ the standard deviation) for the 52 slices were computed, and we obtained an ISNR $= 26.21 \pm 1.79$ dB, NRMSE $= 0.026 \pm 0.014$ and SSIM $= 0.98 \pm 0.14$.

To further study the efficiency of using the label-based segmentation method, the recovered volume was segmented using the template-based segmentation method and the corrupted volume using the labels produced by the JMCMC algorithm. The results of segmentation of GM and WM using these two methods is shown for an axial slice in Figure 3.4 compared to the true labels of the ground truth volume.

Finally, Table 3.1 shows the average SSIM and Dice coefficients of 52 slices computed for the GM and WM segmentation respectively. InDices were computed by comparing the true maps with the following segmentation results: segmentation obtained from 1) corrupted volume using segTemp, 2) corrupted volume using segLabels, 3) recovered volume using segTemp and 4) recovered volume using segLabels.
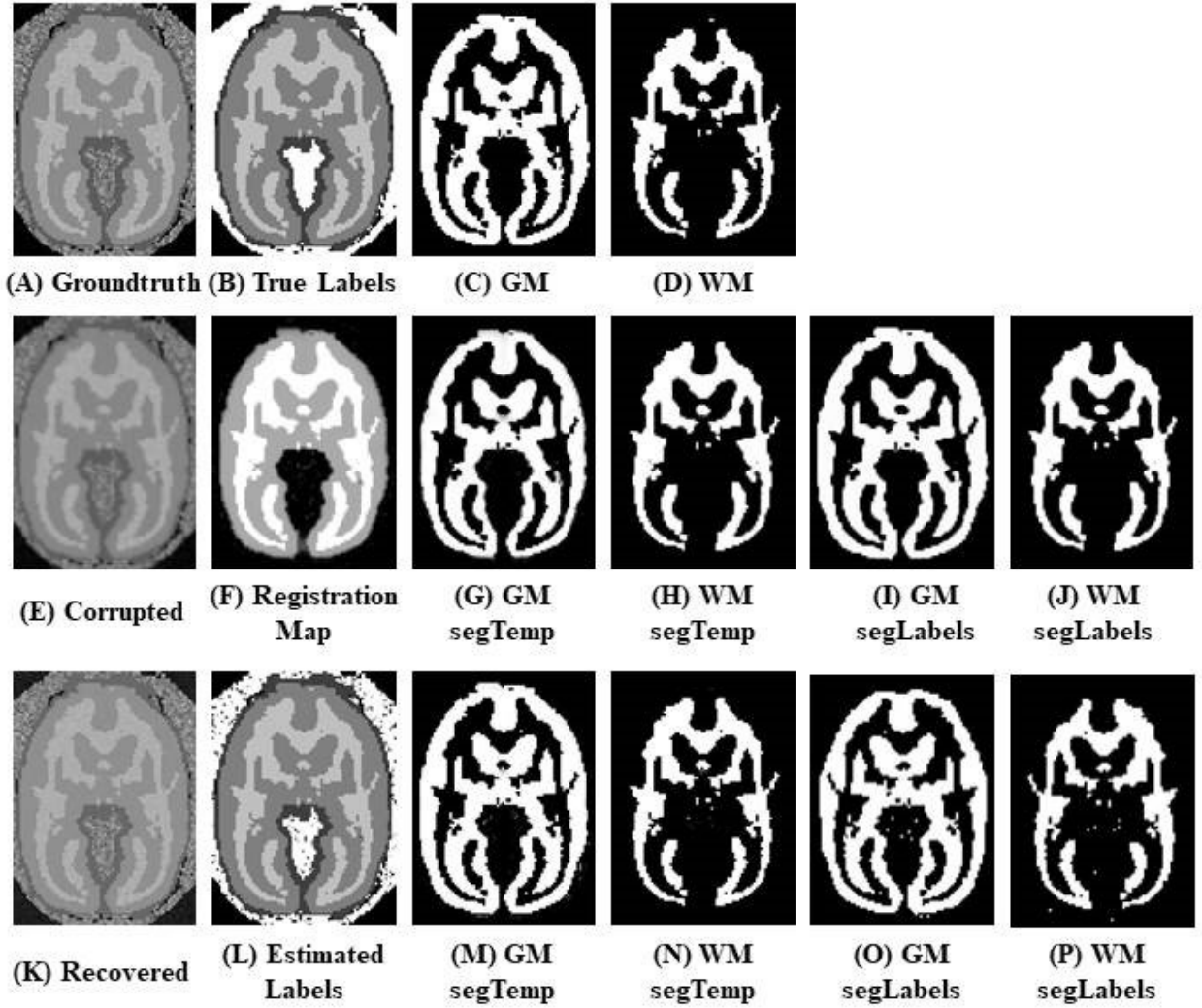
Figure 3.4: Axial slice of (A) the GGD-based simulated volume (ground truth), along with its corresponding (B) true labels, (C) GM and (D) WM maps. (E) is the image slice in (A) corrupted with blur and noise. (F) is the resulting map after the registration of (E) to the marmoset brain template. (K) is the image slice recovered from (E), and (L) is its estimated label map by JMCMC to be used as priors in SPM. Finally, the GM and WM result of the segTemp method for (E) are shown in (G) and (H), and for (K) in (M) and (N), respectively. The results of the segLabels method for (E) are shown in (I) and (J), and for (K) in (O) and (P), respectively.

Table 3.1: Quantitative assessment of the GM and WM segmentation using the segTemp and segLabels methods, by comparing the segmentation of the corrupted and recovered volumes with the true labels.

		segTemp		segLabels	
		corrupted	recovered	corrupted	recovered
SSIM	GM	0.84±0.02	0.90±0.3	0.87±0.02	**0.92±0.09**
	WM	0.92±0.03	0.90±0.01	0.74±0.02	**0.96±0.05**
Dice	GM	0.96±0.003	0.98±0.004	**0.98±0.006**	0.89±0.25
	WM	**0.97±0.007**	0.96±0.004	0.94±0.011	0.80±0.39

3.3.3 Experimental results

The workflow (Figure 3.1) was evaluated on three MRI brain volumes acquired from the same adult marmoset, and for which we have the manual segmentation (MS). These structural T1-weighted volumes were acquired using a Philips MRI scanner dedicated to human and animal research, at a field strength of 3T. A 3D gradient echo sequence was used with $T_R = 10.5\ msec$, $T_E = 4.7\ msec$, flip angle of 8°, isotropic resolution of 0.35 mm and size of $288 \times 288 \times 288$ voxels. To decrease the computational time and focus on the brain region, the volumes were cropped to the size of $78 \times 100 \times 80$.

Figure 3.5 shows the results of deconvolution by JMCMC for axial slices of the three different volumes, chosen so as to depict a clear enhancement of the image's quality, especially at the borders between different regions.

Similar to what was done in the simulation part, the results of the segTemp and segLabels methods were then compared to the manual segmentation of the three volumes. While the segmentation of the native and the enhanced volumes (by JMCMC) required their registration to the marmoset brain template before performing the segmentation task in SPM, the JMCMC method produced the estimated label map which was further used as prior information in SPM to produce the final GM and WM. In order to assess the efficiency of the proposed segLabels algorithm on real data, as compared

to the existing one (segTemp), the native and the enhanced volumes were further segmented using both approaches.
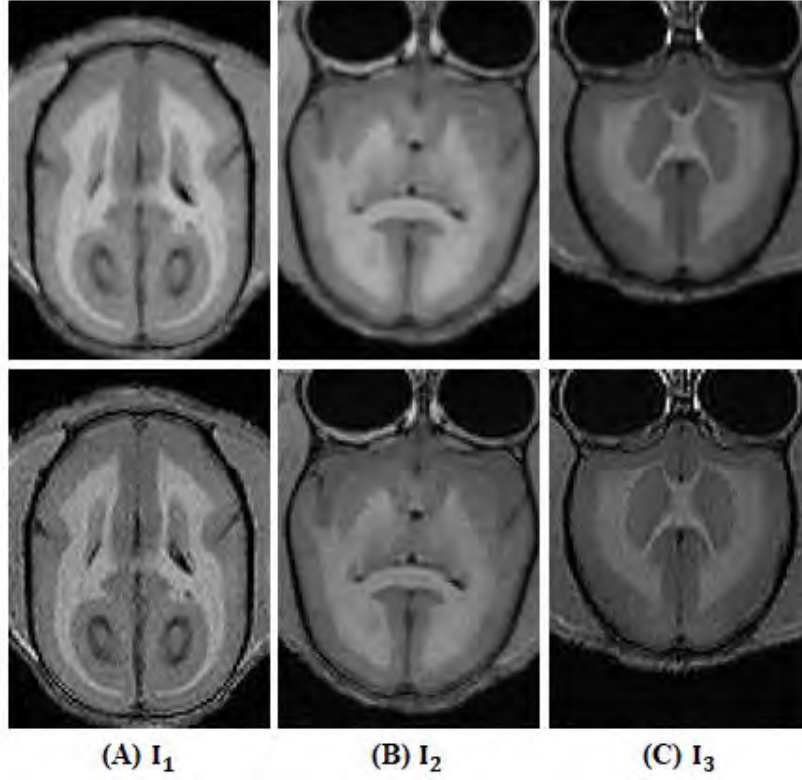
Figure 3.5: Results of image deconvolution by JMCMC algorithm for 3 axial slices (I_1, I_2 and I_3) of the 3 MRI volumes. Top: the native images. Bottom: the enhanced (deconvolved) versions.

Figure 3.6 and Figure 3.7 show the results of GM and WM segmentation respectively of the axial slices presented in Figure 3.5. Moreover, difference maps were computed between the segmentation by segTemp and segLabels and the reference manual segmentation to visualize the accuracy of the results.

The average SSIM (Table 3.2) and Dice coefficients (Table3.3) were computed for the three volumes. In this quantitative study, the manual segmentation of (vol_1, vol_2 and vol_3) was compared with the segmentation of these volumes, and their enhanced versions, using segTemp and segLabels methods.
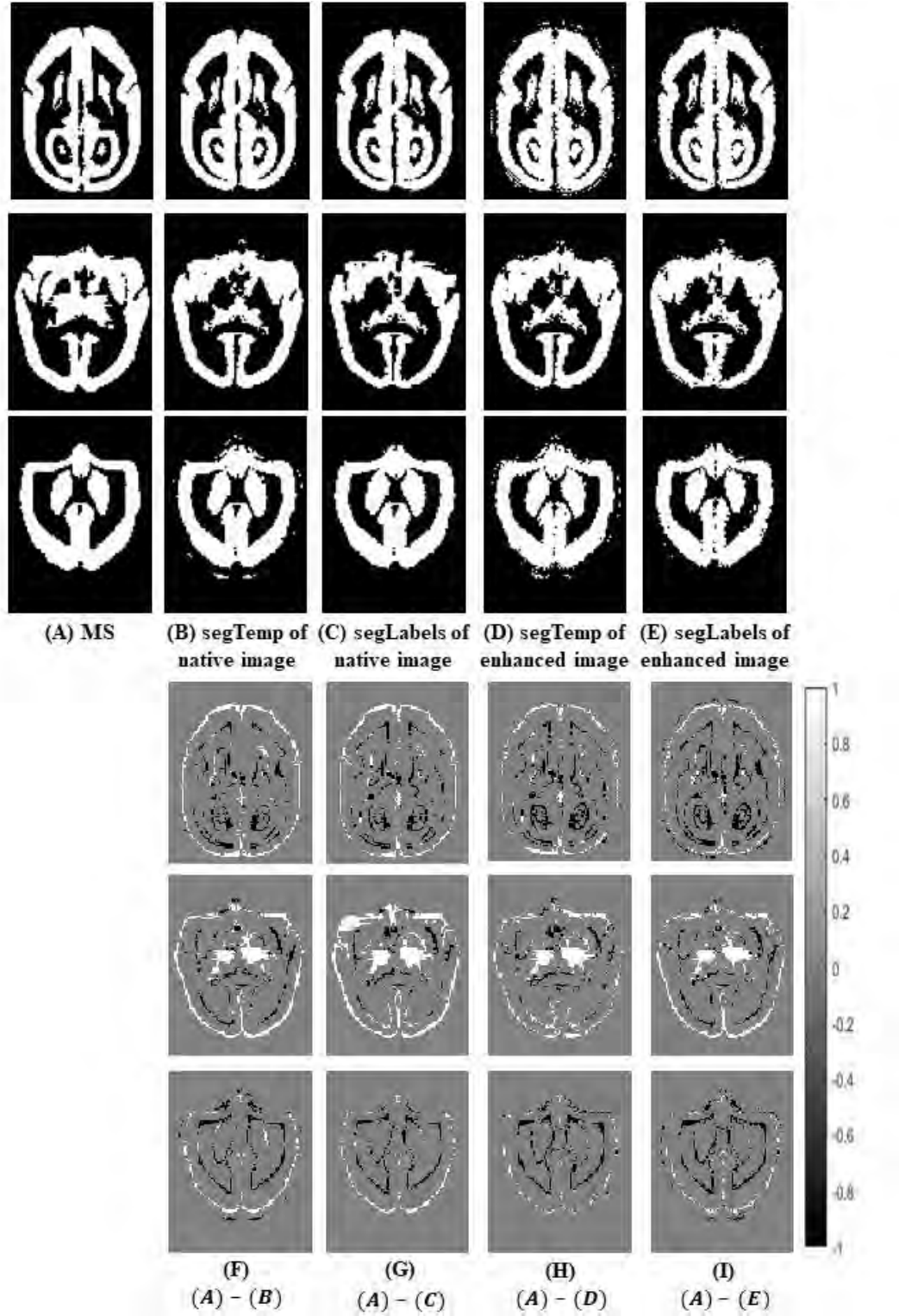
Figure 3.6: GM segmentation from the axial slices (I_1, I_2 and I_3 respectively) of Figure 3.5. (A) Manual segmentation, (B) segTemp result from the native image, (C) segLabels result from the native image, (D) segTemp result from the enhanced image and (E) segLabels result from the enhanced image. (F), (G), (H) and (I) are the difference maps between the reference segmentation in (A) and the segmentation results in (B), (C), (D) and (E), respectively.

(A) MS   **(B) segTemp of**   **(C) segLabels of**   **(D) segTemp of**   **(E) segLabels of**
native image   native image   enhanced image   enhanced image

(F)   **(G)**   **(H)**   **(I)**
$(A) - (B)$ $(A) - (C)$ $(A) - (D)$ $(A) - (E)$

Figure 3.7: WM segmentation from the axial slices (I_1, I_2 and I_3 respectively) of Figure 3.5. (A) Manual segmentation, (B) segTemp result from the native image, (C) segLabels result from the native image, (D) segTemp result from the enhanced image and (E) segLabels result from the enhanced image. (F), (G), (H) and (I) are the difference maps between the reference segmentation in (A) and the segmentation results in (B), (C), (D) and (E), respectively.

Table 3.2: Average SSIM, computed for the segmentation of each volume and their enhanced versions using segTemp and segLabels, with respect to the manual segmentation.

	segTemp		segLabels	
	native	enhanced	native	enhanced
vol_1	0.58±0.13	0.53±0.12	**0.74±0.13**	0.72±0.09
vol_2	0.66±0.17	0.65±0.17	0.73±0.14	**0.76±0.13**
vol_3	0.56±0.19	0.58±0.19	0.73±0.14	**0.73±0.16**

Table 3.3: Average Dice coefficients, computed for the segmentation of each volume and their enhanced versions using segTemp and segLabels, with respect to the manual segmentation.

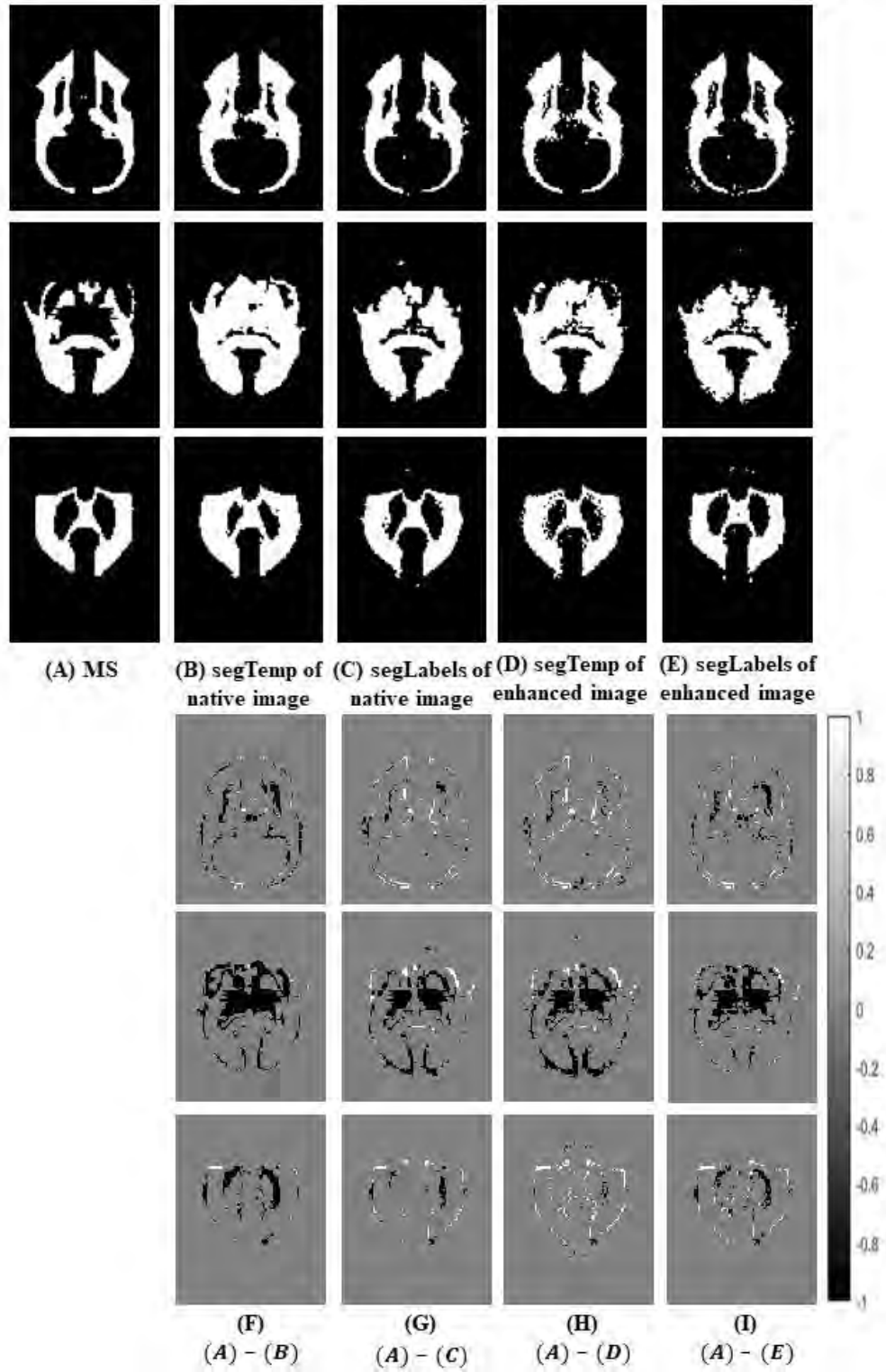|	segTemp		segLabels	
	native	enhanced	native	enhanced
vol_1	0.75±0.23	0.72±0.22	0.82±0.27	**0.85±0.22**
vol_2	0.63±0.35	0.62±0.35	**0.73±0.36**	0.68±0.38
vol_3	0.55±0.34	0.58±0.35	**0.72±0.33**	0.68±0.38

3.3.4 Influence of the hyperparameters' choice

While most of the hyperparameters are automatically estimated in our Bayesian method, a number of parameters has to be tuned manually. In this section we will present the influence of some of these parameters on the algorithm's output and accordingly the motivation of the values chosen in the above results.

Choice of the noise variance (σ_n^2)**:** The proposed method estimates the noise variance using Bayesian inference imposing a non-informative Inverse Gamma prior. However, in MRI images, the noise variance can be determined from the background signals. In order to address the difference between modelling the noise variance during the deconvolution process and pre-estimating it, we

performed the joint segmentation and deconvolution of a real MR image, for which we have the ground truth manual segmentation, with the noise variance being:

- pre-estimated from the background signals ($\sigma_{background} = 2.02$)

- pre-estimated by a Rician noise estimator [178] ($\sigma_{rician} = 1.21$)

- modeled (as in the proposed algorithm) by an Inverse Gamma distribution ($\sigma_{modelled} = 1.16$)

For each case, the deblurred images were further segmented using their estimated labels in SPM. Figure 3.8 shows the results of the GM and WM segmentation compared to the manual segmentation of the native image.
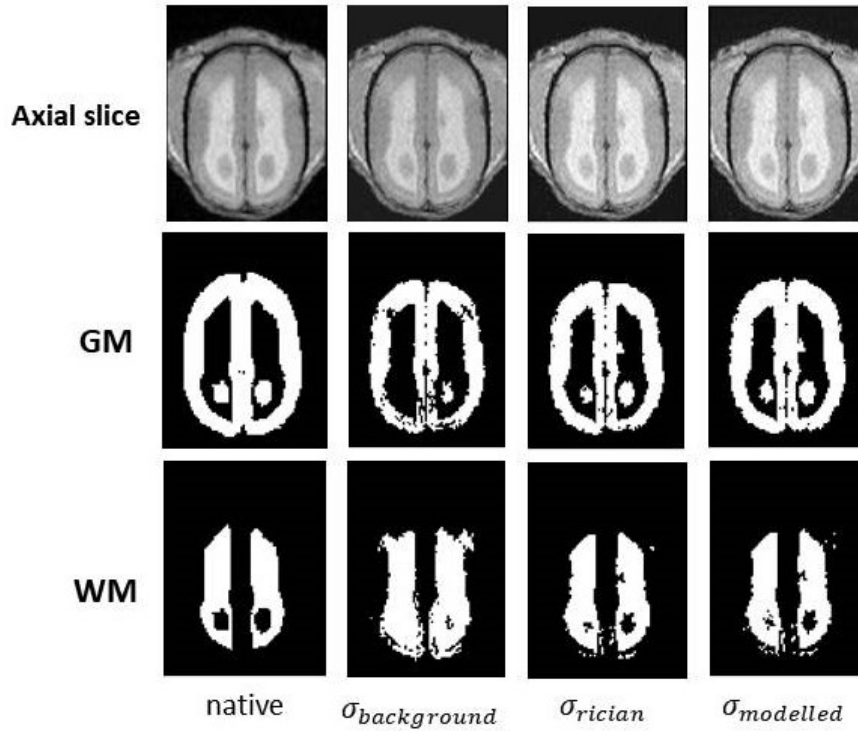

Figure 3.8: Showing the native axial slice with the manual GM and WM segmentation compared to the deblurred images and their respective segmentations with the noise variance being pre-estimated from the background signals, pre-estimated by a Rician noise estimator and modelled respectively.

Moreover, the SSIM index and the Dice coefficients were computed for each segmentation result compared to the manual segmentation (MS). The results are shown in Table 3.4. They show that estimating the noise variance within the proposed method gives comparable or slightly better results than the two approaches of estimating it as a pre-processing step.

Table 3.4: SSIM index and Dice coefficients for GM and WM segmentation of the three cases for noise variance estimation compared to the manual segmentation (MS)

	SSIM			Dice		
	$(\sigma_{background},\text{MS})$	$(\sigma_{rician},\text{MS})$	$(\sigma_{modelled},\text{MS})$	$(\sigma_{background},\text{MS})$	$(\sigma_{rician},\text{MS})$	$(\sigma_{modelled},\text{MS})$
GM	0.6657	0.6806	**0.7137**	0.8575	0.8895	**0.9106**
WM	0.7536	**0.8337**	0.8309	0.8236	0.9106	**0.9143**

Thus, we consider that estimating the noise variance along with all the parameters is more practical than estimating it in a prior step that requires extracting the background region (which could be difficult depending on the image and the size of the background), especially since sampling this parameter is not computationally expensive. Indeed if the size of the the background is small, the pre-estimation is imprecise.

Choice of the granularity coefficient (β): The granularity coefficient in the Ising model (3.9) was tuned manually. Since the impact of the granularity coefficient appears on the labels map, this parameter has been tuned on simulated data with available ground truth labels, and, importantly, fixed to the same value for all the experiments on real data. Since the simulation scenario was based on data extracted from a real MR volume,it was successful to fix the value of the parameter using the simulation data. Figure 3.9 shows the estimated labels map of a real MR image starting with different granularity coefficients.
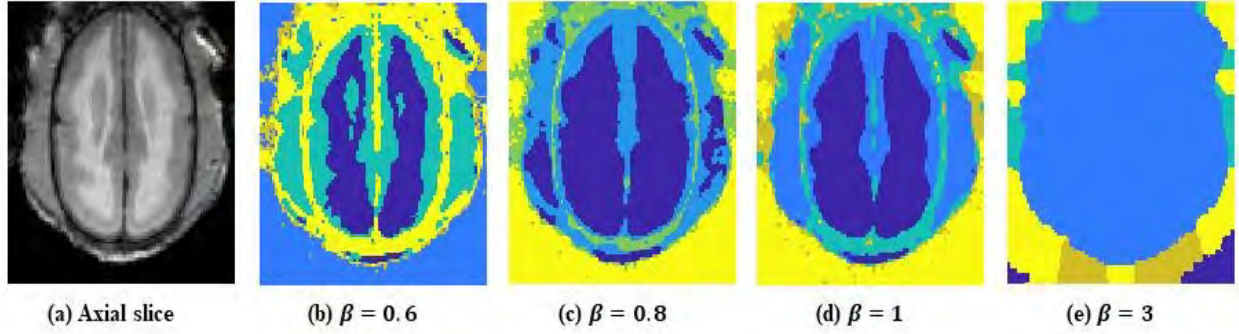
(a) Axial slice   (b) $\beta = 0.6$ (c) $\beta = 0.8$ (d) $\beta = 1$ (e) $\beta = 3$

Figure 3.9: The effect of varying the value of the granularity coefficient β on the labels map produced by the JMCMC algorithm and that would be further used as prior maps for SPM segmentation.

Choice of number of iterations: Due to the complexity of the structures in MR images, performing a huge number of iterations is time and memory consuming. Since our ultimate goal is to produce labels maps as priors for SPM segmentation, we followed the general rule of MCMC sampling by fixing a burn-in period (where the samples generated are discarded) followed by a number of iterations sufficiently large (1650 iterations) for producing good labels map. Hereafter, we present a systematic study for the effect of varying the number of iterations by observing its impact on the deblurred image and its corresponding labels for several iteration numbers (900, 1000, 1400, 2000, 2400, 2800, 3200, 4000, 5500). The JMCMC algorithm was performed on a real MR slice that has been degraded by a blurring kernel and Gaussian noise. The results were then compared to the ground truth image and labels.

Figure 3.10 shows the curves of the SSIM index and improved signal to noise ratio (ISNR) between the deconvolved images and the ground truth. In addition, we plotted the elapsed time (in secs) for each number of iterations. This shows that as the number of iterations increase, the SSIM and ISNR increase until they reach a plateau, however, the compromise is made with respect to the elapsed time required for the MCMC iterations to end. Moreover, Figure 3.11 shows the effect of the number of iterations on the estimated labels of the JMCMC method. As expected, one may remark that within a small number of iterations, the labels could not be constructed successfully.
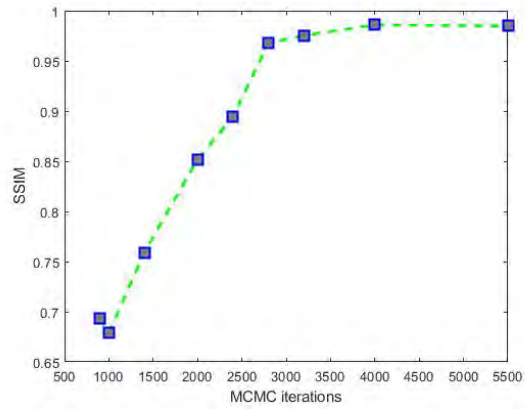
(a) SSIM
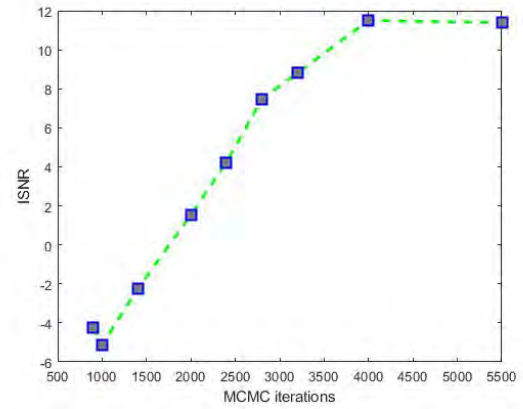
(b) PSNR
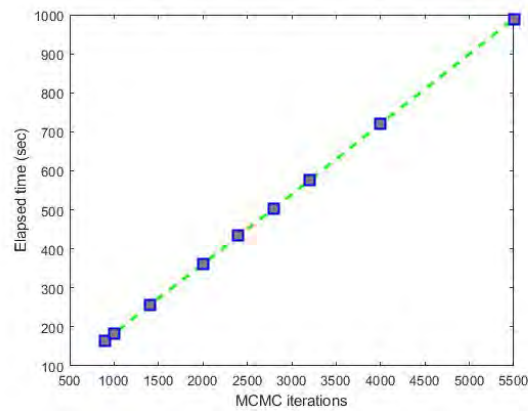
(c) Elapsed time

Figure 3.10: SSIM index and ISNR computed between the deconvolved image and the ground truth for different MCMC iterations and the elapsed time (in secs) for each set of iterations to be completed.
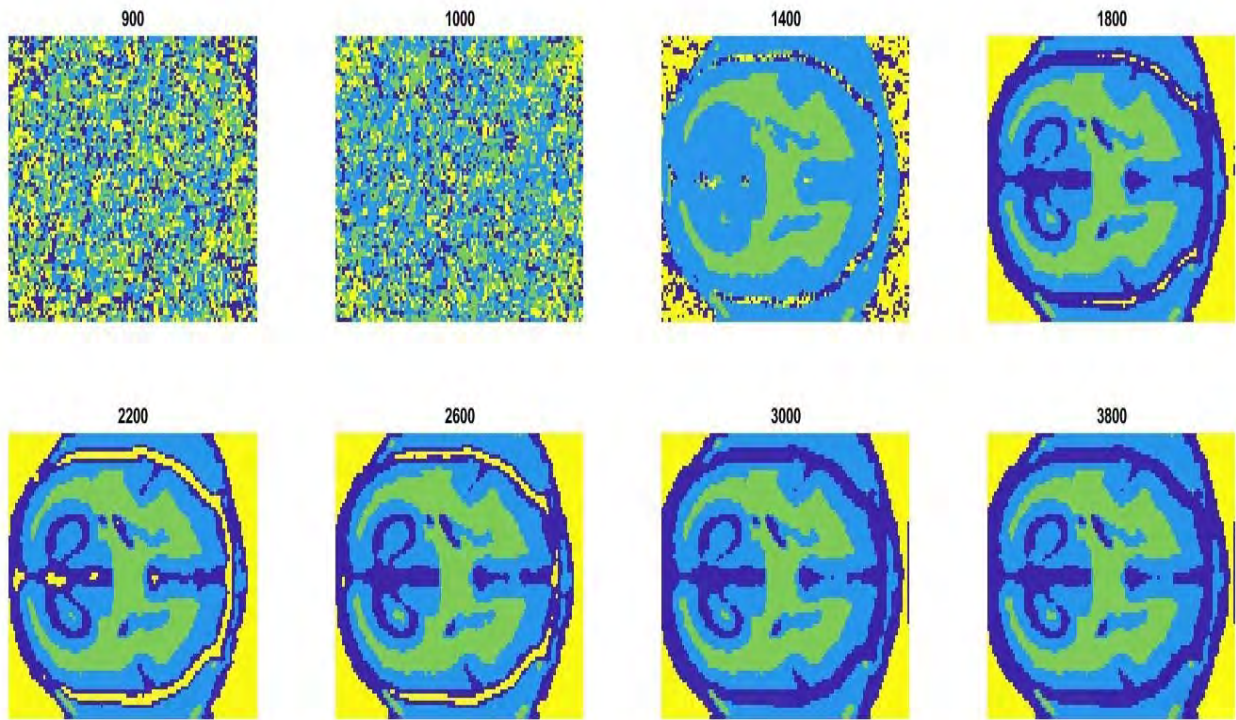
Figure 3.11: Effect of varying the number of iterations on the estimated labels map that will be further used for the segmentation task in SPM.

3.4   Discussion and conclusion

This chapter presented a segmentation method for marmoset brain MR images, which does not rely on a brain template. We proposed a segmentation method based on a Bayesian joint deconvolution and segmentation algorithm, whose outputs are an enhanced version of the input MRI volume and its corresponding labels which can be further used as prior information (maps) for segmenting the brain into its main compartments in SPM. Experiments on simulated and real data show that the proposed method presents results that are comparable to those obtained with the classical method, *i.e.* registering the volumes to a brain template.

Comparing Figure 3.4(K) to 3.4(A) and referring to the quantitative assessment of the simulation experiment, we notice the efficiency of deconvolution using JMCMC algorithm in recovering the simulated volume from its blurred version. As our main objective is to evaluate the proposed methodology of segmentation (segLabels), the SSIM and Dice results presented in Table 3.1 show that segmenting a volume (corrupted or recovered) using the segLabels method gives better results for GM segmentation than segmenting it using the classical segTemp one. However, one can observe that the result of the segmentation using segLabels of the recovered volume (Figure 3.4(O) and (P)) contained outliers in some slices due to the simulate.

Moreover, the quantitative assessment of segLabels and segTemp applied to the recovered volume (see Table 3.1) shows that the proposed label-based method shows significant interest since it does not require any template, representing the main contribution in this segmentation methodology. This result can also be qualitatively observed when comparing the GM and WM outputs of both methodologies in Figure 3.4.

In addition, experimental results presented in Tables 3.2 and 3.3 show that the proposed segmentation method (segLabels) outperforms the segTemp method in segmenting both the native volumes and the enhanced ones. Difference maps computed for GM (Figure 3.6) and WM (Figure 3.7) segmentations show that the proposed method (segLabels) is able to produce segmentations that are as close to the manual segmentation as those produced by the conventional segTemp method. Not only enhancing the MR volumes by deconvolution gives competitive segmentation results regardless

of the method used, but also using the associated labels as segmentation priors presents an important contribution, especially when templates are not available. The segmentation obtained with the proposed method show a good similarity with the manual segmentation, which is most of the time difficult to achieve in practical situations.

Although the registration process may be important for some applications, such as voxel-based-morphometry, yet our method is efficient when brain templates are not available, which is the case in most preclinical applications. Future work will include the investigation of the proposed joint super-resolution and segmentation to further improve the longitudinal analysis whose aim is to obtain insights about the normal or abnormal brain aging. Approaches for accelerating the JMCMC method exist in literature, for example by combining them with optimization methods [179], thus including other sampling schemes in the proposed work is also an interesting future direction aiming at reducing the computational time. Moreover, automatic approaches for choosing the granularity coefficient will be further investigated. Finally, the interest of machine learning in improving marmoset brain segmentation is also an important topic to explore. The major challenge of such approaches is to obtain ground truth data, i.e., by manual segmentation, a cumbersome and time consuming task for the few experts in animal brain MR imaging. Therefore, transfer learning from human databases or weakly supervised machine learning techniques could offer interesting perspectives to this work.

Limited by the heavy computational cost of this method, especially when processing all the data of the marmoset population, we will not further use the deblurred images of the JMCMC algorithm in the longitudinal analysis scheme. In the next chapter, we will investigate the effectiveness of faster super-resolution (SR) methods for the enhancement of marmoset brain MR images. We will evaluate several model- and learning-based methods and study their effect on the segmentation of the brain into its main compartments. This systematic study will allow us to choose the best enhancement methods that will be further used in the longitudinal analysis in Chapter 5.

CHAPTER 4

Super-resolution of 3D Marmoset Brain MR Images

Part of the work in this chapter has been published in [180] and [181].

Contents

4.1 Introduction

As stated in Chapter 2, single image SR is a post-processing method that restores an HR image from one LR observation. Investigations in single image SR of MRI, applied to brain image enhancement, have shown great potential in improving LR images by restoring high-frequency image details lost during image reconstruction. Therefore, this chapter aims to explore the ability of SR techniques in 3D restoration and enhancement of marmoset brain MR images to facilitate the study of cerebral aging bio-markers. In particular, we will validate the effectiveness of SR in enhancing the robustness of automatic segmentation of brain images. We will focus on existing model-based and deep-learning methods that have been validated for several medical imaging applications. We will further compare their performance from the segmentation perspective using a state-of-the-art brain segmentation method applied to native, LR, and estimated HR volumes.

The first part of this chapter introduces model-based techniques for the SR task. In particular, we will assess a 2D fast SR (FSR) method [102] applied to the 3D volume slice by slice, a 3D tensor-factorization (TF) [103] method for general image restoration, and a state-of-the-art method for SR method that combines low-rank and total variation regularization [100]. The second part covers 3D deep learning networks [127, 128] that have been initially published for the SR of human brain MR images and re-trained here using marmoset data. In addition, we will present a preliminary study in which we evaluate the applicability of the deep network proposed in [182] and trained on 3T/7T pairs of human brain images for enhancing the quality of the 3T MRI of the marmoset brain.

SR is followed by the segmentation of the main brain compartments and the computation of their respective volumes. Finally, we will compare super-resolved images provided by different methods to the reference native images in the simulation scenario. Results are then confirmed based on the better differentiation of the gray matter (GM), white matter (WM) and cerebrospinal fluid (CSF) on native and super-resolved images compared to the manual segmentation of the brains. Finally, this will allow us to choose one model-based and one deep-learning method that will be further assessed in the longitudinal brain analysis of Chapter 5.

4.2   Model-based SR methods

4.2.1   2D Fast SR (FSR)

The FSR algorithm originally introduced in [102] for general 2D image restoration purpose has been further validated for medical applications such as acoustic microscopy in [183]. This method exploits the joint properties of the system point spread function (PSF) and the sub-sampling operators to derive a fast algorithm. The authors proposed a new method for handling the decimation and blurring operators simultaneously by exploring their intrinsic properties in the frequency domain thus reducing the computational cost of matrix inversion when solving the SR problem. The FSR method is based on the traditional observation model assuming that the LR image can be expressed as a noisy, blurred and decimated version of the HR image as:

$$\mathbf{y} = \mathbf{SHx} + \mathbf{n},\tag{4.1}$$

where $\mathbf{y} \in \mathbb{R}^{N_l \times 1}$ and $\mathbf{x} \in \mathbb{R}^{N_h \times 1}$ ($N_h = d^2 N_l$) are the vectorized versions of the LR and HR images. $\mathbf{H} \in \mathbb{R}^{N_h \times N_h}$ represents the 2D convolution of the HR image with the PSF of the imaging system. $\mathbf{S} \in \mathbb{R}^{N_l \times N_h}$ corresponds to the down sampling operator with an integer sampling rate d in each spatial direction. $\mathbf{n} \in \mathbb{R}^{N_l \times 1}$ is an independent identically distributed (IID) additive white Gaussian noise (AWGN).

We recall the two basic assumptions about the blurring and decimation matrices upon which the method is built. These assumptions are necessary for the framework and are widely used in image processing applications for image deconvolution and SR methods.

1. The blurring matrix $\mathbf{H}$ is the matrix representation of the cyclic convolution operator, i.e. $\mathbf{H}$ is a block circulant matrix with circulant blocks (BCCB). This allows to write $\mathbf{H}$ and its conjugate transpose $\mathbf{H}^H$ as:

$$\mathbf{H} = \mathbf{F}^H \Lambda \mathbf{F},\tag{4.2}$$

$$\mathbf{H}^H = \mathbf{F}^H \Lambda^H \mathbf{F},\tag{4.3}$$

where the matrices $\mathbf{F}$ and $\mathbf{F}^H$ are associated with the 2D Fourier and 2D inverse Fourier transforms, and $\Lambda = diag\{Fh\}$ is a diagonal matrix whose elements are the Fourier coefficients of the first column of the blurring matrix $\mathbf{H}$, denoted as h [102].

2. The decimation matrix $\mathbf{S} \in \mathbb{R}^{N_l \times N_h}$ is a down-sampling operator, while its conjugate transpose $\mathbf{S}^H \in \mathbb{R}^{N_h \times N_l}$ interpolates the decimated image with zeros as illustrated in Figure 4.1. The decimation matrix satisfies the relationship: $\mathbf{S}\mathbf{S}^H = I_{N_l}$. Starting from $\underline{\mathbf{S}} \triangleq \mathbf{S}^H\mathbf{S}$, then multiplying an image by $\underline{\mathbf{S}}$ is equivalent to the entry-wise multiplication of the image with an $N_h \times N_h$ matrix of ones at the sampled positions and zeros elsewhere [102].
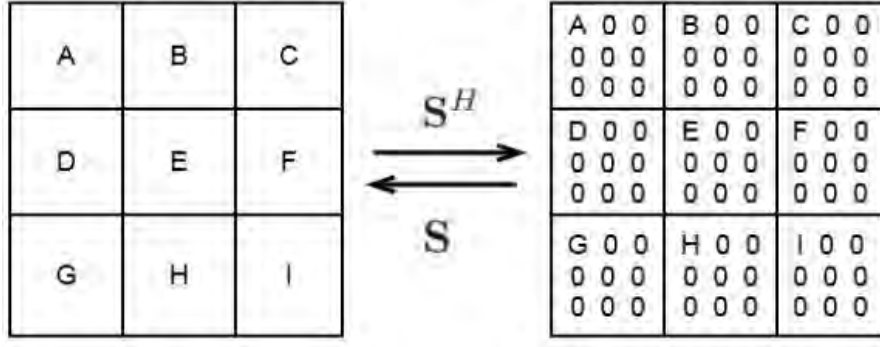
Figure 4.1: Effect of up-sampling matrix $\mathbf{S}^H$ on a 3×3 image and of the down-sampling matrix $\mathbf{S}$ on the corresponding 9×9 images for a scale factor of 3. Figure was collected from [102].

The restoration of the HR image from the LR image is an ill-posed problem which is usually overcome by the use of regularization terms chosen according to the application. Assuming that $\mathbf{n}$ in (4.1) is an AWGN, the maximum *a posteriori* (MAP) estimator of $\mathbf{x}$ can be obtained by solving the following optimization problem

$$\widehat{\mathbf{x}} = \arg\min_x \|\mathbf{y} - \mathbf{S}\mathbf{H}\mathbf{x}\|_2^2 + \tau R(\mathbf{x}), \tag{4.4}$$

where $\|\mathbf{y} - \mathbf{S}\mathbf{H}\mathbf{x}\|_2^2$ is the data fidelity term, $R(\mathbf{x})$ is a regularization or penalty term, and τ is a regularization parameter. The computational efficiency of the FSR approach mainly comes from exploiting the properties of the decimation matrix S. Indeed, while H is diagonalizable in the Fourier domain thus facilitating its implementation, the matrix S does not have the same property; this leads

to high computational burden to directly invert (4.4), even when a classical l_2 regularization is used. In this case the analytical solution of (4.4) is straightforward. Based on [102], such analytic solution becomes tractable in high dimensional cases, and can be further used even with more sophisticated regularizers.

A well suited regularization term for MRI is the total variation (TV) regularization due to its denoising properties and its ability to remove unwanted details while preserving edges [92, 102]. Therefore, the TV regularization for the SR problem can be given by:

$$\phi(\mathbf{x}) = \sqrt{\|\mathbf{D}_{\mathrm{h}}\mathbf{x}\|^2 + \|\mathbf{D}_{\mathrm{v}}\mathbf{x}\|^2}, \tag{4.5}$$

where $\mathbf{D}_{\mathrm{h}}$ and $\mathbf{D}_{\mathrm{v}}$ are the BCCB matrices representing the horizontal and vertical gradients respectively. The problem in (4.4) is solved within FSR using the alternating direction method of multipliers (ADMM) framework. Thus the problem can be rewritten as:

$$\min_{\mathbf{x},\mathbf{u}} \quad \frac{1}{2}\|\mathbf{y} - \mathbf{SHx}\|_2^2 + \tau\phi(\mathbf{u})$$
$$\text{subject to} \quad \mathbf{Ax} = \mathbf{u}. \tag{4.6}$$

where with $\mathbf{A} = [\mathbf{D}_{\mathrm{h}}, \mathbf{D}_{\mathrm{v}}]^T$ and the auxiliary variable $\mathbf{u} = [\mathbf{u}_{\mathrm{h}}, \mathbf{u}_{\mathrm{v}}]^T$. Thus, the Augmented Lagrangian (AL) function associated with it is:

$$\mathcal{L}(\mathbf{x}, \mathbf{u}, \boldsymbol{\lambda}) = \frac{1}{2}\|\mathbf{y} - \mathbf{SHx}\|_2^2 + \tau\phi(\mathbf{u}) + \frac{\mu}{2}\|\mathbf{Ax} - \mathbf{u} + \mathbf{d}\|_2^2, \tag{4.7}$$

where $\mathbf{d}$ is a scaled dual variable and $\boldsymbol{\mu}$ is a hyper parameter. The solution of equation (4.4) is then computed by solving three sub problems iteratively where for each iteration k ($k = 0, 1, ...$) we solve:

$$\begin{cases} \mathbf{x}^{k+1} \in \arg\min_x \frac{1}{2}\|\mathbf{y} - \mathbf{SHx}\|_2^2 + \frac{\mu}{2}\|\mathbf{Ax} - \mathbf{u}^k + \mathbf{d}^k\|_2^2 \\ \mathbf{u}^{k+1} \in \arg\min_u \tau\sqrt{\|\mathbf{u}_{\mathrm{h}}\|^2 + \|\mathbf{u}_{\mathrm{v}}\|^2} + \frac{\mu}{2}\|\mathbf{Ax}^{k+1} - \mathbf{u} + \mathbf{d}^k\|_2^2 \\ \mathbf{d}^{k+1} = \mathbf{d}^k + (\mathbf{Ax}^{k+1} - \mathbf{u}^{k+1}) \end{cases} \tag{4.8}$$

The solution of $\mathbf{x}$ is given by the analytical solution derived in [102] (refer to Algorithm 3 in [102]) and $\mathbf{u}$ is updated using the generalized 2D soft shrinkage operator.

Results of image restoration using the proposed algorithm [102] have shown great computational efficiency with fast and smooth convergence with similar quantitative metrics when compared to classical methods of restoration. In our work, we will evaluate this SR algorithm slice by slice to 3D MR acquisitions of the marmoset brain, i.e. the enhancement will be performed in the x and y directions only. However, we will go further to investigate other SR methods that enhances the whole 3D volume.

4.2.2   3D SR using Tensor Factorization (TF)

The TF method has been recently introduced in [103], validated, and proven computationally-efficient on dental computed tomography images. The idea behind this method is to decompose the image of interest using its canonical polyadic decomposition (CPD). The CPD of a tensor is a representation based on a sum of an appropriate number of rank-1 tensors, whose number depends on the image structure (see Figure 4.2). For self-consistency, we recall hereafter the main steps of this method.
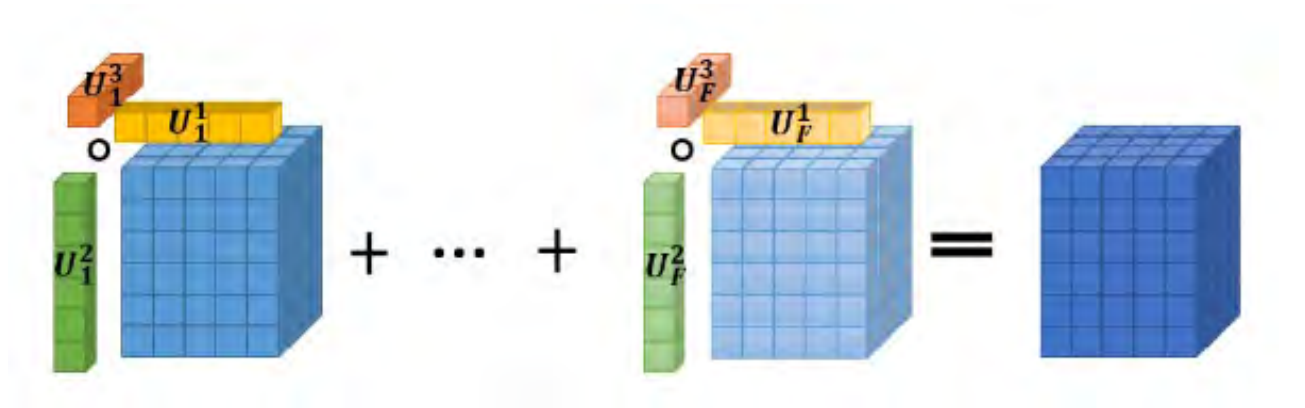
Figure 4.2:   Illustration of Tensor Factorization concept where F is the number of outer products formed by mode-1 ($U^1 := U^1(:, i)$), mode-2 ($U^2 := U^2(:, i)$) and mode-3 ($U^3 := U^3(:, i)$) fibers summing up to a rank-F tensor. Figure was extracted from [103].

Single image SR using TF is based on the traditional image degradation model assuming that the LR image can be expressed as a noisy, blurred and decimated version of the HR image. Within this algorithm, 3D images are associated to tensors of order 3, resulting into the following degradation

model:

$$vec(\boldsymbol{Y}) = \mathbf{DH}vec(\boldsymbol{X}) + vec(\mathbf{N}), \tag{4.9}$$

where vec() vectorizes the elements of the 3D tensor in lexicographical order. $\boldsymbol{Y} \in \mathbb{R}^{I/r \times J/r \times K/r}$ and $\boldsymbol{X} \in \mathbb{R}^{I \times J \times K}$ are the LR and HR images respectively, $\mathbf{H} \in \mathbb{R}^{IJK \times IJK}$ is the block-circulant version of the 3D point spread function (PSF), $\mathbf{N}$ is an independent identically distributed (IID) additive white Gaussian noise (AWGN), I, J and K are the 3D volume dimensions and r is the decimation rate accounting for the voxel resolution loss. Based on the hypothesis of separable PSF (valid in the present study given the choice of Gaussian PSF), $\mathbf{H}$ can be decomposed in three block circulant matrices with circulant blocks (BCCB), $\mathbf{H}_1 \in \mathbb{R}^{I \times I}$, $\mathbf{H}_2 \in \mathbb{R}^{J \times J}$ and $\mathbf{H}_3 \in \mathbb{R}^{K \times K}$. Similarly, the down sampling operators for the three dimensions can be given as $\mathbf{D}_1 \in \mathbb{R}^{I/r \times I}$, $\mathbf{D}_2 \in \mathbb{R}^{J/r \times J}$ and $\mathbf{D}_3 \in \mathbb{R}^{K/r \times K}$.

Using the canonical polyadic decomposition of $\boldsymbol{X}$

$$\mathbf{X} = \sum_{f=1}^{F} U^1(:,f) \circ U^2(:,f) \circ U^3(:,f), \tag{4.10}$$

with

$$\bar{U} = \{U^1 \in \mathbb{R}^{I \times F}, U^2 \in \mathbb{R}^{J \times F}, U^3 \in \mathbb{R}^{K \times F}\}, \tag{4.11}$$

where F is the rank of the tensor, (4.9) can be rewritten as the mode-n product of the separated kernels:

$$\begin{aligned} \boldsymbol{Y} &= \boldsymbol{X} \times_1 D_1 H_1 \times_2 D_2 H_2 \times_3 D_3 H_3 + \mathbf{N} \\ &= [[D_1 H_1 U^1, D_2 H_2 U^2, D_3 H_3 U^3]] + \mathbf{N}. \end{aligned} \tag{4.12}$$

Thus the reconstruction of the HR image from the LR image requires to find the set of matrices $\bar{U}$ by solving the following minimization problem:

$$\min_{\bar{U}} \| \boldsymbol{Y} - [[D_1 H_1 U^1, D_2 H_2 U^2, D_3 H_3 U^3]] \|_F^2. \tag{4.13}$$

Since the minimization problem posed in (4.13) is NP-hard, U^1, U^2 and U^3 are minimized sequentially

as follows:

$$\min_{U^1} \frac{1}{2}\|\mathbf{Y}^{(1)} - D_1 H_1 U^1 (D_3 H_3 U^3 \odot D_2 H_2 U^2)^T\|_F^2$$

$$\min_{U^2} \frac{1}{2}\|\mathbf{Y}^{(2)} - D_2 H_2 U^2 (D_3 H_3 U^3 \odot D_1 H_1 U^1)^T\|_F^2$$

$$\min_{U^3} \frac{1}{2}\|\mathbf{Y}^{(3)} - D_3 H_3 U^3 (D_2 H_2 U^2 \odot D_1 H_1 U^1)^T\|_F^2 \tag{4.14}$$

The solution of the three minimization problems in (4.14) is obtained using the least-square estimator with a Tikhonov regularization. The solution is further computed using the Moore-Penrose pseudo-inverse$^+$:

$$U^1 = (D_1 H_1)^+ \mathbf{Y}^{(1)} (D_3 H_3 U^3 \odot D_2 H_2 U^2)^{+T}$$

$$U^2 = (D_2 H_2)^+ \mathbf{Y}^{(2)} (D_3 H_3 U^3 \odot D_1 H_1 U^1)^{+T}$$

$$U^3 = (D_3 H_3)^+ \mathbf{Y}^{(3)} (D_2 H_2 U^2 \odot D_1 H_1 U^1)^{+T} \tag{4.15}$$

Unlike the conventional unfolding performed in 3D reconstruction algorithms such as in [100], this method unfolds the tensor sequentially, in each direction, thus preserving the local 3D information. The proposed method on dental CT images provided interesting computational advantages and improved image quality with significantly less parameters (only tensor rank and iteration number) to be adjusted by the user. Our interest in this approach is in the 3D handling of the MR volume; i.e. resolution enhancement in the three directions. Additional information on the mathematical derivations of the stated equations can be found in [103].

As mentioned in Section 5.1, we will compare the performance of the two methods (FSR and TF) presented above, and which were not previously applied to MR images, to a state-of-the-art method by Shi et al. [100] originally proposed for the 3D single-image SR of human brain MR images.

4.2.3   3D SR with Low-Rank and TV Regularization (LRTV)

While reconstruction-based algorithms use TV regularizations to retain edge sharpness during image recovery, information from remote voxels is ignored, and only information from local neighbors is used. To mitigate this issue, Shi et al. [100] developed a super–resolution method that integrates both local and global information in the image restoration process. This approach is based on the idea

of matrix completion i.e., considering the recovery of the HR matrix from a low rank (incomplete) matrix by combining low rank and TV regularizations for the compelling image SR.

The authors suggested to consider that the LR 3D MRI image is a low – rank matrix from which a HR image is going to be restored. This property can be integrated in the cost function provided in (4.4) where the regularization can be separated into low-rank and total variation terms. Thus, (4.4) can be rewritten as:

$$\hat{\mathbf{x}} = \arg \min_{x} \|\mathbf{y} - \mathbf{SHx}\|^2 + \lambda_{rank} Rank(\mathbf{x}) + \lambda_{TV} TV(\mathbf{x}), \tag{4.16}$$

where λ_{rank} and λ_{TV} are the tuning parameters for the low – rank and TV terms respectively, $Rank$ is the weighted sum of trace norms of all matrices unfolded along each dimension and TV denotes the integral of the absolute gradients of data. The regularizer $Rank$ takes advantages of the similarity between the slices in different directions. A 3D image with size of $U \times V \times W$ can be unfolded into three 2D matrices with sizes of $U \times (V \times W)$, $V \times (W \times U)$, and $W \times (U \times V)$ respectively. To simulate $\mathbf{x}$ in each dimension i, consider N – redundant variables $\{M_i\}_{i=1}^N$ such that the unfolded x along the i-th dimension $(x_{(i)})$ should be equal to the unfolded M_i along this dimension $(M_{i_{(i)}})$. The new cost function becomes:

$$\min_{x, \{M_i\}_{i=1}^N} \|\mathbf{y} - \mathbf{SHx}\|^2 + \lambda_{rank} \sum_{i=1}^N \alpha_i \|M_{i_{(i)}}\|_{tr} + \lambda_{TV} TV(\mathbf{x})$$
$$\text{subject to} \quad x_i = M_{i_{(i)}}; i = 1, 2, .., N \tag{4.17}$$

where $\{\alpha_i\}_{i=1}^N$ are parameters satisfying $\alpha_i \geq 0$ and $\sum_{i=1}^N \alpha_i = 1$, and $x_{(i)}$ is the unfolded $\mathbf{x}$ along the i-th dimension.

The minimization problem in (4.17) is further divided into three sub problems that are solved iteratively in an alternating direction method of multipliers (ADMM) framework and the total variation (TV) is implemented using gradient descent thus rendering this method computationally expensive [100]. This method will be referred to as LRTV hereafter.

To summarize, in this section, we have presented an overview of the model-based methods that we assessed in the SR problem of the marmoset brain MR images. We will apply these methods and fine-tune their hyperparameters for the maximum performance on our database.

In general, these model-based methods depend on the choice of the regularization term for the optimization process which can further impact the restored images. An alternative approach is to learn the mapping between low- and high- resolution images in a supervised context. This is referred to as learning based SR approaches.

4.3 Deep-learning based SR methods

In this section, we will further emphasize some deep-learning methods that have been originally proposed for the SR of human brain MR data.

4.3.1 3D Residual Convolution Neural Network (ReCNN)

As stated before, deep-learning methods for SR are based on learning a mapping from the LR- to the HR-space. Instead, Pham et al. [127] proposed a 3D deep convolutional neural network for single brain MRI SR that estimates a mapping from the LR space to the high-frequency components by computing the residual between the HR and LR data. Figure 4.3 illustrates the network architecture. The skip connection introduced in the network architectures models the residual learning method. The method is referred to as ReCNN hereafter. Table 4.1 summarizes the network's parameters of
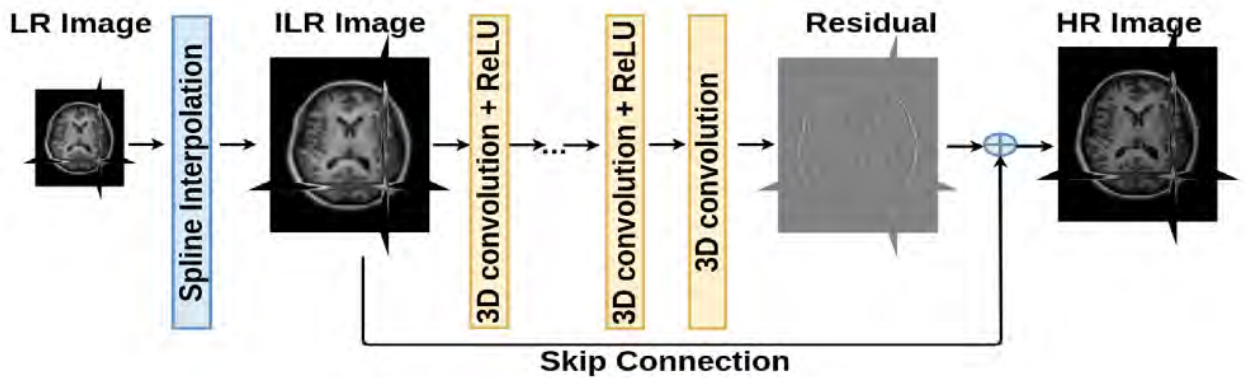

Figure 4.3: Illustration of the 3D ReCNN proposed by Pham et al. [127]. The skip connection in the network adds the residual information learnt between the LR image and the high frequency components. LR is the low resolution image, ILR is the interpolated LR image and HR is the high resolution image. The figure was extracted from [127].

the baseline architecture proposed in [127] consisting of 10 blocks of convolutional layers and rectified linear unit (ReLU) activation function. Each layer is formed of 64 convolution filters of size $3 \times 3 \times 3$. The weights of the convolutional filters are initialized using the Microsoft Research Asia (MRSA) filler [184] that samples weights from a normal distribution $N(0, \sqrt{\frac{2}{(nf^3)}})$, where n is the number of filters and f is the spatial size of the filter. The network's parameters are then optimized using Adam's optimizer [108] by minimizing the mean squared error (MSE) as the loss objective function. The network is trained for 20 epochs with a batch size of 64 and learning rate of 0.0001. However, in their study, the authors have thouroughly investigated the impact of the optimization method, the weights' initialization, the residual-based model, the network depth, the filter size, the filter number, the training patch size, the size of training data set, and the ability of the network to handle arbitrary scales in a single network [127].

Table 4.1: Parameters' initialization of the benchmark network proposed in [127].

Parameter	Assigned Value
Optimization method	Adam (adaptive moment estimation) [108]
Adam's learning rate	0.0001
Loss Function	Mean Squared Error (MSE)
Weight initialization	Microsoft Research Asia - MRSA filler [184]
Network depth	10 layes
Number of filters	64 convolution filters
Filter size	3×3 at each layer
Number of epochs	20

The ReCNN in [127] was originally implemented using Caffe [185] package. Evaluation of the network's performance for the SR task was done using two MRI databases of 3T T1-weighted images of the human brain (Kirby21 data set [186], NAMIC Brain Multimodality data set (`http://hdl.handle.net/1926/1687`)). LR images were simulated by adding Gaussian blur of fixed standard deviation and down-sampling by isotropic scaling factors. Training was performed on 10 MR volumes

from which 3200 patches were randomly extracted, each of size $25 \times 25 \times 25$. Five volumes were then used in the testing phase. Quantitative assessment of the peak signal to noise ratio (PSNR) showed improved performance of the residual network compared to the non-residual SRCNN scheme of Dong et al. [187]. Moreover, better performance can be achieved by using deeper networks of 20 layers, increasing the number of filters, or increasing the filter size. However, a trade-off should be considered regarding the computational cost [127].

SR of neonatal brain MR images was also performed where sharper images with better defined boundaries were obtained. This seems important for our work since, similar to the neonatal brain, marmoset brains are also small in size. Thus evaluating this network for the SR of the marmoset brain is of a great interest.

4.3.2 Convolutional Neural Networks with Intermediate Loss (CNNIL)

In the context of 3D single-image SR, Georgescu et al. [128] has also proposed a deep convolutional neural network (CNN) for CT and MRI scans. The network is composed of two CNNs of similar architecture, but the first CNN performs the SR in the height and width directions, whereas the second CNN increases the resolution in depth (see Figure 4.4). The trained models are combined to provide the 3D super-resolved volume in the testing phase on along the three dimensions. The main contribution in their work is that each of the 10-layers CNN has an intermediate up-scaling layer placed after the first six convolutional layers (see Figure 4.5) which refines the HR image without taking any additional information from the LR image. Therefore, instead of computing only the loss between the final super-resolved image and the ground truth, the authors suggest computing an additional intermediate loss right after the up-scaling layer. This method will be referred to as CNNIL in the rest of the chapter.

Table 4.2 summarizes the network's parameters of the CNN architecture proposed in [128] which is the same for the two CNNs (height-width and depth). As depicted in Figure 4.5, each CNN is composed of 10 convolutional layers followed by a ReLU activation function. These ten layers are divided into 2 blocks, the first block containing six convolution layers followed by a sub-pixel convolutional layer for up-scaling, and the second block containing the last 4 layers. The first 5
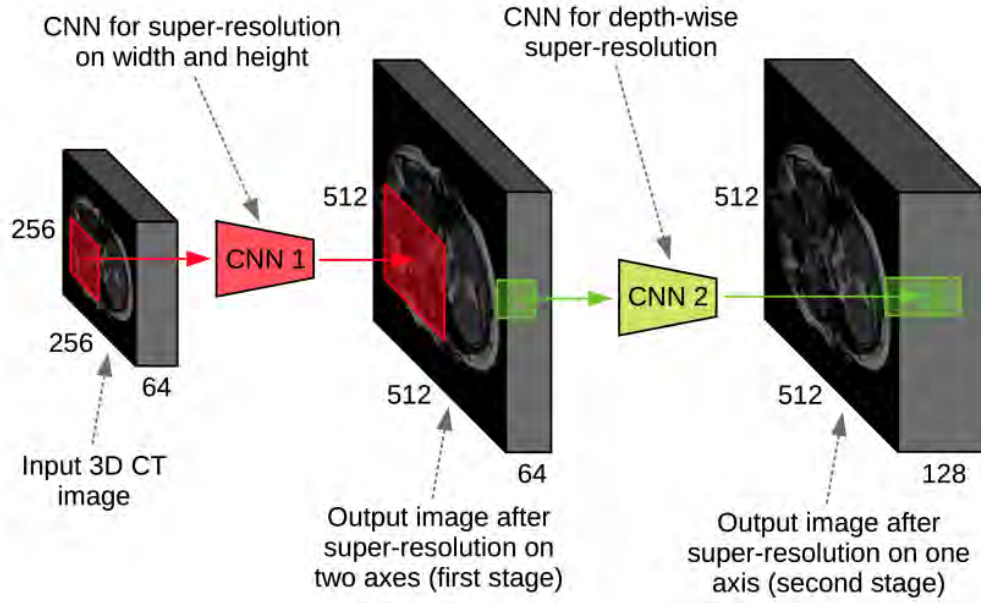
Figure 4.4: Illustration of the CNN proposed by Georgescu et al. [128] where CNN1 resizes the volume in the height and width dimensions and CNN2 resizes it in the depth. The figure was extracted from [128].
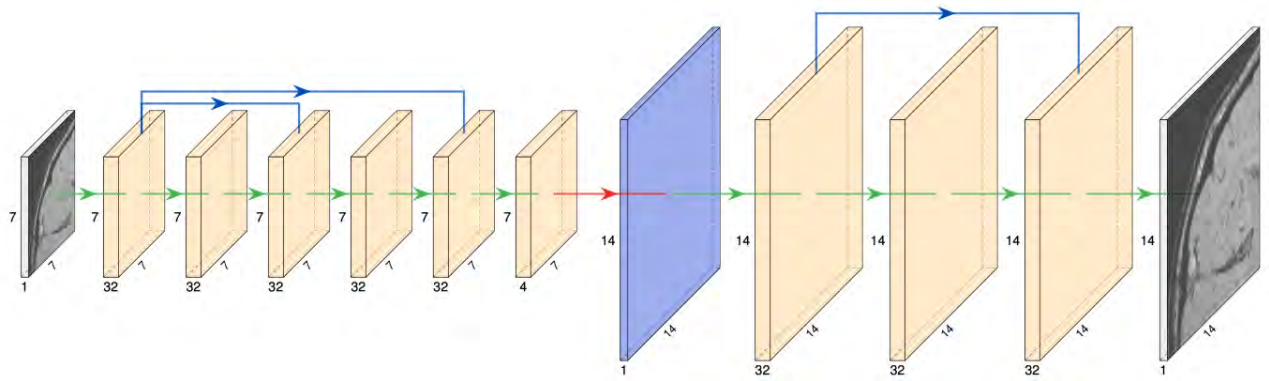
Figure 4.5: The convolutional neural network (CNN1) which performs the SR in the height and width directions. Green arrows represent the convolutional layers, red arrows represent sub-pixel convolutional layers, and blue arrows represent short- and long-skip connections. The figure was extracted from [128].

convolutional layers of the first block are formed of 32 filters of size 3×3. The sixth convolutional layer of CNN1 has d^2 filters, whereas the sixth convolutional layer of CNN2 has d filters, with d being the scaling factor. The first convolutional layer has a short-skip connection to the third layer and a long-skip connection to the fifth layer. In the up-scaling layer, the activation laps produced by the sixth layers are assembled into a single activation map. In the second convolutional block, the first three convolutional layers have 32 filters whereas the last layer has a single convolutional filter. A short-skip connection is also introduced between the seventh and the ninth layers. The network's parameters are then optimized using Adam's optimizer with a learning rate of 0.001 for the first 20 epochs and further decreased to 0.0001 for the last 20 epochs [128].

Table 4.2: Parameters' initialization of the CNNs proposed in [128]

Parameter	Assigned Value
Optimization method	Adam (adaptive moment estimation) [108]
Adam's learning rate	0.001 for 1st 20 epochs
	0.0001 for the last 20 epochs
Loss Function	Mean Absolute Difference
Weights	learned from data in an end-to-end fashion
Network depth	10 layes
Number of filters	32 convolution filters
Filter size	3×3
Number of epochs	40

As highlighted before, the loss function of the proposed method is not computed from the estimated HR image and the ground truth only. Instead, an intermediate loss that minimizes the difference between the up-scaled HR image (at the sixth convolutional layer) and the ground truth

is added. Finally, the full loss of the network, provided here for the height-width CNN, is given by:

$$L_{full}(\theta, I, O) = \underbrace{\sum_{i=1}^{w_0} \sum_{j=1}^{h_0} |f(\theta, I) - O|}_{\mathrm{L}_{standard}} + \underbrace{\sum_{i=1}^{w_0} \sum_{j=1}^{h_0} |f_1(\theta_1, I) - O|}_{\mathrm{L}_{intermediate}}, \tag{4.18}$$

where θ are the CNN weights, θ_1 are the weights of the first convolutional block, W_0 and h_0 are the width and height of the ground truth image O respectively, I is the LR input image, f is the transformation function learned by the CNN and f_1 is the transformation function of the first convolutional block.

Evaluation of the network's performance for MRI 2D and 3D SR was done in [128] using the NAMIC Brain Multimodality data set (http://hdl.handle.net/1926/1687)) containing 20 MR volumes of 176 slices each and of voxel resolution $= 1 \times 1 \times 1 \ mm^3$. LR images were simulated by adding Gaussian blur of a varying standard deviation randomly chosen between 0 and 0.5 and down-sampling by scale factors of 2 and 4. Training was performed on 10 MR volumes from which patches of size 7×7 were extracted whereas the other 10 were spared for testing. Since the network performs 2D and 3D SR, the results of both enhancements were compared to baseline methods of interpolation (nearest-neighbors, bilinear, bicubic and Lanczos) in addition to some state-of-the-art methods ([124, 125, 188]). Quantitative results showed that the 2D SR using the proposed method [128] outperforms all the other stated methods for the up-scaling factors of 2 and 4. Moreover the authors showed that their method even surpasses the method proposed by Pham et al. [127] when tested for the SR of 3D T_2-weighted images. However, in their study, they did not compare the performance of both methods on T_1-weighted images. In our work, we will further conduct this study on the 3D marmoset brain images.

To conclude, several deep-learning-based methods for MR image SR have been covered in this section. Our aim is thus to assess the efficiency of these methods in the SR of marmoset brain images after we re-train and fine-tune the parameter using our database. In the context of image enhancement, we will provide in the next section an overview of a deep-learning method for the synthesis of 7T-like images from 3T images. Although it is not a SR method, we wish to assess the potential enhancement provided by higher magnetic field images.

4.4   Synthesized 7T MRI from 3T MRI (WATNet)

In addition to SR, enhancement of MR images can be further provided by increasing the magnetic field strength for the better quantification of brain changes [189, 190]. However, this is constrained by the limited number of 7T platforms and the expensive acquisitions. An alternative approach to using high magnetic fields is to generate synthetic 7T images from 3T data using deep learning networks. The interest of such approaches was shown in the literature by several studies dedicated to human brain, for example by generating 7T MR images from 3T MR images [191–194]. In these studies, networks are trained using pairs of 3T/7T MR images of the human brain, where features representing the transition between 3T and 7T are learned using different approaches. A recent deep network, proposed by Qu et al. [182] for the synthesis of 7T images out of 3T ones using the information in spatial and wavelet domains, has proven to outperform these methods.

The deep network, called WATNet [182], uses features extracted from the spatial domain and incorporates wavelet features extracted by the image wavelet packet decomposition (WPD) for synthesizing 7T-like images. These features are then modulated with those extracted in the spatial domain through a wavelet-based affine transformation (WAT) layer. The advantage of these layers relies on their ability to combine multi-level frequency components holding information on image contrast and anatomical details. A brief summary of WATNet [182] is provided hereafter. Figure 4.6 shows the network proposed in [182]. WATNet reconstructs a 7T image ($\widehat{O}$), as close as possible to the ground truth 7T (O), from a 3T MR image (I). With θ being the network's parameters and R_θ the mapping function form 3T to 7T, the learning function can be expressed as

$$\widehat{O} = R_\theta(I). \tag{4.19}$$

By incorporating the wavelet information in the learning process using the wavelet decomposition of I, (4.19) can be re-written as:

$$\widehat{O} = R_\theta(I|W_l), \tag{4.20}$$

where W_l are the wavelet coefficients at level l. The WAT layers use the wavelet information and the intermediate feature map F to learn a set of affine parameters γ_l and β_l thus creating modulated
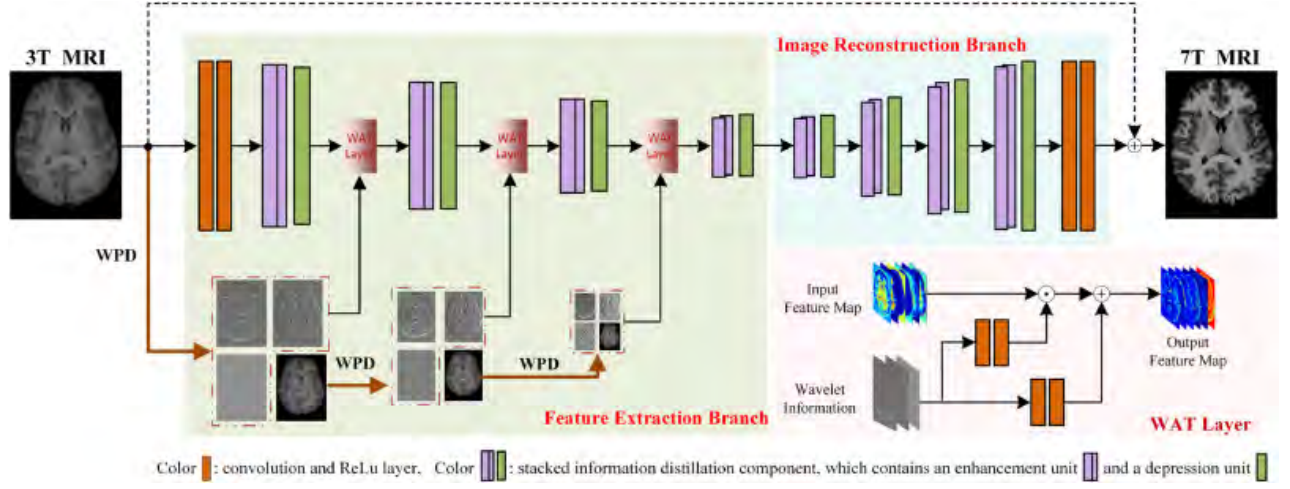
Figure 4.6: WATNet for the synthesis of 7T MRI from 3T MRI of human brain. This figure is extracted from [182]

feature maps as follows:

$$WAT(I|\gamma_l, \beta_l) = \gamma_l \odot F + \beta_l, \tag{4.21}$$

where $\odot$ is the element-wise multiplication. The final 7T image is reconstructed out of these modulated maps. The mean absolute error is then computed between the synthesized 7T MRI and the ground truth image. For a batch of N synthesized images, the network's loss function is given by:

$$L_{MAE} = \sum_i^N \|O^i - \widehat{O}^i\|_1, \tag{4.22}$$

where $\|.\|_1$ stands for the l_1-norm.

The feature extraction process consists in passing an image through two convolutional layers, four stacked information distillation blocks, and three WAT layers. Image reconstruction is then performed by adding the original 3T image to the modulated feature map resulting from the feature extraction block. WATNet was implemented with Caffe [185] and optimized using Adam [108] with a learning rate to 0.002 (halved every 10 epochs). Weights were initialized following Hui et al. [195]. As suggested in [182], the network was trained on 13 pairs of 3T/7T T1-weighted MR images of the human brain with 224 coronal slices and voxel size of $1 \times 1 \times 1\ mm^3$ divided as 9 pairs for training and 4 pairs for validation. The patch size was $64 \times 64 \times 3$, covering 3 consecutive axial slices. Data

augmentation by rotation, scaling, and fitting was performed to prevent over-fitting. Qualitative and quantitative analysis showed that WATNet yielded significantly closer results to the ground truth 7T images. Moreover, they have shown that not only does 7T images improve brain tissue segmentation, but also that segmentation results of the synthesized 7T images were more comparable to that of the ground truth images compared to other methods [182].

Since only 3T MR images are available in our study, we will evaluate the applicability of the deep network proposed in [182] and trained on $3T/7T$ pairs of human brain images for enhancing the quality of the 3T MRI of the marmoset brain. The synthesized 7T MR images are qualitatively and quantitatively compared to the original 3T images and the results of model-based and learning-based methods for SR that have been previously addressed.

4.5   Data preparation

This section presents the MRI dataset of the marmoset brain used to evaluate the performance of the model- and learning-based methods illustrated above. Moreover, we detail the simulation and the experimental setups used in the evaluation process. We finally highlight the segmentation method adopted in this work to perform the automatic tissue brain segmentation.

4.5.1   Marmoset brain dataset

Structural T1-weighted MR images of marmoset brains were acquired using a Philips MRI scanner dedicated to human and animal research at a field strength of 3T. A 3D gradient-echo sequence was used with $T_R = 10.5$ *msec*, $T_E = 4.7$ *msec*, flip angle of 8°, isotropic resolution of 0.35 *mm* and size of $288 \times 288 \times 113$ voxels. Since the marmoset size is small for the machine used, most brain scans include the neck and the shoulders regions. Thus, analyzing the whole image would increase the image processing time and lead to increased errors due to intensity artifacts. Therefore, it is preferable to reduce the image's Field of View (FOV) to include the head only. Reduction of FOV was achieved during the rigid registration of the MR scans to the T_1-weighted marmoset brain template that have been previously developed by Risser et al. [196] using SPM. This template was

built from a single fully segmented marmoset brain image, which was transported onto the Karcher mean [197] of 13 adult marmoset brain images using a diffeomorphic strategy that fully preserves the brain topology. Finally, the registration process, illustrated in Figure 4.7, reduces all the scan's size to $126 \times 110 \times 81$. This step is important later on for the segmentation purpose since all the brains are now in the template space.
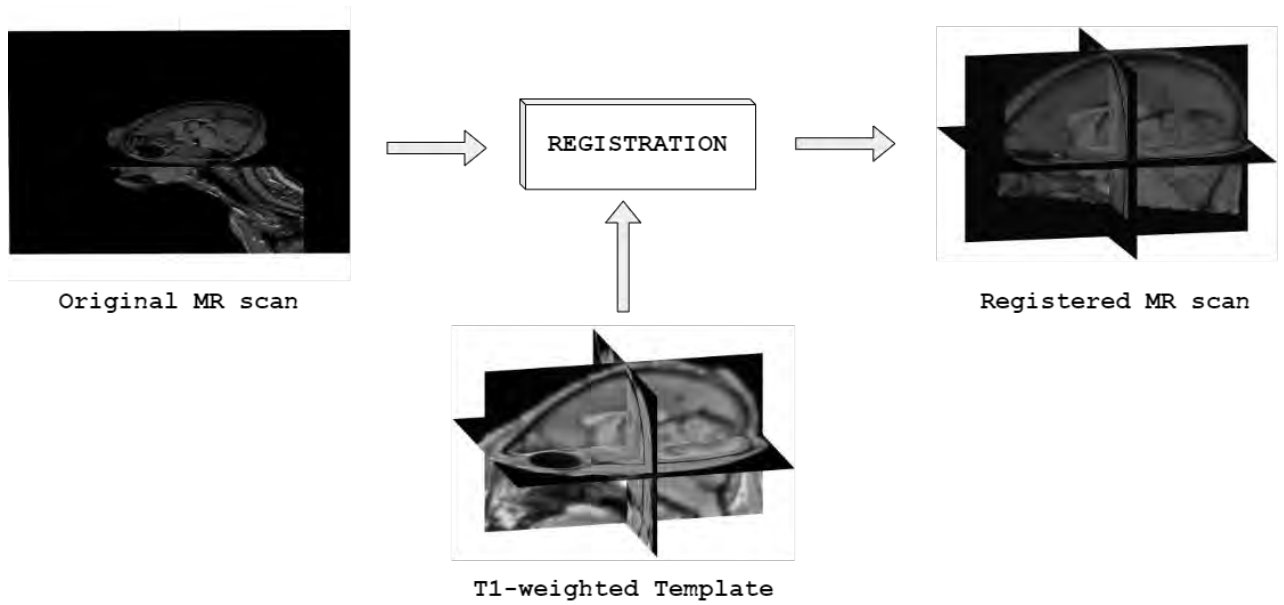
Figure 4.7: Registration of the original MR scans to the T1-weighted marmoset brain template reduces the FOV to the head region only and ensures that all scans are in the template space.

For the remainder of the chapter, we will refer to the registered MR scans as the native images that we will use in our simulation and experimental setups.

4.5.2 LR data simulation

To evaluate the SR performance of the different methods, LR/HR pairs of scans for each brain should be acquired. An alternative approach in the absence of these pairs is to simulate LR volumes from the available MR scans considered as high in resolution (Figure 4.8). In our work, LR images have been generated by convolving the HR data (native images) with a Gaussian kernel and down sampling by an isotropic factor.
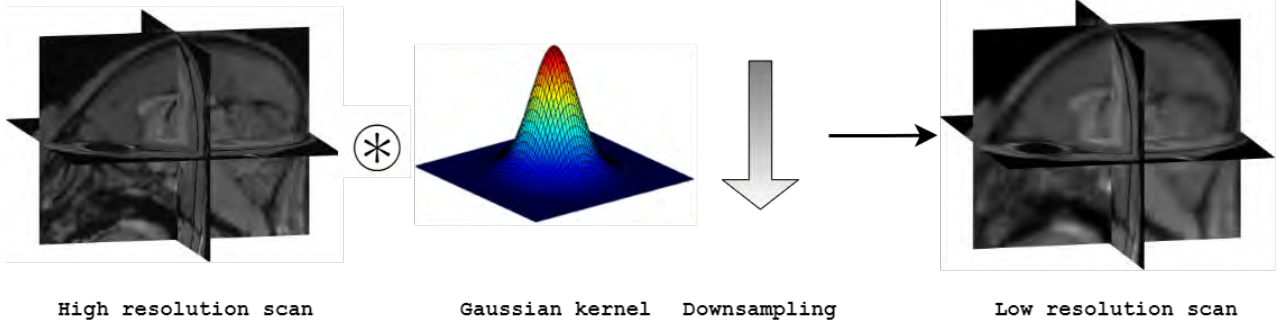
Figure 4.8: Simulation of LR images from native images considered as HR by convolving by a Gaussian blurring kernel and down sampling by a factor of 2. ⊛ represents the convolution operation and the down arrow represents down sampling.

Training data　Following the work in [128], we generated LR patches for the training phase of both learning-based methods by applying a Gaussian blur of size 7×7 and a random standard deviation chosen between 0 and 1.5. The training data set of the 3D ReCNN compromised 23 subjects of which 3200 patches of size $21 \times 21 \times 21$ were were randomly sampled per subject. On the other hand, the training dataset of the CNNIL contained 10 subjects of which 115000 patches of size $7 \times 7 \times 7$ were sampled.

Testing data　Based on the image formation model, LR images used for assessment in the simulation setup were generated from their HR correspondence using a Gaussian kernel of a fixed standard deviation $\sigma = 0.7$ and size 3×3 and down-sampled by a scale of 2. The same LR scans were used to test all the methods to perform a fair comparison. The proposed methods were evaluated using three MR volumes, for which the manual segmentation is available, in the simulation and the experimental setups. Moreover, 7T-like images were synthesized out of these volumes, and their segmentations were compared to the ground truth manual segmentation in the experimental setup. The testing data will be referred to as Scan1, Scan2 and Scan3 in the rest of the chapter.

Figure 4.9 illustrates the data used for training and testing phases. Moreover it shows the different inputs an outputs for simulation and experimental setups. LR images of size $(\frac{m}{d} \times \frac{n}{d} \times \frac{k}{d})$ are simulated from native data of size $(m \times n \times k)$, where d is the scaling factor. These LR/HR pairs are further

used for training the deep-learning networks. Moreover, the LR simulated images are used in the simulation setup to test the performance of model-based and learning-based methods with the ground truth native data available. The output images of the simulation setup are then expected to be as close to the native images as possible. In the experimental setup, the native images are fed into the methods evaluated to get super-resolved volumes of size $dm \times dn \times dk$ that are better in resolution compared to the native images.
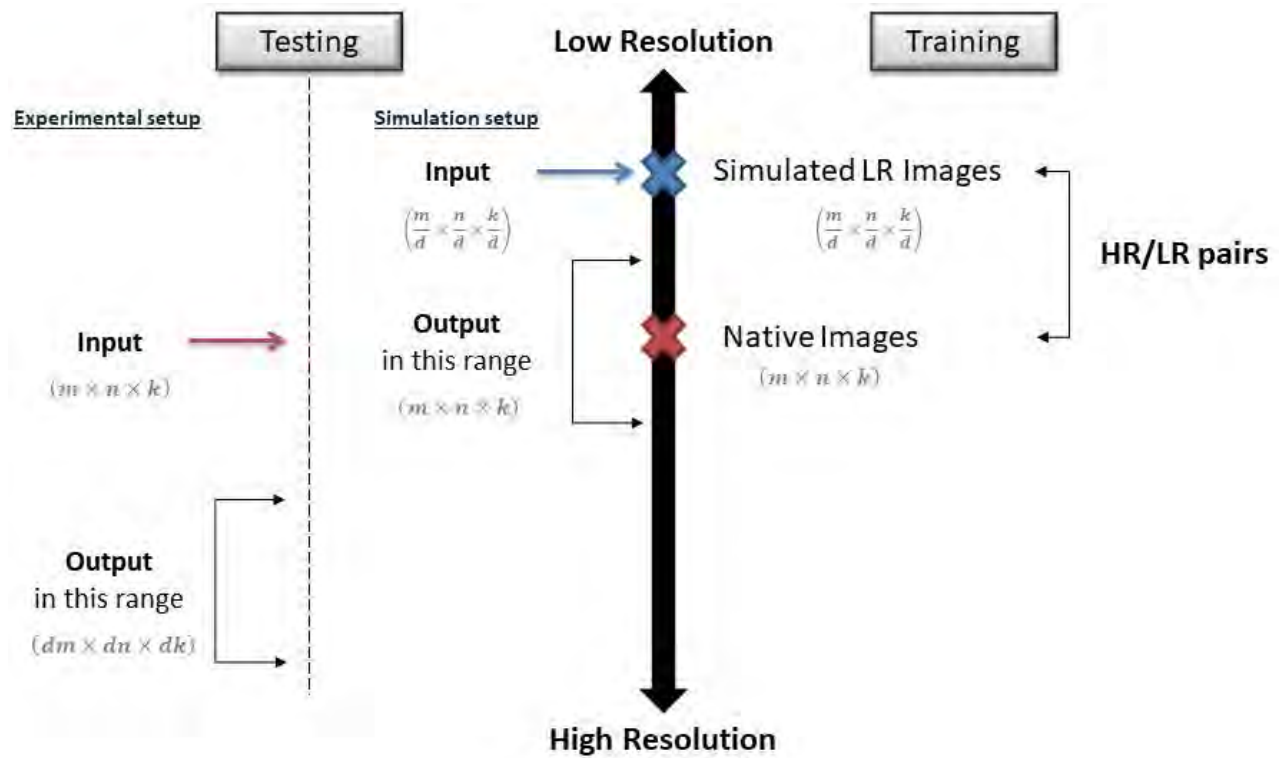
Figure 4.9: Illustration of the data used in the training phase and the testing phase including simulation and experimental setups. LR images are simulated from native images to create LR/HR pairs that are further used in the training phase. Testing phase includes two setups: the simulation and the experimental. In the simulation setup, simulated LR images are used for testing with the native ground truth image available, whereas in the experimental setup the native images are directly used for testing different methods.

4.5.3 Image segmentation

In this chapter, we performed cross-sectional brain segmentation of each volume in SPM. To recall from Chapter 2, SPM segmentation requires the presence of tissue probability maps that represent the prior information used to create the final segmentation. These tissue probability maps were previously created at CERCO lab (`cerco.cnrs.fr/en/cerco-umr5549-2/`) from an initial automatic brain segmentation of 43 marmoset subjects to represent the whole population. The procedure, called DARTEL (Diffeomorphic Anatomical Registration using Exponential Lie Algebra) template creation [198], begins by creating a mean of all the segmentation images, which is used as an initial template. Deformations from this template to each of the individual images are computed, and the template is then re-generated by applying the inverses of the deformations to the images and averaging. This procedure is repeated auntil convergence and the final maps are created. MR volumes registered to the T_1-weighted template, and the DARTEL priors are then fed into SPM to create the final segmentation. Figure 4.10 illustrates the segmentation procedure. Following the suggestion in [141, 142], the native 3D T_1-weighted volumes are enlarged to five times the head size to make the images usable in software for human brains.

4.6 Results

Several model-based and learning-based SR techniques have been presented. In this section, we will compare the performance of these methods versus classical interpolation methods, i.e. bicubic, cubic, and spline interpolation. Quantitative and qualitative analysis will be performed for simulation and experimental results. Moreover, we will further analyze the results from the 2D and 3D SR perspective.
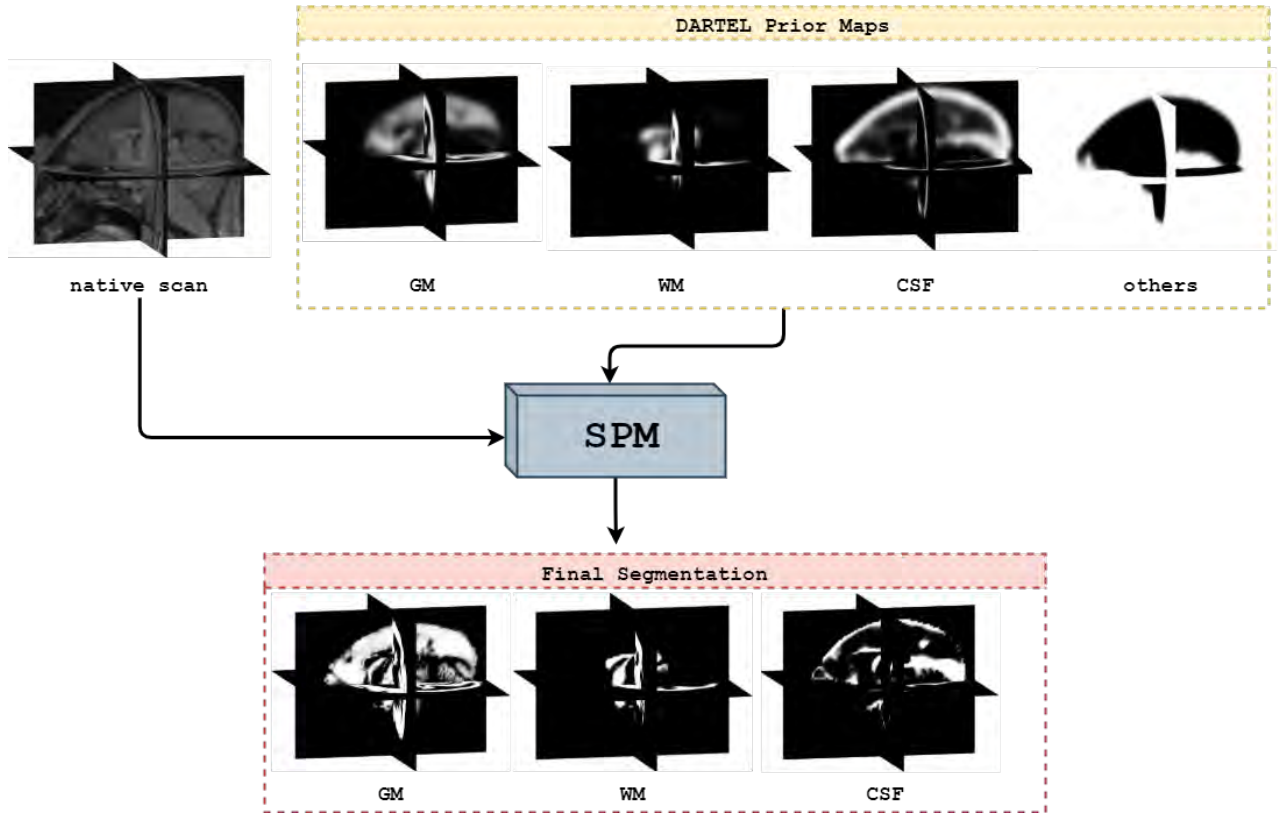
Figure 4.10: Segmentation of the native scan (already registered to the marmoset IMPEC brain template) in SPM using DARTEL prior maps as input to create the final segmentation of GM, WM and CSF. Note that for human brain, two additional priors exist for the head and skull that are not available in our study.

4.6.1 Image quality assessment

To quantify the quality of the super-resolved images and their corresponding segmentation, we have used different metrics. In addition to ISNR and SSIM, previously introduced in Chapter 3, we used the peak signal-to-noise ratio (PSNR), the information fidelity criterion (IFC) [199, 200], and the mean squared error (MSE) as classical criterion to evaluate the similarity between gray level images. Although IFC has been scarcely used in literature, Yang et al. [201] has proved the effectiveness of this metric being highly correlated with the human perception of the super-resolved mages. IFC metric is designed to evaluate the loss of image information by extracting wavelet features with focus

on high-frequency details rather than low-frequency components. Higher IFC values correspond to a better enhancement. The MSE and the PSNR are defined as:

$$\text{MSE} = \frac{1}{N}\sum_{i=1}^{N}(\mathbf{x}_i - \hat{\mathbf{x}}_i)^2, \tag{4.23}$$

$$\text{PSNR} = 10\log_{10}\frac{(\max(\mathbf{x}) - \min(\mathbf{x}))}{MSE}, \tag{4.24}$$

where $\mathbf{x}$, $\mathbf{y}$, and $\hat{\mathbf{x}}$ are the ground truth, the corrupted image and the restored image by SR respectively, and N is the total number of elements in $\mathbf{x}$. max and min are the maximum and minimum intensity values of the HR image $\mathbf{x}$.

Segmentation results were assessed based on the SSIM index computed for segmentation maps, and the Dice coefficient computed for segmentations binarized by thresholding.

4.6.2   Choice of the hyperparameters

Since model-based SR algorithms require the previous knowledge or estimation of the blurring point spread function (PSF), we have followed the conclusion drawn by [42] and [81] by approximating the PSF as a Gaussian function with its full width at half maximum (FWHM) equal to the selected slice width. The standard deviation is then computed by:

$$\sigma = \frac{\text{FWHM}}{4\sqrt{2ln2}} \tag{4.25}$$

The dimensionality of the PSF kernel generated depends on the SR problem to be solved, i.e. in 2D or 3D. While the FSR performs the SR in 2D (slice by slice), the TF and LRTV algorithms require a 3D kernel. The parameters used in the LRTV algorithm were kept as suggested by the authors in [100] given that the original paper already addressed an MR application. The TF method only requires one hyperparameter, the tensor rank F which was set to its best value of 1200, while LRTV requires the right tuning of the weights of each regularization term and the parameters of the ADMM and gradient descent optimizer. Similarly, the hyperparameters of the FSR algorithm were set by cross-validation to their best values, $\mu = 0.005$ and $\tau = 0.02$.

Starting from the initial parameters suggested by the authors for learning-based methods, several trials were conducted to choose the best values for the available marmoset database. Finally, Table

4.3 and Table 4.4 summarize the parameters used in the training phase for the 3D ReCNN and the CNNIL respectively. The 3D ReCNN algorithm was re-implemented in Tensorflow(2.3.0).

Table 4.3: Parameters' initialization for the training phase of the 3D ReCNN

Parameter	Assigned Value
Optimization method	Adam (adaptive moment estimation)
Loss Function	Mean Squared Error (MSE)
Number of epochs	20
Adam's learning rate	0.001
Scale	[2,2,2]
Blur	$N \frown (0, \sigma)$
σ	random number $\in [0, 1.5]$
Batch size	128
Patch size	$21 \times 21 \times 21$
Patch stride	7
Number of filters	64 convolution filters
Filter size	3×3 at each layer
Number of subjects	23
Samples/subject	3200
Number of samples	106141

Figure 4.11 shows the evolution of loss function and the PSNR (in dB) during the training phase of the 3D ReCNN as function of training epochs. Similarly, Figure 4.12 shows these values computed for the height-width sub-network of CNNIL (CNN1) and the depth sub-network of CNNIL (CNN2) respectively.

Table 4.4: Parameters' initialization for the training phase of the CNNIL

Parameter	Assigned Value
Optimization method	Adam (adaptive moment estimation)
Loss Function	Mean Absolute Error
Number of epochs	40
Adam's learning rate	0.001 for 1st 20 epochs 0.0001 for the last 20 epochs
Scale	[2,2,2]
Blur	$N \frown (0, \sigma)$
σ	random number $\in [0, 1.5]$
Batch size	128
Patch size (CNN1)	7×7
Patch size (CNN2)	14×7
Patch stride	7
Number of filters	32 convolution filters
Filter size	3×3
Number of subjects	10
Number of patches	115000
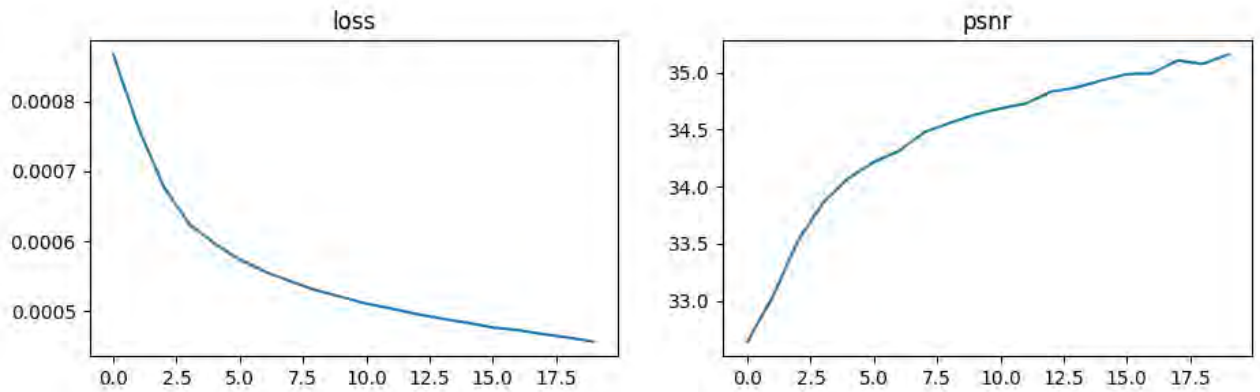
Figure 4.11: Evolution of the loss and PSNR of 3D ReCNN with respect to the number of epochs
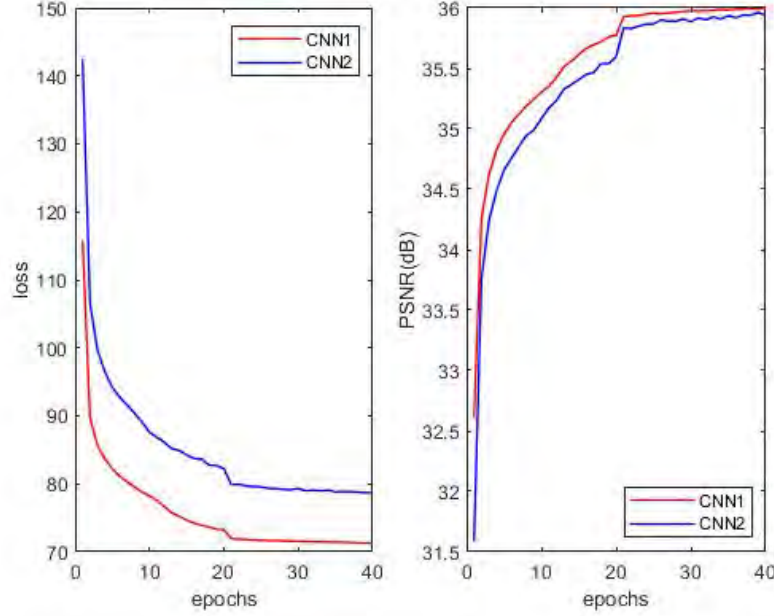
Figure 4.12: Evolution of the loss and PSNR of CNNIL with respect to the number of epochs. The figure shows the metrics' evolution of CNN1 in red and CNN2 in blue.

While the 3D ReCNN starts by an LR image interpolated using Spline interpolation in order to train the SR network, the CNNIL network is trained without resizing the input image due to the architecture of the network having an intermediate up-scaling convolutional layer. As stated previously, the WATNet for 7T-like image synthesis from 3T images was tested directly using the trained model on $3T/7T$ pairs of the human brain as provided by the author [182] due to the lack of $3T/7T$ T_1-weighted pairs for the marmoset brain.

4.6.3 Simulation results

As stated in Section 4.5, the simulation setup consists in applying SR to simulated LR data of the marmoset brain where the ground truth HR data is available. Restored images are thus compared, quantitatively, to their HR reference using the evaluation metrics. Similarly, segmentations of images restored by SR are compared quantitatively to the segmentation of the HR reference. Results are

collected for the three MR scans used as testing data. Table 4.5 provides the model-based SR results for the FSR, TF and, LRTV compared to standard resizing methods based on interpolation schemes, namely bicubic and cubic interpolation, in terms of SSIM, PSNR, ISNR, MSE and IFC. In addition, Table 4.5 shows the elapsed time (in *secs*) to complete the SR task for FSR, LRTV, and TF methods performing 800, 20, and 20 iterations respectively. Similarly, Table 4.6 provides the learning-based SR results for the ReCNN, the CNNIL along height-width axes (CNNIL-2D), and the CNNIL along the 3 axes (CNNIL-3D) compared to standard Spline interpolation method. Note that we have included the Spline interpolation in learning-based comparisons since it is the interpolation method used to upscale the LR image in the ReCNN method.

Table 4.5: Model-based SR results of FSR, TF, LRTV Bicubic interpolation and Cubic interpolation methods on three MR scans of the marmoset brain (Scan1, Scan2, and Scan3). The SSIM, PSNR, ISNR, MSE and IFC values are reported for an up-scaling factor of 2. Elapsed time (in *secs*) to complete the SR task for FSR, TF, and LRTV is given for 800, 20, and 20 iterations respectively. The best result from the three methods is highlighted in bold for each scan.

	Method	SSIM	PSNR	ISNR	MSE	IFC	Time (*secs*)
Scan1	FSR	0.725	**34.574**	**3.369**	**0.0088**	**4.843**	**8.13**
	TF	**0.894**	29.920	1.107	0.0134	3.6021	55.97
	LRTV	0.700	30.637	0.374	0.0105	3.3050	751.28
	Bicubic	0.650	30.465	-	0.0118	2.554	-
	Cubic	0.829	27.729	-	0.0145	2.6702	-
Scan2	FSR	**0.760**	34.947	3.713	**0.0003**	**4.989**	**7.78**
	TF	0.710	30.663	**3.891**	0.0008	3.8695	56.15
	LRTV	0.724	31.481	0.202	0.0020	3.5504	736.08
	Bicubic	0.699	31.234	-	0.0021	2.640	-
	Cubic	0.702	23.096	-	0.0026	2.8145	-
Scan3	FSR	**0.739**	33.295	2.998	**0.0005**	**4.723**	**8.23**
	TF	0.685	29.840	1.249	0.0013	3.4221	55.82
	LRTV	0.707	33.148	0.0202	0.0020	3.1852	723.49
	Bicubic	0.668	30.297	-	0.0024	2.508	-
	Cubic	0.671	22.638	-	0.0030	2.5638	-

Table 4.6: Learning-based SR results of ReCNN, CNNIL-2D, CNNIL-3D, and Spline interpolation methods on three MR scans of the marmoset brain (Scan1, Scan2, and Scan3). The SSIM, PSNR, ISNR, MSE and IFC values are reported for an up-scaling factor of 2. The best result from the three methods is highlighted in bold for each scan.

	Method	SSIM	PSNR	ISNR	MSE	IFC
Scan1	ReCNN	**0.946**	**34.063**	2.003	0.0174	**4.1304**
	CNNIL-2D	0.662	29.374	2.277	**0.0099**	2.616
	CNNIL-3D	0.680	28.304	**6.124**	0.0107	3.1712
	Spline	0.916	32.060	-	0.0144	2.5385
Scan2	ReCNN	**0.962**	**35.223**	2.337	0.0013	**4.4701**
	CNNIL-2D	0.918	31.564	**6.179**	0.0009	2.703
	CNNIL-3D	0.932	31.576	5.922	**0.0007**	3.9980
	Spline	0.910	32.059	-	0.0144	3.8130
Scan3	ReCNN	**0.940**	**33.252**	1.981	0.0026	**3.9980**
	CNNIL-2D	0.902	30.422	5.760	**0.0011**	2.528
	CNNIL-3D	0.906	28.888	**7.548**	0.0016	3.0698
	Spline	0.905	31.271	-	0.0043	3.3745

In addition to the quantitative results shown in Tables 4.5 and 4.6, we present qualitative illustration of the model-based SR results and learning-based SR results in Figure 4.13 and Figure 4.14 respectively for three axial slices from Scan1, Scan2, and Scan3.

In order to further assess the recovered images by SR, we performed the brain tissue segmentation of the HR and the recovered images into GM, WM and CSF. Although the segmentation of CSF is not accurate since it can not be distinguished from the skull, this error is present in the segmentation of HR and recovered scans, thus presenting its results here is acceptable. Table 4.7 and Table 4.8 compares, respectively, the SSIM index and Dice coefficient computed between the HR image segmentation and the recovered image segmentation using model- and learning-based methods.

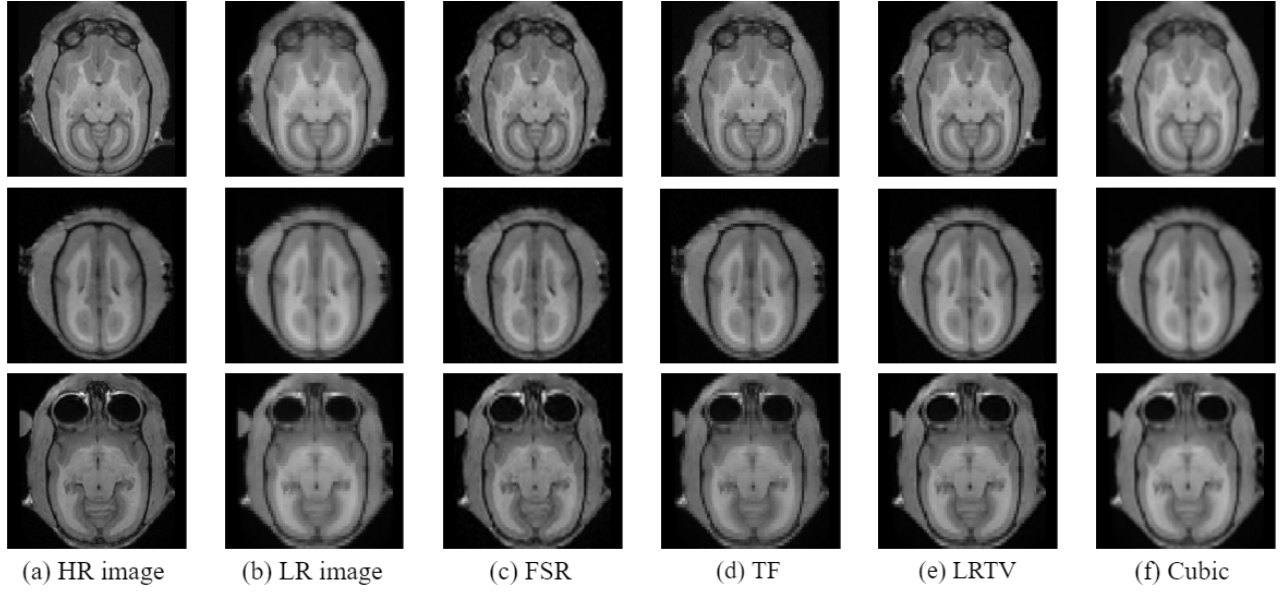(a) HR image (b) LR image (c) FSR (d) TF (e) LRTV (f) Cubic

Figure 4.13: Axial slices showing SR model-based results of the LR image in (b) using (c) FSR, (d) TF, (e) LRTV, and (f) Cubic interpolation with respect to the ground truth HR image (a). First, second, and third row represent the axial slice from Scan1, Scan2, and Scan3 respectively. The LR images were blurred using Gaussian kernel and downsampled by a scale of 2.

Table 4.7: SSIM index computed for the segmentation of each recovered scan using different model-based and learning-based SR methods with respect to the segmentation of the HR image. The best results from the model-based and learning-based methods are highlighted in bold for each scan.

		Model-based					Learning-based			
		FSR	TF	LRTV	Bicubic	Cubic	ReCNN	CNNIL-2D	CNNIL-3D	Spline
Scan1	GM	**0.9352**	0.8843	0.8943	0.8751	0.8594	**0.9231**	0.8925	0.8759	0.8960
	WM	**0.9113**	0.8632	0.8778	0.8782	0.8592	**0.8892**	0.8826	0.8670	0.8794
	CSF	**0.7983**	0.7533	0.7794	0.7495	0.7083	0.6019	**0.8184**	0.7231	0.6414
Scan2	GM	0.8975	0.8595	**0.9097**	0.8299	0.8386	**0.9461**	0.8592	0.8900	0.8486
	WM	0.8807	0.8977	**0.9025**	0.8983	0.8954	**0.9257**	0.8941	0.8863	0.9137
	CSF	0.7312	0.7363	**0.8333**	0.7653	0.7732	0.7179	0.7539	**0.8170**	0.7457
Scan3	GM	**0.9218**	0.8620	0.8754	0.8111	0.7972	**0.9145**	0.8757	0.8413	0.8162
	WM	**0.8997**	0.8463	0.8496	0.8483	0.8477	**0.8802**	0.8604	0.8343	0.8651
	CSF	**0.7400**	0.6457	0.6384	0.5956	0.6254	**0.7856**	0.7213	0.6302	0.7715

(a) HR image   (b) LR image   (c) ReCNN   (d) CNNIL-2D   (e) CNNIL- 3D   (f) Spline
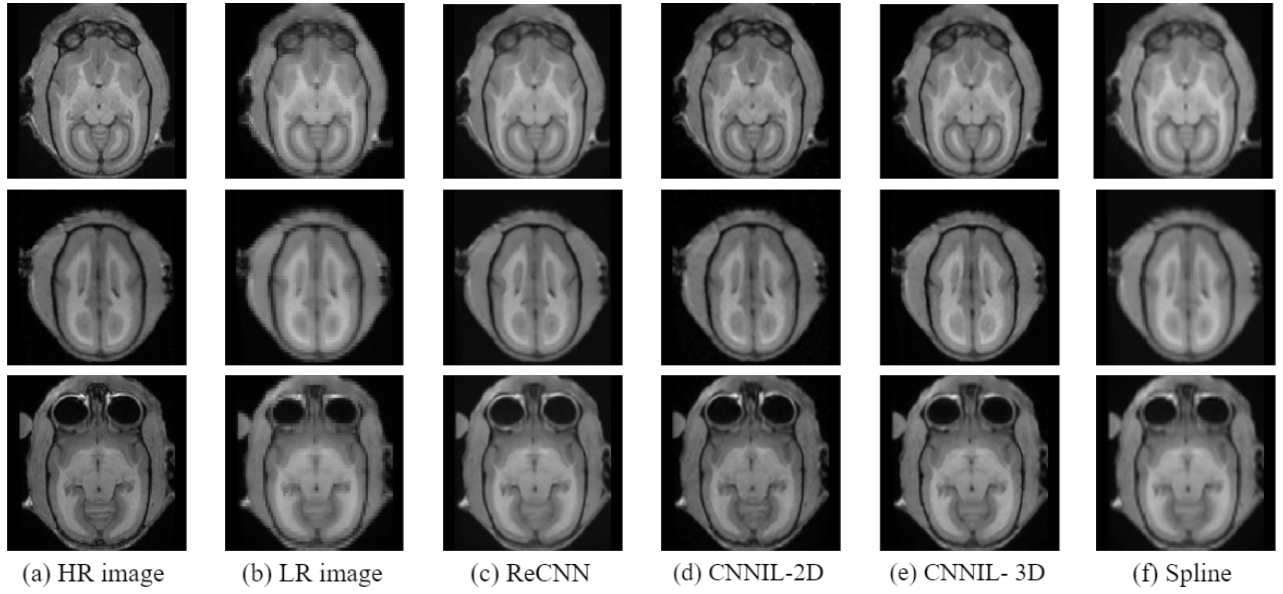
Figure 4.14: Axial slices showing SR model-based results of the LR image in (b) using (c) ReCNN, (d) CNNIL-2D, (e) CNNIL-3D, and (f) Spline interpolation with respect to the ground truth HR image (a). First, second, and third row represent the axial slice from Scan1, Scan2, and Scan3 respectively. The LR images were blurred using Gaussian kernel and downsampled by a scale of 2.

Table 4.8: Dice coefficient computed for the segmentation of each recovered scan using different model-based and learning-based SR methods with respect to the segmentation of the HR image. The best results from the model-based and learning-based methods are highlighted in bold for each scan.

		Model-based					Learning-based			
		FSR	TF	LRTV	Bicubic	Cubic	ReCNN	CNNIL-2D	CNNIL-3D	Spline
Scan1	GM	**0.9521**	0.9100	0.9200	0.9054	0.9067	**0.9383**	0.9248	0.9126	0.9272
	WM	**0.9371**	0.8882	0.8932	0.8851	0.8889	**0.9176**	0.8963	0.8904	0.9086
	CSF	**0.9095**	0.8901	0.9015	0.8815	0.8601	0.7544	**0.9128**	0.8702	0.7982
Scan2	GM	**0.9303**	0.8872	0.9297	0.8560	0.8791	**0.9571**	0.8829	0.9237	0.8935
	WM	**0.9231**	0.9071	0.9118	0.9014	0.8997	**0.9447**	0.9091	0.9031	0.9157
	CSF	0.8899	0.8886	**0.9292**	0.8974	0.9016	0.8678	0.8917	**0.9218**	0.8929
Scan3	GM	**0.9512**	0.8957	0.9121	0.8389	0.8458	**0.9445**	0.9239	0.9076	0.8703
	WM	**0.9261**	0.8766	0.8800	0.8723	0.8646	**0.9082**	0.8833	0.8753	0.8860
	CSF	**0.9108**	0.8548	0.8374	0.8225	0.8401	**0.9279**	0.9028	0.8339	0.8507

Finally, based on the quantitative results in Tables 4.7 and 4.8 favoring the 2D FSR and the 3D ReCNN, and to further illustrate the effect of MRI SR on tissue brain segmentation, Figure 4.15 shows the GM and WM segmentation of an axial slice of Scan1 for these methods compared to that of the LR and HR images.

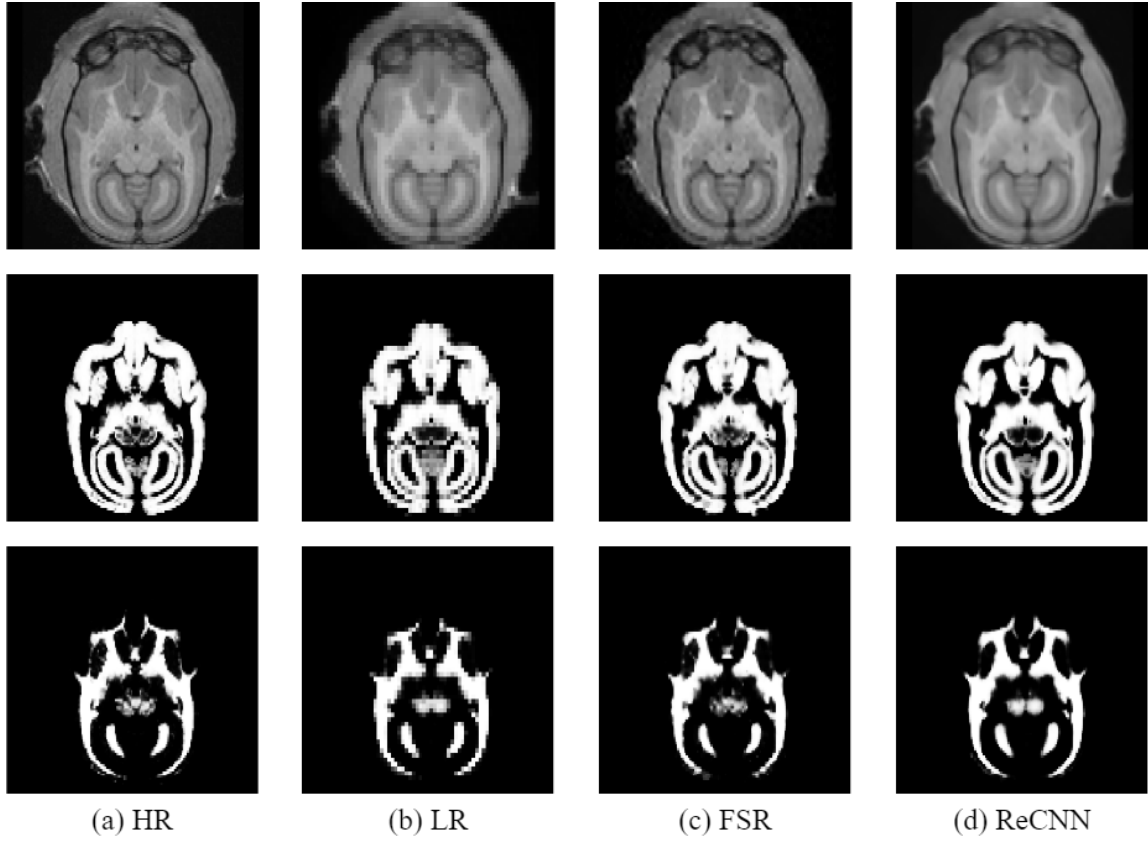(a) HR   (b) LR   (c) FSR   (d) ReCNN

Figure 4.15: GM (second row) and WM (third row) segmentation of an axial slice of Scan 1 for the (a) HR ground truth image, (b) LR simulated image, (c) recovered image by 2D FSR, and (d) recovered image by 3D ReCNN.

4.6.4   Experimental results

Herein, we have applied the SR methods directly to the MR scans, thus considered as the LR. SR was performed using an isotropic upsampling factor of 2. Figure 4.16 and Figure 4.17 compare the qualitative results of HR image restoration using model-based and learning-based methods respectively for an axial slice of Scan1. In this experimental setup, the ground truth HR data are not available for calculating metrics.

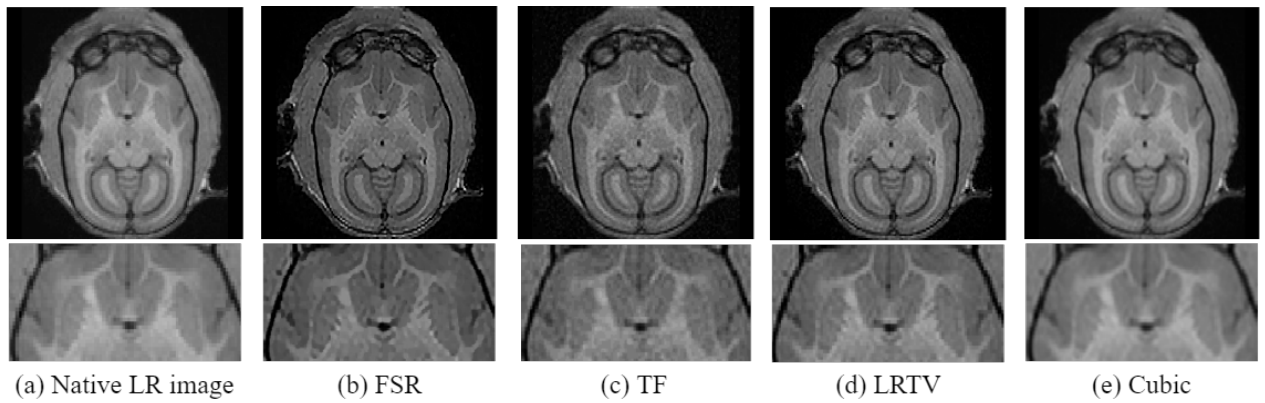(a) Native LR image   (b) FSR   (c) TF   (d) LRTV   (e) Cubic

Figure 4.16:   Illustration of model-based SR results on the native LR data of the marmoset brain with isotropic voxel upsampling factor of 2. The first row shows the recovered axial slice of (a) native LR data using (b) FSR, (c) TF, (d) LRTV, and (d) Cubic interpolation. The second row shows a close-up visualization of a cropped region of the corresponding images.

Moreover, we have tested the 7T image synthesis from 3T scans of the marmoset brain using the WATNet. In order to create a dataset similar to the one used for training, the skull and head parts were removed and voxels' values were normalized between 0 and 1. A qualitative analysis between the original 3T image and the synthesized 7T image is done by observing some regions of the brain that are interesting to investigate during the aging process. Fig. 4.18 shows axial and sagittal slices of a 3T image (a and b) and their corresponding synthesized 7T image (c and d) respectively. A closer look at the CSF ventricles, on the different slices, reveals the important visual enhancement in the definition of the borders of this region enabled by the synthesized 7T image, further validated by an expert in marmoset brain images.
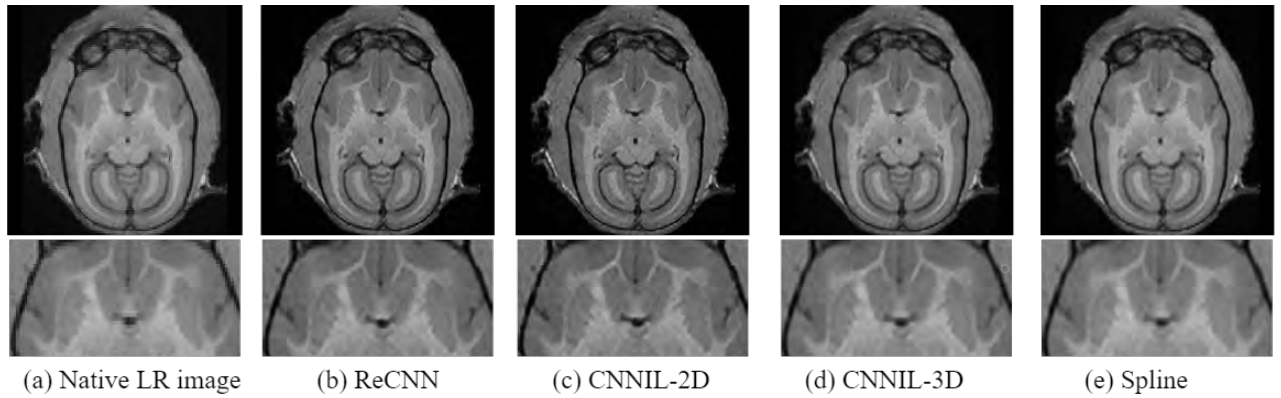
Figure 4.17: Illustration of model-based SR results on the native LR data of the marmoset brain with isotropic voxel upsampling factor of 2. The first row shows the recovered axial slice of (a) native LR data using (b) ReCNN, (c) CNNIL-2D, (d) CNN-3D, and (e) Spline interpolation. The second row shows a close-up visualization of a cropped region of the corresponding images.
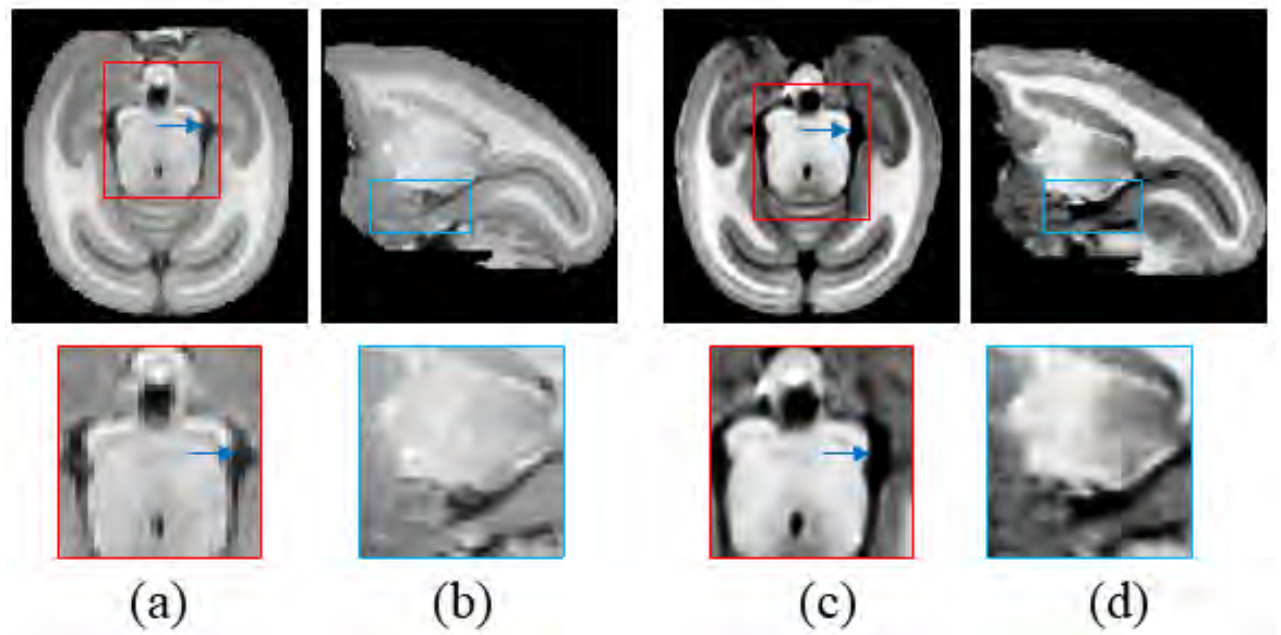

Figure 4.18: Axial and sagittal slices of a 3T image (a, b) and the corresponding 7T synthesized image (c, d) in the first row. The second row provides a close up visualization of the CSF ventricles for the different slices.

Validation of the enhancement provided by synthesizing 7T MRI from 3T MRI was further performed by the quantification of the GM, WM and CSF volumes after segmentation. The results were then compared to the values computed from the manual segmentation (MS) of the native scans used for testing. In order to quantitatively assess segmentation results, Table 4.9 shows these volumes (in mm^3) calculated for the three MRI acquisitions, for the original 3T, as well as for the results of model-based and learning-based SR methods and the synthesized 7T. For a better comparison of the results, Table 4.10 provides the absolute difference between the volumes computed and the volume of the manual segmentation. As mentioned before, the segmentation of the CSF remains not as accurate as the manual segmentation since it is hard to differentiate the CSF from the skull using the T_1-weighted MRI sequence. Indeed, the CSF volume is systematically overestimated here.

Table 4.9: Volumes in mm^3 of the GM, WM and CSF tissues segmented for the native 3T, the super-resolved 3T volumes with model-based and learning-based methods, and the synthesized 7T with WATNet volumes of three scans. Results are compared to the volumes computed from the manual segmentation (MS). The values closer to the MS are highlighted in bold.

				Model-based					Learning-based				
		MS	Native	FSR	TF	LRTV	Bicubic	Cubic	ReCNN	CNNIL-2D	CNNIL-3D	7T-synthesis	Spline
Scan1	GM	5.504	5	5.18	5.099	**5.230**	4.83	4.824	**5.545**	5.04	5.135	5.415	4.974
	WM	1.6916	1.896	1.67	1.750	**1.679**	1.89	1.897	1.771	1.81	1.761	**1.639**	1.869
	CSF	0.3053	4.696	5.53	**4.364**	5.567	5.52	5.723	5.731	5.4	5.619	**3.883**	6.019
Scan2	GM	5.2303	4.864	**5.56**	4.610	4.938	4.89	4.838	5.550	**5.24**	4.795	4.864	4.580
	WM	1.7243	1.984	**1.76**	1.923	1.893	1.96	2.024	1.917	1.86	1.864	**1.792**	2.079
	CSF	0.2586	4.984	**4.95**	5.327	5.670	5.36	5.514	5.465	5.43	5.920	**3.437**	6.112
Scan3	GM	5.2155	**5.072**	5.41	4.869	4.921	4.69	4.680	**5.192**	5.11	5.368	4.573	4.790
	WM	1.6841	1.872	**1.73**	1.796	1.800	1.96	1.969	1.933	1.84	**1.780**	1.907	1.972
	CSF	0.2761	**4.864**	5.30	5.158	5.580	5.4	5.597	5.592	5.32	5.437	**3.671**	5.721

Table 4.10: Absolute volume difference of the GM, WM and CSF tissues segmented for the native 3T, the super-resolved 3T volumes with model-based and learning-based methods, and the synthesized 7T with WATNet volumes of three scans with respect to the volumes computed from the MS. The best results, representing the smallest difference, from the model-based and learning-based methods are highlighted in bold for each scan.

| | | Native | Model-based | | | | | Learning-based | | | | |
			FSR	TF	LRTV	Bicubic	Cubic	ReCNN	CNNIL-2D	CNNIL-3D	7T-synthesis	Spline
Scan1	GM	0.504	0.342	0.404	**0.273**	0.674	0.679	**0.041**	0.464	0.368	0.088	0.529
	WM	0.204	0.021	0.059	**0.011**	0.198	0.205	0.080	0.118	0.070	**0.052**	0.1744
	CSF	4.390	5.224	**4.058**	5.261	5.214	5.418	5.426	5.094	5.314	**3.577**	5.713
Scan2	GM	0.456	**0.239**	0.709	0.381	0.430	0.482	0.230	**0.080**	0.525	0.455	0.739
	WM	0.259	**0.035**	0.198	0.168	0.235	0.300	0.193	0.135	0.140	**0.0682**	0.355
	CSF	4.725	**4.691**	5.069	5.411	5.101	5.255	5.207	5.171	5.661	**3.179**	5.845
Scan3	GM	**0.143**	0.194	0.346	0.294	0.525	0.535	**0.023**	0.105	0.153	0.642	0.424
	WM	0.187	**0.045**	0.111	0.116	0.275	0.285	0.249	0.155	**0.096**	0.223	0.288
	CSF	**4.587**	5.023	4.882	5.304	5.1239	5.321	5.316	5.043	5.161	**3.395**	5.445

4.7 Discussion

In this chapter, we have evaluated several model-based and learning-based SR methods for the enhancement of marmoset brain images. Simulation results were carried out on LR images that have been degraded from the native dataset using a Gaussian blurring kernel and an isotropic down scaling factor of 2. Moreover, experimental results carried on the native data were assessed from the segmentation perspective where volumes of GM, WM and CSF were computed and compared to the MS.

The comparison of model-based methods in terms of quantitative metrics presented in Table 4.5 reveals that FSR outperforms TF and LRTV in recovering HR images providing the highest SSIM, PSNR, ISNR, and IFC and the lowest MMSE scores. However, the three proposed methods present better results than classical bicubic and cubic interpolation. These results further appear on the axial slices of Figure 4.13 where the recovered HR images by FSR (Fig.4.13(c)) from the LR (Fig.4.13(b))

are closer to the ground truth (HR) than other methods and show better defined boundaries between GM, WM, and CSF. Furthermore, SSIM index and Dice coefficient computed for the brain tissues with respect to the segmentation of the HR ground truth image support the previous results. For Scans 1 and 3, FSR provided the best similarity with the HR segmentation, while LRTV was better for Scan2. These results also show that the volumes recovered by TF method and LRTV method provide almost equivalent results in comparison to the ground truth with TF being faster and more efficient in HR image recovery compared to LRTV (Table 4.5).

In the same context, learning-based results addressed in Table 4.6 reveal an out-performance of the 3D ReCNN over the CNNIL in 2D and 3D and spline interpolation. It is also worth mentioning that spline interpolation is a strong baseline method with very close results to the ReCNN and CNNIL. While the qualitative inspection of images recovered by different learning-based methods in Figure 4.14 show similar performance, with well defined structures, compared to the LR images, spline interpolated images came out more blurry. To further assess these super-resolved images, the SSIM and Dice coefficient of their segmentation were the highest using ReCNN. In most cases, values computed from ReCNN and CNNIL recovered images were very close.

Qualitative analysis of segmentation results of Figure 4.15 confirms that SR has provided regions with borders that are better defined, with more confident mapping of the tissues and less partial volume effect, compared to LR segmentations. This may lead to an underestimation of the gray matter, and inversely to an overestimation of the white matter, in this region. The texture of the GM region also appears smoother in Figure 4.15(d) compared to Figure 4.15(c).

Experimental results on the native volumes, that are considered as LR in this case, show the enhancement provided by SR to the quality of the images. The close up inspection in Figures 4.16 and 4.17 reveals sharper images using FSR (Figure4.16(b)), ReCNN (Figure 4.17(b)), and CNNIL-2D (Figure 4.17(c)). Moreover, qualitative assessment of the 7T-like generated images showed that the 7T synthesis method provided additional information in the images, barely visible in 3T data. The comparison to the native 3T images in Figure 4.18 revealed the power of the 7T images in contrast enhancement. In order to show the importance of having high quality images for better brain tissue segmentation, Table 4.10 demonstrates the absolute volume difference computed from the volumes

provided in Table 4.9 for GM, WM and CSF with respect to the MS. While the segmentation of native images presents a big difference with the MS, this difference decreased significantly after SR. FSR and LRTV provided the best enhancement for model-based methods, while 7T synthesized images clearly enhanced WM and CSF segmentation compared to ReCNN with CNNIL-2D presenting some competitive results. Classical interpolation methods did not show any improvement with respect to the segmentation.

Finally, another comparison could be done regarding the methods evaluated which is 2D SR versus 3D SR. In what we have presented, FSR, CNNIL-2D, and bicubic interpolation upscales the LR images along two axes only, while TF, LRTV, ReCNN, CNNIL-3D, cubic interpolation, and spline interpolation perform the SR task along the three axes. Similar to what has been reported in [128], 2D SR methods show higher IFC values compared to 3D SR. Moreover, CNNIL-2D has slightly better performance than CNNIL-3D since the 3D SR task is harder than the 2D one. For all the quantified metrics, FSR was better than CNNIL-2D and bicubic interpolation, and ReCNN was the best among the other 3D methods.

4.8   Conclusion

To conclude, several SR approaches exist for MR image enhancement classified herein as model-based and learning-based methods. Our objective was then to study the effect of image SR on brain tissue segmentation. Qualitative and quantitative results on simulated LR data show that the segmentations of the recovered images was closer to the ground truth (MS). Using classical interpolation did not provide results as promising as SR methods. The practical application of SR on native data and the computation of tissue volumes revealed that the segmentation of enhanced images were closer to the MS performed by an expert than that of the native images. This demonstrates the importance of using SR in future morphometric analysis for the study of cerebral aging. 7T-like image synthesis out of 3T images revealed a great enhancement in the contrast between brain tissues. However, we believe that this method could provide better results if the network was trained using 3T/7T pairs of

marmoset brain images. With the possibility of having few pairs of 3T/7T marmoset brain images, one may also consider transfer learning where we would train the network on human brain images and fine-tune it with the marmoset brain images to compare the results. Although the evaluation on synthetic LR data remains a limited approach to quantify the effect of SR on real MR data, acquiring LR/HR pairs is a challenging task. Moreover, while learning-based methods learn the mapping from the LR space to the HR space of a given dataset, model-based methods depend on the accurate choice of the PSF kernel, which can affect the SR results.

In the following chapter, we will introduce the longitudinal segmentation and analysis scheme of the marmoset brain for the detection of cerebral aging biomarkers. Based on the results of this chapter, we will further compare the longitudinal analysis using native data to that using super-resolved images using the 2D FSR and the 3D ReCNN.

CHAPTER 5

Longitudinal Segmentation and Analysis of Marmoset MR Brain Images for the Detection of Cerebral Aging Markers

Contents

5.1 Introduction

When studying anatomical changes in the brain for a given population, the high heterogeneity within individuals limits the accuracy of detecting variations related to age. Therefore, a cross-sectional analysis, where one measurement per individual is only available, remains sub-optimal since the data is

analyzed individually. In this context, longitudinal studies, with repeated scans of the same individual over his course of life, provide an alternative scheme that considers intra-individual variability reflecting the possible changes in brain structures of an individual. This chapter will start with an overview of the volumetric brain changes reported in the literature for the human brain. Then, we will present a framework developed and adapted for the longitudinal segmentation of the marmoset brain. We will model trajectories of volumetric GM and WM changes with age and the whole brain volume considered as the sum of the gray and white matter volumes, thus excluding the brain-stem and both intra- (ventricles) and extra-cerebral CSF. Moreover, we will conduct the VBM analysis for the statistical estimation of local changes in GM and WM between different scans with age. We will also compare the analysis performed on native images with that performed on super-resolved images using the model-based FSR method and the learning-based ReCNN method proved efficient in Chapter 4. Finally, we will compare the findings related to the marmoset brain aging with those reported for the human brain to assess the homology of the aging process between the two species.

5.2   Aging of the human brain: a state-of-the art

The normal aging process is thought to be accompanied by several structural changes in the brain. Thus, a better understanding of the markers of normal aging helps to distinguish it from possible pathologies and diseases occurring with the aging process. Several cross-sectional and longitudinal studies have investigated the normal brain aging providing trajectories of volumetric (global and local; subcortical and cortical), microstructural, and focal (presence of microbleeds, lacunar or cortical infarcts) markers in aging [202]. In this section, we will focus on the reported volumetric changes of GM and WM in the human brain with age since these regions are the main scope of the marmoset brain study. We will thus exclude the CSF in our study since it is over-estimated with the skull on the T_1-weighted images of the marmoset brain.

5.2.1 Changes in GM volume

5.2.1.1 Global effects of age

The study of GM volume through life can reveal brain networks undergoing GM tissue loss as a result of aging. Indeed, there is an expected age-related reduction in gray matter volume in specific brain regions, which is thought to arise from cortical neuronal degeneration and synaptic density reduction [11]. Different studies have investigated GM changes in distinct age groups and modeled the trajectory of these volumetric changes. In the cross-sectional study performed by Good et al. [6], using MR scans of 465 normal adult human brains with an age range between 17 and 79 years, a linear decline of global GM volume was noted (Figure 5.1(a)). On the other hand, Sowell et al. [203] reported a significant quadratic (non-linear) decrease of the total GM volume (Figure 5.1(b)) on a population of 176 normal individuals with age ranging from 7 to 87 years old. In their study, a significant nonlinear decline in GM density with age was observed over dorsal frontal and parietal association cortices on both the lateral and inter-hemispheric surfaces. Age effects were inverted in the left posterior temporal region, where GM density gain continued up to age 30 and then rapidly declined [203]. In the study of tissue volume differences in older age, Fotenos et al. [204] examined a population of 370 adults (aged 18–97 years) including 79 elders followed longitudinally for an average of 1.8 years. They compared cross-sectional and longitudinal head-size corrected whole brain measures and found that among non-demented adults the GM volume decreased non-linearly (with a quadratic fit) from an early age at about 0.45% per year although exact differences varied by brain region (frontal being greatest) and tissue type. Their study confirmed that volume reductions begin relatively early in adulthood and tend to accelerate with age. In one of the most recent and largest studies conducted, Coupé et al. [205] performed a cross-sectional study with a total of 2944 subjects, with age ranging from 9 months to older than 94 years. Instead of using linear or low order polynomial models for volumetric trajectories, they used combinations of cumulative exponential functions to enable the modelling of rapid growth and complex degenerative processes which is another factor limited in the previous studies. They observed a 4-stage evolution in global absolute GM volume: fast growth until $8-10$ years, a fast decrease until the age of 40 years, a plateau, and an accelerated

decrease around 80 years (Figure 5.3). The longitudinal study by Lebel et al. [206] of 103 individuals scanned at least twice across ages 5–32 years reported a linearly decrease in total gray matter volume (Figure 5.1(c)) across this age span. Moreover, a recent longitudinal investigation of GM changes in later stages of life [202] was performed with a total of 5286 MRI scans with age ranging from 45 to 95 years, with an average of 2 scans per individual, with a mean interval between MRI scans of 3.3 years, and with an average follow-up time of 5.2 years. They reported a non-linear decrease of GM volume with age (Figure 5.1(d)). However, after approximately the age of 50–55 years, GM volume showed a more linear decrease with age with a relative decrease in frontal, occipital and parietal lobes.

5.2.1.2 Voxel-wise effects of age

Several studies have also reported the voxel-wise linear regression of age, i.e. the VBM analysis, on the GM volume maps. For instance, Good et al. [6] found a relative accelerated loss of GM volume in the superior parietal gyri, pre-and postcentral gyri, insula/frontal operculum, right cerebellum and anterior cingulate. In a study on 29 individuals of similar age range, i.e. between 23 and 84 years, Bergfield et al. [207] identified an extensive GM reduction in bilateral dorsolateral and medial frontal, anterior cingulate, insula/perisylvian, precuneus, parietotemporal, and caudate regions. However regions of relative GM preservation were also identified including the bilateral cerebellum, thalamus, putamen, mid cingulate, and temporal pole regions. Raz et al. [208] investigated the regional heterogeneity of gray matter differences across the life span in a longitudinal study of 127 participants ranging from 31 to 83 years of age. Manual measurements of structures revealed substantial volume declines in caudate nucleus and cerebellum gray matter, moderate declines in hippocampus, lateral prefrontal cortex, orbitofrontal cortex, inferior temporal cortex, and inferior parietal cortex, and smaller but still significant declines in entorhinal cortex. They found no significant age-related differences in primary visual cortex gray matter. Further, volume losses in the hippocampus, entorhinal cortex, and inferior temporal cortex increased with advancing age. Moreover, Ramanoel et al. [209] studied the GM differences between two groups: 16 adults with mean age of 41 years and 14 old aged subjects with a mean of 71 years. Results showed more GM reduction in old aged group compared to

adults in the frontal, parietal, temporal and occipital regions, as well as of the cerebellum. Giorgio et al. [210] performed the study on 66 subjects aged between 23 and 81 years to find an extensive linear negative correlation of GM volume with age in the left superior frontal gyrus (SFG), right middle frontal gyrus (MFG), left postcentral gyrus, right superior parietal lobule and right lateral occipital cortex. For most studies, results are generally in favor of a linear negative association between GM volume and age.

5.2.2 Changes in WM volume

5.2.2.1 Global effects of age

While extensive researches have been conducted to understand the volumetric trajectory of GM change through the lifespan, relatively fewer studies exist for analyzing the impact of aging on WM volume [11]. For instance, the study performed by Good et al. [6] did not find any significant decline in the WM volume with age ranging between 17 and 79 years (Figure 5.2 (a)). On the other hand, Sowell et al. [203] reported a quadratic effect of age on WM volume, where the the WM volume peaked at age 43 years and declined thereafter (Figure 5.2 (b)). The longitudinal studies of Fotenos et al. [204] and Raz et al. [208] examining difference in regional WM volume found significant age-related volume losses in prefrontal and inferior parietal WM and demonstrated that prefrontal white matter volume loss tended to accelerate with greater age. In the same context, the longitudinal study of Lebel et al. [206] showed a significant quadratic increase in WM volume across the age range of 5–32 years (Figure 5.2 (c)). For the age range of $45 - 95$ years, Vinke et al. [202] showed a spline non-linear decrease in the WM volume with an accelerated change after approximately age $50 - 55$ years (Figure 5.2 (d)). In the study of Coupé et al. [205], which analysed a high number of subjects with a wide age range and more complex models, the authors reported a fast non-linear increase of WM volume until a peak around $30 - 40$ years, followed by a decrease, at a slower rate (Figure 5.3).

5.2.2.2 Voxel-wise effects of age

Similar to the global effects study of WM, fewer studies exist on the linear correlation between WM volume and age using T1-weighted images. Good et al. [6] reported areas of accelerated WM loss in

the frontal WM, optic radiations, and posterior limbs of internal capsule while other areas exhibited a preservation of WM volume such as the posterior central lobe, cerebellum, and right temporal lobe. However, Giorgio et al. [210] found a linear negative correlation of WM volume with age in the anterior thalamic radiations, anterior limb of the internal capsule (ALIC), cerebral peduncle (CP), cerebellum and bilaterally in the external capsule (EC) with no significant linear positive correlation between WM volumes and age. On the other hand, Smith et al. [4] reported no significant global WM volume loss with old ages ranging between 58 and 95 years. In the group compariosn of older subjects (mean age 68 years) to younger ones (mean age 27 yrs), Farokhian et al. [211] observed significant WM increases in the pericentral and occipital areas among older subjects, and an age-related decline in the WM volume in the thalamic radiations.

5.2.3 Summary

The differences in volumetric trajectories and voxel-based studies reported in the literature make it hard to acknowledge a consistent developmental trajectory for the brain volumes. One of the differences appears in the restricted and distinct life periods of the analyzed subjects. Consequently, this makes it difficult to compare the results and limits the global understanding of brain modifications during the entire life span. Moreover, the use of a limited number of scans, especially in certain age ranges, produces less reliable results. Finally, the acquisition protocols and methods used in imaging processing, namely segmentation and volumetric measurements, can also lead to the disagreement between researchers [205].
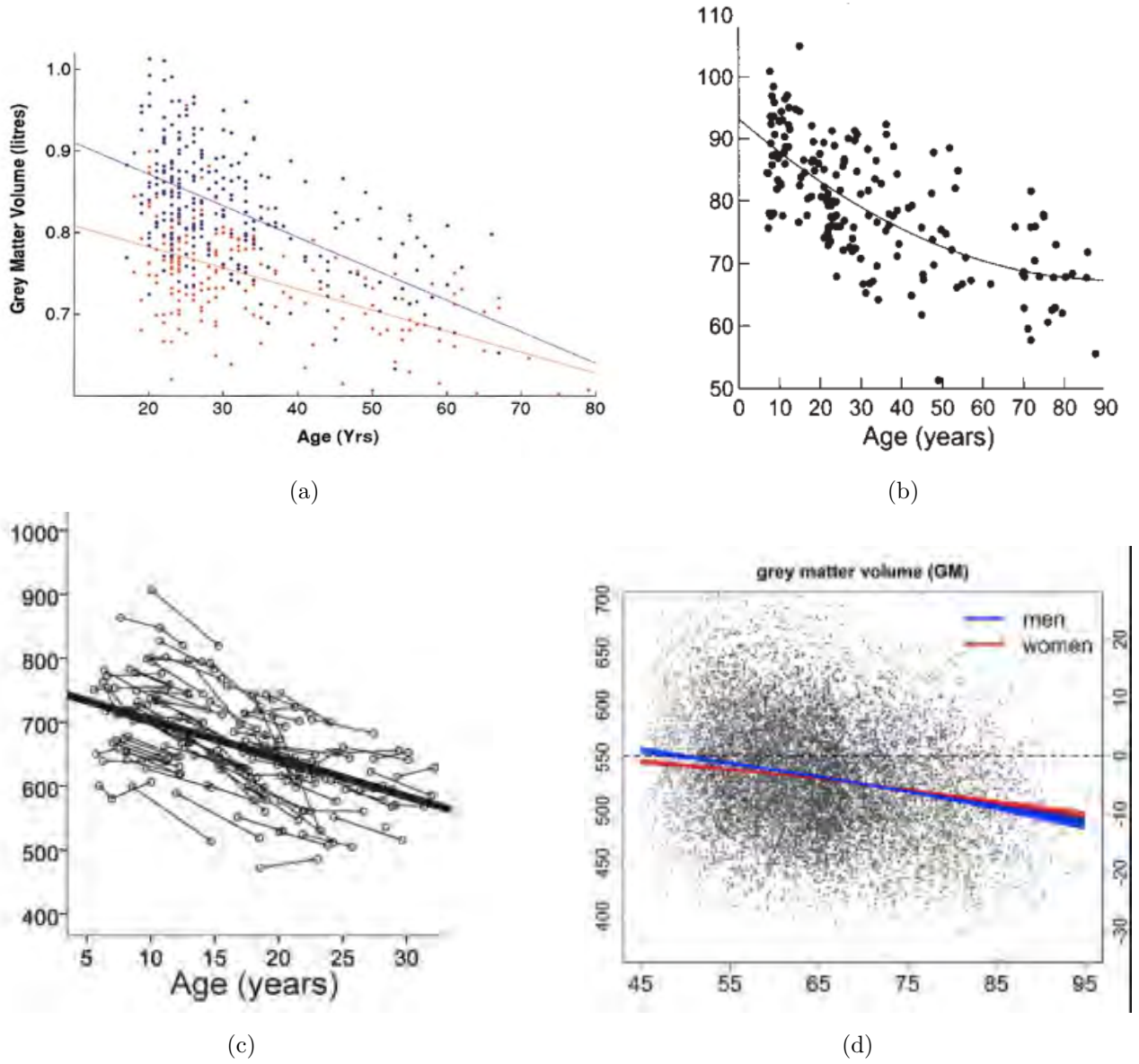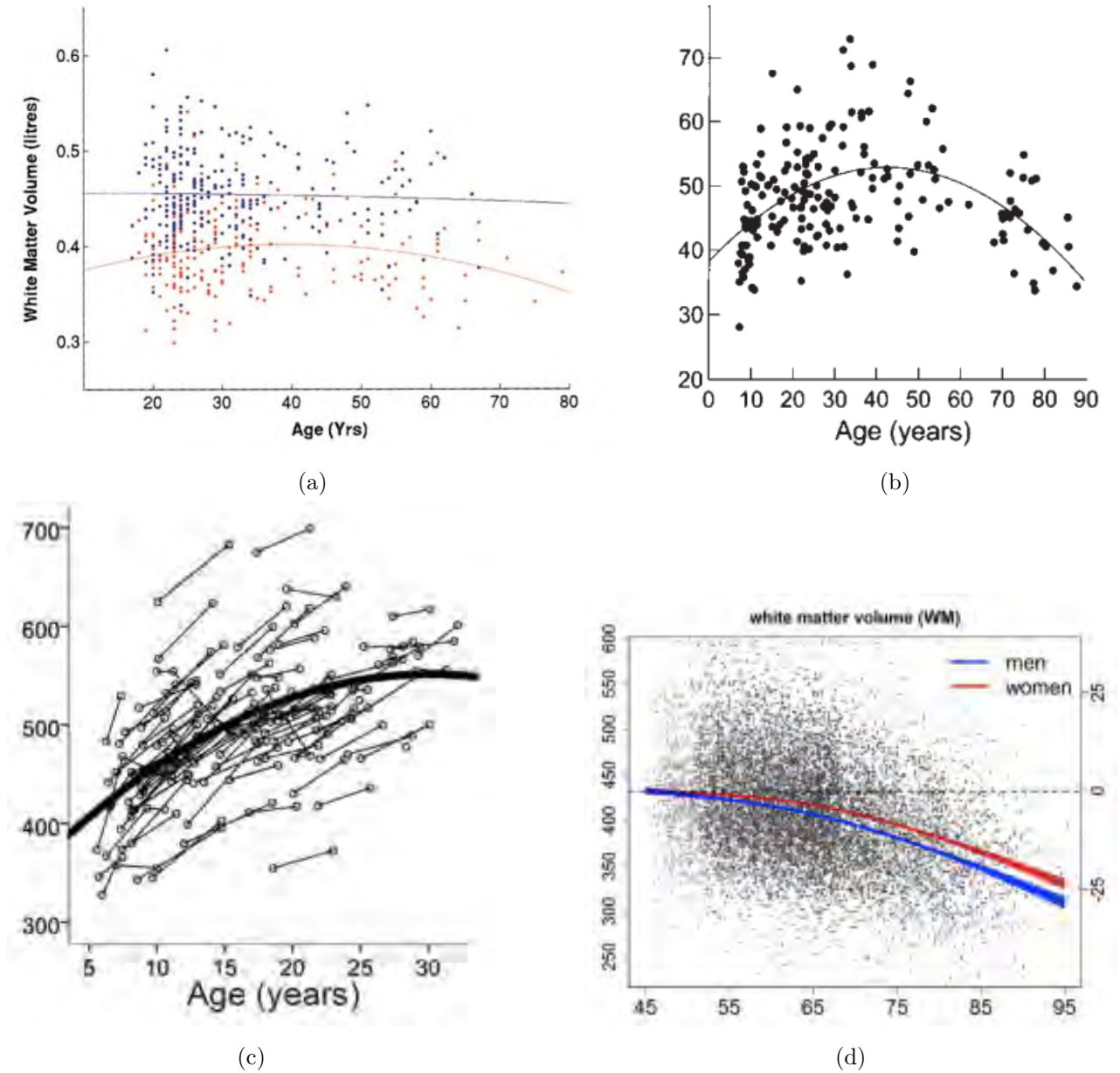
(a)

(b)

(c)

(d)

Figure 5.1:   Different volumetric trajectory of GM with age as reported by (a) Good et al. [6] for men (blue line) and women (red line), (b) Sowell et al. [203], (c) Lebel et al. [206], and (d) Vinke et al. [202] where measurements from the same participant are shown in 3 shades of gray. The x-axis represents the age in years, and the y-axis is the total GM volume in liters for (a), mm^3 for (b), and cm^3 for (c) and (d).

(a)

(b)

(c)

(d)

Figure 5.2:   Different volumetric trajectory of WM with age as reported by (a) Good et al. [6] for men (blue line) and women (red line), (b) Sowell et al. [203], (c) Lebel et al. [206], and (d) Vinke et al. [202] where measurements from the same participant are shown in 3 shades of gray. The x-axis represents the age in years, and the y-axis is the total WM volume in liters for (a), mm^3 for (b), and cm^3 for (c) and (d).
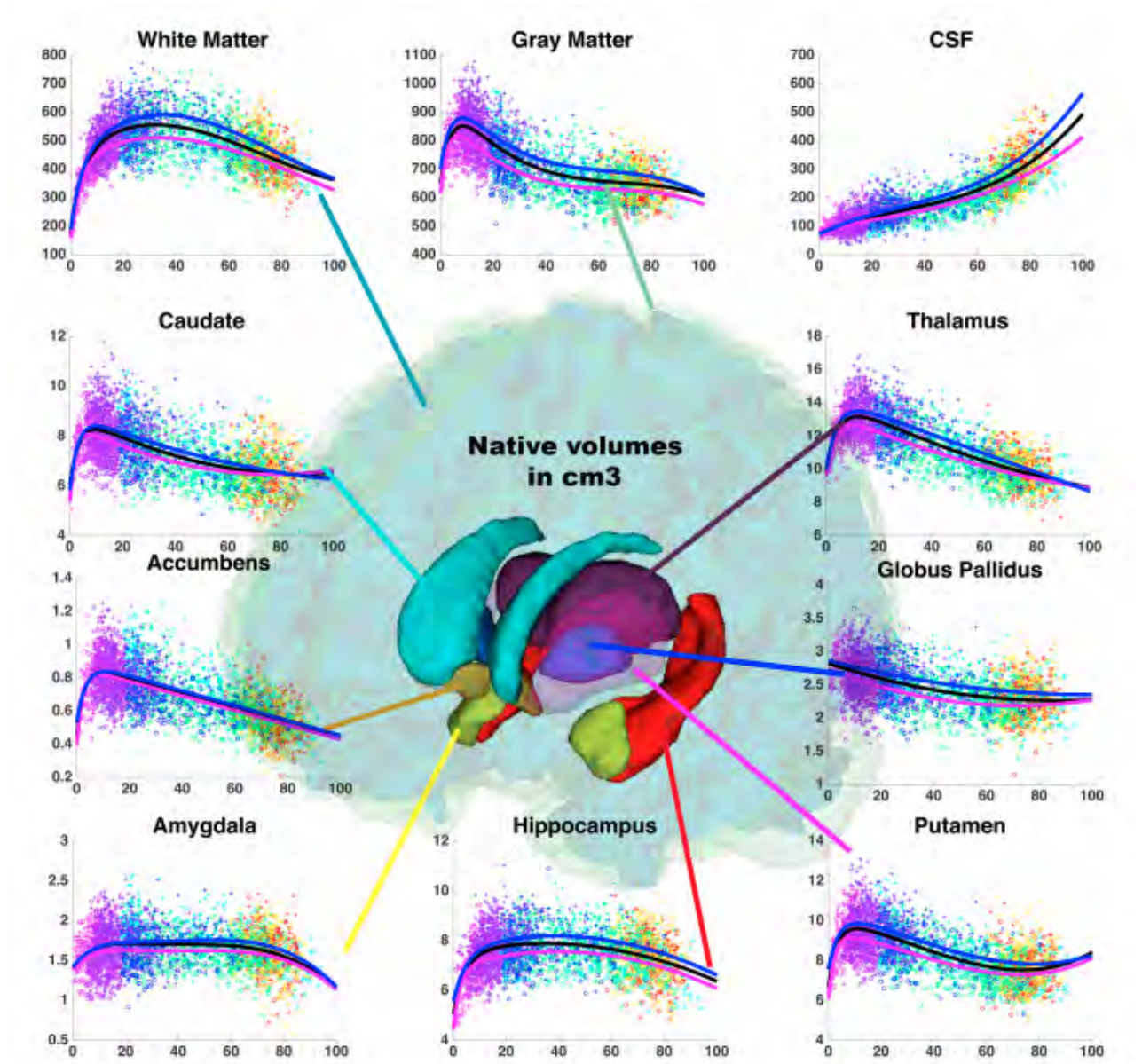
Figure 5.3: Volume trajectories based on absolute volume in cm^3 (y-axis) with age (x-axis) for brain tissues and subcortical structures across the entire lifespan as appeared in the study of Coupé et al. [205], estimated on 2944 subjects from 9 months to 94 years. Male and female models are presented in blue and magenta while the general model is shown in black. Colored dots represent the different datasets used in there study. Figure was extracted from [205].

5.3   Longitudinal segmentation of the marmoset brain

5.3.1   The marmosets

A total of 42 marmoset animals (21 males, 21 females, minimum age = 2.59 years, maximum age = 14.71 years) were used in this study. The marmosets were bred in CerCo (agreement $B3155501$ from Haute Garonne Prefecture, France), housed in pairs or small groups, and maintained in a $12:12$ h light–dark cycle. Food and water were withdrawn from the cages in the morning preceding the imaging session. All imaging sessions were conducted in the afternoons, between 1 and 5 pm. During the MRI acquisition session of a typical duration of about $36 - 37$ minutes, the animals were anesthetized with Alphaxalone (i.m., 1.85 ml/kg Alfaxan, 10 mg/ml, Jurox, Worcestershire, UK). Peripheral oxygen saturation (SpO_2), heart and respiratory rates were constantly monitored during the image acquisition. All experimental procedures were conform to Directive 2010/63/EU and were carried out according to the National Committee for Ethical Reflection on Animal Testing. The project received the regional ($MP/03/76/11/12$) and the governmental authorizations from the MENESR (project #05215.03) [196].

5.3.2   MRI acquisition

The brains of the 42 marmosets were scanned, and structural T_1-weighted MR images were acquired using a Philips MRI scanner dedicated to human and animal research at a field strength of 3T. A 3D gradient-echo sequence was used with $T_R = 10.5$ $msec$, $T_E = 4.7$ $msec$, flip angle of 8°, isotropic resolution of 0.35 mm, and size of $288 \times 288 \times 113$ voxels. Images were acquired with an antero-posterior (AP) encoding direction, and the sagittal plane was chosen to avoid fold over effects. Images were obtained with an 8-channel receiving human wrist coil (6.5 cm internal diameter) [196]. A total of 185 T_1-weighted scans were obtained with an average of 5 scans (± 3) per individual at different ages of their life span.

5.3.3 Longitudinal processing pipeline

The proposed longitudinal processing method has been adapted from the longitudinal segmentation scheme of CAT12 toolbox (`www.neuro.uni-jena.de/cat/`) originally developed for the longitudinal segmentation of the human brain and integrated into SPM. More information regarding the step-by-step implementation of the steps to be explained can be found in [212] and [213]. The pipeline consists of two main steps: a cross-sectional pre-processing of all the individuals' scans and a longitudinal processing procedure including the scans of each individual.

5.3.3.1 Image pre-processing

The standard pre-processing steps are applied to each native $T1$-weighted scan N_n ($n = 1, .., 185$). Figure 5.4 summarizes the pre-processing steps followed. These steps are further detailed hereafter.

Standard reorientation During image acquisition of small animals using an MRI platform dedicated to humans, the orientation of the marmoset head is not always uniform. Therefore, all the scans were reoriented into the standard orientation space where the plane through the midline of the left and right hemispheres is the sagittal plane, the AC–PC plane is the horizontal plane, and the plane orthogonal to the horizontal plane passing through the center of the anterior commissure is the coronal plane [196]. The origin of each scan was checked and re-positioned, manually, at the anterior commissure using the display module of SPM12. This step further facilitates the registration of the scans to the template.

Noise reduction MR images are usually corrupted with random noise inherent to the acquisition process that would further affect the accuracy of the quantitative measurements of the analyzed tissues. Although noise can be reduced by averaging multiple images acquired from the same scanner on a non-moving subject, this is not a common practice since it would increase the acquisition time. Instead, different noise filters are commonly used to remove image noise without damaging image quality. Unfortunately, some filters have the drawback of removing relevant high-frequency components from the image resulting in blurred edges and introducing bias to the image. In this

context, a Spatial Adaptive Non-Local Means (SANLM) filter has been developed by Manjon et al. [214] that takes into consideration both the Rician nature of the MR data and the spatially varying noise patterns thus preserving edges while removing noise. The strength of the filter is automatically estimated based on the standard deviation of the Rician noise [178]. The SANLM filter has been integrated as a module into CAT12 toolbox where we used it directly on our scans as proposed. Figure 5.5 shows the effect of denoising on the quality of the processed images.
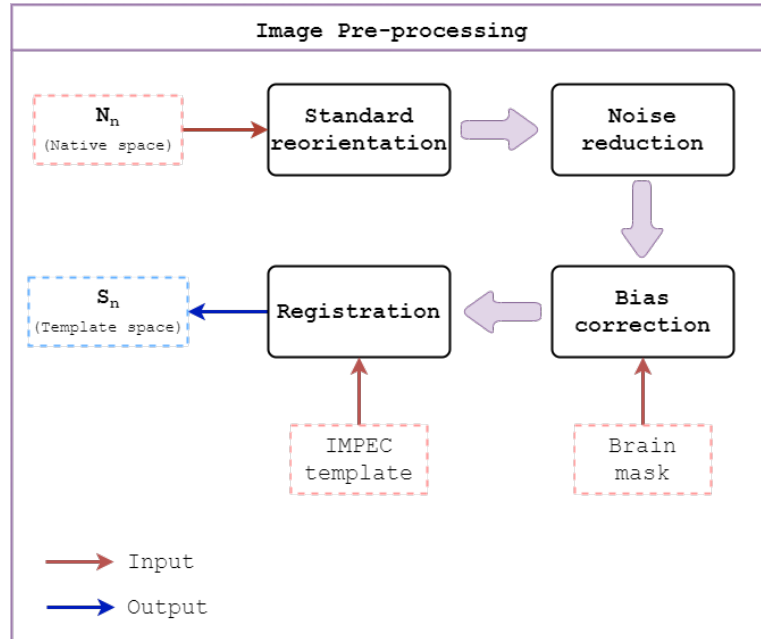
Figure 5.4: Flow diagram of the cross-sectional image pre-processing steps. All native T_1-weighted scans N_n ($n = 1, .., 185$) are checked for the standard orientation position with the origin positioned at the anterior commissure. Reoriented scans are denoised using the spatial adaptive non-local means filter module integrated into CAT12 toolbox. Denoised scans are then corrected for intensity non-uniformity using the N4ITK MRI Bias Correction module of 3D Slicer which requires a mask for the brain region. Finally, the FOV is reduced to the head region by registering the scans to the marmoset IMPEC brain template rendering all the scans in the template space using SPM12. Red arrows represent the input to each module and the blue arrow represents the output of the process.
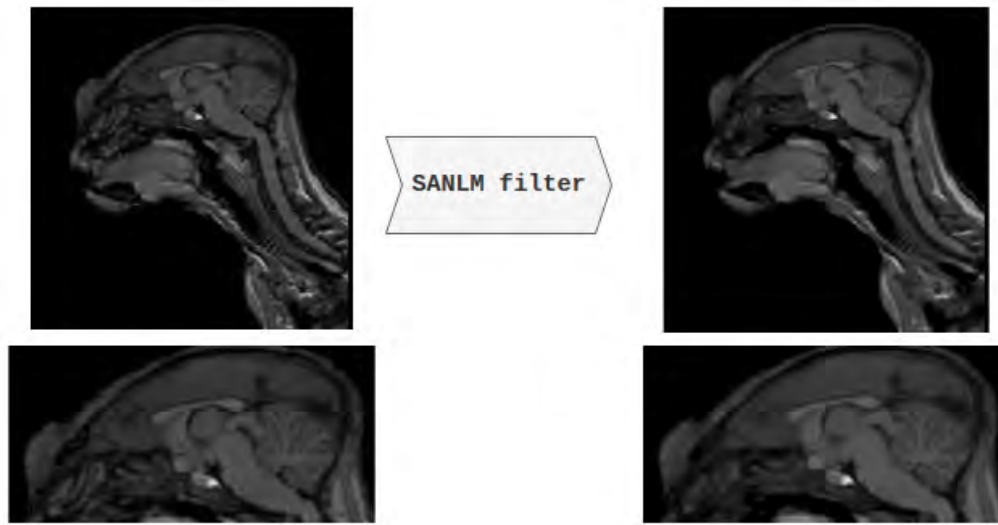
Figure 5.5: Denoising of the reoriented native scans using the SANLM filter with a close up visualization of a cropped region.

Bias field correction Intensity non-uniformity of an MR signal from a homogeneous tissue is usually due to radio frequency coil variations forming a low frequency non-uniform intensity in voxels, gradient-driven eddy currents, and patient anatomy. While non-uniformity due to the frequency response of the receiver and spatial sensitivity of the RF coils can be corrected for by regular calibration or theoretical modelling, non-uniformity due to induced currents and the spatial in-homogeneity of the excitation field depending on the subjects may be inevitable. This non-uniformity artifact, referred to as bias field, is assumed to be a smooth, slowly varying multiplicative field corrupting image intensities [215]. As an alternative to improving intensity uniformity during data acquisition, a number of post-processing methods to compensate for non-uniformity have been proposed ([215–218]) and the choice of the correction method is usually let to the user. In our study, we have used the popular N4ITK MRI Bias Correction module [219, 220] which is an implementation of the N3 algorithm [215] for the Insight Toolkit (ITK: https://itk.org/) and proven to outperform the N3 method in effectiveness and efficiency [221]. The N4 bias correction method represents an improved variant of the N3 algorithm where, at each iteration, the correction of the image is performed using the results of the previous iteration. The N4ITK module is integrated into 3D Slicer and requires a

mask image for the brain region (Figure 5.7). Bias correction of the marmoset MR images was then performed with a shrink factor of 4 and 200 iterations per scale. These values were fixed using a cross-validation study conducted on the effect of these parameters on the segmentation of corrected images. All other parameters were kept unchanged. The mask image was created by registering the complement of the fourth tissue probability map (representing structures other than GM, WM, and CSF) to the each scan using the coregistration module in SPM12.
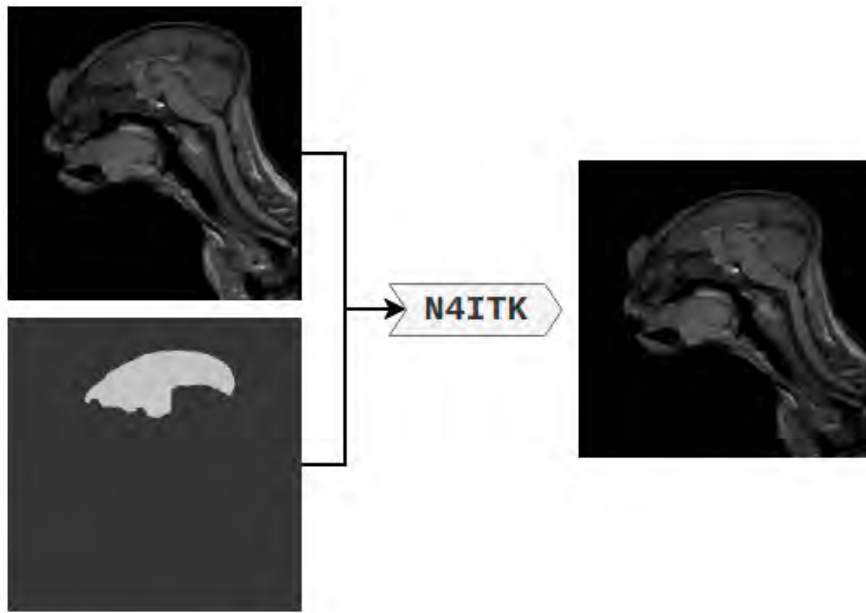
Figure 5.6: Bias correction of the acquired scans using the N4ITK module of 3D Slicer. Although the effect of the correction is not visually clear, its impact appears in the segmentation of the brain.

Image registration   The registration procedure, previously detailed in Chapter 4, was also performed here. To recall, the reduction of FOV to the head region only was achieved by the rigid registration (using SPM) of the MR scans to the T_1-weighted marmoset brain template (IMPEC template) that have been previously developed by Risser et al. [196], reducing the residual positional variability between scans. Figure 5.7 shows a sagittal slice before and after registration. The registration step is important to guarantee that all the scans are in the template space and to correct any misalignment in the head position between scans. This inverse consistent rigid registration, with 6

degrees of freedom ensures inverse consistency, keeping individual registrations unbiased and reducing the influence of outlier regions. This results in highly accurate brain registrations, even in the presence of local differences, such as lesions and skull artifacts [222].
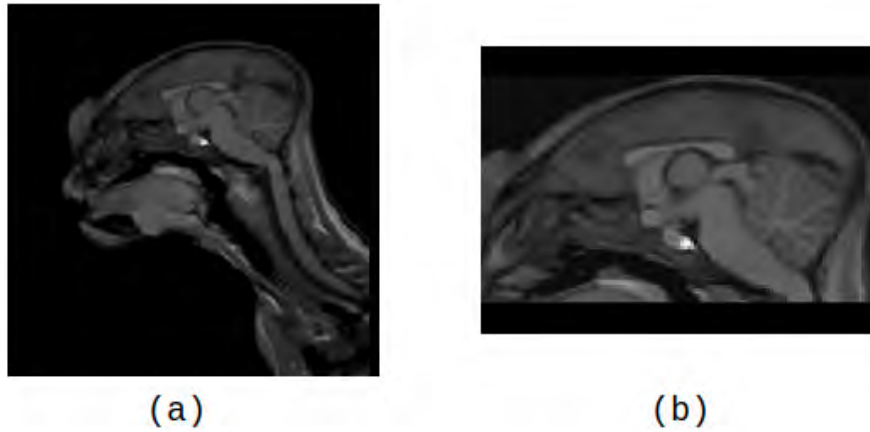

Figure 5.7: Registering the pre-processed scans to the brain template reduces the FOV to the head only and ensures a correct alignment between scans. The figure shows a sagittal slice (a) before and (b) after the registration step.

5.3.3.2   Longitudinal segmentation

The longitudinal segmentation pipeline is summarized in Figure 5.8. Since each individual marmoset has been scanned several times throughout its life span, $S_{i,j}$ represents the scan from time point i $(i = (1, .., I))$ of the marmoset j $(j = (1, 2, ..., J))$, where I is the total number of scans per individual and J is the total number of individuals (42 in our study).

Intra-subject realignment   Intra-subject realignment is used for motion correction and averaging of several intra-session scans to increase the signal to noise ratio while accurately aligning longitudinal image data [222]. A time-series of images acquired for the same individual, and previously registered to the IMPEC template in the pre-processing step, are realigned using a least-squares approach and a 6 parameters (rigid body) spatial transformation. During this period, a mean image of the realigned images is created and updated iteratively until convergence. This mean image is considered as the
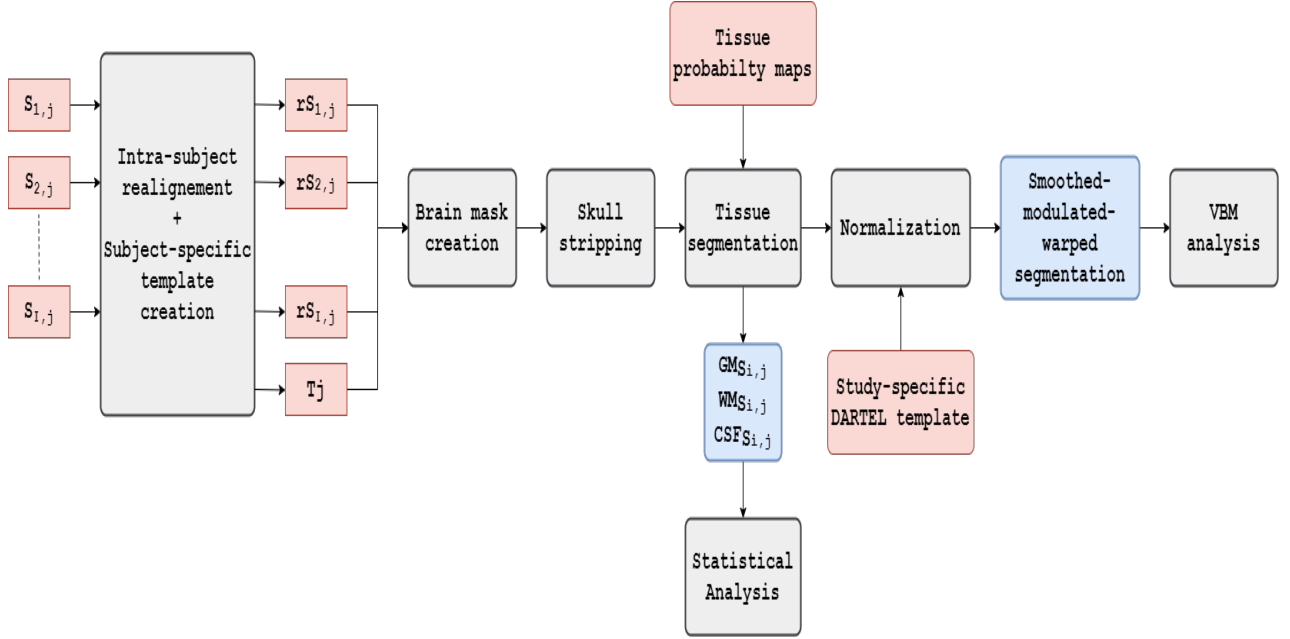
Figure 5.8: The longitudinal segmentation pipeline used for the segmentation of the marmoset brain. Intra-rigid realignment of all the time points $(S_{1,j}, S_{2,j}, ..., S_{I,j})$ of a given subject results in the creation of re-aligned scans $(rS_{1,j}, rS_{2,j}, ..., rS_{I,j})$ and a subject specific template (T_j). A brain mask is then created from the re-aligned scans and the template T_j and further used for skull stripping of all the individual's images. Skull-stripped scans and template are now segmented individually using tissue probability maps in SPM12 into $GM_{S_{i,j}}$, $WM_{S_{i,j}}$, and $CSF_{S_{i,j}}$. These segmentations are used in the statistical analysis to model the volumetric trajectories of the brain tissues. Next, deformation fields are estimated from the segmentation of the subject-specific template then applied to the segmentation of the scans. This results in smoothed, modulated and warped segmentations that are ready for the VBM analysis $(smwGM_{S_{i,j}}, smwWM_{S_{i,j}}, smwCSF_{S_{i,j}})$. Red boxes represent the input for each stage and blue boxes represent the output expected from each stage.

subject-specific template (T) in our study. All the realigned images undergo equivalent processing steps. This process was performed using the 'Realign: Estimate & Reslice' batch of VBM8 module integrated into SPM12. The only parameter that we changed is the separation (in mm) between the points sampled where we set it to 0.4 since the voxel size of our MR data is 0.35 mm^3. All other parameters were kept to their default values as changing them did not bring any additional difference

to the results.

Brain mask creation and skull stripping   For an accurate segmentation of MR images, it is necessary to process the marmoset brain without its surrounding skull and head regions. A brain mask for skull stripping has been created for each individual by registering each of its scans, including the mean image, to the marmoset MRI standard brain template (`https://brainatlas.brain.riken.jp/marmoset/modules/xoonips/detail.php?id=004`) created by Hikishima et al. [142] since it includes all the marmoset brain regions. The final mask is constructed as the union of the registered brain masks across time, i.e. a voxel is included in the brain mask if it is included in any time point [159]. Skull stripping of all the time points and the mean image is finally performed using the final brain mask.

Tissue segmentation   Brain tissue segmentation into GM, WM and CSF was performed using the 'New Segment' module of SPM12. Basics of SPM tissue classification and segmentation were already explained in chapters 2 and 3. For the optimal performance of the SPM segmentation module, the voxel size of the marmoset MR images were first multiplied by five following the work in [141]. Tissue probability maps, which were created from the DARTEL template of 43 marmoset segmented brains, were used to initialize the segmentation of all the scans. To recall from Chapter 4, a DARTEL template for each tissue class is created by rigidly aligning and averaging gray, white and CSF images. While the 'New Segment' module requires 6 tissue probability priors for the segmentation task (GM, WM, CSF, skull, head, and other outside regions), only 4 of these priors are available for the marmoset brain, i.e. GM, WM, CSF, and other regions. Accordingly, the segmentation batch was modified to accept 4 priors instead of 6. Moreover, since we had performed bias field correction as a pre-processing step, we applied a very light bias regularization, with a bias FWHM of 30mm cutoff. After the segmentation is complete, images of GM, WM, and CSF are generated for each scan with the prefix $c1, c2$, and $c3$ respectively. Additionally, for the segmentation of the subject-specific template, DARTEL imported versions of the tissue class images ($rc1, rc2$, and $rc3$) are generated, which will be used to create the study-specific template.

Study-specific template In order to be able to compare all the subject-specific longitudinal deformation trajectories, a study specific template was created to have these deformations normalized in the same common reference anatomy. To this end, the study-specific template was created from the respective segmentations of the subject-specific templates of all the individuals in the study. Similar to the DARTEL template constructed for the cross-sectional study described in Chapter 4, the study-specific template was built using the imported segmentation images ($rc1, rc2$, and $rc3$) of all the subject-specific templates available. All parameters were kept to their default values. At the end of this step, a DARTEL template (study-specific) is created, along with a DARTEL flow field (a file named u_rc1) for each subject which encodes the deformations that warps (maps) each subject-specific template to the study-specific template (see Figure 5.9).

Normalization In order to compare data from several scans and /or subjects, all the brain images have to be in the same 3D space. In SPM this is accomplished by normalizing the images into a standard space, i.e. warping a native space anatomical image into standard space. The normalization step was performed using the 'Normalize to MNI Space' batch in DARTEL tools of SPM12. This mainly requires a DARTEL template (which is the study-specific template in our case), the flow field image of each individual created during the construction of the study-specific template, and the segmentation images of all time points of a given subject. The voxel size of the loaded images was $(1.56, 2, 1.56)$ mm^3 and the bounding box was evaluated from the dataset in SPM12. We chose to preserve the amount of signal from each region of the spatially smoothed and normalized images, i.e. areas that are expanded during warping are correspondingly reduced in intensity. A spatial smoothing of the data before performing the statistical testing ensures that the residual differences, after fitting the model, are closer to Gaussian. This makes the data less likely to violate the assumptions required for parametric statistical testing and reduces more of the intersubject registration error. It also ensures a more conservative statistical analysis, in which fewer regions are found significantly different, thus reducing false positive or type 1 error [223]. The FWHM of the Gaussian blurring kernel in mm was thus fixed to $[10, 10, 10]$ as recommended by [212]. This value of the FWHM is reasonable in our study since we have resized the MR data to resemble the human brain volume in size. At the end of

this step, smoothed, modulated, and warped versions of the segmentation images ($smwc1, smwc2,$ and $smwc3$) are generated. These images will be further used in the VBM analysis that compares, in a voxel-by-voxel analysis, the volume of a tissue among population of subjects [223].

Global Statistical Analysis Using the tissue segmentation results, the mixed-effects modelling [224] was employed to estimate volume trajectories of GM, WM and total brain volume (GM plus WM). This analysis method allows an estimation of the fixed effects of measured variables on volume change, while incorporating the longitudinal nature of the data by including within-person variation as nested random effects [225]. We performed the trajectory estimation of brain tissues' changes using the linear model given as:

$$Volume = Intercept + \alpha * age \tag{5.1}$$

where α is the constant term defining the effects of each fixed term [225]. All computations were performed in *R version 3.6.3.*

VBM analysis Age related GM and WM changes were evaluated for the smoothed, modulated and warped segmentation images of all the individuals scan (total of 185 scans). Since we are performing a longitudinal analysis of the brain with multiple scans per individual, the most suitable design model was the flexible factorial analysis [213]. Sex, gender, and total intracranial volume (GM+WM+CSF) were included as covariates of the regression model. We computed t-statistics for each model and evaluated longitudinal increase and decrease in regional brain volume with age. Results were limited to areas with a tissue prior probability greater than 0.2. For each tissue brain (GM or WM), a corresponding mask was applied to determine which voxels to be included in the analysis.
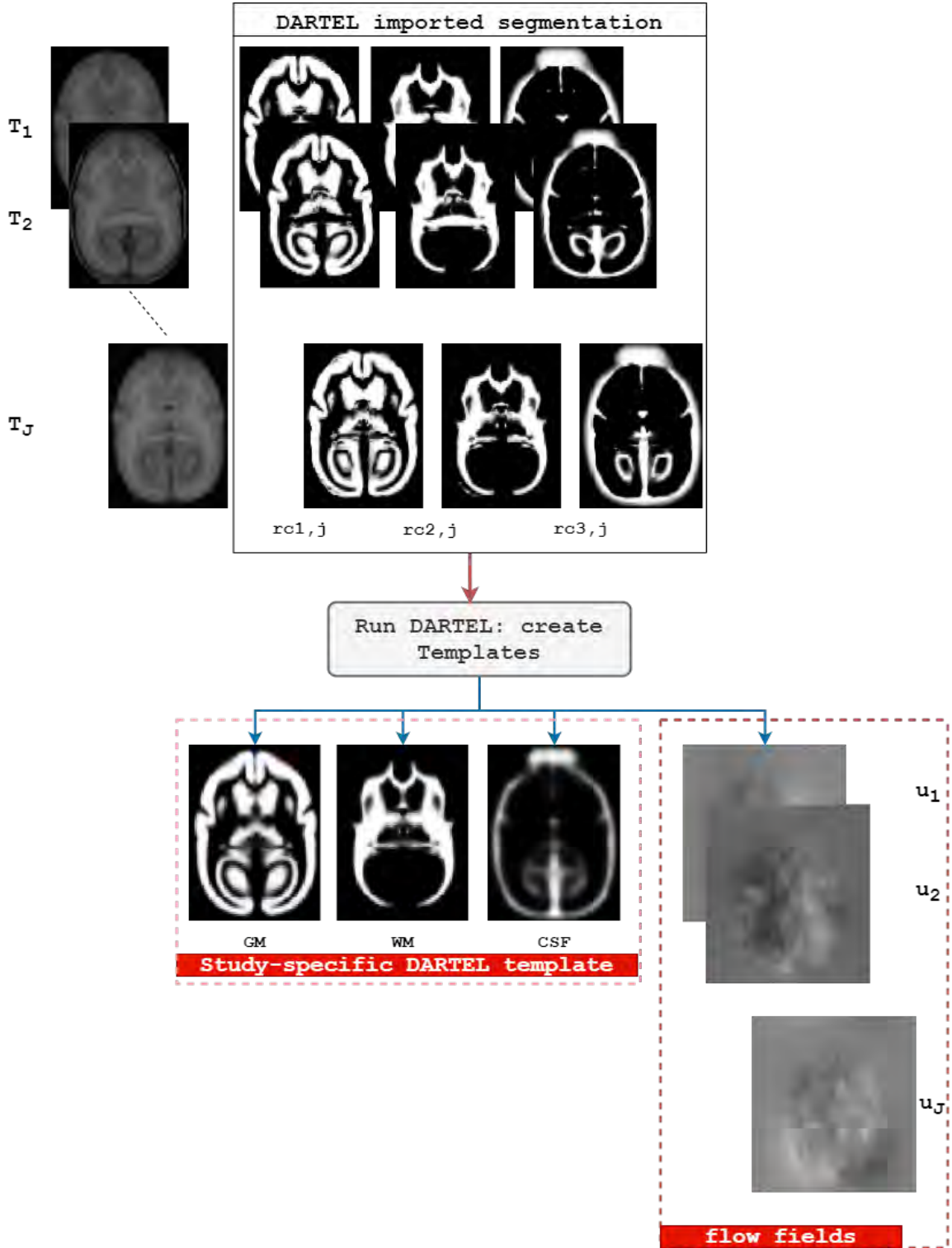
Figure 5.9: Creation the study-specific template. The imported segmentation images $rc1, rc2$ and $rc3$, corresponding to GM, WM, and CSF respectively, of the subject-specific templates $(T_1, T_2, .., T_J)$ of all the individuals $(j = 1, 2, .., J)$ are used to create the study-specific DARTEL template. This step results also in the formation of a deformation flow field $(u_1, u_2, .., u_J)$ for each individual.

5.4 Results and discussion

This section presents the statistical and VBM results of the longitudinal segmentation pipeline applied on the original scans and enhanced scans by SR. To elaborate, since we have shown in Chapter 4 that SR enhances the segmentation results, we further tested the effect of using super-resolved images on the statistical and VBM results. To this end, we applied the $2D$ model-based FSR method and the $3D$ learning-based ReCNN method to the output images of the pre-processing step (S_n in Figure 5.4) and compared their results to those obtained when using the original images (Figure 5.10).
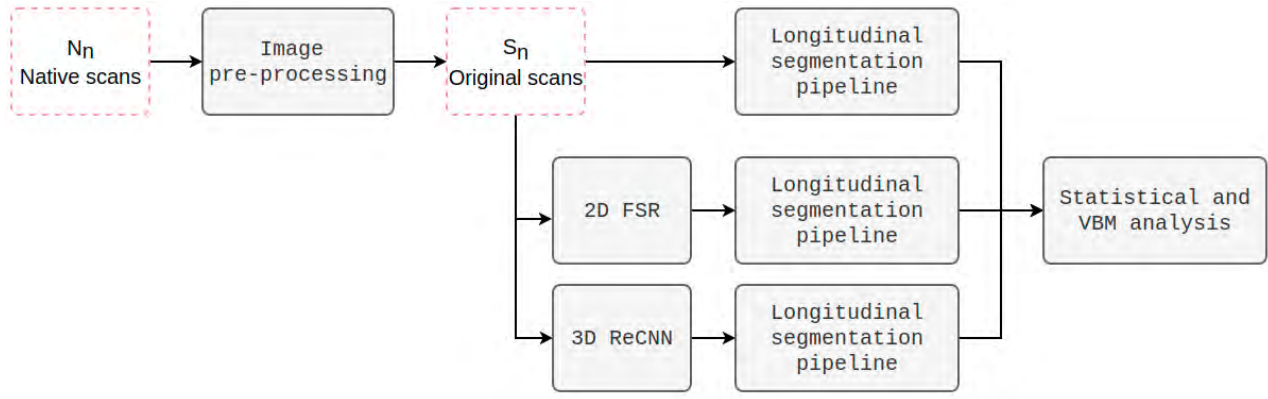

Figure 5.10: In addition to performing the longitudinal segmentation of the original images (S_n) resulting from the pre-processing step, we further applied a 2D FSR method and a 3D ReCNN method to enhance the original images. The resulting images from each SR method were then fed into the longitudinal segmentation pipeline. Finally the longitudinal segmentation results from the original scans, and the super-resolved ones by the 2 different methods were further independently analyzed.

Based on the literature, maturation of the marmoset brain occurs around 2.5 years [226] while aging starts around 8 years [227]. Three main groups were thus formed as follows for the statistical analyses of collected volume information:

- Adulthood group including all the 185 scans with age ranging from 2.5 to 14.7 years

- Young to middle adulthood group with age between 2.5 and 8 years containing 95 scans per 33

subjects

- Late adulthood group with age greater than 8 years containg 90 scans per 24 subjects

Global volume and VBM results were further assessed for each group in order to analyze the GM and WM changes per age-range. CSF results were excluded from the analysis due to the overestimation of the CSF volume from segmentation. This is mainly due to the difficulty of distinguishing CSF from the skull on T_1-weighted images, where both tissues appear dark.

5.4.1 Global statistical analysis

In what follows, we will present the global statistical analysis of the volumetric GM, WM and total brain changes in the three groups mentioned before. More precisely, we will comparatively present the linear trajectory fitted to volumes extracted from the original scans, from scans enhanced by 2D FSR, and from scans enhanced by 3D ReCNN. Models' parameters (estimated slope with 95% confidence interval) will be shown in different tables.

5.4.1.1 Adulthood group analysis

All scans available (185 MRI scans) from 42 marmosets were included in this analysis with an age range between 2.5 and 14.7 years.

Table 5.1 shows the results of modelling the GM volume trajectory using a linear model. In addition, Figure 5.11 shows the predicted linear fit to GM volumes as a function of age, computed from the segmentation of the original and the enhanced scans. Although not very steep, a linear decrease in GM volume was detected using both the original and the enhanced scans. This supports the hypothesis of a possible linear decrease in GM volume with age in the marmoset brain. Note that a similar GM decrease has been previously reported in the human brain, which favors the hypothesis of an homologous evolution of the GM between marmoset and human brains [6] (Figure 5.1 (a)).

Table 5.1: Global statistical analysis of the volumetric GM changes with age for the marmoset adulthood in the study (with age ranging from 2.5 to 14.7 years) including 185 scans. The table shows the slope and the 95% confidence interval of the linear model fitted to GM volumes.

	Tested Model	Slope	Confidence Interval
Original scans	linear	- 0.0179	[-0.0321 , -0.0034]
Enhanced scans by 2DFSR	linear	-0.0225	[-0.0358 , -0.0089]
Enhanced scans by 3DReCNN	linear	-0.0209	[-0.0359 , -0.00560]

Similarly, Table 5.2 shows the results of modelling the WM volume trajectory using a linear model. In this context, using a linear fit could not provide a significant change in WM volume when using either the segmentations from the original scans, or the segmentations from the enhanced scans (Figure 5.12). Indeed, these results may imply that either the WM volume does not linearly change with age, or the changes in WM are too small to be detected with respect to the observation scale. However, in the study of the human brain, Sowell et al. [203] (Figure 5.2 (b)) and Good et al. [6] (Figure 5.2 (a)) showed a quadratic fit for the WM trajectory with a peak around the age of 40 years.

Table 5.2: Global statistical analysis of the volumetric WM changes with age for the marmoset adulthood in the study (with age ranging from 2.5 to 14.7 years) including 185 scans. The table shows the slope and the 95% confidence interval of the linear model fitted to WM volumes.

	Tested Model	Slope	Confidence Interval
Original scans	linear	-0.0036	[- 0.0012 , 0.0055]
Enhanced scans by 2DFSR	linear	0.0023	[- 0.0045 , 0.0091]
Enhanced scans by 3DReCNN	linear	- 0.0024	[- 0.0120 , 0.0073]

Similar to GM and WM, the sum of these two volumes, considered in this study as the total brain volume, was also analysed. Consistent results of a significant linear decrease of the total volume with age was observed (Table 5.3). Results from original and enhanced scans were similar (Figure 5.13).

This is mainly due to the fact that possible errors in gray and white matter segmentation due to misclassification are now compensated when added together.

Table 5.3: Global statistical analysis of the total brain volume changes with age for the marmoset adulthood in the study (with age ranging from 2.5 to 14.7 years) including 185 scans. The table shows the slope and the 95% confidence interval of the linear model fitted to total brain (GM + WM) volumes.
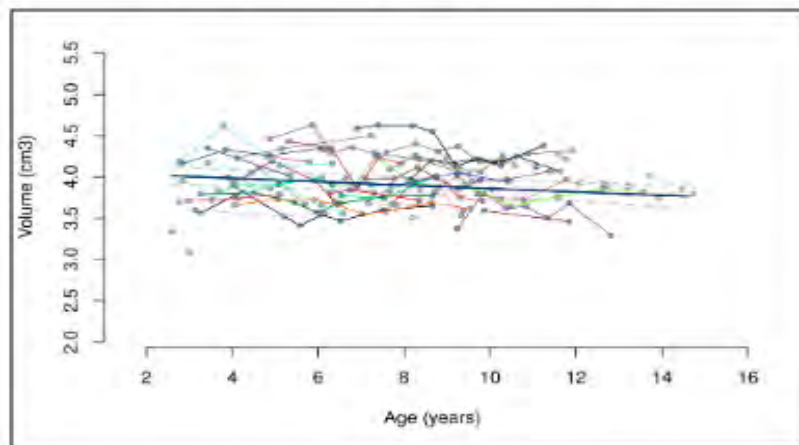
|	Tested Model	Slope	Confidence Interval
Original scans	linear	-0.0284	[- 0.0432 , - 0.0131]
Enhanced scans by 2DFSR	linear	-0.025	[- 0.0381 , - 0.0115]
Enhanced scans by 3DReCNN	linear	-0.0298	[- 0.0449 , -0.0144]
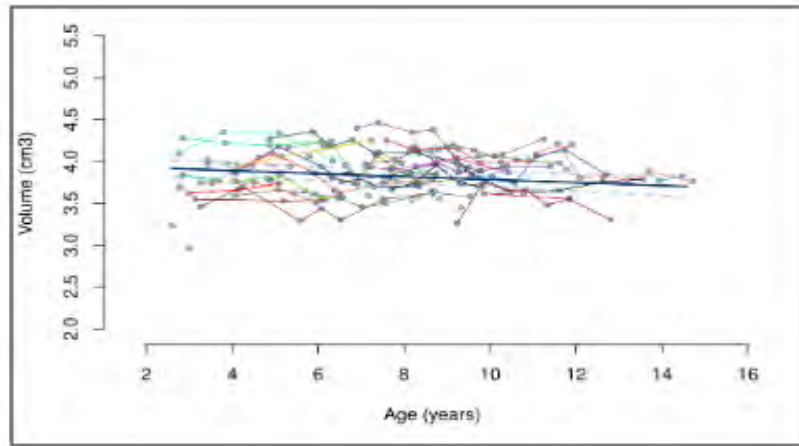
(a) GM volume: original scans
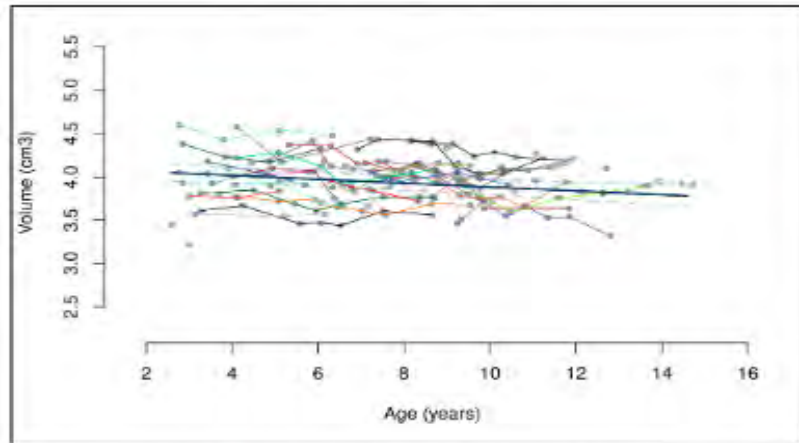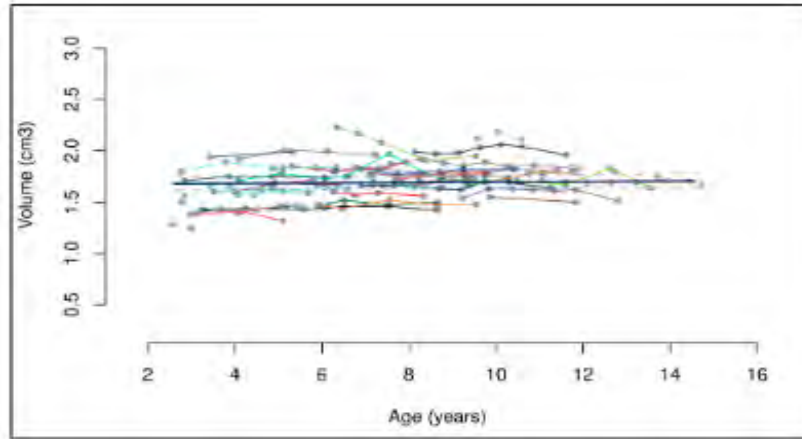

(b) GM volume: 2DFSR enhanced scans

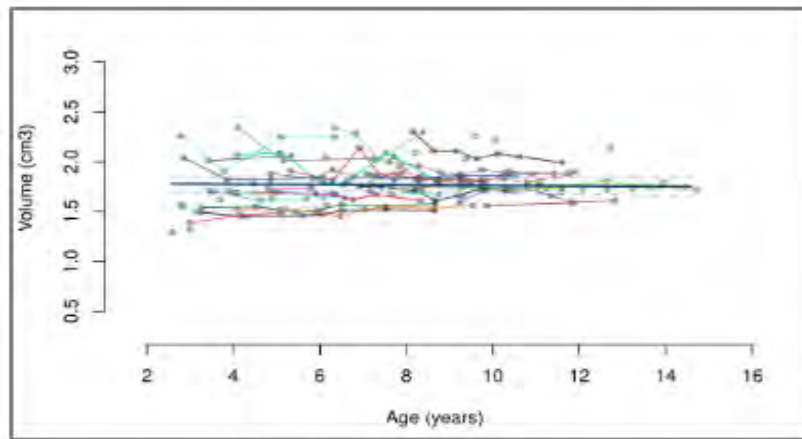(c) GM volume: 3DReCNN enhanced scans

Figure 5.11: GM volume trajectory with age, along with the predicted linear fit. GM segmentations were computed from (a) original scans, (b) scans enhanced by 2D FSR, and (c) scans enhanced by 3DReCNN. Different lines' colors represent different individuals in the study. All the scans per individual are connected with each others. The black line represents the fitted model and the dashed lines are the confidence interval.
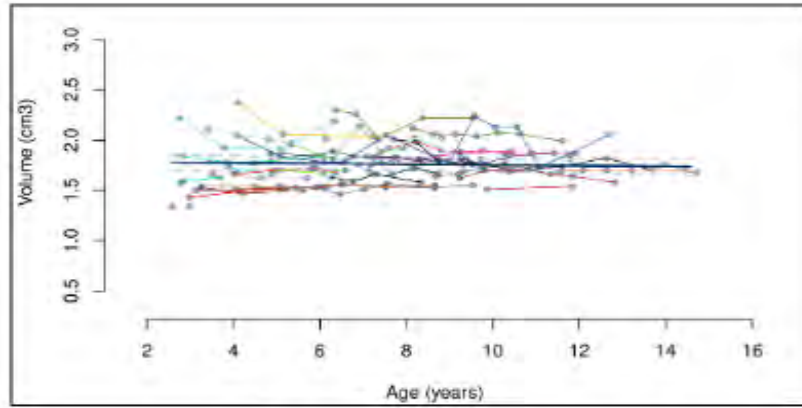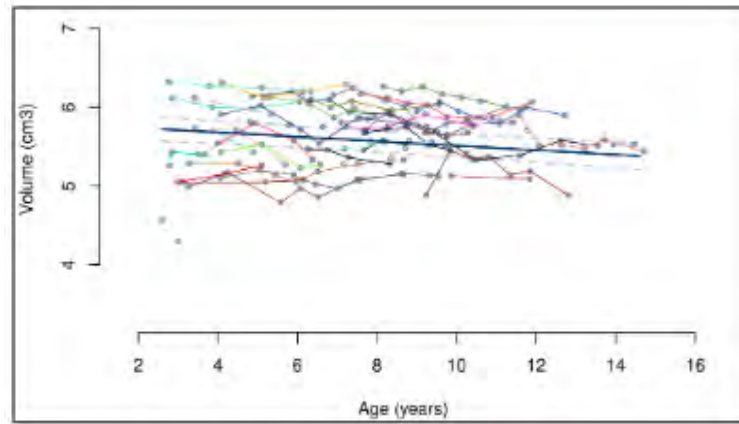
(a) WM volume: original scans
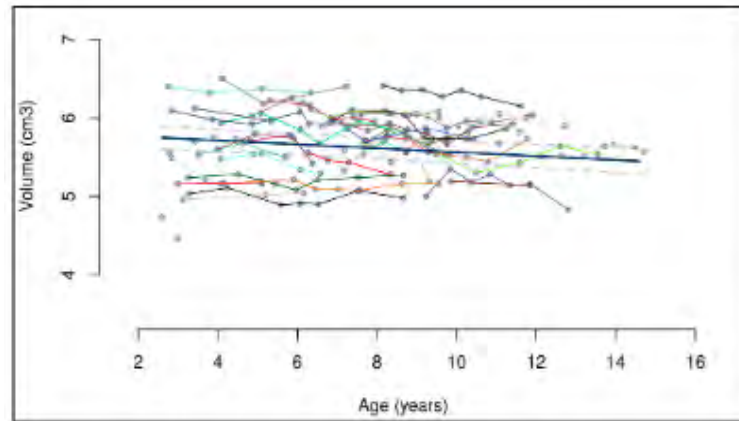

(b) WM volume: 2DFSR enhanced scans

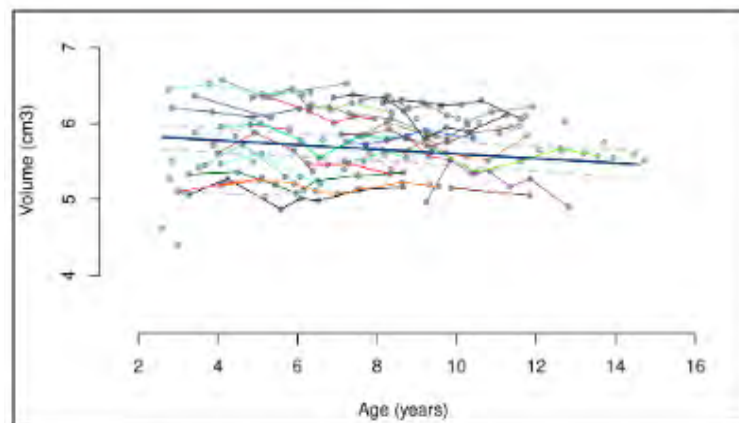(c) WM volume: 3DReCNN enhanced scans

Figure 5.12: WM volume trajectory with age, along with the predicted linear fit. WM segmentations were computed from (a) original scans, (b) scans enhanced by 2D FSR, and (c) scans enhanced by 3DReCNN. Different colors represent different subjects and connected points refer to the scans per individual. The black line represents the fitted model and the dashed lines are the confidence interval.

(a) Total volume: original scans

(b) Total volume: 2DFSR enhanced scans

(c) Total volume: 3DReCNN enhanced scans

Figure 5.13: Total brain volume trajectory with age, along with the predicted linear fit. Total brain segmentations were computed from (a) original scans, (b) scans enhanced by 2D FSR, and (c) scans enhanced by 3DReCNN. Different colors represent different subjects and connected points refer to the scans per individual. The black line represents the fitted model and the dashed lines are the confidence interval.

5.4.1.2   Young to middle adulthood group

As mentioned before, 95 scans from 33 subjects with age ranging between 2.5 and 8 years were included in this analysis. The aim is thus to quantify the volumetric change in brain tissues during the young to middle adulthood period of the marmoset life.

This time, Table 5.4 shows that there is no significant linear decrease in GM volume with age when computing volumes from segmentations of original scans or scans enhanced by 3D ReCNN. However, a linear decrease in GM volumes was detected when volumes were computed from segmentations of images enhanced by 2D FSR. Figure 5.14 shows the difference between the linear model fit to GM segmentation of the original, enhanced by 2D FSR, and enhanced by 3D ReCNN scans. Such differences in the results may be due to a reduced variability, especially intra-subject, in volumes computed from segmentations obtained after enhancement with SR. Referring back to the longitudinal study performed by Lebel et al. [206], a similar linear decrease in the GM volume of the human brain was detected between 5 and 32 years, i.e. in the young to middle adulthood. Therefore, even though a linear decrease in the marmosets' brain during this period would be in accordance with the changes occurring in the human brain during this life period, one should keep in mind that the most significant decrease found here is still very small. Again, despite enhancement with SR, which can at best reduce segmentation errors, the observed changes are still very small with respect to the acquisition spatial resolution, and may not be detected.

Table 5.4: Global statistical analysis of the total brain volume changes with age for the marmosets in their young to middle adulthood (with ages between 2.5 and 8 years) including 95 scans. The table shows the slope and the 95% confidence interval of the linear model fitted to GM volumes.

	Tested Model	Slope	Confidence Interval
Original scans	linear	- 0.0125	[- 0.0387 , 0.0153]
Enhanced scans by 2DFSR	linear	- 0.0351	[- 0.0567 , - 0.0121]
Enhanced scans by 3DReCNN	linear	-0.0213	[- 0.0487 , 0.0075]

As for the WM volume, the only linear model that showed a significant relationship between

volume and age was the model fitted to volumes computed from segmentations of scans enhanced by the 2D FSR method. However, the linear increase in WM volume was not significant using segmentations of original scans or scans enhanced by 3D ReCNN. This WM increase in the young to middle adulthood period of the marmoset life can be linked to the human brain WM increase reported in [6] and [203] until the age of 40 years, and in the longitudinal study of Lebel et al. for ages between 5 and 32 years [206]. But again, one should not conclude too fast based on these results since the confidence interval on the slope is still close to zero with this model.

Table 5.5: Global statistical analysis of the volumetric WM changes with age for the marmosets in their young to middle adulthood (with ages between 2.5 and 8 years) including 95 scans. The table shows the slope and the 95% confidence interval of the linear model fitted to WM volumes.

|	Tested Model	Slope	Confidence Interval
Original scans	linear	0.00033	[- 0.0165 , 0.0181]
Enhanced scans by 2DFSR	linear	0.0158	[0.0073 , 0.0246]
Enhanced scans by 3DReCNN	linear	0.0018	[- 0.0116 , 0.0211]

Finally, Table 5.6 and Figure 5.16 show that, for the three kinds of scans, the linear model reveals a significant decrease in the total brain volume during the young to middle adulthood period of the marmoset.

Table 5.6: Global statistical analysis of the total brain volume changes with age for the marmosets for the marmosets in their young to middle adulthood (with ages between 2.5 and 8 years) including 95 scans.. The table shows the slope and the 95% confidence interval of the linear model fitted to total brain (GM + WM) volumes.

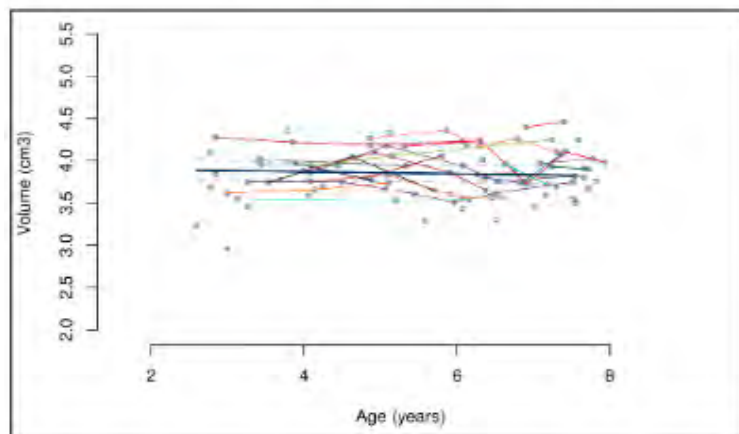|	Tested Model	Slope	Confidence Interval
Original scans	linear	- 0.0262	[- 0.0499 , -0.0013]
Enhanced scans by 2DFSR	linear	-0.0243	[- 0.0467 , - 0.0010]
Enhanced scans by 3DReCNN	linear	-0.0333	[- 0.0578 , -0.0078]
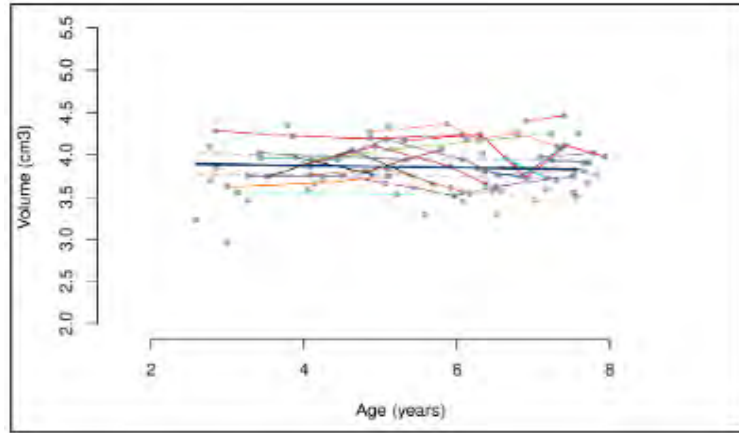
(a) GM volume: original scans
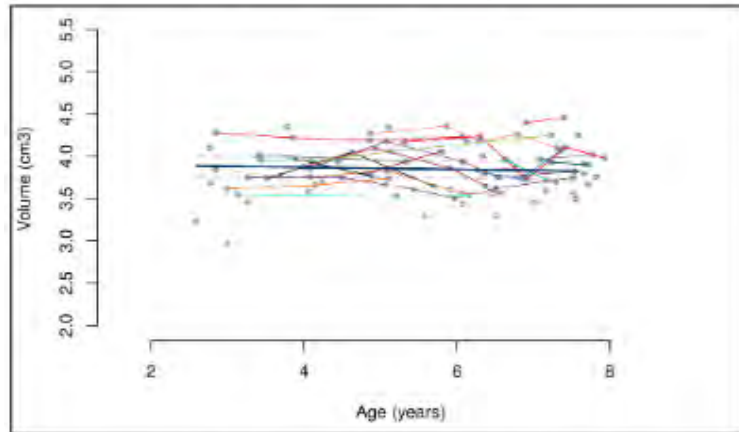
(b) GM volume: 2DFSR enhanced scans

(c) GM volume: 3DReCNN enhanced scans

Figure 5.14: GM volume trajectory with age in the young to middle adulthood period, along with the predicted linear fit. GM segmentations were computed from (a) original scans, (b) scans enhanced by 2D FSR, and (c) scans enhanced by 3DReCNN. Different colors represent different subjects and connected points refer to the scans per individual. The black line represents the fitted model and the dashed lines are the confidence interval.
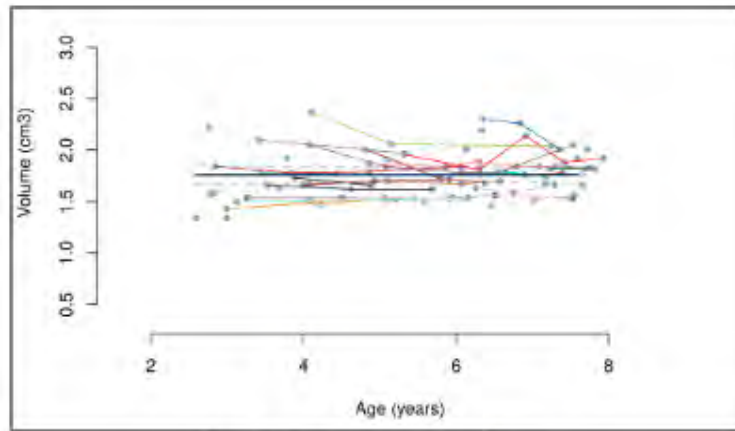
(a) WM volume: original scans
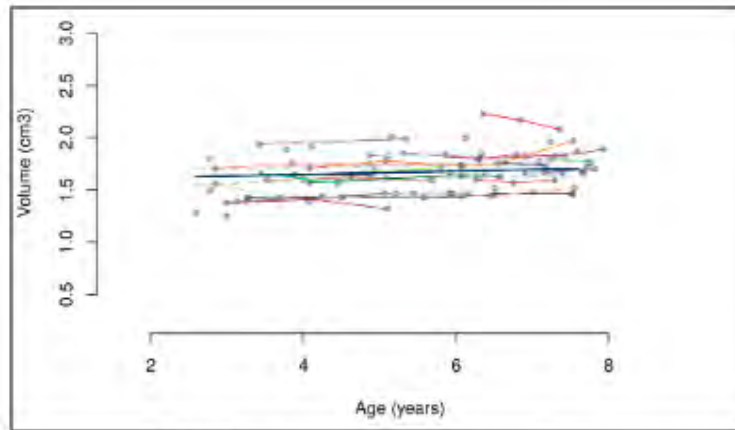

(b) WM volume: 2DFSR enhanced scans

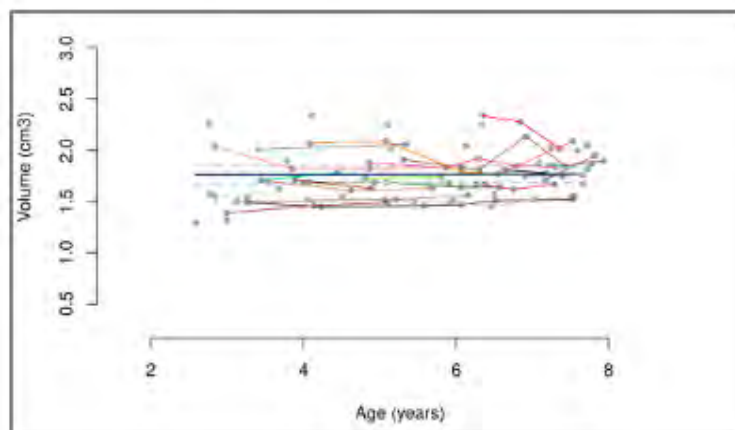(c) WM volume: 3DReCNN enhanced scans

Figure 5.15: WM volume trajectory with age in the young to middle adulthood period, along with the predicted linear fit. WM segmentations were computed from (a) original scans, (b) scans enhanced by 2D FSR, and (c) scans enhanced by 3DReCNN. Different colors represent different subjects and connected points refer to the scans per individual. The black line represents the fitted model and the dashed lines are the confidence interval.
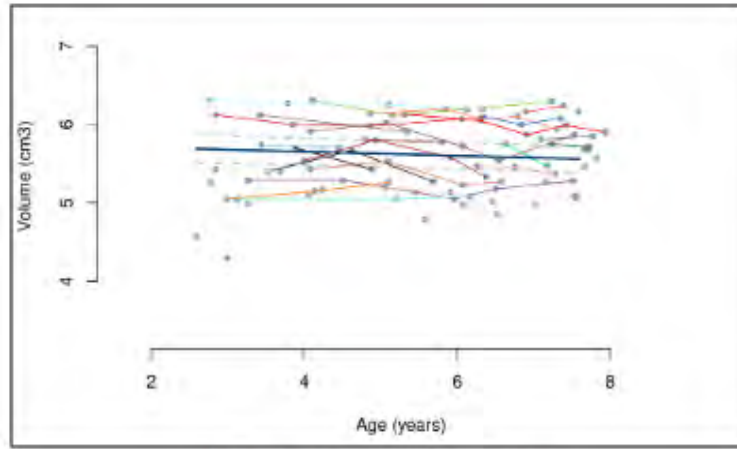
(a) Total volume: original scans
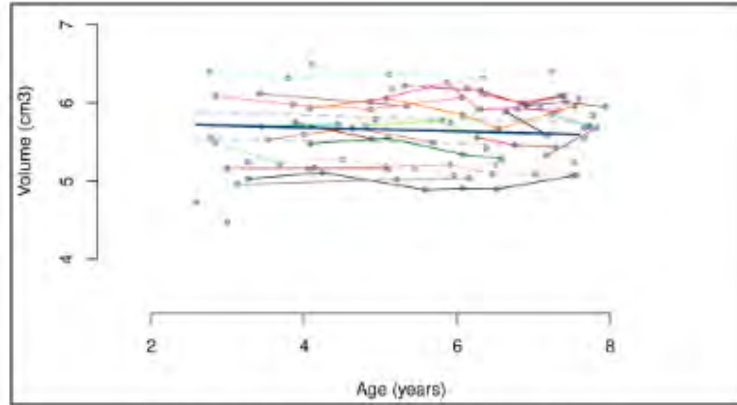
(b) Total volume: 2DFSR enhanced scans
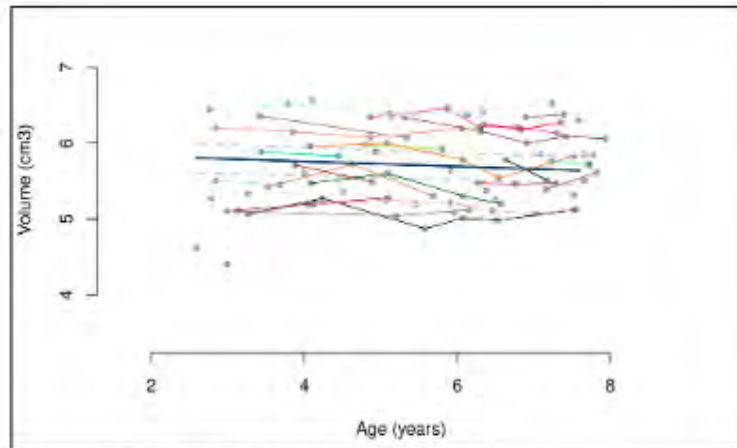
(c) Total volume: 3DReCNN enhanced scans

Figure 5.16: Total brain volume trajectory with age in the young to middle adulthood period, along with the predicted linear fit. Total brain segmentations were computed from (a) original scans, (b) scans enhanced by 2D FSR, and (c) scans enhanced by 3DReCNN. Different colors represent different subjects and connected points refer to the scans per individual. The black line represents the fitted model and the dashed lines are the confidence interval.

5.4.1.3   Late adulthood group

Volumetric markers of cerebral aging of the marmoset brain was longitudinally studied with a group of marmosets of 24 subjects having a total of 90 scans and age ranging between 8 and 14.7 years.

A linear decrease in GM volume was detected using GM segmentations from original and 3D enhanced scans (Table 5.7). This is in accordance with the human-brain theory that GM declines with late age. Figure 5.17 illustrates the linear model of GM trajectory using original and 3D enhanced scans.

Table 5.7: Global statistical analysis of the volumetric GM changes with age for the marmosets in their late adulthood period (with ages greater than 8 years) including 90 scans. The table shows the slope and the 95% confidence interval of the linear model fitted to GM volumes.

	Tested Model	Slope	Confidence Interval
Original scans	linear	- 0.0293	[- 0.0533 , - 0.0047]
Enhanced scans by 2DFSR	linear	- 0.0234	[- 0.0487 , 0.0019]
Enhanced scans by 3DReCNN	linear	- 0.0276	[- 0.0530 , - 0.0018]

However, during the late adulthood period, no significant relationship was observed between WM volumes and age (Table 5.8). This could be interpreted as either no linear changes in the WM of the marmoset's brain occur after the age of 8, or that the data in this group is not precise enough to detect such tiny changes in the WM volume.

Table 5.8: Global statistical analysis of the volumetric WM changes with age for the marmosets in their late adulthood period (with ages greater than 8 years) including 90 scans. The table shows the slope and the 95% confidence interval of the linear model fitted to WM volumes.

	Tested Model	Slope	Confidence Interval
Original scans	linear	- 0.0099	[- 0.0258 , 0.0059]
Enhanced scans by 2DFSR	linear	- 0.0049	[-0.0182 , 0.0085]
Enhanced scans by 3DReCNN	linear	- 0.0059	[- 0.0212 , 0.0091]

Finally, although still very small, a consistent significant linear decrease of the total brain volume with age was detected using original, 2D enhanced, and 3D enhanced scans of older subjects. Figure 5.19 shows the total brain volume as a function of age, along with its predicted linear fit.

Table 5.9: Global statistical analysis of the total brain volume changes with age or the marmosets in their late adulthood period (with ages greater than 8 years) including 90 scans. The table shows the slope and the 95% confidence interval of the linear model fitted to total brain (GM + WM) volumes.

	Tested Model	Slope	Confidence Interval
Original scans	linear	- 0.0419	[- 0.0687 , - 0.0147]
Enhanced scans by 2DFSR	linear	-0.0303	[- 0.0547 , - 0.0056]
Enhanced scans by 3DReCNN	linear	-0.0352	[- 0.0623 , -0.0079]
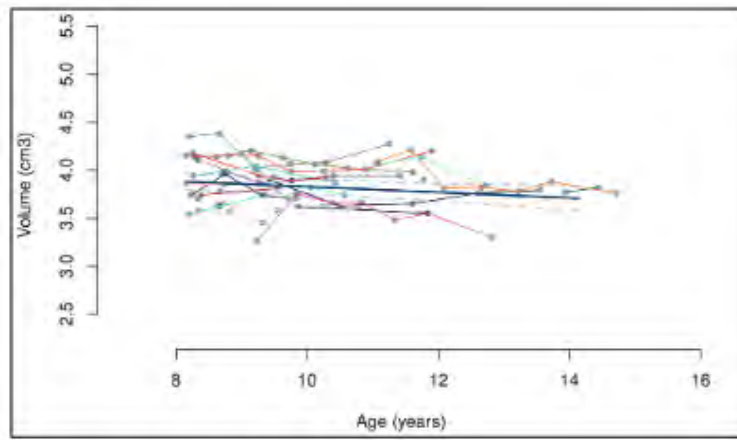
(a) GM volume: original scans
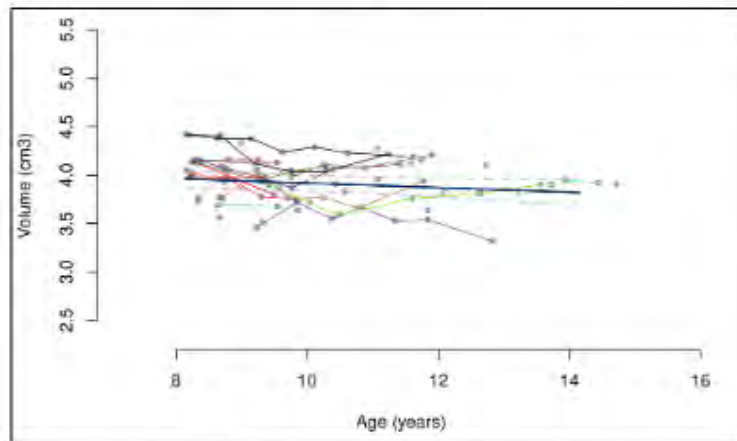
(b) GM volume: 2DFSR enhanced scans
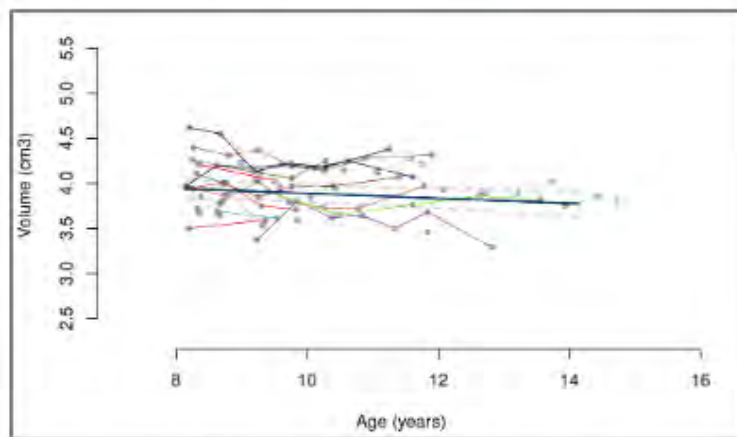
(c) GM volume: 3DReCNN enhanced scans

Figure 5.17: GM volume trajectory in the late adulthood period fitted with a linear model using the segmentation of (a) original scans and (b) enhanced scans by 3D ReCNN. Different colors represent different subjects and connected points refer to the scans per individual. The black line represents the fitted model and the dashed lines are the confidence interval.
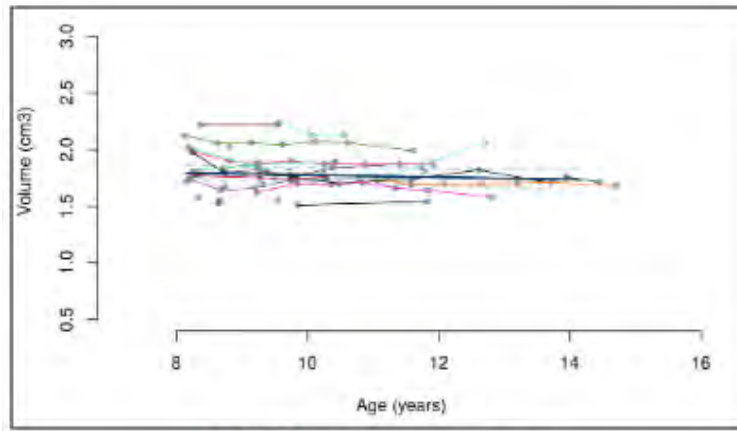
(a) WM volume: original scans
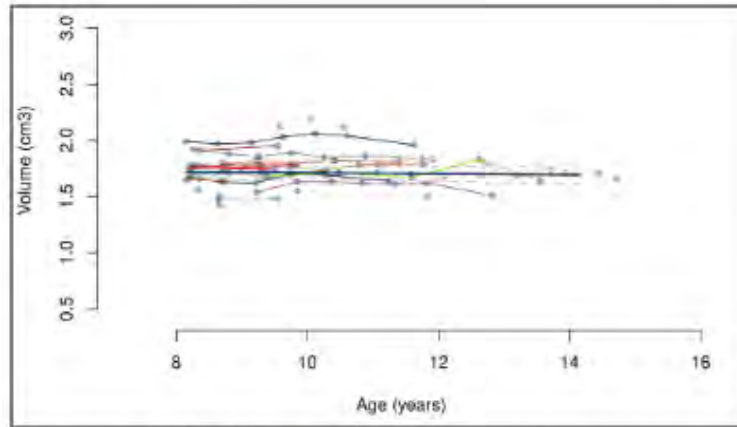
(b) WM volume: 2DFSR enhanced scans
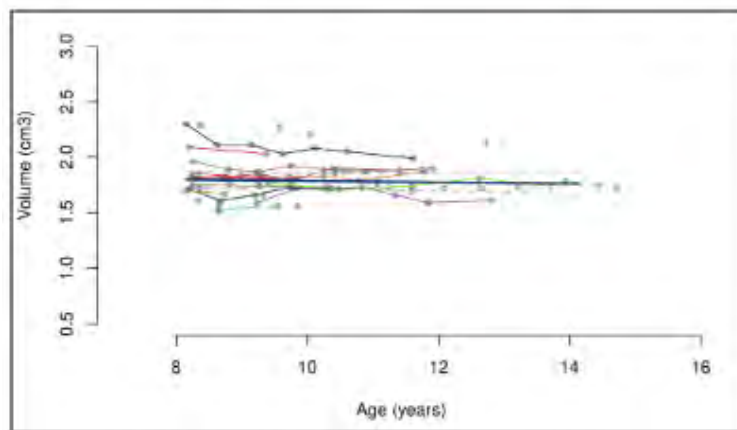
(c) WM volume: 3DReCNN enhanced scans

Figure 5.18: WM volume trajectory with age in the late adulthood period, along with the predicted linear fit. WM segmentations were computed from (a) original scans, (b) scans enhanced by 2D FSR, and (c) scans enhanced by 3DReCNN. Different colors represent different subjects and connected points refer to the scans per individual. The black line represents the fitted model and the dashed lines are the confidence interval.

(a) Total volume: original scans
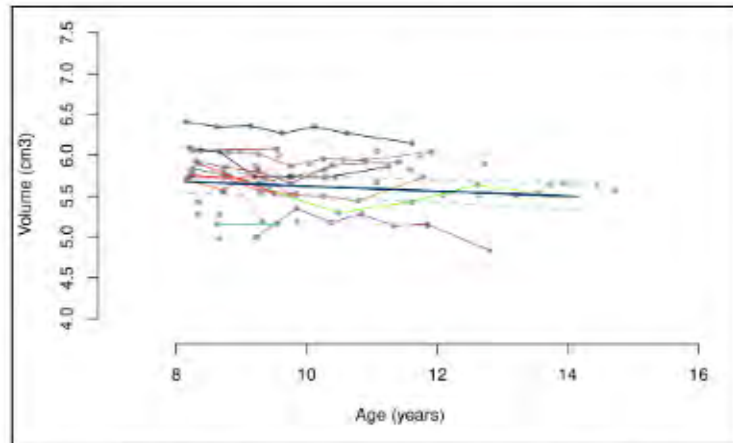
(b) Total volume: 2DFSR enhanced scans
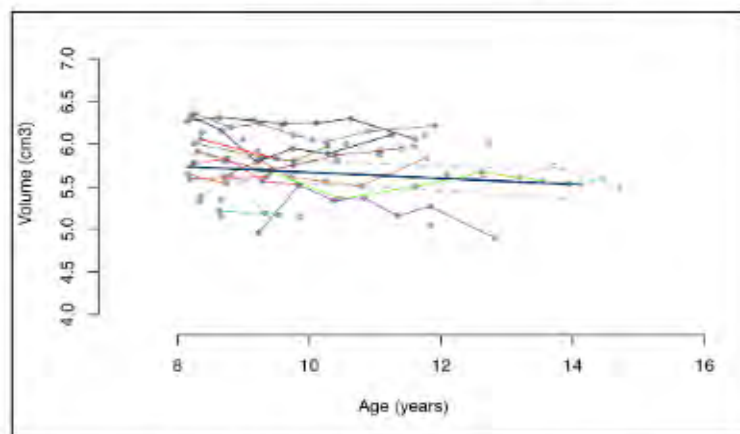
(c) Total volume: 3DReCNN enhanced scans

Figure 5.19: Total brain volume trajectory with age in the late adulthood period, along with the predicted linear fit. Total brain segmentations were computed from (a) original scans, (b) scans enhanced by 2D FSR, and (c) scans enhanced by 3DReCNN. Different colors represent different subjects and connected points refer to the scans per individual. The black line represents the fitted model and the dashed lines are the confidence interval.

5.4.1.4 Discussion

In this section, we modelled the volumetric changes in the brain tissue volumes with age using a mixed effects linear model. During our study, we tried also to fit the data using quadratic and cubic models as already tested in previous studies of the human brain [225]. We found that the three models (linear, quadratic and cubic) similarly described the data implying that adding complexity to th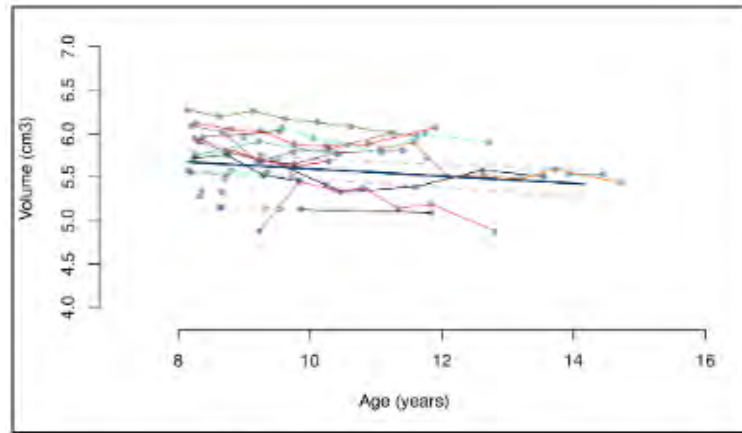e model does not bring much. Worse, such models can over fit the data and hide true changes. In such conditions, it is generally advised to apply the principle of parsimony, and choose the simplest model, which is the linear model in our case. The small value of the slope, rendering the increase or decrease of the fitted curve not obviously visible, can be related to the fact that the changes occurring in the marmoset brain are too small with respect to the voxel size. Thus, the detection of such changes may require acquiring data with a higher spatial resolution. To this end, our global statistical analysis is still a preliminary study where further investigations should be conducted.

Despite these limitations, to sum up our findings, GM volume of the marmoset brain was found to decrease over time, indicating a possible shrinkage with age. Volumetric changes in WM could not be detected in the adulthood analysis, whether the images were previously enhanced or not by 2D FSR or 3D ReCNN methods. We were able to detect an increase, although still very small, in WM volume in the young to middle adulthood period of the marmosets' life using the segmentations of the enhanced scans by 2D FSR. Even though enhancing images with SR may reduce the intra- and inter-individual variability in segmentations and hence in volumes, the acquisition resolution is probably too low to detect such subtle changes. Besides, we believe that additional studies on WM, including the analysis of myelin in WM fibers, using different but complementary MRI techniques, may be more suitable for this brain tissue. Finally, the total brain volume composed of the gray and white matters tends to decrease throughout the life span of the marmoset starting from age of 2.5 years. Information about the total brain trajectory before this age is not available in this study.

As this analysis has provided information about the global volumetric changes of GM and WM, we are more interested in the regional changes occurring in the brain. Such changes are more likely to be linked with cognitive and behavioral observations in future studies. Therefore, the following section will highlight the VBM study of the GM and WM changes of the marmoset brain.

5.4.2 VBM analysis

Similar to the global statistical analysis conducted on the three age-groups, the regional volumes' changes were studied, voxel-by-voxel, in a VBM analysis of GM and WM tissues. We will hereafter show the results of this VBM analysis while highlighting regions showing an increase or decrease with age. We will, as before, show these results for the original, 2D enhanced, and 3D enhanced scans.

5.4.2.1 Adulthood group

Statistical inferences were made at voxel-level using a significativity level of 0.05 with family-wise error (FWE) correction for multiple comparisons across the whole brain, and with no extent threshold. For the analysis of GM volume change, more specifically, a GM mask was applied to exclude any non-GM voxels in the analysis. The difference between the VBM results on GM extracted from original scans, from scans enhanced by 2D FSR, and from scans enhanced by 3D ReCNN, are depicted in Figure 5.20. A GM volume decrease with age was observed in the lateral and medial prefrontal cortex, cingulate gyrus, caudate nucleus, hippocampus and parahippocampal gyrus, parietal lobe, and occipital posterior areas. No voxels in GM were found to significantly increase in this analysis. These results can be related to the GM reduction in the human brain reported in [207] and [208]. Although the analysis of the human brain involved more GM regions, our results remain interesting as they show a similar behaviour of the aging process between the marmoset and the human GM volume. As hippocampal reduction accelerates in the middle age [228], detection of this loss is in accordance with the process occurring in the human brain. Moreover, the reduction in the caudate nucleus, which is usually associated with memory decline in the human brain [229, 230], seems to be coherent with the aging of the marmoset brain. In the study of WM regional decrease, few pixels were found in the occipital area, but it may be strongly due to a misclassification error in the segmentation step since this region had the most acquisition-related artifacts. This result is in contradiction with the WM loss reported in [6, 210] for the human brain. Since we test only for a linear regression with age, this result may be due to the fact that WM exhibits a non-linear relation with age which could not be detected, or that changes occur at a smaller scale and could not be captured with sufficient precision. On the other hand, a WM increase was observed in the prefrontal areas, the parietal lobe,

and frontal and parietal connections. Figure 5.21 shows the global maximum increase in WM for the three kinds of scans studied.
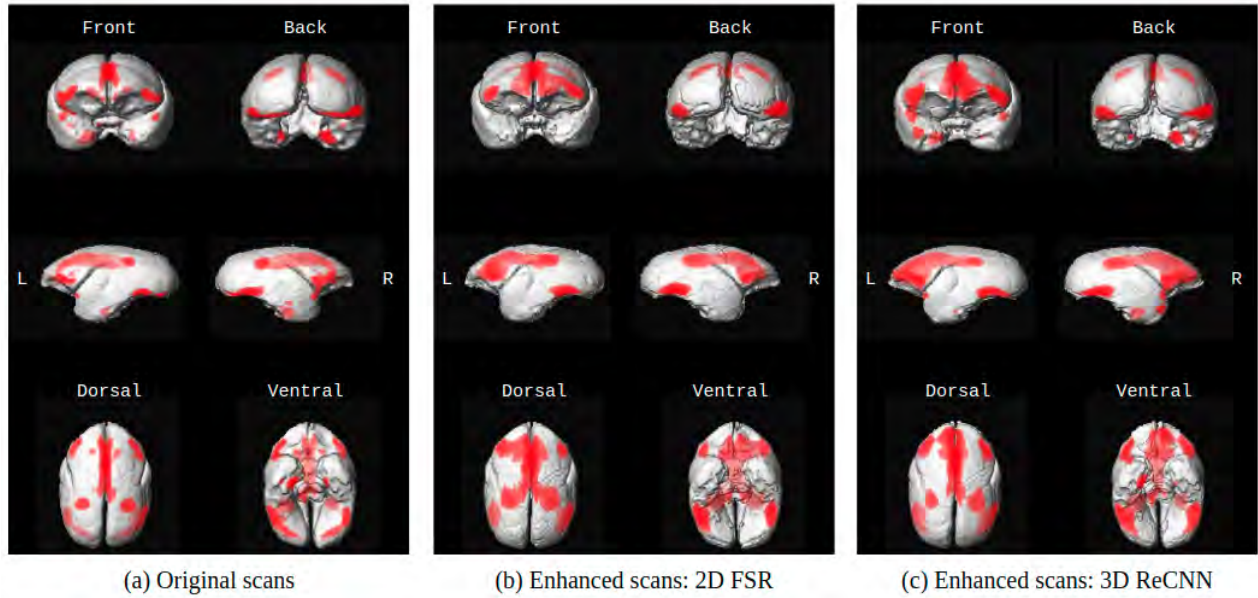
Figure 5.20: VBM analysis of GM decrease for 185 MRI scans from 42 marmosets with an age range of 2.5 to 14.7 years using smwGM segmentation from (a) original scans, (b) enhanced scans by 2D FSR, and (c) enhanced scans by 3D ReCNN. Darker shades of red represent a more significant decrease in a specific region than lighter shades.

5.4.2.2 Young to middle adulthood group

Statistical inferences were made at voxel-level using an uncorrected p-value of $p < 0.001$, and with no extent threshold. A smaller uncorrected p-value was necessary since the studied sample is smaller than the previous one with only 95 scans available. Again, a mask was applied to exclude any non-GM voxels in the analysis. A decrease in GM volume was observed in the lateral prefrontal cortex. However, we were not able to detect a decrease in the medial prefrontal cortex. The caudate nucleus did not show a strong decrease and no decrease in the hippocampus was reported. These results are expected as these areas start to decrease in late ages in the human (Figure 5.22).

(a) Original scans   (b) Enhanced scans: 2D FSR   (b) Enhanced scans: 3D ReCNN
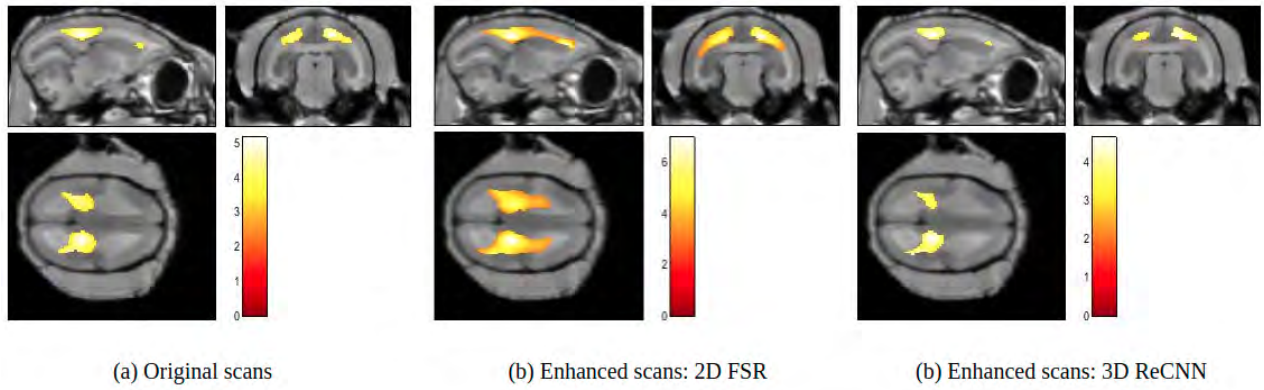
Figure 5.21: VBM analysis of WM increase for 185 MRI scans from 42 marmosets with an age range of 2.5 to 14.7 years using smwWM segmentation from (a) original scans, (b) enhanced scans by 2D FSR and (c) enhanced scans by 3D ReCNN. This figure shows the pixels of global maximum for each case. The color bar ranges from least (red) to most significant (white) change.

(a) Original scans   (b) Enhanced scans: 2D FSR   (c) Enhanced scans: 3D ReCNN
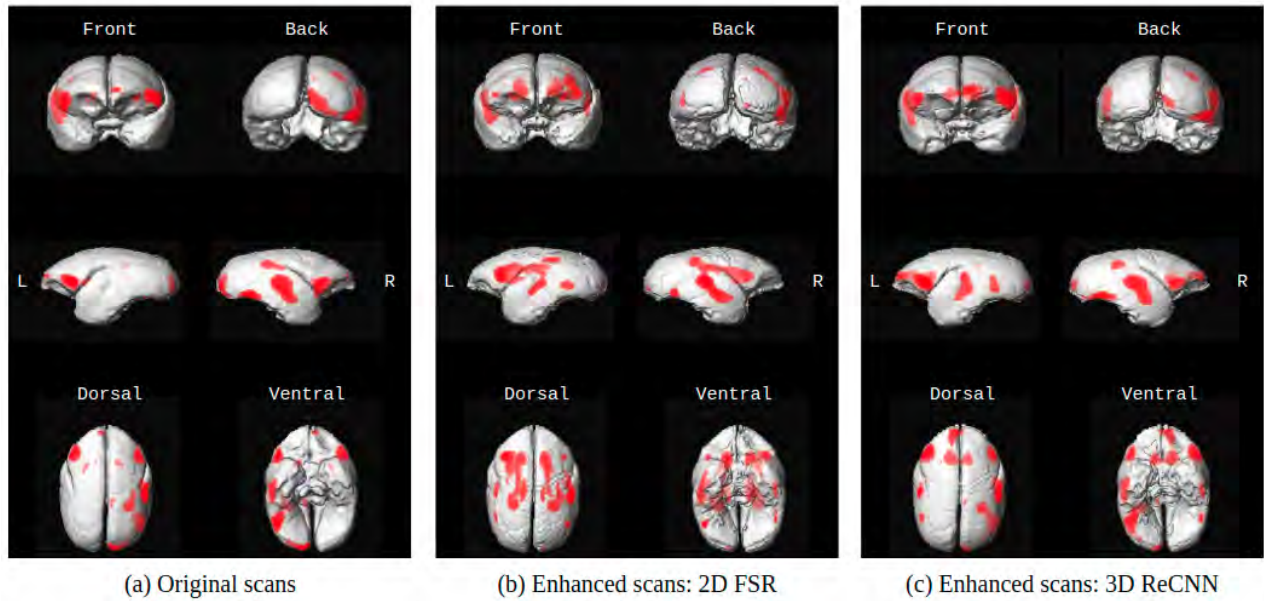
Figure 5.22: VBM analysis of GM decrease for 95 MRI scans from 33 marmosets during their young to middle adulthood with an age range of 2.5 to 8 years using smwGM segmentation from (a) original scans, (b) enhanced scans by 2D FSR, and (c) enhanced scans by 3D ReCNN. Darker shades of red represent a more significant decrease in a specific region than lighter shades.

No decrease was observed in the WM region either for the young to middle adulthood analysis. However, an increase in the prefrontal area was observed, which may be due to brain maturation, especially in younger subjects. Figure 5.23 shows the effect of SR on the VBM analysis of WM. While using the original scans no pixels were highlighted, the segmentation enhancement by 2D FSR allowed for a stronger VBM result. This result is in accordance with the results in Table 5.5 where the linear increase of WM was only detectable using the super-resolved scans by 2D FSR. Similar to the original scans, no voxels were found significant when using scans enhanced by 3D ReCNN.

(a) Original scans   (b) Enhanced scans: 2D FSR
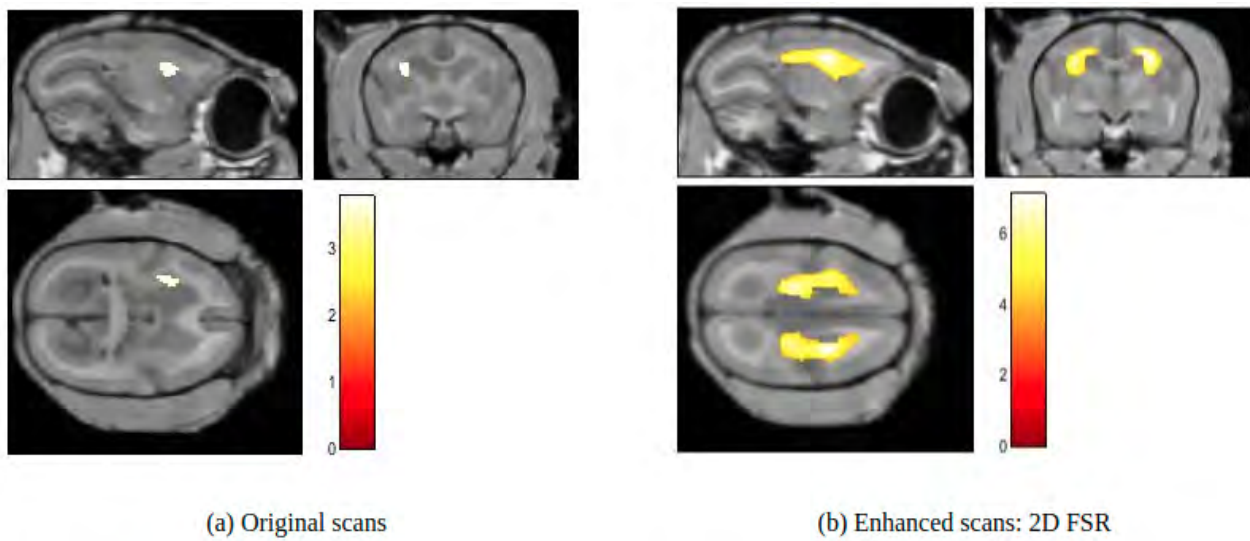
Figure 5.23: VBM analysis of WM increase for 95 MRI scans from 33 marmosets during their young to middle adulthood with an age range of 2.5 to 8 years using smwWM segmentation from (a) original scans and (b) enhanced scans by 2D FSR. No significant pixels of WM increase were detected using the enhanced scans by 3D ReCNN. This figure shows the pixels of global maximum for each case. The color bar ranges from least (red) to most significant (white) change.

5.4.2.3 Late adulthood group

Similar to the VBM analysis of the young to middle adulthood group, the analysis of the 90 scans of old ages was performed at voxel-level using an uncorrected p-value of $p < 0.001$, and with no extent threshold. A GM volume decrease was observed in hippocampus and parahippocampal gyrus, limbic

lobe and the cingulate gyrus. More GM volume decrease was detected in the posterior cingulate which is associated with memory and connected to the hippocampus, and the medial pre-frontal lobe. However, less decrease occurred in the lateral area of the brain. Detection of the hippocampal changes in the late adulthood group represents an interesting result as several studies have reported the effect of hippocampal reduction on the cognitive abilities in late ages in humans [231, 232]. Cognitive flexibility deficits in marmosets have been previously reported by Sadoun et al. after the age of 7 years in a study based on reversal learning and delayed-matching-to-position tasks and which can be linked to the reduction observed in the hippocampus [23]. For this age group, a WM volume decrease was observed in the body of corpus callosum, the hippocampus connection, and the cingulum bundle. No increase in WM volume was observable as illustrated in Figure 5.25 even after image enhancement. Indeed, a similar difficulty had already been encountered while modelling the trajectory for this age range, where none of the models tested successfully predicted WM changes.
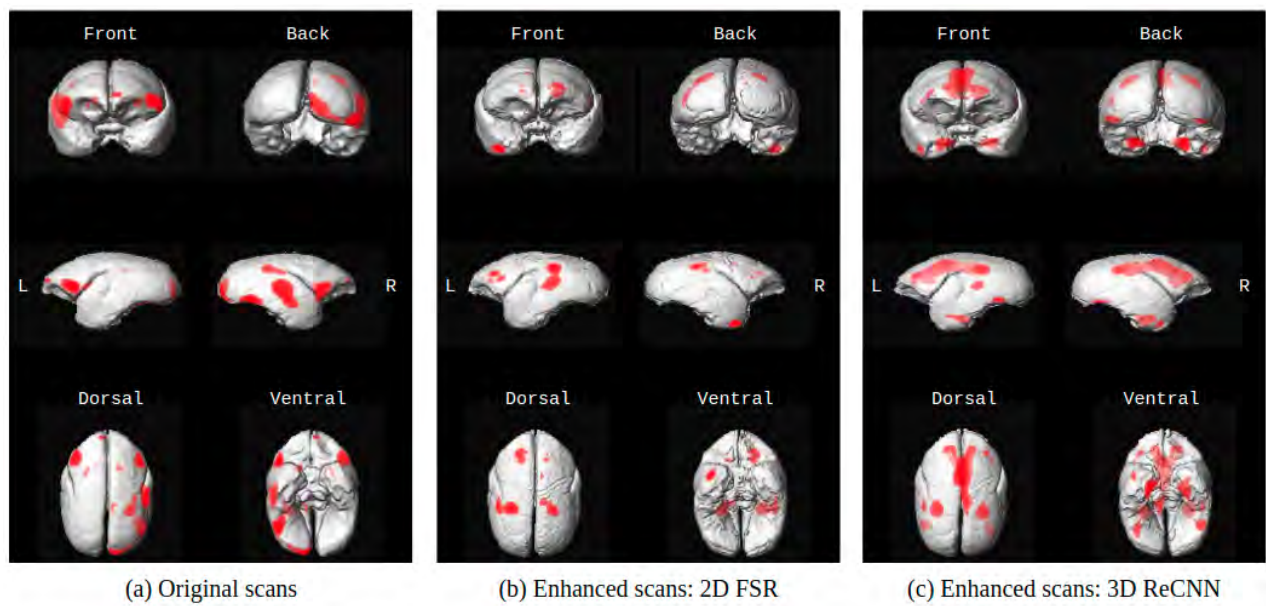
Figure 5.24: VBM analysis of GM decrease for 90 MRI scans from 24 marmosets during in their late adulthood period with age greater than 8 years using smwGM segmentation from (a) original scans, (b) enhanced scans by 2D FSR, and (c) enhanced scans by 3D ReCNN. Darker shades of red represent a more significant decrease in a specific region than lighter shades.

(a) Original scans   (b) Enhanced scans: 2D FSR
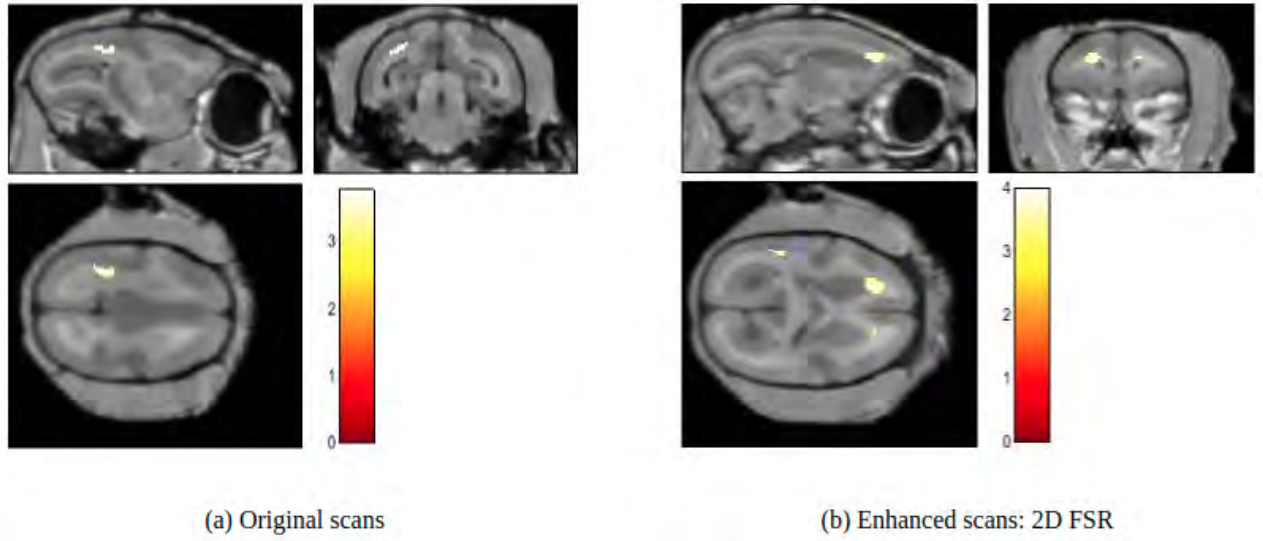
Figure 5.25: VBM analysis of WM increase for 90 MRI scans from 24 marmosets during in their late adulthood period with age greater than 8 years using smwWM segmentation from (a) original scans and (b) enhanced scans by 2D FSR. No significant pixels of WM increase were detected using the enhanced scans by 3D ReCNN. This figure shows the pixels of global maximum for each case. The color bar ranges from least (red) to most significant (white) change.

5.5   Conclusion

In this chapter, we have proposed a longitudinal segmentation pipeline for the segmentation of the marmoset brain MRI scans. Scans were first corrected for position and orientation, noise reduction, and bias field correction before being registered to the marmoset brain template. Then, scans of each individual marmoset were processed to obtain GM, WM, and CSF segmentations while taking into consideration intra-individual variability. Brain tissue segmentations were used in the statistical analysis of the volumetric trajectory of each tissue, while smoothed, modulated, and warped segmentations were used in a VBM analysis to detect a regional increase or decrease in GM and WM volume. The study was performed for three age ranges: the adulthood period with age between 2.5 and 14.7 years, the young to middle adulthood period with age between 2.5 and 8 years, and

the late adulthood period for ages greater than 8. Statistical and VBM analyses using the original marmoset scans were further compared to the analyses using enhanced scans by 2D FSR and 3D ReCNN methods, which have been previously proven efficient for segmentation. We have showed that the GM volume decreases with age with a variability in the regional decrease within each studied group. On the other hand, WM was observed to increase during young to middle adulthood with no additional information that could be detected of what happens after. Moreover, the total brain volume, which is made up of the sum of GM and WM, is thought to decrease throughout the life of the marmosets. These results were consistent with previous studies on modelling the volumetric trajectory of GM and WM in the human brain, which supports the idea of considering the marmoset brain aging as a model for the human brain aging. Starting from the conclusion of Chapter 4, stating that SR enhances the segmentation of the brain, the effect of this enhancement was validated in the global statistical analysis and was further obvious in the VBM analysis. Artifacts detected as a possible increase or decrease of GM and WM on original scans were suppressed on enhanced scans by SR. However, as SR increased the precision around the estimated slope allowing to detect significant changes, they could not uncover changes occurring with aging and that are smaller than scale of the acquired images. This shows the importance of having high resolution acquisitions with smaller voxel size suitable for detecting such small changes. The study on intra- and extra-cerebral CSF was further limited by the overestimation of the CSF, which is confounded with the skull in T_1-weighted MRI. Future perspectives will include the regional statistical analysis of cortical volumes in the marmoset brain.

CHAPTER **6**

Conclusions and perspectives

6.1 Conclusions

The objective of this PhD was to develop resolution enhancement methods for the preclinical detection of biomarkers of cerebral aging using MR images of the marmoset brain. We investigated the effectiveness of several image enhancement methods on MRI data sets of the marmoset brain, including image deblurring, image SR using model-based methods, and image SR using learning-based methods. We further tested the impact of image enhancement on the segmentation of brain tissues. Finally, statistical and VBM analyses were conducted to detect age-related volumetric trajectories and regional changes of the GM and WM of the marmoset brain.

The first work conducted in this thesis was introduced in Chapter 3, where we presented a segmentation method for marmoset brain MR images, which does not rely on a brain template. Rather, we proposed a segmentation method based on a Bayesian joint deconvolution and segmentation algorithm. The method is based on modeling locally the image statistics using a Generalized Gaussian distribution (GGD) and couples the deconvolved image and its corresponding label map using the GGD-Potts model. The outputs (enhanced version of the input MRI volume and its corresponding labels) were further used as prior information (maps) for segmenting the brain into its main compartments with SPM. Enhancing the MR volumes by deconvolution resulted in competitive segmentation results regardless of the method used. Using the associated labels as segmentation priors presented a significant contribution, especially when templates are not available. The segmentation obtained with the proposed method showed a good similarity with the manual segmentation.

In Chapter 4, we evaluated several methods for SR of marmoset brain MR images. The first part introduced model-based techniques for the SR task. In particular, we assessed a 2D fast SR method

187

(FSR) and a 3D tensor-factorization (TF) method for general image reconstruction and compared them to the existing state-of-the-art methods. The second part covered deep learning networks that have been initially published for the SR of human brain MR images and trained using a marmoset data set. The results of these methods were evaluated from a brain segmentation perspective, using a state-of-the-art brain segmentation method applied to native, LR, and estimated HR volumes. The objective was to study the effect of SR on the final segmentation of the brain. Qualitative and quantitative results on simulated LR data showed that the segmentation of the recovered images were closer to the ground truth. Using classical interpolation did not provide as promising results as SR methods. The practical application of SR on native data and the computation of tissue volumes revealed that the segmentation of enhanced images were closer to the MS performed by an expert than that of the native images. Moreover, we tried to synthesize $7T$-like MRI images using $3T$ images using a network that has been trained on human brain images which revealed a great enhancement in the contrast between brain tissues. The best performing SR methods, the 2D FSR model-based method and the 3D ReCNN learning-based method, were further used in the statistical and VBM analyses for the marmoset brain.

Finally, in Chapter 5, we have introduced an original work on the longitudinal segmentation and analysis of the marmoset brain MR images. In this context, we have proposed a longitudinal pipeline for the segmentation that starts by correcting the brain scans for position and orientation, noise reduction, and bias field correction before registering them to the marmoset brain template. Then, scans of each individual marmoset were processed to obtain GM, WM and CSF segmentations while taking into consideration intra-individual variability. The statistical analysis of the volumetric trajectory of GM, WM and the total brain showed a decrease in GM volume with age, a potential increase in WM volume until the age of 8 years, and a global decrease in the total volume with age. We further studied the voxel-by-voxel analysis of the regional brain changes in the GM and WM areas where we have detected a decrease in GM with age in regions such as lateral and medial prefrontal cortex, cingulate gyrus, caudate nucleus, hyppocampus and parahippocampal gyrus, parietallobe, and occipital posterior areas. A WM increase with age was also observed in the pre-frontal areas, the parietal lobe, and frontal and parietal connections. The study was conducted for the adulthood

and the senescent stages of the marmoset life. Results showed a potential homology between the human and the marmoset brain. The global decrease in GM volume and increase in WM volume have been already reported in the human brain. Moreover, GM shrinkage of some regions, such as the caudate nucleus and the hippocampus, is highly linked to signs of aging in humans, such as cognitive decline and memory loss. Finally, we studied the effect of SR by performing the same analysis using scans enhanced by 2D FSR and 3D ReCNN. SR showed more precision in the statistical analysis by reducing uncertainty and inter- and intra-subject variability. However, the changes occurring with aging remains too small to be detected using super-resolved scans and require higher resolution acquisitions.

6.2 Future perspectives

Several interesting perspectives could further complete the work performed in this PhD.

- **Model-based hyper-parameters:** The choice of hyperparameters in the model-based SR methods was either done by cross-validation or manually, based on visual inspection of images and using appropriate metrics. However, it would be interesting to investigate some methods to tune these hyperparameters automatically from the data. This was already stated in Chapter 3 as in the possible automatic estimation of the noise variance [178] and the granularity coefficient [172].

- **PSF estimation:** In experimental setups, when applying different SR methods on real MR images, the choice of the PSF kernel is important and it usually depends on the MRI sequence performed. More specifically, the shape of the PSF depends on the trajectory in the k-space (Cartesian, radial, spiral). Performing blind deconvolution, independent of the PSF model, and adapting the algorithms to estimate the kernel based on any sequence performed could be a major future step. Further research should focus on a better PSF estimation scheme of the MRI data studied with the flexibility of having data from different sources.

- **Learning-based image enhancement:** With the rapid advancements in deep learning methods and the abundant networks proposed in literature, SR can now be performed using multimodal MRI data. To elaborate, these networks integrate scans from different modalities or sequences (T_1-weighted, T_2-weighted, PD, etc..) to perform the SR task as in [127, 233]. Moreover, since obtaining abundant or HR data for deep learning networks could be a challenging task in the case of animal studies, transfer learning [234] could be considered. The idea is to train networks using not only animal MR scans but also human brain scans since these are now available online. As this method has been proven efficient in machine learning applications, its applicability to deep learning could be further investigated and tested.

- **Learning-based image segmentation:** Automated image segmentation methods using deep learning techniques require the presence of a huge dataset with images having ground truth labels for training, validation and evaluation of the proposed networks. With the lack of ground truth labels, segmentation techniques using deep learning were not a choice in this thesis. However, by obtaining more manual segmentations of the marmoset brain, investigating learning-based segmentation would be an interesting future work. Since GM, WM and CSF contrasts on $T1$-weighted marmoset brain images are similar to those in the human brain, increasing the data sets by transfer learning could be a possible alternative. In this context, Delannoy at al. [235] have already performed the segmentation of the neonatal brain cerebral cortex using generative adversarial network. A similar implementation could be investigated for the segmentation of tissue brain structures.

- **Marmoset brain analysis:** The preliminary results of the statistical and VBM analysis could be further elaborated for more interesting investigation of the marmoset brain. While we only performed the statistical trajectory analysis for the whole GM and WM volumes, regional changes of brain areas could be studied independently to analyze the changes and relate them to the human brain as performed by Coupé et al. [205]. This will aid the study of the possibility of using the marmoset as a human aging model. Moreover, we can further link these regional changes with age with cognitive and behavioral studies, and their ability to perform specific

task that they have learned in their adulthood [22, 23, 236].

192

Bibliography

[1] J. M. Aburto, F. Villavicencio, U. Basellini, S. Kjærgaard, and J. W. Vaupel, "Dynamics of life expectancy and life span equality," *Proceedings of the National Academy of Sciences*, vol. 117, no. 10, pp. 5250–5259, 2020.

[2] W. H. Organization *et al.*, "Active ageing: A policy framework," World Health Organization, Tech. Rep., 2002.

[3] C. N. Ross, "Marmosets in aging research," *The common marmoset in captivity and biomedical research*, pp. 355–376, 2019.

[4] C. D. Smith, H. Chebrolu, D. R. Wekstein, F. A. Schmitt, and W. R. Markesbery, "Age and gender effects on human brain anatomy: a voxel-based morphometric study in healthy elderly," *Neurobiology of aging*, vol. 28, no. 7, pp. 1075–1087, 2007.

[5] F. M. Gunning-Dixon, A. M. Brickman, J. C. Cheng, and G. S. Alexopoulos, "Aging of cerebral white matter: a review of MRI findings," *International Journal of Geriatric Psychiatry: A journal of the psychiatry of late life and allied sciences*, vol. 24, no. 2, pp. 109–117, 2009.

[6] C. D. Good, I. S. Johnsrude, J. Ashburner, R. N. Henson, K. J. Friston, and R. S. Frackowiak, "A voxel-based morphometric study of ageing in 465 normal adult human brains," *Neuroimage*, vol. 14, no. 1, pp. 21–36, 2001.

[7] R. Verwer, R. Baker, E. Boiten, E. Dubelaar, C. Van Ginkel, A. Sluiter, and D. Swaab, "Post-mortem brain tissue cultures from elderly control subjects and patients with a neurodegenerative disease," *Experimental gerontology*, vol. 38, no. 1-2, pp. 167–172, 2003.

[8] O. Piguet, K. Double, J. Kril, J. Harasty, V. Macdonald, D. McRitchie, and G. Halliday, "White matter loss in healthy ageing: a postmortem analysis," *Neurobiology of aging*, vol. 30, no. 8, pp. 1288–1295, 2009.

[9] R. L. Hendren, I. De Backer, and G. J. Pandina, "Review of neuroimaging studies of child and adolescent psychiatric disorders from the past 10 years," *Journal of the American Academy of Child & Adolescent Psychiatry*, vol. 39, no. 7, pp. 815–828, 2000.

[10] V. Pergher, P. Demaerel, O. Soenen, C. Saarela, J. Tournoy, B. Schoenmakers, M. Karrasch, and M. M. Van Hulle, "Identifying brain changes related to cognitive aging using vbm and visual rating scales," *NeuroImage: Clinical*, vol. 22, p. 101697, 2019.

[11] S. N. Lockhart and C. DeCarli, "Structural imaging measures of brain aging," *Neuropsychology review*, vol. 24, no. 3, pp. 271–289, 2014.

[12] A. M. Fjell and K. B. Walhovd, "Structural brain changes in aging: courses, causes and cognitive consequences," *Rev Neurosci*, vol. 21, no. 3, pp. 187–221, 2010.

[13] S. Sigurdsson, T. Aspelund, L. Forsberg, J. Fredriksson, O. Kjartansson, B. Oskarsdottir, P. V. Jonsson, G. Eiriksdottir, T. B. Harris, A. Zijdenbos *et al.*, "Brain tissue volumes in the general population of the elderly: the ages-reykjavik study," *Neuroimage*, vol. 59, no. 4, pp. 3862–3870, 2012.

[14] A. F. for Aging Research, *Animal Models in Aging Research: An introduction to aging science*, 2016. [Online]. Available: www.afar.org

[15] G. Santulli, C. Borras, J. Bousquet, L. Calzà, A. Cano, M. Illario, C. Franceschi, G. Liotta, M. Maggio, W. D. Molloy *et al.*, "Models for preclinical studies in aging-related disorders: one is not for all," *Translational Medicine@ UniSa*, vol. 13, p. 4, 2015.

[16] S. J. Mitchell, M. Scheibye-Knudsen, D. L. Longo, and R. de Cabo, "Animal models of aging research: implications for human aging and age-related diseases," *Annu. Rev. Anim. Biosci.*, vol. 3, no. 1, pp. 283–303, 2015.

[17] K. E. Fischer and S. N. Austad, "The development of small primate models for aging research," *ILAR journal*, vol. 52, no. 1, pp. 78–88, 2011.

[18] D. L. Palliyaguru, C. Vieira Ligo Teixeira, E. Duregon, C. di Germanio, I. Alfaras, S. J. Mitchell, I. Navas-Enamorado, E. J. Shiroma, S. Studenski, M. Bernier *et al.*, "Study of longitudinal aging in mice: Presentation of experimental techniques," *The Journals of Gerontology: Series A*, vol. 76, no. 4, pp. 552–560, 2021.

[19] R. J. Colman, "Non-human primates as a model for aging," *Biochimica et Biophysica Acta (BBA)-Molecular Basis of Disease*, vol. 1864, no. 9, pp. 2733–2741, 2018.

[20] S. Sawiak, Y. Shiba, L. Oikonomidis, C. Windle, A. M. Santangelo, H. Grydeland, G. Cockcroft, E. Bullmore, and A. Roberts, "Trajectories and milestones of cortical and subcortical development of the marmoset brain from infancy to adulthood," *Cerebral Cortex*, vol. 28, no. 12, pp. 4440–4453, 2018.

[21] M. Fukushima, N. Ichinohe, and H. Okano, "Neuroanatomy of the marmoset," in *The common marmoset in captivity and biomedical research*.   Elsevier, 2019, pp. 43–62.

[22] A. Sadoun, K. Strelnikov, E. Bonté, C. Fonta, and P. Girard, "Cognitive impairment in a young marmoset reveals lateral ventriculomegaly and a mild hippocampal atrophy: a case report," *Scientific reports*, vol. 5, no. 1, pp. 1–11, 2015.

[23] A. Sadoun, M. Rosito, C. Fonta, and P. Girard, "Key periods of cognitive decline in a nonhuman primate model of cognitive aging, the common marmoset (callithrix jacchus)," *Neurobiology of aging*, vol. 74, pp. 1–14, 2019.

[24] S. Herculano-Houzel, "The human brain in numbers: a linearly scaled-up primate brain," *Frontiers in human neuroscience*, vol. 3, p. 31, 2009.

[25] B. J. Bedell and P. A. Narayana, "Volumetric analysis of white matter, gray matter, and csf using fractional volume analysis," *Magnetic resonance in medicine*, vol. 39, no. 6, pp. 961–969, 1998.

[26] I. I. Rabi, "Space quantization in a gyrating magnetic field," *Physical Review*, vol. 51, no. 8, p. 652, 1937.

[27] F. Bloch, "Nuclear induction," *Physical review*, vol. 70, no. 7-8, p. 460, 1946.

[28] E. M. Purcell, H. C. Torrey, and R. V. Pound, "Resonance absorption by nuclear magnetic moments in a solid," *Physical review*, vol. 69, no. 1-2, p. 37, 1946.

[29] X. Wang, "Real-time MRI and model-based reconstruction techniques for parameter mapping of spin-lattice relaxation," Ph.D. dissertation, Niedersächsische Staats-und Universitätsbibliothek Göttingen, 2017.

[30] W. Siemens-Aktiengesellschaft Berlin and A. Hendrix, *Magnets, Spins, and Resonances: An introduction to the basics of Magnetic Resonance.* Siemens AG, 2003.

[31] P. C. Lauterbur, "Image formation by induced local interactions: examples employing nuclear magnetic resonance," *nature*, vol. 242, no. 5394, pp. 190–191, 1973.

[32] M. Symms, H. Jäger, K. Schmierer, and T. Yousry, "A review of structural magnetic resonance neuroimaging," *Journal of Neurology, Neurosurgery & Psychiatry*, vol. 75, no. 9, pp. 1235–1244, 2004.

[33] L. Lemieux, G. Hagemann, K. Krakow, and F. G. Woermann, "Fast, accurate, and reproducible automatic segmentation of the brain in t1-weighted volume MRI data," *Magnetic Resonance in Medicine: An Official Journal of the International Society for Magnetic Resonance in Medicine*, vol. 42, no. 1, pp. 127–135, 1999.

[34] D. J. Schaeffer, C. Liu, A. C. Silva, and S. Everling, "Magnetic resonance imaging of marmoset monkeys," *ILAR journal*, 2021.

[35] G. Helms, E. Garea-Rodriguez, C. Schlumbohm, J. König, P. Dechent, E. Fuchs, and M. Wilke, "Structural and quantitative neuroimaging of the common marmoset monkey using a clinical MRI system," *Journal of neuroscience methods*, vol. 215, no. 1, pp. 121–131, 2013.

[36] W. Siemens-Aktiengesellschaft Berlin and A. Hendrix, *Magnets, Flow, and Artifacts Techniques and Applications of Magnetic Resonance.* Siemens AG, 2003.

[37] K. Krupa and M. Bekiesińska-Figatowska, "Artifacts in magnetic resonance imaging," *Polish journal of radiology*, vol. 80, p. 93, 2015.

[38] J. Ashburner and K. J. Friston, "Voxel-based morphometry—the methods," *Neuroimage*, vol. 11, no. 6, pp. 805–821, 2000.

[39] J. L. Whitwell, "Voxel-based morphometry: an automated technique for assessing structural changes in the brain," *Journal of Neuroscience*, vol. 29, no. 31, pp. 9661–9664, 2009.

[40] C. Scarpazza and M. S. De Simone, "Voxel-based morphometry: current perspectives," *Neuroscience and Neuroeconomics*, vol. 5, pp. 19–35, 2016.

[41] E. Van Reeth, I. W. Tham, C. H. Tan, and C. L. Poh, "Super-resolution in magnetic resonance imaging: a review," *Concepts in Magnetic Resonance Part A*, vol. 40, no. 6, pp. 306–325, 2012.

[42] E. Carmi, S. Liu, N. Alon, A. Fiat, and D. Fiat, "Resolution enhancement in MRI," *Magnetic resonance imaging*, vol. 24, no. 2, pp. 133–154, 2006.

[43] F. Lüsebrink, A. Sciarra, H. Mattern, R. Yakupov, and O. Speck, "T 1-weighted in vivo human whole brain MRI dataset with an ultrahigh isotropic resolution of 250 μm," *Scientific data*, vol. 4, no. 1, pp. 1–12, 2017.

[44] R. A. Moats, S. Velan-Mullan, R. Jacobs, I. Gonzalez-Gomez, D. J. Dubowitz, T. Taga, V. Khankaldyyan, L. Schultz, S. Fraser, M. D. Nelson *et al.*, "Micro-MRI at 11.7 t of a murine brain tumor model using delayed contrast enhancement," *Molecular imaging*, vol. 2, no. 3, p. 15353500200303112, 2003.

[45] S. C. Park, M. K. Park, and M. G. Kang, "Super-resolution image reconstruction: a technical overview," *IEEE signal processing magazine*, vol. 20, no. 3, pp. 21–36, 2003.

[46] J. A. Fessler, "Model-based image reconstruction for MRI," *IEEE signal processing magazine*, vol. 27, no. 4, pp. 81–89, 2010.

[47] T. K. Jhamb, V. Rejathalal, and V. Govindan, "A review on image reconstruction through MRI k-space data," *International Journal of Image, Graphics and Signal Processing*, vol. 7, no. 7, p. 42, 2015.

[48] X. Wang, Z. Tan, N. Scholand, V. Roeloffs, and M. Uecker, "Physics-based reconstruction methods for magnetic resonance imaging," *Philosophical Transactions of the Royal Society A*, vol. 379, no. 2200, p. 20200196, 2021.

[49] R. M. Henkelman, "Measurement of signal intensities in the presence of noise in mr images," *Medical physics*, vol. 12, no. 2, pp. 232–233, 1985.

[50] J. Sijbers, A. J. den Dekker, J. Van Audekerke, M. Verhoye, and D. Van Dyck, "Estimation of the noise in magnitude mr images," *Magnetic resonance imaging*, vol. 16, no. 1, pp. 87–90, 1998.

[51] H. Gudbjartsson and S. Patz, "The rician distribution of noisy mri data," *Magnetic resonance in medicine*, vol. 34, no. 6, pp. 910–914, 1995.

[52] M. E. Osadebey, M. Pedersen, D. L. Arnold, and K. E. Wendel-Mitoraj, "Blind blur assessment of MRI images using parallel multiscale difference of gaussian filters," *Biomedical engineering online*, vol. 17, no. 1, pp. 1–22, 2018.

[53] D. C. Noll, J. M. Pauly, C. H. Meyer, D. G. Nishimura, and A. Macovskj, "Deblurring for non-2d fourier transform magnetic resonance imaging," *Magnetic Resonance in Medicine*, vol. 25, no. 2, pp. 319–333, 1992.

[54] M. D. Robson, J. C. Gore, and R. T. Constable, "Measurement of the point spread function in MRI using constant time imaging," *Magnetic resonance in medicine*, vol. 38, no. 5, pp. 733–740, 1997.

[55] S. Y. Moon and J. P. Hornak, "A volume resolution phantom for MRI," *Magnetic resonance imaging*, vol. 28, no. 2, pp. 286–289, 2010.

[56] C. Fellner, W. Müller, J. Georgi, U. Taubenreuther, F. A. Fellner, and W. A. Kalender, "A high-resolution phantom for MRI," *Magnetic resonance imaging*, vol. 19, no. 6, pp. 899–904, 2001.

[57] H. Tan and Y. Zheng, "Point spread function optimization for MRI reconstruction," in *Proceedings.(ICASSP'05). IEEE International Conference on Acoustics, Speech, and Signal Processing, 2005.*, vol. 2. IEEE, 2005, pp. ii–477.

[58] Z. Yan and Y. Lu, "Super resolution of MRI using improved ibp," in *2009 International Conference on Computational Intelligence and Security*, vol. 1. IEEE, 2009, pp. 643–647.

[59] J. T. Hsu, C. Yen, C.-C. Li, M. Sun, B. Tian, and M. Kaygusuz, "Application of wavelet-based pocs super-resolution for cardiovascular MRI image enhancement," in *Third International Conference on Image and Graphics (ICIG'04)*. IEEE, 2004, pp. 572–575.

[60] A. Gholipour, J. A. Estroff, M. Sahin, S. P. Prabhu, and S. K. Warfield, "Maximum a posteriori estimation of isotropic high-resolution volumetric MRI from orthogonal thick-slice scans," in *International Conference on Medical Image Computing and Computer-Assisted Intervention*. Springer, 2010, pp. 109–116.

[61] H. Greenspan, G. Oz, N. Kiryati, and S. Peled, "MRI inter-slice reconstruction using super-resolution," *Magnetic resonance imaging*, vol. 20, no. 5, pp. 437–446, 2002.

[62] E. Ahunbay and J. G. Pipe, "Rapid method for deblurring spiral MRimages," *Magnetic Resonance in Medicine: An Official Journal of the International Society for Magnetic Resonance in Medicine*, vol. 44, no. 3, pp. 491–494, 2000.

[63] P. Getreuer, M. Tong, and L. A. Vese, "A variational model for the restoration of MRimages corrupted by blur and rician noise," in *International Symposium on Visual Computing.* Springer, 2011, pp. 686–698.

[64] G. Sainarayanan, R. Nagarajan, C. D. Raman, and M. Phanindranath, "Iterative image deblurring approach for coronary artery enhancement in MRI image," in *2005 1st International Conference on Computers, Communications, & Signal Processing with Special Track on Biomedical Engineering.* IEEE, 2005, pp. 320–323.

[65] S. Gou, Y. Wang, J. Wu, P. Lee, and K. Sheng, "Lung dynamic MRI deblurring using low-rank decomposition and dictionary learning," *Medical physics*, vol. 42, no. 4, pp. 1917–1925, 2015.

[66] L. Ma, L. Moisan, J. Yu, and T. Zeng, "A dictionary learning approach for poisson image deblurring," *IEEE Transactions on medical imaging*, vol. 32, no. 7, pp. 1277–1289, 2013.

[67] N. Zhao, A. Basarab, D. Kouamé, and J.-Y. Tourneret, "Joint segmentation and deconvolution of ultrasound images using a hierarchical bayesian model based on generalized gaussian priors," *IEEE transactions on Image Processing*, vol. 25, no. 8, pp. 3736–3750, 2016.

[68] S. Setzer, G. Steidl, and T. Teuber, "Deblurring poissonian images by split bregman techniques," *Journal of Visual Communication and Image Representation*, vol. 21, no. 3, pp. 193–199, 2010.

[69] M. A. Figueiredo and J. M. Bioucas-Dias, "Restoration of poissonian images using alternating direction optimization," *IEEE transactions on Image Processing*, vol. 19, no. 12, pp. 3133–3145, 2010.

[70] A. Papoulis, "Generalized sampling expansion," *IEEE transactions on circuits and systems*, vol. 24, no. 11, pp. 652–654, 1977.

[71] J. Yen, "On nonuniform sampling of bandwidth-limited signals," *IRE Transactions on circuit theory*, vol. 3, no. 4, pp. 251–257, 1956.

[72] R. Tsai, "Multiframe image restoration and registration," *Advance Computer Visual and Image Processing*, vol. 1, pp. 317–339, 1984.

[73] S. Kim, N. K. Bose, and H. M. Valenzuela, "Recursive reconstruction of high resolution image from noisy undersampled multiframes," *IEEE Transactions on Acoustics, Speech, and Signal Processing*, vol. 38, no. 6, pp. 1013–1027, 1990.

[74] R. R. Makwana and N. D. Mehta, "Survey on single image super resolution techniques," *IOSR Journal of Electronics and Communication Engineering (IOSR-JECE)*, vol. 5, no. 5, pp. 23–33, 2013.

[75] M. Irani and S. Peleg, "Motion analysis for image enhancement: Resolution, occlusion, and transparency," *Journal of Visual Communication and Image Representation*, vol. 4, no. 4, pp. 324–335, 1993.

[76] ——, "Super resolution from image sequences," in *[1990] Proceedings. 10th International Conference on Pattern Recognition*, vol. 2. IEEE, 1990, pp. 115–120.

[77] A. J. Patti, M. I. Sezan, and A. M. Tekalp, "High-resolution image reconstruction from a low-resolution image sequence in the presence of time-varying motion blur," in *Proceedings of 1st International Conference on Image Processing*, vol. 1. IEEE, 1994, pp. 343–347.

[78] P. Cheeseman, B. Kanefsky, R. Kraft, J. Stutz, and R. Hanson, "Super-resolved surface reconstruction from multiple images," in *Maximum Entropy and Bayesian Methods*. Springer, 1996, pp. 293–308.

[79] H. Shekarforoush and R. Chellappa, "Data-driven multichannel superresolution with application to video sequences," *JOSA A*, vol. 16, no. 3, pp. 481–492, 1999.

[80] D. Fiat, "Method of enhancing an MRI signal," *Number US Patent*, vol. 6, 1997.

[81] S. Peled and Y. Yeshurun, "Superresolution in mri: application to human white matter fiber tract visualization by diffusion tensor imaging," *Magnetic Resonance in Medicine: An Official*

Journal of the International Society for Magnetic Resonance in Medicine, vol. 45, no. 1, pp. 29–35, 2001.

[82] C.-H. Pham, "Deep learning for medical image super resolution and segmentation," Ph.D. dissertation, Ecole nationale supérieure Mines-Télécom Atlantique, 2018.

[83] N. Zhao, "Inverse problems in medical ultrasound images-applications to image deconvolution, segmentation and super-resolution," Ph.D. dissertation, 2016.

[84] M. Irani and S. Peleg, "Improving resolution by image registration," *CVGIP: Graphical models and image processing*, vol. 53, no. 3, pp. 231–239, 1991.

[85] A. N. Tikhonov and V. Y. Arsenin, "Solutions of ill-posed problems," *New York*, vol. 1, p. 30, 1977.

[86] S. Mallat and G. Yu, "Super-resolution with sparse mixing estimators," *IEEE transactions on image processing*, vol. 19, no. 11, pp. 2889–2900, 2010.

[87] R. Morin, A. Basarab, and D. Kouamé, "Alternating direction method of multipliers framework for super-resolution in ultrasound imaging," in *2012 9th IEEE International Symposium on Biomedical Imaging (ISBI)*.   IEEE, 2012, pp. 1595–1598.

[88] S. Boyd, N. Parikh, and E. Chu, *Distributed optimization and statistical learning via the alternating direction method of multipliers*.   Now Publishers Inc, 2011.

[89] P. L. Combettes and J.-C. Pesquet, "Proximal splitting methods in signal processing," in *Fixed-point algorithms for inverse problems in science and engineering*.   Springer, 2011, pp. 185–212.

[90] A. Beck and M. Teboulle, "A fast iterative shrinkage-thresholding algorithm for linear inverse problems," *SIAM journal on imaging sciences*, vol. 2, no. 1, pp. 183–202, 2009.

[91] L. I. Rudin, S. Osher, and E. Fatemi, "Nonlinear total variation based noise removal algorithms," *Physica D: nonlinear phenomena*, vol. 60, no. 1-4, pp. 259–268, 1992.

[92] V. V. Estrela, H. A. Magalhães, and O. Saotome, "Total variation applications in computer vision," in *Handbook of Research on Emerging Perspectives in Intelligent Pattern Recognition, Analysis, and Image Processing*. IGI Global, 2016, pp. 41–64.

[93] J. Luo, Z. Mou, B. Qin, W. Li, F. Yang, M. Robini, and Y. Zhu, "Fast single image super-resolution using estimated low-frequency k-space data in MRI," *Magnetic resonance imaging*, vol. 40, pp. 1–11, 2017.

[94] F. Rousseau, "Brain hallucination," in *European Conference on Computer Vision*. Springer, 2008, pp. 497–508.

[95] F. Rousseau, A. D. N. Initiative *et al.*, "A non-local approach for image super-resolution using intermodality priors," *Medical image analysis*, vol. 14, no. 4, pp. 594–605, 2010.

[96] J. V. Manjón, P. Coupé, A. Buades, D. L. Collins, and M. Robles, "MRI superresolution using self-similarity and image priors," *International journal of biomedical imaging*, vol. 2010, 2010.

[97] J. V. Manjón, P. Coupé, A. Buades, V. Fonov, D. L. Collins, and M. Robles, "Non-local MRI upsampling," *Medical image analysis*, vol. 14, no. 6, pp. 784–792, 2010.

[98] A. Gholipour, J. A. Estroff, and S. K. Warfield, "Robust super-resolution volume reconstruction from slice acquisitions: application to fetal brain MRI," *IEEE transactions on medical imaging*, vol. 29, no. 10, pp. 1739–1758, 2010.

[99] F. Rousseau, K. Kim, C. Studholme, M. Koob, and J.-L. Dietemann, "On super-resolution for fetal brain MRI," in *International conference on medical image computing and computer-assisted intervention*. Springer, 2010, pp. 355–362.

[100] F. Shi, J. Cheng, L. Wang, P.-T. Yap, and D. Shen, "LRTV: MR image super-resolution with low-rank and total variation regularizations," *IEEE transactions on medical imaging*, vol. 34, no. 12, pp. 2459–2466, 2015.

[101] A. Marquina and S. J. Osher, "Image super-resolution by tv-regularization and bregman iteration," *Journal of Scientific Computing*, vol. 37, no. 3, pp. 367–382, 2008.

[102] N. Zhao, Q. Wei, A. Basarab, N. Dobigeon, D. Kouamé, and J.-Y. Tourneret, "Fast single image super-resolution using a new analytical solution for $l_2 - l_2$ problems," *IEEE Transactions on Image Processing*, vol. 25, no. 8, pp. 3683–3697, 2016.

[103] J. Hatvani, A. Basarab, J.-Y. Tourneret, M. Gyöngy, and D. Kouamé, "A tensor factorization method for 3-d super resolution with application to dental ct," *IEEE transactions on medical imaging*, vol. 38, no. 6, pp. 1524–1531, 2018.

[104] Y. Li, "Joint super-resolution/segmentation approaches for the tomographic images analysis of the bone micro-structure," Ph.D. dissertation, Université de Lyon, 2018.

[105] O. I. Abiodun, A. Jantan, A. E. Omolara, K. V. Dada, N. A. Mohamed, and H. Arshad, "State-of-the-art in artificial neural network applications: A survey," *Heliyon*, vol. 4, no. 11, p. e00938, 2018.

[106] I. H. Witten, E. Frank, M. A. Hall, C. Pal, and M. DATA, "Practical machine learning tools and techniques," in *DATA MINING*, vol. 2, 2005, p. 4.

[107] Y. LeCun, L. Bottou, Y. Bengio, and P. Haffner, "Gradient-based learning applied to document recognition," *Proceedings of the IEEE*, vol. 86, no. 11, pp. 2278–2324, 1998.

[108] D. P. Kingma and J. Ba, "Adam: A method for stochastic optimization," *arXiv preprint arXiv:1412.6980*, 2014.

[109] R. Atienza, *Advanced Deep Learning with TensorFlow 2 and Keras: Apply DL, GANs, VAEs, deep RL, unsupervised learning, object detection and segmentation, and more*. Packt Publishing Ltd, 2020.

[110] A. Maier, C. Syben, T. Lasser, and C. Riess, "A gentle introduction to deep learning in medical image processing," *Zeitschrift für Medizinische Physik*, vol. 29, no. 2, pp. 86–101, 2019.

[111] D. Mahapatra, B. Bozorgtabar, and R. Garnavi, "Image super-resolution using progressive generative adversarial networks for medical image analysis," *Computerized Medical Imaging and Graphics*, vol. 71, pp. 30–39, 2019.

[112] C. You, G. Li, Y. Zhang, X. Zhang, H. Shan, M. Li, S. Ju, Z. Zhao, Z. Zhang, W. Cong *et al.*, "Ct super-resolution gan constrained by the identical, residual, and cycle learning ensemble (gan-circle)," *IEEE transactions on medical imaging*, vol. 39, no. 1, pp. 188–203, 2019.

[113] H. Yu, D. Liu, H. Shi, H. Yu, Z. Wang, X. Wang, B. Cross, M. Bramler, and T. S. Huang, "Computed tomography super-resolution using convolutional neural networks," in *2017 IEEE International Conference on Image Processing (ICIP)*. IEEE, 2017, pp. 3944–3948.

[114] J. Hatvani, A. Horváth, J. Michetti, A. Basarab, D. Kouamé, and M. Gyöngy, "Deep learning-based super-resolution applied to dental computed tomography," *IEEE Transactions on Radiation and Plasma Medical Sciences*, vol. 3, no. 2, pp. 120–128, 2018.

[115] O. Oktay, E. Ferrante, K. Kamnitsas, M. Heinrich, W. Bai, J. Caballero, S. A. Cook, A. De Marvao, T. Dawes, D. P. O'Regan *et al.*, "Anatomically constrained neural networks (acnns): application to cardiac image enhancement and segmentation," *IEEE transactions on medical imaging*, vol. 37, no. 2, pp. 384–395, 2017.

[116] A. S. Chaudhari, Z. Fang, F. Kogan, J. Wood, K. J. Stevens, E. K. Gibbons, J. H. Lee, G. E. Gold, and B. A. Hargreaves, "Super-resolution musculoskeletal MRI using deep learning," *Magnetic resonance in medicine*, vol. 80, no. 5, pp. 2139–2154, 2018.

[117] A. Mansoor, T. Vongkovit, and M. G. Linguraru, "Adversarial approach to diagnostic quality volumetric image enhancement," in *2018 IEEE 15th International Symposium on Biomedical Imaging (ISBI 2018)*. IEEE, 2018, pp. 353–356.

[118] C. Ledig, L. Theis, F. Huszár, J. Caballero, A. Cunningham, A. Acosta, A. Aitken, A. Tejani, J. Totz, Z. Wang *et al.*, "Photo-realistic single image super-resolution using a generative adversarial network," in *Proceedings of the IEEE conference on computer vision and pattern recognition*, 2017, pp. 4681–4690.

[119] C. Zhao, A. Carass, B. E. Dewey, and J. L. Prince, "Self super-resolution for magnetic reso-nance images using deep networks," in *2018 IEEE 15th International Symposium on Biomedical Imaging (ISBI 2018)*. IEEE, 2018, pp. 365–368.

[120] A. Jog, A. Carass, and J. L. Prince, "Self super-resolution for magnetic resonance images," in *International Conference on Medical Image Computing and Computer-Assisted Intervention*. Springer, 2016, pp. 553–560.

[121] B. Lim, S. Son, H. Kim, S. Nah, and K. Mu Lee, "Enhanced deep residual networks for single image super-resolution," in *Proceedings of the IEEE conference on computer vision and pattern recognition workshops*, 2017, pp. 136–144.

[122] Y. Chen, Y. Xie, Z. Zhou, F. Shi, A. G. Christodoulou, and D. Li, "Brain MRI super resolution using 3d deep densely connected neural networks," in *2018 IEEE 15th International Symposium on Biomedical Imaging (ISBI 2018)*. IEEE, 2018, pp. 739–742.

[123] J. Chun, H. Zhang, H. M. Gach, S. Olberg, T. Mazur, O. Green, T. Kim, H. Kim, J. S. Kim, S. Mutic *et al.*, "MRI super-resolution reconstruction for MRI-guided adaptive radiotherapy using cascaded deep learning: In the presence of limited training data and unknown translation model," *Medical physics*, vol. 46, no. 9, pp. 4148–4164, 2019.

[124] K. Zeng, H. Zheng, C. Cai, Y. Yang, K. Zhang, and Z. Chen, "Simultaneous single-and multi-contrast super-resolution for brain MRI images based on a convolutional neural network," *Computers in biology and medicine*, vol. 99, pp. 133–141, 2018.

[125] X. Du and Y. He, "Gradient-guided convolutional neural network for MRI image super-resolution," *Applied Sciences*, vol. 9, no. 22, p. 4874, 2019.

[126] X. Zhao, Y. Zhang, T. Zhang, and X. Zou, "Channel splitting network for single MRimage super-resolution," *IEEE Transactions on Image Processing*, vol. 28, no. 11, pp. 5649–5662, 2019.

[127] C.-H. Pham, C. Tor-Díez, H. Meunier, N. Bednarek, R. Fablet, N. Passat, and F. Rousseau, "Multiscale brain MRI super-resolution using deep 3d convolutional networks," *Computerized Medical Imaging and Graphics*, vol. 77, p. 101647, 2019.

[128] M.-I. Georgescu, R. T. Ionescu, and N. Verga, "Convolutional neural networks with intermediate loss for 3d super-resolution of ct and MRI scans," *IEEE Access*, vol. 8, pp. 49 112–49 124, 2020.

[129] C. Baillard, P. Hellier, and C. Barillot, "Segmentation of brain 3d MRimages using level sets and dense registration," *Medical image analysis*, vol. 5, no. 3, pp. 185–194, 2001.

[130] T. Kapur, W. E. L. Grimson, W. M. Wells III, and R. Kikinis, "Segmentation of brain tissue from magnetic resonance images," *Medical image analysis*, vol. 1, no. 2, pp. 109–127, 1996.

[131] N. Gordillo, E. Montseny, and P. Sobrevilla, "State of the art survey on MRI brain tumor segmentation," *Magnetic resonance imaging*, vol. 31, no. 8, pp. 1426–1438, 2013.

[132] M. A. Balafar, A. R. Ramli, M. I. Saripan, and S. Mashohor, "Review of brain MRI image segmentation methods," *Artificial Intelligence Review*, vol. 33, no. 3, pp. 261–274, 2010.

[133] D. W. Shattuck, S. R. Sandor-Leahy, K. A. Schaper, D. A. Rottenberg, and R. M. Leahy, "Magnetic resonance image tissue classification using a partial volume model," *NeuroImage*, vol. 13, no. 5, pp. 856–876, 2001.

[134] K. Kamnitsas, C. Ledig, V. F. Newcombe, J. P. Simpson, A. D. Kane, D. K. Menon, D. Rueckert, and B. Glocker, "Efficient multi-scale 3d cnn with fully connected crf for accurate brain lesion segmentation," *Medical image analysis*, vol. 36, pp. 61–78, 2017.

[135] U. Amato, M. Larobina, A. Antoniadis, and B. Alfano, "Segmentation of magnetic resonance brain images through discriminant analysis," *Journal of neuroscience methods*, vol. 131, no. 1-2, pp. 65–74, 2003.

[136] P. Anbeek, K. L. Vincken, G. S. Van Bochove, M. J. Van Osch, and J. van der Grond, "Probabilistic segmentation of brain tissue in MRimaging," *Neuroimage*, vol. 27, no. 4, pp. 795–804, 2005.

[137] F. Dong and J. Peng, "Brain MRimage segmentation based on local gaussian mixture model and nonlocal spatial regularization," *Journal of Visual Communication and Image Representation*, vol. 25, no. 5, pp. 827–839, 2014.

[138] B. Caldairou, N. Passat, P. A. Habas, C. Studholme, and F. Rousseau, "A non-local fuzzy segmentation method: application to brain MRI," *Pattern Recognition*, vol. 44, no. 9, pp. 1916–1927, 2011.

[139] M. A. G. Ballester, A. Zisserman, and M. Brady, "Segmentation and measurement of brain structures in MRI including confidence bounds," *Medical Image Analysis*, vol. 4, no. 3, pp. 189–200, 2000.

[140] D. G. McLaren, K. J. Kosmatka, E. K. Kastman, B. B. Bendlin, and S. C. Johnson, "Rhesus macaque brain morphometry: a methodological comparison of voxel-wise approaches," *Methods*, vol. 50, no. 3, pp. 157–165, 2010.

[141] K. Hikishima, K. Ando, Y. Komaki, K. Kawai, R. Yano, T. Inoue, T. Itoh, M. Yamada, S. Momoshima, H. Okano *et al.*, "Voxel-based morphometry of the marmoset brain: in vivo detection of volume loss in the substantia nigra of the mptp-treated parkinson's disease model," *Neuroscience*, vol. 300, pp. 585–592, 2015.

[142] K. Hikishima, M. Quallo, Y. Komaki, M. Yamada, K. Kawai, S. Momoshima, H. J. Okano, E. Sasaki, N. Tamaoki, R. Lemon *et al.*, "Population-averaged standard template brain atlas for the common marmoset (callithrix jacchus)," *Neuroimage*, vol. 54, no. 4, pp. 2741–2749, 2011.

[143] X. Palazzi and N. Bordier, "The marmoset brain in stereotaxic coordinates," in *The Marmoset Brain in Stereotaxic Coordinates*. Springer, 2008, pp. 1–59.

[144] A. Woodward, T. Hashikawa, M. Maeda, T. Kaneko, K. Hikishima, A. Iriki, H. Okano, and Y. Yamaguchi, "The brain/minds 3d digital marmoset brain atlas," *Scientific data*, vol. 5, no. 1, pp. 1–12, 2018.

[145] C. Liu, Q. Y. Frank, C. C.-C. Yen, J. D. Newman, D. Glen, D. A. Leopold, and A. C. Silva, "A digital 3d atlas of the marmoset brain based on multi-modal MRI," *Neuroimage*, vol. 169, pp. 106–116, 2018.

[146] A. Iriki, H. J. Okano, E. Sasaki, and H. Okano, *The 3-Dimensional Atlas of the Marmoset Brain: Reconstructible in Stereotaxic Coordinates.* Springer, 2018.

[147] C. Tan, Y. Guan, Z. Feng, H. Ni, Z. Zhang, Z. Wang, X. Li, J. Yuan, H. Gong, Q. Luo *et al.*, "Deepbrainseg: Automated brain region segmentation for micro-optical images with a convolutional neural network," *Frontiers in neuroscience*, vol. 14, 2020.

[148] R. De Feo, A. Shatillo, A. Sierra, J. M. Valverde, O. Gröhn, F. Giove, and J. Tohka, "Automated joint skull-stripping and segmentation with multi-task u-net in large mouse brain MRI databases," *NeuroImage*, vol. 229, p. 117734, 2021.

[149] Z. Akkus, A. Galimzianova, A. Hoogi, D. L. Rubin, and B. J. Erickson, "Deep learning for brain mri segmentation: state of the art and future directions," *Journal of digital imaging*, vol. 30, no. 4, pp. 449–459, 2017.

[150] W. Zhang, R. Li, H. Deng, L. Wang, W. Lin, S. Ji, and D. Shen, "Deep convolutional neural networks for multi-modality isointense infant brain image segmentation," *NeuroImage*, vol. 108, pp. 214–224, 2015.

[151] P. Moeskops, M. A. Viergever, A. M. Mendrik, L. S. De Vries, M. J. Benders, and I. Išgum, "Automatic segmentation of mr brain images with a convolutional neural network," *IEEE transactions on medical imaging*, vol. 35, no. 5, pp. 1252–1261, 2016.

[152] S. Bao and A. C. Chung, "Multi-scale structured cnn with label consistency for brain mr image

segmentation," *Computer Methods in Biomechanics and Biomedical Engineering: Imaging & Visualization*, vol. 6, no. 1, pp. 113–117, 2018.

[153] D. Nie, L. Wang, Y. Gao, and D. Shen, "Fully convolutional networks for multi-modality isointense infant brain image segmentation," in *2016 IEEE 13Th international symposium on biomedical imaging (ISBI)*. IEEE, 2016, pp. 1342–1345.

[154] M. Havaei, N. Guizard, H. Larochelle, and P.-M. Jodoin, "Deep learning trends for focal brain pathology segmentation in mri," in *Machine learning for health informatics*. Springer, 2016, pp. 125–148.

[155] J. Ashburner and K. J. Friston, "Unified segmentation," *Neuroimage*, vol. 26, no. 3, pp. 839–851, 2005.

[156] R. M. Neal and G. E. Hinton, "A view of the em algorithm that justifies incremental, sparse, and other variants," in *Learning in graphical models*. Springer, 1998, pp. 355–368.

[157] B. P. Flannery, W. H. Press, S. A. Teukolsky, and W. Vetterling, "Numerical recipes in c," *Press Syndicate of the University of Cambridge, New York*, vol. 24, no. 78, p. 36, 1992.

[158] Z. Xue, D. Shen, and C. Davatzikos, "Classic: consistent longitudinal alignment and segmentation for serial image computing," *NeuroImage*, vol. 30, no. 2, pp. 388–399, 2006.

[159] M. Reuter, N. J. Schmansky, H. D. Rosas, and B. Fischl, "Within-subject template estimation for unbiased longitudinal image analysis," *Neuroimage*, vol. 61, no. 4, pp. 1402–1418, 2012.

[160] M. Hadj-Hamou, M. Lorenzi, N. Ayache, and X. Pennec, "Longitudinal analysis of image time series with diffeomorphic deformations: a computational framework based on stationary velocity fields," *Frontiers in neuroscience*, vol. 10, p. 236, 2016.

[161] B. Aubert-Broche, V. S. Fonov, D. García-Lorenzo, A. Mouiha, N. Guizard, P. Coupé, S. F. Eskildsen, and D. L. Collins, "A new method for structural volume analysis of longitudinal brain MRI data and its application in studying the growth trajectories of anatomical brain structures in childhood," *Neuroimage*, vol. 82, pp. 393–402, 2013.

[162] Y. Dai, Y. Wang, L. Wang, G. Wu, F. Shi, D. Shen, A. D. N. Initiative *et al.*, "abeat: A toolbox for consistent analysis of longitudinal adult brain MRI," *PloS one*, vol. 8, no. 4, p. e60344, 2013.

[163] F. Bazzi, M. Mescam, A. Diab, O. Falou, H. Amoud, A. Basarab, and D. Kouamé, "Marmoset brain segmentation from deconvolved magnetic resonance images and estimated label maps," *Magnetic resonance in medicine*, 2021.

[164] F. Schick, "Tissue segmentation: a crucial tool for quantitative mri and visualization of anatomical structures," 2016.

[165] M. Lorenzi, X. Pennec, G. B. Frisoni, N. Ayache, A. D. N. Initiative *et al.*, "Disentangling normal aging from alzheimer's disease in structural magnetic resonance images," *Neurobiology of aging*, vol. 36, pp. S42–S52, 2015.

[166] D. J. Bora, "Importance of image enhancement techniques in color image segmentation: a comprehensive and comparative study," *arXiv preprint arXiv:1708.05081*, 2017.

[167] L. W. Hall, "I. introduction," in *An Approach to Definite Forecasting*. University of Pennsylvania Press, 2017, pp. 1–8.

[168] H. Ayasso and A. Mohammad-Djafari, "Joint ndt image restoration and segmentation using gauss–markov–potts prior models and variational bayesian computation," *IEEE Transactions on Image Processing*, vol. 19, no. 9, pp. 2265–2277, 2010.

[169] A. Toma, "Joint super-resolution/segmentation approaches for the tomographic images analysis of the bone micro-architecture," Ph.D. dissertation, Université de Lyon, 2016.

[170] C. Dong, C. C. Loy, and X. Tang, "Accelerating the super-resolution convolutional neural network," in *European conference on computer vision*. Springer, 2016, pp. 391–407.

[171] K. Bahrami, I. Rekik, F. Shi, and D. Shen, "Joint reconstruction and segmentation of 7t-like mr images from 3t mri based on cascaded convolutional neural networks," in *International*

Conference on Medical Image Computing and Computer-Assisted Intervention. Springer, 2017, pp. 764–772.

[172] M. Pereyra, N. Dobigeon, H. Batatia, and J.-Y. Tourneret, "Estimating the granularity coefficient of a potts-markov random field within a markov chain monte carlo algorithm," *IEEE Transactions on Image Processing*, vol. 22, no. 6, pp. 2385–2397, 2013.

[173] J. Besag, "Spatial interaction and the statistical analysis of lattice systems," *Journal of the Royal Statistical Society: Series B (Methodological)*, vol. 36, no. 2, pp. 192–225, 1974.

[174] T. Elguebaly and N. Bouguila, "Bayesian learning of generalized gaussian mixture models on biomedical images," in *IAPR Workshop on Artificial Neural Networks in Pattern Recognition.* Springer, 2010, pp. 207–218.

[175] M. Mansouri and A. Mohammad-Djafari, "Joint super-resolution and segmentation from a set of low resolution images using a bayesian approach with a gauss-markov-potts prior," *International Journal of Signal and Imaging Systems Engineering*, vol. 3, no. 4, pp. 211–221, 2010.

[176] W. K. Hastings, "Monte carlo sampling methods using markov chains and their applications," 1970.

[177] R. M. Neal *et al.*, "Mcmc using hamiltonian dynamics," *Handbook of markov chain monte carlo*, vol. 2, no. 11, p. 2, 2011.

[178] P. Coupé, J. V. Manjón, E. Gedamu, D. Arnold, M. Robles, and D. L. Collins, "Robust rician noise estimation for mr images," *Medical image analysis*, vol. 14, no. 4, pp. 483–493, 2010.

[179] M.-C. Corbineau, D. Kouamé, E. Chouzenoux, J.-Y. Tourneret, and J.-C. Pesquet, "Preconditioned p-ula for joint deconvolution-segmentation of ultrasound images," *IEEE Signal Processing Letters*, vol. 26, no. 10, pp. 1456–1460, 2019.

[180] F. Bazzi, J. D. D. Rodriguez-Callejas, C. Fonta, A. Diab, H. Amoud, O. Falou, M. Mescam, A. Basarab, and D. Kouamé, "Brain segmentation from super-resolved magnetic resonance

images," in *2019 Fifth International Conference on Advances in Biomedical Engineering (ICABME)*. IEEE, 2019, pp. 1–4.

[181] F. Bazzi, M. Mescam, A. Basarab, and D. Kouamé, "On single-image super-resolution in 3d brain magnetic resonance imaging," in *2019 41st Annual International Conference of the IEEE Engineering in Medicine and Biology Society (EMBC)*. IEEE, 2019, pp. 2840–2843.

[182] L. Qu, Y. Zhang, S. Wang, P.-T. Yap, and D. Shen, "Synthesized 7t mri from 3t mri via deep learning in spatial and wavelet domains," *Medical image analysis*, vol. 62, p. 101663, 2020.

[183] A. Basarab, D. Rohrbach, N. Zhao, J.-Y. Tourneret, D. Kouamé, and J. Mamou, "Enhancement of 250-mhz quantitative acoustic-microscopy data using a single-image super-resolution method," in *2017 IEEE 14th International Symposium on Biomedical Imaging (ISBI 2017)*. IEEE, 2017, pp. 827–830.

[184] K. He, X. Zhang, S. Ren, and J. Sun, "Delving deep into rectifiers: Surpassing human-level performance on imagenet classification," in *Proceedings of the IEEE international conference on computer vision*, 2015, pp. 1026–1034.

[185] Y. Jia, E. Shelhamer, J. Donahue, S. Karayev, J. Long, R. Girshick, S. Guadarrama, and T. Darrell, "Caffe: Convolutional architecture for fast feature embedding," in *Proceedings of the 22nd ACM international conference on Multimedia*, 2014, pp. 675–678.

[186] B. A. Landman, A. J. Huang, A. Gifford, D. S. Vikram, I. A. L. Lim, J. A. Farrell, J. A. Bogovic, J. Hua, M. Chen, S. Jarso *et al.*, "Multi-parametric neuroimaging reproducibility: a 3-t resource study," *Neuroimage*, vol. 54, no. 4, pp. 2854–2866, 2011.

[187] C. Dong, C. C. Loy, K. He, and X. Tang, "Image super-resolution using deep convolutional networks," *IEEE transactions on pattern analysis and machine intelligence*, vol. 38, no. 2, pp. 295–307, 2015.

[188] J. Shi, Z. Li, S. Ying, C. Wang, Q. Liu, Q. Zhang, and P. Yan, "Mr image super-resolution

via wide residual networks with fixed skip connection," *IEEE journal of biomedical and health informatics*, vol. 23, no. 3, pp. 1129–1140, 2018.

[189] B. J. Soher, B. M. Dale, and E. M. Merkle, "A review of mr physics: 3T versus 1.5T," *Magnetic resonance imaging clinics of North America*, vol. 15, no. 3, pp. 277–290, 2007.

[190] J. Alvarez-Linera, "3T mri: Advances in brain imaging," *European journal of radiology*, vol. 67, no. 3, pp. 415–426, 2008.

[191] K. Bahrami, F. Shi, I. Rekik, Y. Gao, and D. Shen, "7T-guided super-resolution of 3T mri," *Medical physics*, vol. 44, no. 5, pp. 1661–1677, 2017.

[192] K. Bahrami, F. Shi, I. Rekik, and D. Shen, "Convolutional neural network for reconstruction of 7T-like images from 3T mri using appearance and anatomical features," in *Deep Learning and Data Labeling for Medical Applications*.   Springer, 2016, pp. 39–47.

[193] K. Bahrami, F. Shi, X. Zong, H. W. Shin, H. An, and D. Shen, "Hierarchical reconstruction of 7T-like images from 3t mri using multi-level cca and group sparsity," in *International Conference on Medical Image Computing and Computer-Assisted Intervention*.   Springer, 2015, pp. 659–666.

[194] Y. Zhang, J.-Z. Cheng, L. Xiang, P.-T. Yap, and D. Shen, "Dual-domain cascaded regression for synthesizing 7t from 3t mri," in *International Conference on Medical Image Computing and Computer-Assisted Intervention*.   Springer, 2018, pp. 410–417.

[195] Z. Hui, X. Wang, and X. Gao, "Fast and accurate single image super-resolution via information distillation network," in *Proceedings of the IEEE conference on computer vision and pattern recognition*, 2018, pp. 723–731.

[196] L. Risser, A. Sadoun, M. Mescam, K. Strelnikov, S. Lebreton, S. Boucher, P. Girard, N. Vayssière, M. G. Rosa, and C. Fonta, "In vivo localization of cortical areas using a 3d computerized atlas of the marmoset brain," *Brain Structure and Function*, vol. 224, no. 5, pp. 1957–1969, 2019.

[197] J. Lawson and Y. Lim, "Karcher means and karcher equations of positive definite operators," *Transactions of the American Mathematical Society, Series B*, vol. 1, no. 1, pp. 1–22, 2014.

[198] J. Ashburner, "A fast diffeomorphic image registration algorithm," *Neuroimage*, vol. 38, no. 1, pp. 95–113, 2007.

[199] H. R. Sheikh, A. C. Bovik, and G. De Veciana, "An information fidelity criterion for image quality assessment using natural scene statistics," *IEEE Transactions on image processing*, vol. 14, no. 12, pp. 2117–2128, 2005.

[200] H. R. Sheikh, M. F. Sabir, and A. C. Bovik, "A statistical evaluation of recent full reference image quality assessment algorithms," *IEEE Transactions on image processing*, vol. 15, no. 11, pp. 3440–3451, 2006.

[201] C.-Y. Yang, C. Ma, and M.-H. Yang, "Single-image super-resolution: A benchmark," in *European conference on computer vision*. Springer, 2014, pp. 372–386.

[202] E. J. Vinke, M. de Groot, V. Venkatraghavan, S. Klein, W. J. Niessen, M. A. Ikram, and M. W. Vernooij, "Trajectories of imaging markers in brain aging: the rotterdam study," *Neurobiology of Aging*, vol. 71, pp. 32–40, 2018.

[203] E. R. Sowell, B. S. Peterson, P. M. Thompson, S. E. Welcome, A. L. Henkenius, and A. W. Toga, "Mapping cortical change across the human life span," *Nature neuroscience*, vol. 6, no. 3, pp. 309–315, 2003.

[204] A. F. Fotenos, A. Snyder, L. Girton, J. Morris, and R. Buckner, "Normative estimates of cross-sectional and longitudinal brain volume decline in aging and ad," *Neurology*, vol. 64, no. 6, pp. 1032–1039, 2005.

[205] P. Coupé, G. Catheline, E. Lanuza, J. V. Manjón, and A. D. N. Initiative, "Towards a unified analysis of brain maturation and aging across the entire lifespan: A mri analysis," *Human brain mapping*, vol. 38, no. 11, pp. 5501–5518, 2017.

[206] C. Lebel and C. Beaulieu, "Longitudinal development of human brain wiring continues from childhood into adulthood," *Journal of Neuroscience*, vol. 31, no. 30, pp. 10 937–10 947, 2011.

[207] K. L. Bergfield, K. D. Hanson, K. Chen, S. J. Teipel, H. Hampel, S. I. Rapoport, J. R. Moeller, and G. E. Alexander, "Age-related networks of regional covariance in mri gray matter: reproducible multivariate patterns in healthy aging," *Neuroimage*, vol. 49, no. 2, pp. 1750–1759, 2010.

[208] N. Raz, U. Lindenberger, K. M. Rodrigue, K. M. Kennedy, D. Head, A. Williamson, C. Dahle, D. Gerstorf, and J. D. Acker, "Regional brain changes in aging healthy adults: general trends, individual differences and modifiers," *Cerebral cortex*, vol. 15, no. 11, pp. 1676–1689, 2005.

[209] S. Ramanoël, E. Hoyau, L. Kauffmann, F. Renard, C. Pichat, N. Boudiaf, A. Krainik, A. Jaillard, and M. Baciu, "Gray matter volume and cognitive performance during normal aging. a voxel-based morphometry study," *Frontiers in aging neuroscience*, vol. 10, p. 235, 2018.

[210] A. Giorgio, L. Santelli, V. Tomassini, R. Bosnell, S. Smith, N. De Stefano, and H. Johansen-Berg, "Age-related changes in grey and white matter structure throughout adulthood," *Neuroimage*, vol. 51, no. 3, pp. 943–951, 2010.

[211] F. Farokhian, C. Yang, I. Beheshti, H. Matsuda, and S. Wu, "Age-related gray and white matter changes in normal adult brains," *Aging and disease*, vol. 8, no. 6, p. 899, 2017.

[212] J. Ashburner, "Vbm tutorial," *Tech. repWellcome Trust Centre for Neuroimaging, London, UK*, 2010.

[213] C. Gaser and F. Kurth, "Manual computational anatomy toolbox-cat12," *Structural brain mapping Group at the Departments of Psychiatry and Neurology, University of Jena*, 2017.

[214] J. V. Manjón, P. Coupé, L. Martí-Bonmatí, D. L. Collins, and M. Robles, "Adaptive non-local means denoising of mr images with spatially varying noise levels," *Journal of Magnetic Resonance Imaging*, vol. 31, no. 1, pp. 192–203, 2010.

[215] J. G. Sled, A. P. Zijdenbos, and A. C. Evans, "A nonparametric method for automatic correction of intensity nonuniformity in mri data," *IEEE transactions on medical imaging*, vol. 17, no. 1, pp. 87–97, 1998.

[216] B. B. Avants, N. J. Tustison, G. Song, P. A. Cook, A. Klein, and J. C. Gee, "A reproducible evaluation of ants similarity metric performance in brain image registration," *Neuroimage*, vol. 54, no. 3, pp. 2033–2044, 2011.

[217] K. Van Leemput, F. Maes, D. Vandermeulen, and P. Suetens, "Automated model-based bias field correction of mr images of the brain," *IEEE transactions on medical imaging*, vol. 18, no. 10, pp. 885–896, 1999.

[218] M. Styner, C. Brechbuhler, G. Szckely, and G. Gerig, "Parametric estimate of intensity inhomogeneities applied to mri," *IEEE transactions on medical imaging*, vol. 19, no. 3, pp. 153–165, 2000.

[219] N. Tustison and J. Gee, "N4itk: Nick's n3 itk implementation for mri bias field correction," *Insight Journal*, vol. 9, 2009.

[220] N. J. Tustison, B. B. Avants, P. A. Cook, Y. Zheng, A. Egan, P. A. Yushkevich, and J. C. Gee, "N4itk: improved n3 bias correction," *IEEE transactions on medical imaging*, vol. 29, no. 6, pp. 1310–1320, 2010.

[221] S. Song, Y. Zheng, and Y. He, "A review of methods for bias correction in medical images," *Biomedical Engineering Review*, vol. 1, no. 1, 2017.

[222] M. Reuter, H. D. Rosas, and B. Fischl, "Highly accurate inverse consistent registration: a robust approach," *Neuroimage*, vol. 53, no. 4, pp. 1181–1196, 2010.

[223] J. Ashburner, "Computational anatomy with the spm software," *Magnetic resonance imaging*, vol. 27, no. 8, pp. 1163–1174, 2009.

[224] J. Pinheiro and D. Bates, *Mixed-effects models in S and S-PLUS*. Springer Science & Business Media, 2006.

[225] K. L. Mills, A.-L. Goddings, M. M. Herting, R. Meuwese, S.-J. Blakemore, E. A. Crone, R. E. Dahl, B. Güroğlu, A. Raznahan, E. R. Sowell *et al.*, "Structural brain development between childhood and adulthood: Convergence across four longitudinal samples," *Neuroimage*, vol. 141, pp. 273–281, 2016.

[226] S. D. Tardif, D. A. Smucny, D. H. Abbott, K. Mansfield, N. Schultz-Darken, and M. E. Yamamoto, "Reproduction in captive common marmosets (callithrix jacchus)," *Comparative medicine*, vol. 53, no. 4, pp. 364–368, 2003.

[227] S. D. Tardif, K. G. Mansfield, R. Ratnam, C. N. Ross, and T. E. Ziegler, "The marmoset as a model of aging and age-related diseases," *ILAR journal*, vol. 52, no. 1, pp. 54–65, 2011.

[228] L. Nobis, S. G. Manohar, S. M. Smith, F. Alfaro-Almagro, M. Jenkinson, C. E. Mackay, and M. Husain, "Hippocampal volume across age: Nomograms derived from over 19,700 people in uk biobank," *NeuroImage: Clinical*, vol. 23, p. 101904, 2019.

[229] A. Abedelahi, H. Hasanzadeh, H. Hadizadeh, and M. T. Joghataie, "Morphometric and volumetric study of caudate and putamen nuclei in normal individuals by mri: effect of normal aging, gender and hemispheric differences," *Polish journal of radiology*, vol. 78, no. 3, p. 7, 2013.

[230] E. Bauer, M. Toepper, H. Gebhardt, B. Gallhofer, and G. Sammer, "The significance of caudate volume for age-related associative memory decline," *brain research*, vol. 1622, pp. 137–148, 2015.

[231] I. Driscoll, D. A. Hamilton, H. Petropoulos, R. A. Yeo, W. M. Brooks, R. N. Baumgartner, and R. J. Sutherland, "The aging hippocampus: cognitive, biochemical and structural findings," *Cerebral cortex*, vol. 13, no. 12, pp. 1344–1351, 2003.

[232] J. P. Lister and C. A. Barnes, "Neurobiological changes in the hippocampus during normative aging," *Archives of neurology*, vol. 66, no. 7, pp. 829–833, 2009.

[233] M. Brudfors, Y. Balbastre, P. Nachev, and J. Ashburner, "A tool for super-resolving multimodal clinical mri," *arXiv preprint arXiv:1909.01140*, 2019.

[234] J. M. Valverde, V. Imani, A. Abdollahzadeh, R. De Feo, M. Prakash, R. Ciszek, and J. Tohka, "Transfer learning in magnetic resonance brain imaging: A systematic review," *Journal of Imaging*, vol. 7, no. 4, p. 66, 2021.

[235] Q. Delannoy, C.-H. Pham, C. Cazorla, C. Tor-Díez, G. Dollé, H. Meunier, N. Bednarek, R. Fablet, N. Passat, and F. Rousseau, "Segsrgan: Super-resolution and segmentation using generative adversarial networks—application to neonatal brain mri," *Computers in Biology and Medicine*, vol. 120, p. 103755, 2020.

[236] A. Sadoun, "Etude des fonctions exécutives chez le marmouset: effet du vieillissement dans un environnement semi-naturel," Ph.D. dissertation, Toulouse 3, 2017.

————-